Faculty of Science and Engineering
Department of Exploration Geophysics

Rock Physics Changes due to CO_2 Injection: The CO2CRC Otway Project

Putri Sari Wisman

This thesis is presented for the Degree of
Doctor of Philosophy
of
Curtin University

September 2012

Declaration

To the best of my knowledge and belief this thesis contains no material previously published by any other person except where due acknowledgment has been made.

This thesis contains no material which has been accepted for the award of any other degree or diploma in any university.

Signature: .....

Date: 28 May 2013

DEDICATION

This work is dedicated to my dearest husband - Petrus - and our daughters - Pheodora and Phoebe - also to my parents for their constant support and encouragement during my years of study

ABSTRACT

The CO2CRC Otway Project aims to demonstrate that CO_2 can be safely stored in a depleted gas field and that an appropriate monitoring strategy can be deployed to verify its containment. The project commenced in 2005, with the baseline 3D seismic collected early in January 2008. CO_2 was injected into depleted gas reservoir known as Waarre-C at Naylor field in April 2008. The first monitor survey was recorded in January 2009, shortly after the injection of 35,000 tonnes of CO_2. Early predictions in the program suggested that the resulting time-lapse seismic effect will be very subtle because of the reservoir depth, small area, complexity, small amount of CO_2/CH_4 in 80/20 ratio injected and most of all partial saturation of the reservoir sand. The key challenge than presented to this research was how subtle exactly is the effect going to be? To answer that question I had to develop a workflow that will produce very accurate prediction of the elastic property changes in the reservoir caused by CO_2 injection. Then the sensitivity of time-lapse seismic methodology in detecting subtle changes in the reservoir is investigated.

The rock physics model I propose uses the "effective" grain bulk modulus (K_{grain}) to represent the average mineralogy of the grains. The validity of this approach is confirmed by good agreement achieved between V_{psat} core with V_{psat} computed from the log data using the "effective" modulus. . The use of "effective" K_{grain} was further justified by petrographic analysis. This has increased the modelling precision and changed the predicted time-lapse effect due to CO_2 injection from 3% as an average over the reservoir sequence as previously computed to nearly 6%. The significance is that 6% change could be detected with high precision monitoring methodologies. The *in-situ* saturation type is homogeneous, according to the analysis path assumed in this thesis. If some patchiness exists in the reservoir it will be away from the wells and it would further elevate CO_2 related seismic effect.

The time-lapse seismic methodology at Otway site utilised very high survey density in order to increase sensitivity. On the negative side, weak sources and the change of the source type between the surveys resulted in non-repeatability greater or of the similar order as the time-lapse signal were expected to be. Hence the interpretation of

the time-lapse P-wave seismic data assumed somewhat different path. I used the model-based post-stack seismic acoustic inversion in a similar way that history matching is used in reservoir simulation studies. I performed successive fluid substitutions, followed by the well ties and inversions. The objective was to look into the inversion error. Then the modelled fluid saturation case that result in minimal inversion error reflects the most likely state of the reservoir. Modelling using 35,000 tonnes of CO_2/CH_4 mix with 35% water saturation and 65% CO_2/CH_4 mix produced the smallest error when reinstating logs to the 2009 reservoir state.

The time-lapse anomaly observed in the data exceeds predictions derived through the rock physics model, seismic modelling and simulation models. This is likely to be the case in general as the effect of CO_2 onto a reservoir is difficult to predict. A "conservative" approach may result in an under-prediction of time-lapse seismic effects. Consequently, the predicted and measured seismic effects can be used as the lower and the upper bound of the time-lapse effects at Naylor field, respectively. The method presented here for analysis of a subtle time-lapse signal could be applied to the cases with similar challenges elsewhere.

ACKNOWLEDGEMENTS

First of all, I would like to thank Curtin University of Technology for making it possible for me to attend their Department of Exploration Geophysics through the CIRTS program. This work was sponsored by Australian Commonwealth Government through CO2CRC.

I would like to express my personal thanks for their support and for allowing me to work on this project during my research period. In particular I would like to thank Sandeep Sharma, Kevin Dodds, Dr. Don Sherlock, Professor John Kaldi, Tony Siggins, and Dr. Josh Xu for his useful input parameters from reservoir simulation.

I would especially like to acknowledge my supervisor, Associate Professor Milovan Urosevic, for his advice, motivation, and insight during my research period. It was a pleasure to work with him and I truly appreciate the support that he provided and the effort he put forth in assisting me with my work. I am also thankful to Professor Boris Gurevich who has helped me and encouraged me to finish my study, to Professor Brian Evans who "found" me, to Associate Professor Bruce Hartley, to Tess Dance (CSIRO) and to Post-Doctoral Dr. Ruiping Li for serving as a member of my supervisor panel which has provided me with important theoretical and technical input, to Eva Caspari for giving me very useful suggestions to my last chapter, and the last member of the team I also would like to express my gratitude to Deirdre who helped me with the administration procedures, and made sure everything went smoothly.

My thanks go to ConocoPhillips Indonesia for their support, Jesse Baker – my mentor who has proofread my thesis, John Hughes - Chief Geophysicist, Pak Asfamudi – Sr. Personal Manager for Exploration, Redo – my boss, and all my colleagues I have worked with over the last two years. Last but not least, for all my friends at Curtin: Dina, Said, Marcos, Mohammed, Shahid, Nasser, Chris, and Dariush, Elmar, Floren, Osni, Yousuf, Abdullah; for all my friends at CO2CRC team member: Allison, Jim, Linda, Ulrike; big thank you for all discussions, for sharing in my research and life and for our friendship. My deep thanks go to my cousin – Iin - who let me stay with her in Perth while I was away from home.

Finally, special thanks go to my lovely husband – *Petrus* - for his patience, devotion and continued support for me to finish this study, to my children – *Pheodora* and *Phoebe*, they are my source of inspiration, and to *my parents*, they have helped me through this busy time by looking after me and my family.

TABLE OF CONTENTS

LIST OF FIGURES

LIST OF TABLES

Chapter 1 INTRODUCTION

1.1 World energy review

1.1.1 Energy demand

Fossil fuels will continue to be the primary source of energy supplying the world's demand for decades to come. The International Energy Agency projects (IEA, 2011) predicted that global energy demand in the New Policies Scenario (NPS 450S) will increase by more than one-third from 2010 to 2035. The Agency projected that increased demand will be met mainly by fossils fuels. Growth in demand for fossil fuels is led by the transportation and industry sector. More than 70 per cent of the increase in demand is forecasted to come from developing countries such as India, Indonesia, Brazil, China, and the Middle East. There will be a large increase in demand for all fuels, but the share of fossil fuels in global primary energy consumption will fall slightly from 81% in 2010 to 75% in 2035; natural gas will be the only fossil fuel to increase its share in the global mix over the period to 2035. This is despite the projected rapid increases in the use of renewable energies, led by hydropower and others such as geothermal, wind, solar, biofuels, and so forth (Figure 1.1).

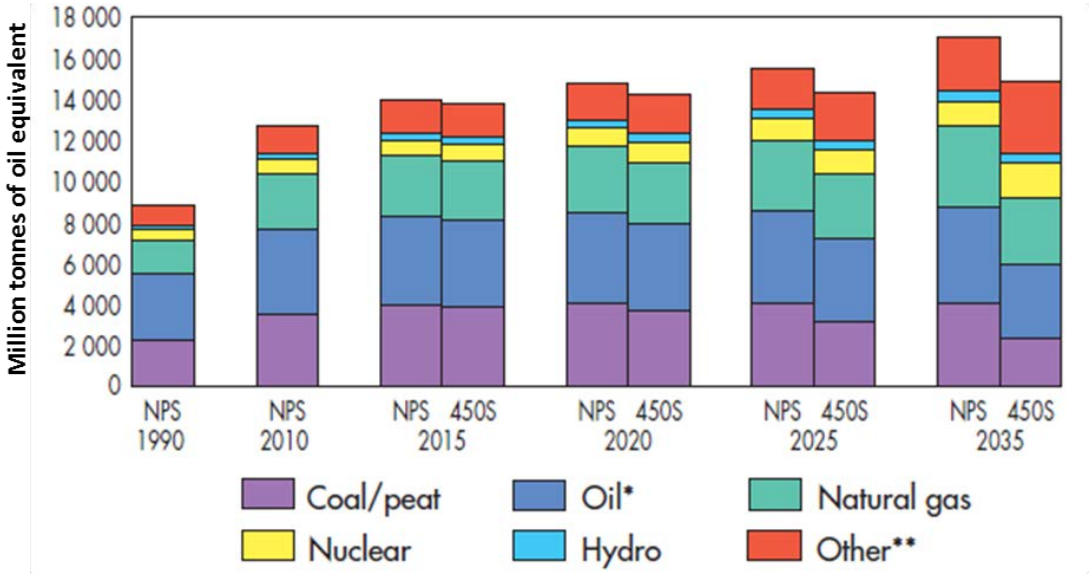

Figure 1.1 World primary energy demand in the New Policies Scenario (IEA, 2011).

The Agency projected an increase in carbon dioxide emissions from fossil-fuels energy demand from 30.2 billion metric tons in 2008 to 35.2 billion metric tons in 2020 and 43.2 billion metric tons in 2035 (IEA, 2011). Even if governments around the world successfully introduced all the policies and measures they are currently considering to reduce emissions, carbon dioxide emissions would still grow by 43 per cent by year 2035, with the major contributor being coal.

1.1.2 Energy production

Fossil fuels remain the most important energy source for transportation, electricity and industry. To meet the increase in world energy demand (conventional and unconventional resources), according to International Energy Outlook (2011), total supply will increase by a total of 26.6 million barrels per day from 2008 to 2035. This scenario assumes that OPEC producers will choose to maintain their market share of world energy production, and that OPEC member countries will invest in incremental production capacity so that their conventional oil production represents approximately 40% of total global energy production throughout the projection. Figure 1.2 shows world energy production and demand by region projection from the year 2009 to 2035 in three cases of Reference, High Oil Price, and Low Oil Price, depicting the total production from conventional and unconventional resources by OPEC, Non-OPEC members, Organization for Economic Cooperation and Development (OECD), and Non-OECD.

By 2035 most of the liquids producers will come from the OPEC Middle East, which will account for 36 million barrels of oil equivalent per day, while other OPEC members will account for 20 million barrels of oil equivalent per day and non-OPEC members for 61 million barrels of oil equivalent per day. OECD liquids demand will grow to 47.9 million barrels per day, while non-OECD liquids demand will grow to 62.9 million barrels per day by 2035, as a shown in Figure 1.2.

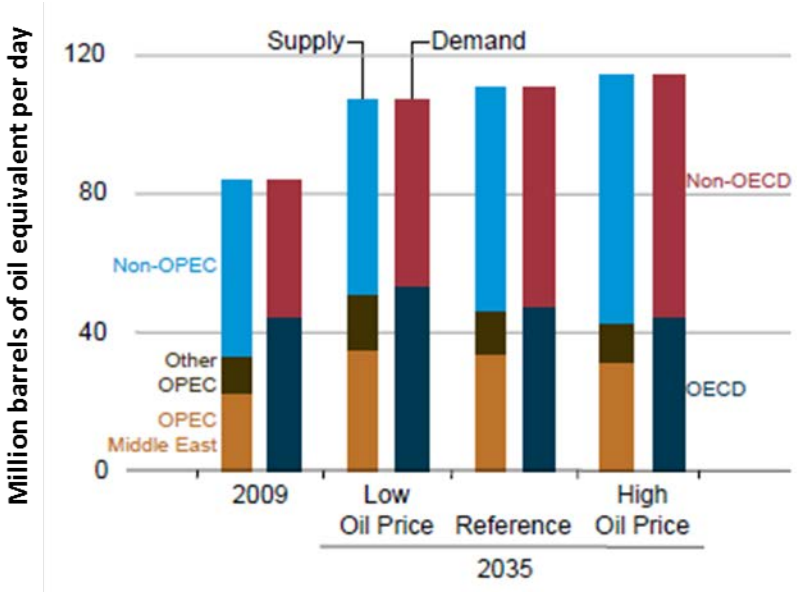

Figure 1.2 World energy production and demand by region in three cases, 2009 and 2035 (EIA, 2011).

Annual Energy Outlook (2011) forecasted the increasing trend of unconventional resources from 2000 to 2035 to meet the energy demand while the other products of energy remain stable (Figure 1.3). In general the increase in energy demand and its production will increase carbon dioxide emissions into the atmosphere, which in effect will have a certain degree of impact on global warming and climate change.

Increasing energy production in Australia is anticipated by planning liquefied natural gas projects with a total value of around $20 billion to meet the domestic demand (Cook et al., 2000).

1.2 CO_2 geosequestration

One of the promising ways of mitigating greenhouse gas emissions and potentially slowing or reversing the undesired effects of global warming is to capture and store or sequester CO_2 into deep geological formations. Geosequestration - capturing carbon dioxide that would otherwise be emitted to the atmosphere and injecting it into deep geological formations (reservoir units which have good porosity and

permeability and have been proven to be overlain by an excellent seal to prevent leakage) is one viable option.

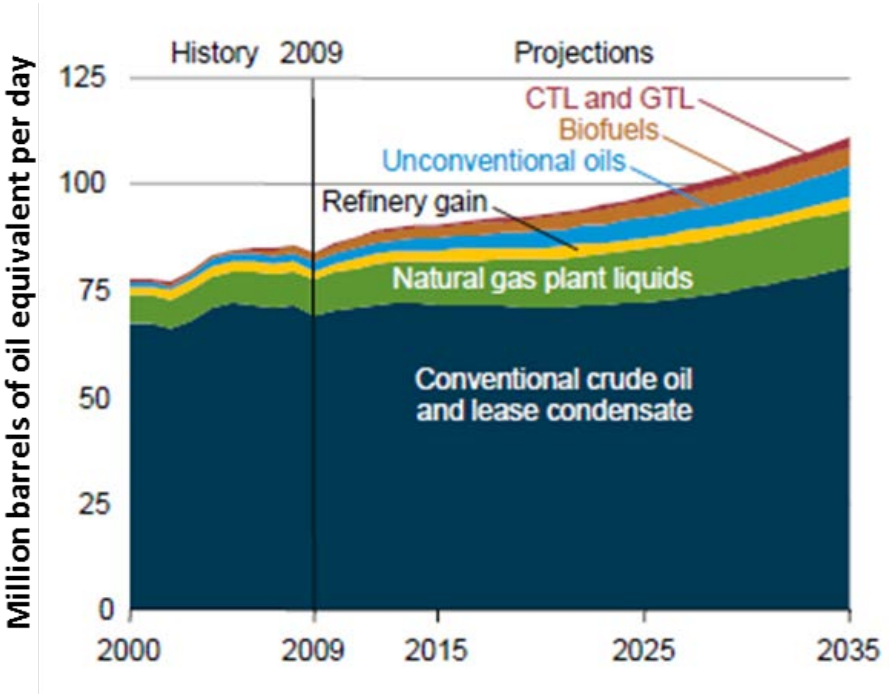

Figure 1.3 World energy production by source from Reference case, 2000 – 2035 (EIA, 2011).

The International Energy Agency describes it as "one of the most promising options for mitigating emissions in the longer term". In its Special Report on Carbon Dioxide Capture and Storage, the Intergovernmental Panel on Climate Change (IPCC) said that geosequestration has the potential to reduce overall (greenhouse gas) mitigation costs and increase flexibility in achieving greenhouse gas emission reductions. In its Climate Change 2007: Mitigation of Climate Change, the IPCC concluded that geosequestration was among the technologies with the largest economic potential to reduce emissions from electricity generation, as well as in the cement, ammonia, and iron manufacturing industries. It also found that attempts to stabilise greenhouse gas concentrations in the atmosphere at lower levels increased the emphasis on technologies such as geosequestration. This approach involves the capture and storage of carbon dioxide (Carbon Capture and Storage - CCS). CCS enables the combustion of fossil fuels (coal, gas or oil) without significant emissions of carbon into the atmosphere. It utilises technologies that have been widely practiced in the oil and gas industry for many years.

Extensive examinations around the world of geosequestration objectives established that the largest quantities of CO_2 could be stored in saline aquifers. However the major CO_2 producing plants are rarely located near large saline aquifers. An additional and perhaps more economically viable option is to store CO_2 into depleted gas and oil fields as their occurrence is widespread and where some or all of the infrastructure is already in place. Figure 1.4 shows an overview of geological storage options which are considered and/or available for use.

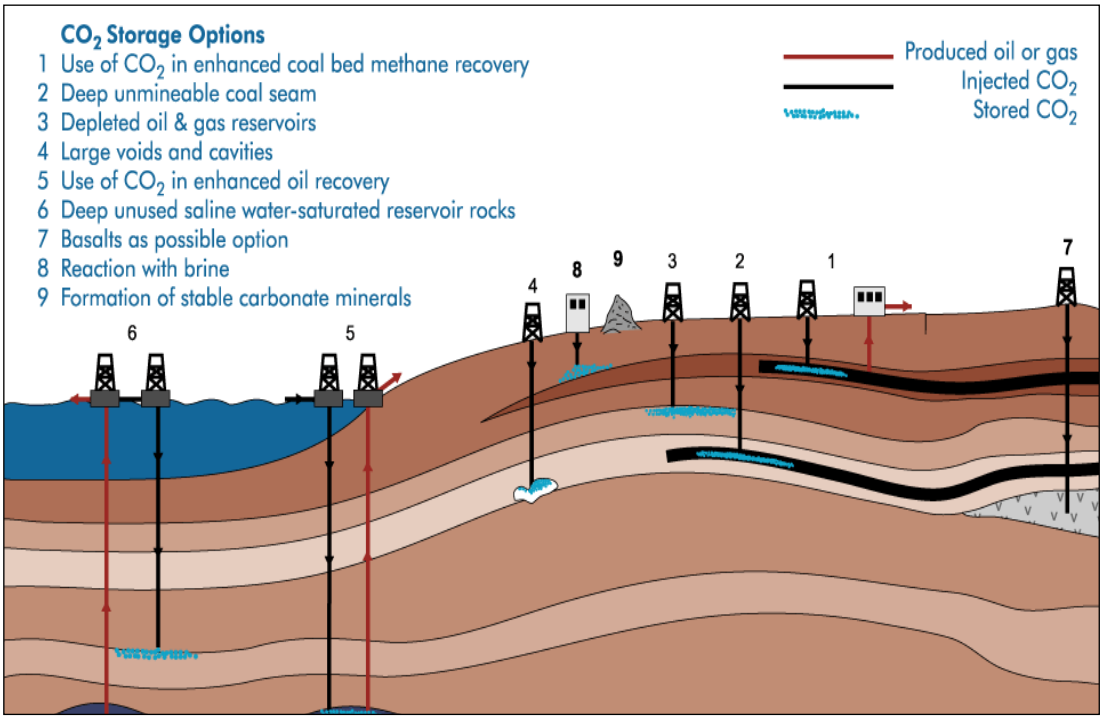

Figure 1.4 Overview of geological storage options (CO2CRC).

The world's first industrial application of CO_2 storage in a saline aquifer commenced in the *Sleipner* Field in 1996 (Arts et al., 2004; McKenna, 2004). Apart from the *Weyburne* project in Alberta, Canada (Brown, 2002; Davis and Benson, 2004; Davis et al., 2003; Herawati, 2002; Herawati and Davis, 2003; Terrell et al.), *In Salah* project in Algeria (Riddiford et al., 2005) and *Gorgon* project in Western Australia, all other projects are strictly of a scientific nature such as the *Frio* project in Texas (Hovorka et al., 2006) and *Ketzin* in Germany (Forster et al., 2006). Current sequestration projects around the world are shown in Figure 1.5.

Figure 1.5 Carbon Capture and Storage projects around the world. Yellow, red, blue, and green balloons represent in planning, cancelled, pilot, and operational projects, respectively (courtesy of Scottish Carbon Capture and Storage, 2013).

Australia's first experiment in deep geosequestration is ongoing. The CO2CRC Otway Project aims to demonstrate geosequestration is a viable option for CO_2 mitigation under Australian conditions (Cook, 2006). The project differs significantly in the nature of its geological character and storage process from the existing *Sleipner*, *Weyburn*, *Frio* and *Ketzin* sequestration projects. Besides allowing international collaboration in research, this project offers an opportunity to gain important additional information on the permanence and safety of CO_2 geosequestration. The Otway project also addresses the more general issue of the viability of seismic monitoring of CO_2 storage in depleted gas reservoirs.

1.3 Seismic monitoring of CO_2

While the concept of CO_2 storage underground is a straightforward process, its long-term containment must be monitored and verified to prevent further CO_2 leakage and release to the atmosphere. Time-lapse (TL) seismic methods have proven successful in monitoring hydrocarbon movement during production and for increasing understanding of recovery processes. The application of time-lapse methodology is

therefore attractive as a primaryethod for monitoring of CO_2 plume migration over time.

Surface seismic methods, with their excellent horizontal resolution power, are important for seismic monitoring. The full power of the method is accomplished through time-lapse seismic methodology. Differences in seismic amplitudes or travel times (time lapse signal) between the surveys allow for mapping of the fluid migration within a reservoir over time during the EOR/EGR. The time-lapse signal can be related to changes in rock properties caused by injection which allows optimisation of the field's production. Borehole seismic methods add value to surface seismic methods with their increased vertical resolution power and the specific geometry of borehole surveys, which allows analysis of the transmitted wave field and hence fundamental investigations of wave motion and propagation. Consequently most of the geosequestration projects utilise a combination of surface and borehole seismic methodologies.

The world's first industrial application of CO_2 storage using time-lapse seismic monitoring techniques (TL seismic) in a saline aquifer commenced in the *Sleipner* Field in 1996 (Arts et al., 2004; Chadwick et al., 2005; Chadwick et al., 2002; McKenna, 2004; Skov et al., 2002). They observed that the effects of CO_2 on the seismic data are large both in term of seismic amplitude and in velocity push down effects. The Reservoir Characterisation Project of the Colorado School of Mines – *Weyburn* project - used high resolution time-lapse and multi-component surface and borehole seismic data (VSP and cross-hole) to monitor a miscible CO_2 flood in a fractured carbonate reservoir (Davis and Benson, 2004). The *In Salah* project in Algeria (Riddiford et al., 2005), the world's first CO_2 storage project performed in an actively producing gas reservoir, used the seismic method for monitoring the CO_2 plume. CO_2 storage projects such as *Frio* in Texas used VSP (Hovorka and Cohen, 2006; Hovorka and Knox, 2003) and *Ketzin* in Germany used 3D seismic for monitoring the CO_2 plume (Juhlin et al., 2007; Yordkayhun). These two projects investigated CO_2 storage in saline formations. The CO2CRC Otway Project in Australia however is injecting CO_2 into a depleted natural gas field and uses a combination of 3D seismic and 3D VSP to verify the containment of CO_2 within the reservoir. This project also attempts to analyse the plume disposition in clastic

sediments (Li et al., 2006; Wisman et al., 2005; Wisman and Urosevic, 2007). Through repeated monitor surveys over time a series of seismic images can be made and related to rock property changes and fluid distribution in the reservoir.

1.4 Rock physics model of CO_2

Seismic velocities are sensitive to the changes of pore fluid, porosity, mineral composition, pore pressure, and fluid saturation. Such changes become difficult to quantify if the sensitivities are not understood. The changes are very subtle when compared to the seismic wavelength. Thus, discovering and understanding the relationship between the seismic data and the reservoir has become increasingly important for hydrocarbon detection, reservoir characterisation, and reservoir monitoring.

The Injection of CO_2 into a heterogeneous reservoir, where residual gas saturation is present throughout most of the sand column and the thickness is less than 25 meters, is expected to cause very subtle changes in the elastic properties of the reservoir rock. The result from a rock physics model based on Texas Gulf Coast showed that a wedge of CO_2 in 10 m thick sand could be detected (Myer et al., 2003). However, such a small effect could be "lost" even through appropriate fluid substitution methodology. Considering the inherently low repeatability of land seismic it becomes even more important to accurately predict the time-lapse seismic response at this site.

Wang (1997) has shown that the feasibility of repeatability consists of two aspects: the physical aspect and the seismic. The physical aspect involves the changes in reservoir properties such as pressure, temperature, elastic properties, and contrast in pore fluid compressibility. Thus, to quantity these effects, rock physics modelling plays an important role in bridging reservoir and seismic properties. Rock physics modelling has been used to quantify time-lapse seismic modelling and relate interpretation of elastic properties changes to variations in fluid saturation and pressure during monitoring (Avseth et al., 2005; McKenna et al., 2003; Wang et al., 1998; Wulff et al., 2008).

Rock physics modelling links rock properties and seismic properties by taking into account variations in local geology. It helps to ascertain and validate whether time-lapse seismic methodology is a feasible technique for monitoring. The rock physics model here is used in conjunction with time-lapse seismic changes, thus enabling quantification of the seismic interpretation. Furthermore, detailed rock physics analysis provides the capability to forecast the changes in the time-lapse seismic response during long-term CO_2 storage within the basin prior to project commencement.

1.5 Aim of the research

The CO2CRC Otway Project - the first CO_2 storage project in Australia - aims to demonstrate that CO_2 can be safely stored in a depleted gas field and that an appropriate monitoring strategy can be deployed to verify its containment. The advantage of injecting CO_2 into a depleted gas field is the access to well-established infrastructure and existing data, including wells for monitoring, seismic data for property analysis and down-hole data for hydrocarbon interpretation. Historically, CO_2 distribution and containment are assessed through time-lapse seismic changes. The geological complexity of Naylor gas field in Australia with a relatively deep, small-sized reservoir, and with the presence of residual methane provides a challenge in designing a successful geophysical monitoring program. Because of this, the monitoring program will be limited to the application of seismic methods only. Considering the inherently low repeatability of land seismic, it becomes even more important to accurately predict the time-lapse seismic response at this site. Achieving successful seismic monitoring will depend on the magnitude of change in the elastic properties of the depleted gas reservoir. Since seismic technology may not be applicable in all situations, a feasibility study must be conducted prior to project commencement.

A feasibility study involving a simulation of time-lapse seismic response for this reservoir showed that the injection of CO_2 in the residual methane-saturated zone will produce very subtle changes in elastic properties, hence, very small changes in seismic response (Li et al., 2006). Such a small effect could be "lost" even through appropriate fluid substitution methodology. Therefore, an accurate prediction of

elastic properties of the reservoir rock should be made using the calibration of log and petrophysical data with core samples.

Similar studies on the seismic monitoring of CO_2 injection have been done (Arts et al., 2003; Davis and Benson, 2001; Fanchi, 2001; Herawati, 2002; Herawati and Davis, 2003; McKenna, 2004; McKenna et al., 2003; Terrell et al.; Wang et al., 1998; Xue and Ohsumi, 2004), mostly on saline or carbonate reservoirs. However, seismic monitoring of CO_2 injection into a depleted gas reservoir in a clastic environment has not been previously studied, especially the rock physics aspect of such a system.

One of the aims of this research is to find and apply appropriate fluid substitution methodology for the Naylor-1 and CRC-1 wells to be able to accurately predict time-lapse signals resulting from CO_2 injection. For that I need to build rock physics models using well log data that are calibrated with core sample analyses. These models can then be used to quantify the change in elastic properties of the reservoir rock due to CO_2 injection at varying pressures and saturations. The results are then applied to a time-lapse seismic synthetic response prediction model for long-term CO_2 storage. This research also relates variations of seismic attributes computed from seismic reflection data to the changes in elastic properties that will help further refine the analysis including distinguishing the seismic effects caused by CO_2 injection from the existing residual methane saturation. Finally, this study will comment on the CO_2 migration path and containment within the reservoir.

The rock physics modelling results of this research project are general in nature and can be used and applied to similar CO_2 storage projects to quantify elastic property changes and predict seismic responses prior and after CO_2 injection. to acquisition of monitoring surveys. By better understanding the limitations of the existing data, pitfalls and wasted effort can be avoided in future long-term CO_2 storage projects.

1.6 Thesis configuration

The structure of this thesis is designed to follow the chronological development of the project. Chapter 1 presents a review of world energy uses, their impact on global climate change and the subsequent need for this research program. Chapter 2

introduces the concept of geological sequestration. The chapter begins with a general discussion of various geological storage sites and of trapping mechanisms, with an emphasis on depleted gas reservoirs. It concludes with a general discussion of potential seismic monitoring and verification technologies including several similar project examples from the geophysical literature. Also included is an introduction to CO_2 geological storage in Australia with a focus on the CO2CRC Otway Project. Chapter 3 discusses the background theory applied in this project, examining the fundamental theories of seismic and rock physics. Chapter 4 then discusses the aims of the CO2CRC Otway Project, the geological setting of Otway Basin (focusing on the Naylor gas field study area), an overview of previous studies, how the data was collected and conditioned (pre-production and pre-injection data), and current reservoir characterisation. Chapter 5 presents the development workflow of a rock physics model for Waarre sandstone unit-C (Waarre-C) taking into account the local geology. This work involved the calibration of ultrasonic core measurements with log data and core sample analysis (petrology). The chapter concludes with a discussion of how the rock physics model could be used to improve the monitoring strategy. Chapter 6 presents seismic modelling results from fluid substitution methodology (rock physics model) and provides the basis of the analysis of rock physics changes due to CO_2 injection. This chapter also describes the work that relates variations of seismic attributes to the changes in reservoir elastic properties. A discussion on the success and limitation from the investigated methodology identified during this research concludes the chapter. The final conclusion and recommendation of the research are outlined in Chapter 7. The cited reference list and references for general reading are at the end of the thesis.

Chapter 2 CO_2 GEOLOGICAL SEQUESTRATION

2.1 Introduction

A comprehensive geological characterization of several gas accumulations across Otway basin has been conducted over the past few decades. The wealth of knowledge that has been gained by industry and research institutions has formed the fundamental basis for development of the Otway basin pilot CO_2 sequestration project.

CO_2 can be stored underground in various ways, depending on the geological setting, reservoir properties, local pressure and temperature conditions, etc. This chapter reviews the potential of CO_2 storage in different geological settings and introduces the monitoring methodology with particular emphases on the CO2CRC Otway Project.

2.2 Type of CO_2 storages

Figure 2.1 gives an illustration of various options for an underground CO_2 storage system. The three main alternatives are: depleted oil and gas fields, saline formations and un-mineable coal-beds (Bachu, 2000; Baines and Worden, 2004; Lewis and Shinn, 2001). Only those three main options of storage are discussed in this document. Other storage options will be referred to as future geologic sequestration (DOE, 2008).

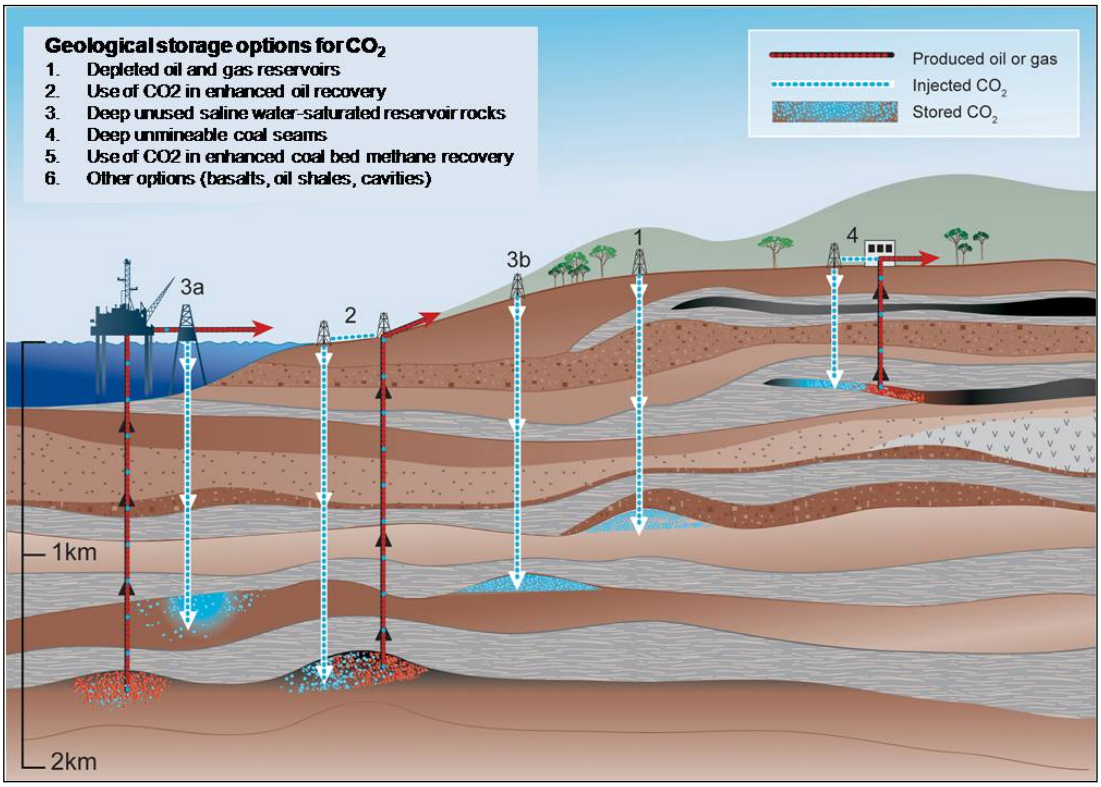

Figure 2.1 Candidate geologic reservoirs for storing CO_2 (CO2CRC, 2008).

2.2.1 Depleted oil and gas reservoir and use of CO_2 in enhance oil/gas recovery

Depleted oil and gas reservoirs are good candidates for CO_2 storage as they have very high probability of retaining the fluid on the geological time scale. In addition, depleted reservoirs have favourable characteristics such as good porosity and permeability. Abundance of pre-existing geological and geophysical information, well-developed infrastructure and low-cost maintenance make these reservoirs highly attractive for CO_2 storage. However the available pore space for CO_2 storage could actually be small. Moreover, rapid depletion of hydrocarbon pore space could result in partial pore collapse. The old wells could provide potential leak points, and the timing of availability of depleted fields with respect to the source of CO_2 (Bradshaw and Rigg, 2001; Streit and Siggins, 2005) may be yet another issue.

Despite all the potential drawbacks, CO_2 injection into depleted oil and gas reservoirs enable us in general to accurately calculate potential CO_2 storage capacity (Holloway, 1997). Stevens et al. (2001) estimated the worldwide capacity for CO_2

storage in depleted oil and gas reservoirs approximately at 900 Gt. This number represents almost 150 years of the world's power plant emissions.

Injecting CO_2 into depleted oil and gas reservoirs has additional economical benefits through enhanced oil/gas recovery for the extension of field life by improving rate of recovery and improved pressure support. This method has been used widely for tertiary recovery/enhanced production. A major research project combining EOR with CO_2 storage was started in 2000 at the *Weyburn* field, Canada. The 4D-3C time-lapse seismic surveys at Marly zone before and after injection showed the significant amplitude anomaly difference over time in Figure 2.2 a) and b). It appears that repeated seismic reflection measurements (time-lapse) can be utilized at this location for direct monitoring of CO_2 displacement in the reservoir.

a)

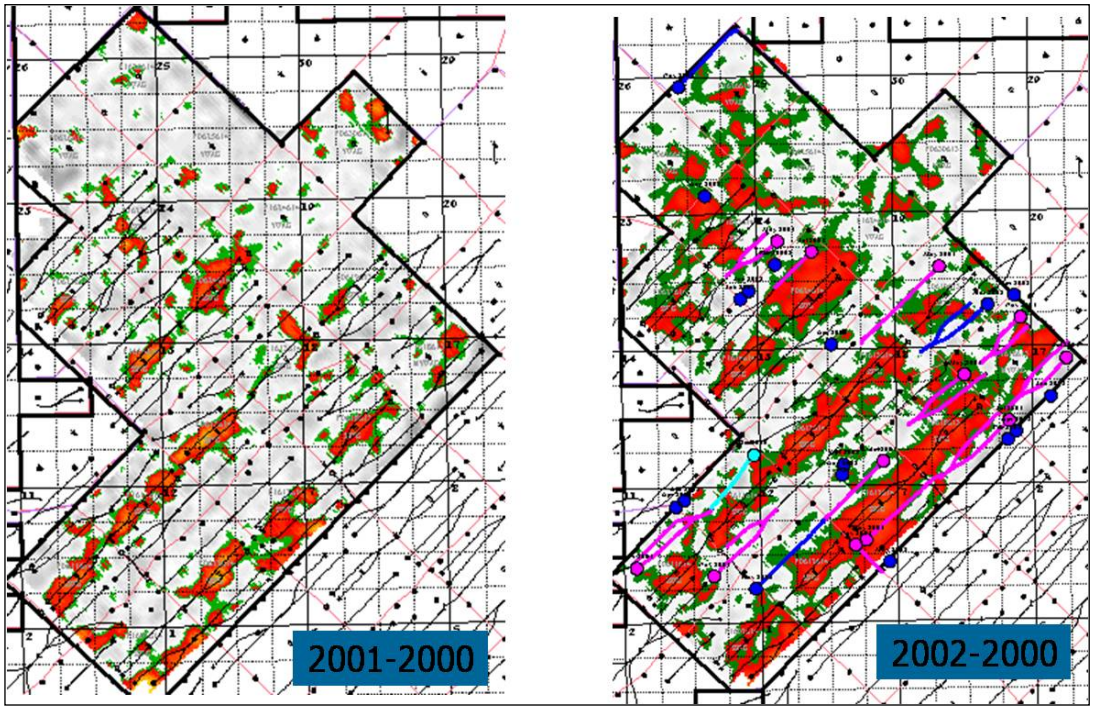
2001-2000
2002-2000

b)

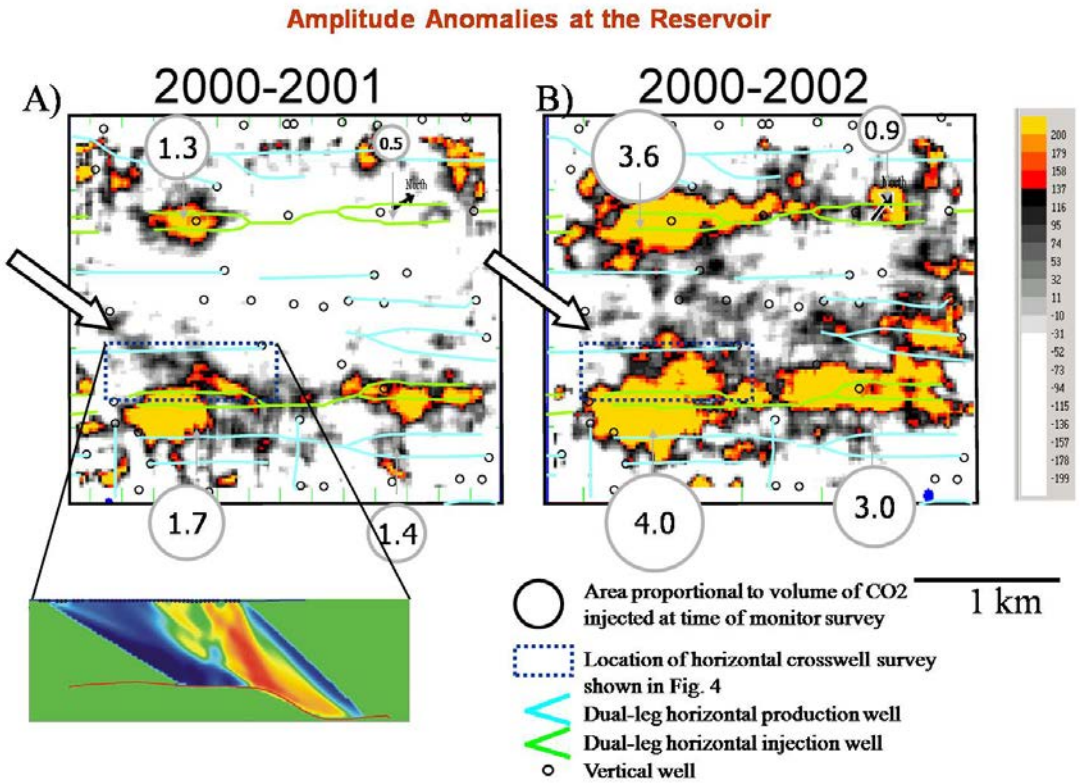
Amplitude Anomalies at the Reservoir
A) 2000-2001
B) 2000-2002
1.3
0.5
1.7
1.4
3.6
0.9
4.0
3.0
Area proportional to volume of CO2 injected at time of monitor survey
1 km
Location of horizontal crosswell survey shown in Fig. 4
Dual-leg horizontal production well
Dual-leg horizontal injection well
Vertical well

(Courtesy of EnCana Corporation)

Figure 2.2 a) Amplitude anomaly difference map of Marly zone over time and b) Marly zone location of injection and production wells associated with amplitude anomalies at the reservoir and surrounding area.

2.2.2 Saline formation

Saline formations are characterised as porous sedimentary rocks saturated with formation waters that are not considered suitable for human consumption or agriculture or industrial use. Saline formations are considered as an ideal CO_2 storage site since they can often store large volumes of CO_2 (Bachu, 2000; Bradshaw et al., 2002; Holloway, 1997). Davidson et al. (2001) studied globally saline aquifers could account for between 20% and 500% of the projected total CO_2 emissions to 2050 where in the U.S. alone could potentially store up to 500 billion tons of CO_2 (DOE, 2008).

Supercritical CO_2 can be effectively stored in deep saline formations because of its high density and high solubility in formation water. These formations are commonly less understood because of the lack of geological and geophysical data. Thus, injecting CO_2 into saline formations is less attractive as it does not have direct economical benefit other than to prevent CO_2 release into the atmosphere. The main advantage of saline aquifers is that they are widely distributed over the world and have large potential storage capacity. Hence it is not a surprise that *Sleipner* field in North Sea was the world's first industrial CO_2 storage project in a saline formation. Long term studies of *Sleipner* CO_2 storage confirmed that saline aquifers are indeed favourable for CO_2 sequestration and particularly favourable for monitoring due to large elastic properties contrast (Arts et al., 2000; Chadwick et al., 2002). Further storage projects are already being planned in North West Shelf, Australia, the biggest being the Gorgon field where about 3 millions tones of CO_2 per year are planned to be injected over a period of at least 20 years. The gas contains up to 14% CO_2 and will be injected into saline formation about 2000m below the producing reservoir (IEA, 2003).

2.2.3 Un-mineable coal-beds and use of CO_2 in enhanced coal bed methane recovery

Coal beds typically contain large amounts of methane that is absorbed onto the surface of the coal. Extraction of the gas requires depressurisation, usually by pumping water out of the coal seam. Coal beds represent an attractive opportunity for near-term sequestration of large volume of anthropogenic CO_2 at low costs. Roughly twice as much CO_2 can be absorbed on coal as methane, such that injected CO_2 has the potential to displace methane and remain sequestered in the coal seam (Gunter et al., 1997; Reeves, 2003) . Storage density is greatest in coals at depths less than 600m when CO_2 is in the gaseous phase, not supercritical (Ennis-King and Paterson, 2001), as shown in Figure 2.3. A pilot project in San Juan Basin, New Mexico suggests that methane production from the extensive coal beds could be increased by 75% with injection of CO_2 (Reeves, 2001).

Finally and predictably, most coal reserves are located nearby large CO_2 emission sources such as power plants. Furthermore, injection of CO_2 into coal beds actually enhances the coal beds methane recovery, albeit only for a short time as CO_2 causes so-called swelling of the permeable paths in coal seams which is typically mean cleat system (face cleats).

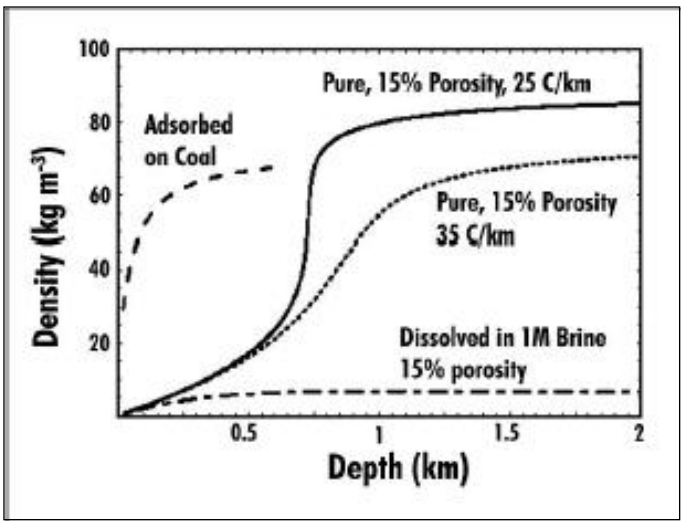

Figure 2.3 Total storage densities as a function of depth. The hydrostatic pressure gradient is 10.5 MPa/km, the mean surface temperature is 15 C and

the geothermal gradient is 25 C/km unless noted. This highligthing how the storage density of CO_2 absorbed onto coal at subcritical depths is comparable to the storage density of CO_2 captured in pore space at supercritical depths (Ennis-King and Paterson, 2001).

2.3 CO_2 trapping mechanism

CO_2 can be sequestered in geological formations by five principal trapping mechanisms: structural/stratigraphic, hydrodynamics, solubility/dissolution, mineral and residual (Hitchon, 1996; Watson et al., 2004; Watson and Gibson-Poole, 2005).

2.3.1 Structural/stratigraphic trapping

Structural/stratigraphic trapping relates to the CO_2 that is not dissolved in formation water. When supercritical CO_2 rises upwards by buoyancy it can be trapped in a structural type of closure or by reduction of permeability due stratigraphic changes. Common structural traps include anticlines and tilted fault blocks (Figure 2.4 a) and stratigraphic traps include a lateral change in facies up-dip or a depositional pinch-out (Figure 2.4 b) (Biddle and Wielchowsky, 1994). These provide physical traps for geological storage of CO_2.

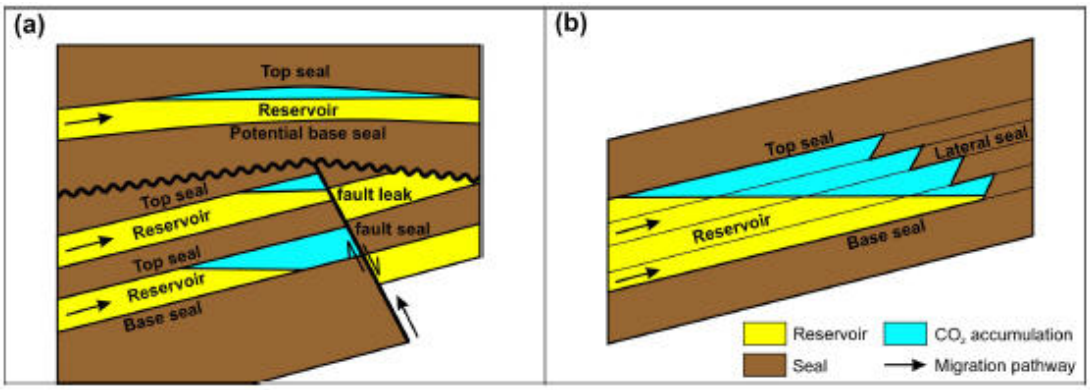

Figure 2.4 Illustration of a) structural and b) stratigraphic trap for CO_2 trapping mechanism (Biddle and Wielchowsky, 1994).

2.3.2 Hydrodynamic trapping

CO_2 can be trapped as a gas or supercritical fluid under a low-permeability (<50 md) reservoir/seal. The presence of clays and cements in these low-permeability formations result in high residual gas trapping and a higher formation water saturation in high permeability formations (>100 md) (Watson and Gibson-Poole, 2005). The impact of higher residual gas trapping and water saturation is beneficial for sequestration where the very low flow velocity occurred for hydrodynamic trapping (Bachu et al., 1994; Ennis-King and Paterson, 2001; Flett et al., 2004). The trapping mechanism follows the flow of the CO_2 on the dip of the sealing formation and the flow velocity and direction of the *in-situ* formation water. This flow can lead to very long residence times, in the order of thousands to millions of years in horizontal or gentle dipping reservoirs (Figure 2.5) (Bachu et al., 1994).

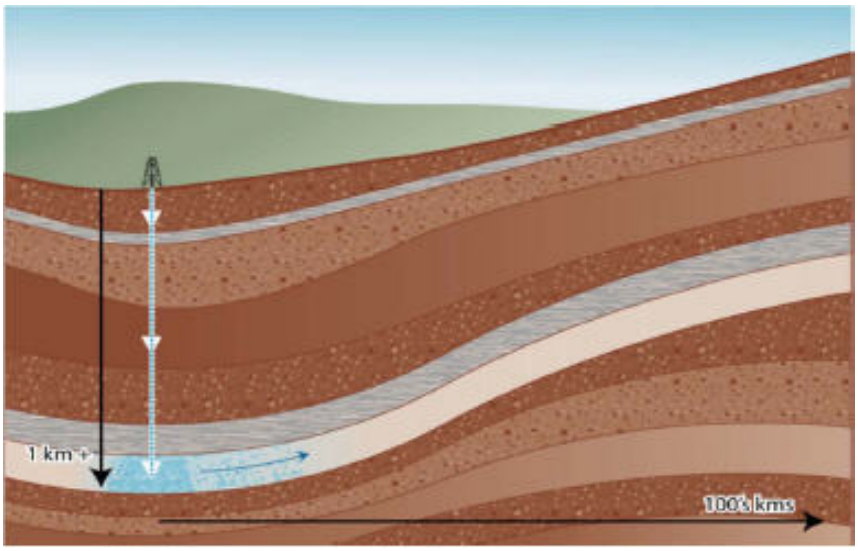

Figure 2.5 Hydrodynamic trapping of CO_2 where the CO_2 migration pathway is 10s to 100s km long allowing for a long residence time follows the bedding plane (Bachu et al., 1994).

2.3.3 Solubility trapping (immiscible CO_2)

When the amount of CO_2 exceeds the amount soluble in water, CO_2 enters an immiscible phase. CO_2 starts as a separate phase when injected, and over time dissolves into the water (Ennis-King and Paterson, 2001). This occurs at the CO_2/water interface and is subject to a rate of dissolution that is dependent on the

area of interface and rate at which CO_2-saturated water is transmitted away from the interface or by the diffusion rate driven by the introduced chemical gradient (Bachu et al., 1994).

The solubility of CO_2 is controlled by the pressure, temperature and salinity of the water (Vargaftik, 1975). Solubility decreases with increasing temperature and salinity, and increases with pressure (Spycher et al., 2003). Once the CO_2 is dissolved, the chemistry of the system controls what will happen in the short- and long-term future of CO_2 sequestration.

2.3.4 Mineralogical trapping

For mineralogical trapping of CO_2 to occur, the reservoir rock requires a sufficient supply of cautions to precipitate with bicarbonate in solution. While there is abundant bicarbonate from the dissolution of CO_2 to form carbonate minerals, the limiting factor is the caution source, either from formation water or the host minerals. This trapping mechanism is the most permanent form of geological storage of CO_2 (Bachu et al., 1994; Hitchon, 1996; Watson et al., 2004).

2.3.5 Residual trapping

Residual trapping occurs when CO_2 becomes trapped in the pore space by capillary forces and cease to flow (Figure 2.6). Residual CO_2 saturation varies between 5-30% based on typical relative permeability. Over time, the residual trapped CO_2 dissolves into the formation water (Ennis-King and Paterson, 2001; Flett et al., 2004).

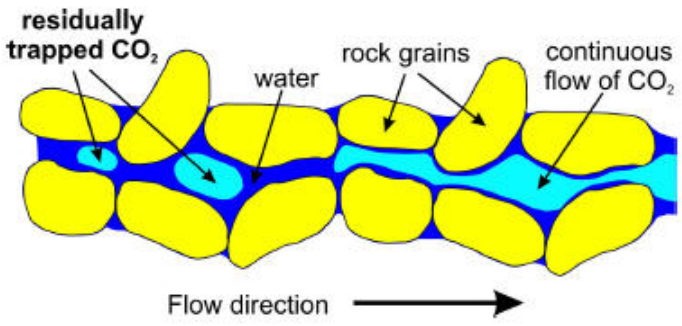

Figure 2.6 Residual trapping of CO_2.

2.4 Monitoring and verification methodology

For CO_2 to be injected into the geological formations, a monitoring and verification (M&V) methodology needs to be defined. The ultimate objective of any M&V program is to verify CO_2 containment in the reservoir over a specified period of time. Cost-effective monitoring and verification of fluid movement during CO_2 injection is a necessary part of a practical geologic sequestration strategy (Gasperikova et al., 2004). Monitoring can be categorized into baseline and operational monitoring while verification monitoring consists of both subsurface and environmental confirmation of performance criteria (Dodds et al., 2006). Seismic techniques are well-known and well-developed for monitoring production in petroleum reservoirs as well as recovery process (EOR/EGR/ECBM). Because seismic properties depends on fluid content, pressure, saturation and elastic properties changes of the reservoir itself, it is expected that seismic methods will be the fundamental technology used to monitor CO_2 sequestration, but other geophysical, non-seismic methods and non geophysical methods which might provide sufficient monitoring resolution at a significant lower cost need to be considered. Of particular interest to this research is CO_2 sequestration at Otway Project. A comprehensive M&V program is illustrated in Figure 2.7.

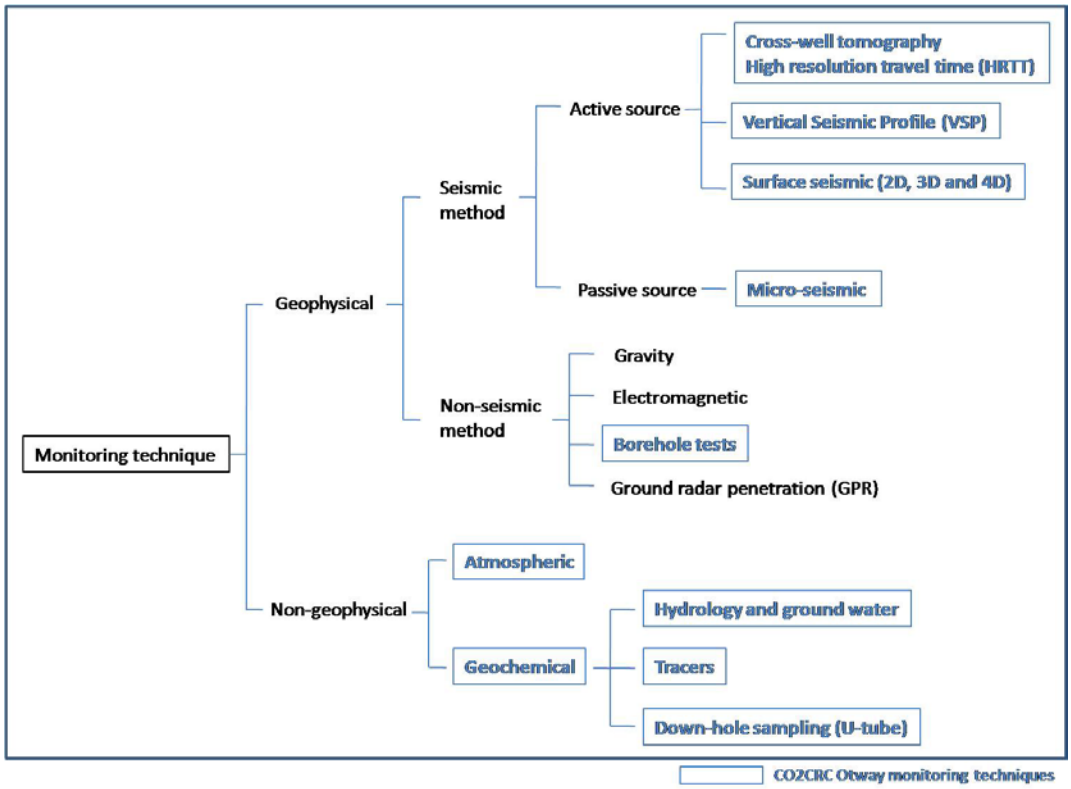

Figure 2.7 Schematics of the monitoring techniques that are applied in the CO2CRC Otway Project.

2.4.1 CO_2 sequestration monitoring with seismic methods

The seismic method is by far the most important geophysical technique used for oil and gas field production, including the recovery process (extending the reservoir life time). The techniques developed for enhanced recovery processes in the oil and gas industry are directly applicable to monitoring of CO_2 sequestration. Its predominance is due to accuracy, resolution and penetration. Accuracy can be achieved by defining high data density seismic surveys. The dependence of seismic resolution on frequency bandwidth of the received signal implies that there is a trade-off between the distance that seismic energy can travel and the resolution that can be achieved (Esmersoy et al., 1998). Two types of resolution are considered - lateral and vertical, both of which are controlled by signal bandwidth. The resolution in general is based on the Fresnel zone, a circular area on a reflector whose size depends on the depth of the reflector, the velocity above it and the dominant frequency of the source wavelet. Increasing frequency content and decreasing the width of Fresnel zone will

improve the lateral resolution. The depth of penetration depends primarily on the source strength and the rate of signal attenuation.

The real power of 3D surface reflection seismic is in sensing or detecting, rather than resolving, lateral variations in lithology and fluid content. Temporal or vertical resolution of individual layers is generally limited to tens of meters along the depth axis. However, depending on the reflection contrast, very thin layers can produce reflections and be detected, albeit we cannot tell much about the properties of the layer itself.

Very high resolution is typically achieved with sonic logging, producing resolution in the order of centimetres. Unfortunately such high-frequency signal can typically penetrate less than a meter into the formation away from the borehole. Vertical seismic profile and cross-well/borehole seismic are used to bridge the gap between sonic logging and surface seismic in creating high resolution image away from the well. For the CO2CRC Otway Project, apart from 2D and 3D VSP surveys aimed at producing a high resolution image around a borehole, the so-called high resolution travel time method (HRTT) was also deployed in Naylor-1 well (monitoring well). This methodology utilises permanent geophone installation and has the potential to monitor fluid movement, fine changes in fluid level and verify the volume of CO_2 injected in monitoring well. Figure 2.8 illustrates the degree of resolution versus the range of penetration offered by the various seismic methods. A combination of different seismic methods may be used to provide satisfactory resolution and adequate coverage of the sequestration site. Passive seismic (micro-seismic monitoring) and time-lapse borehole surveys were also deployed in Otway for early leak detection purposes that could be caused by stress changes yielding to fault reactivation. A wealth of methodologies deployed at Otway creates very good model for studying CO_2 injection process in a depleted gas reservoir. Application of multi-component seismic in a time-lapse (TL) fashion, could offer the ability to define contrast in elastic properties, subtle changes in fluid content and/or density changes. The full potential of multi-component TL surveys is still to be assessed.

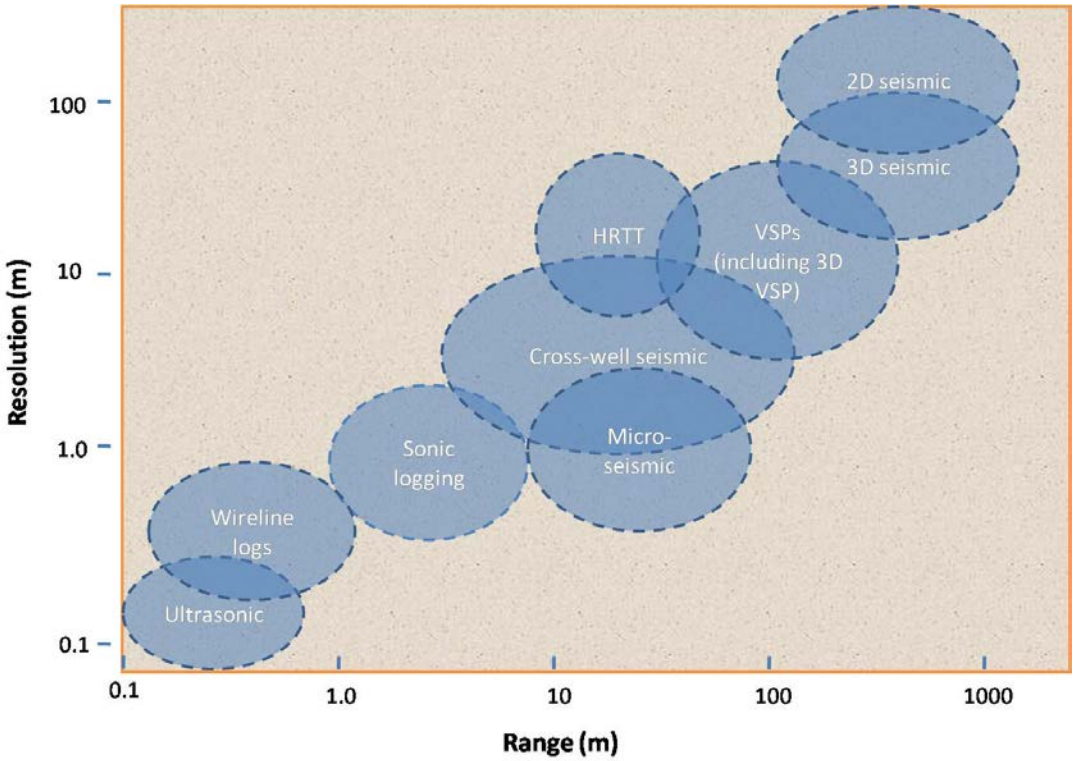

Figure 2.8 A schematic representation of the range and resolution available from different seismic methods. The resolution is typically controlled by the frequency bandwidth of the received signal. The maximum range of each method is primarily controlled by signal attenuation that increases rapidly with frequency and the minimum range is determined by the resolution limit and the source –receiver geometry (Esmersoy et al., 1998).

2.4.1.1 Surface seismic

The use of surface seismic for monitoring has been growing steadily during the last decade and is now a well-established technique for reservoir monitoring especially related to enhance recovery process. Extensive lateral coverage makes surface seismic a suitable tool to monitor the CO_2 distribution before and after injection which are not sampled by wells through the repetition of the measurements. This is referred to as time-lapse seismic or 4D seismic. These measurements have observed changes in compressional (P-) and shear (S-) wave velocity, amplitude anomalies, variation in anisotropy and attenuation as a consequence of CO_2 injection (Benson and Davis, 1998).

The *Sleipner* CO_2 sequestration showed time-lapse seismic to be a highly suitable method for monitoring CO_2 injection in a saline aquifer. The effect of the CO_2 on the seismic data is large both in terms of seismic amplitude and in observed velocity pushdown effects as shown by Figure 2.9 (Arts et al., 2004; Chadwick et al., 2005).

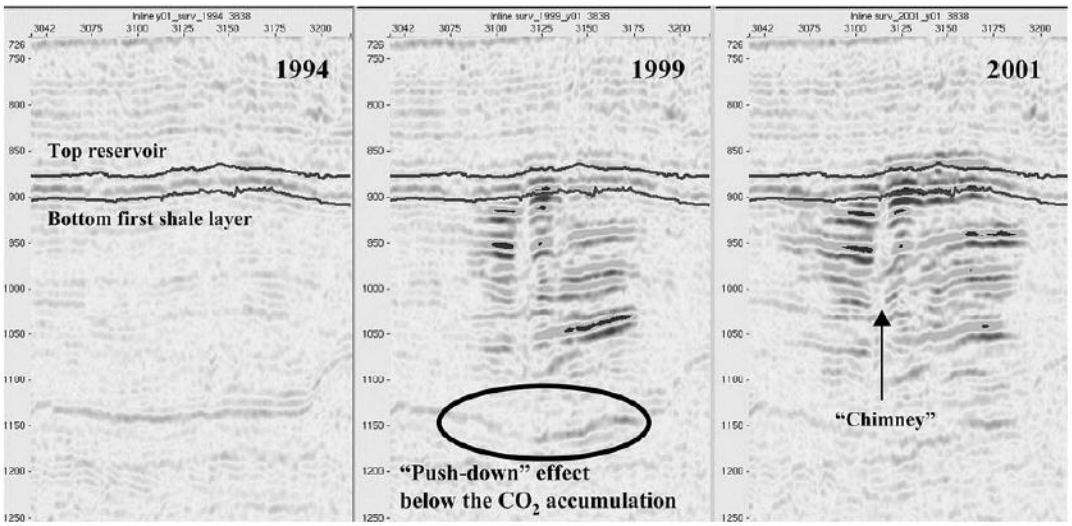

Figure 2.9 Seismic amplitude in 1994 (before injection), 1999 and 2001 (during injection). A number of strong negative reflections (black peak) are observed both on the 1999 and 2001 time-lapse survey (Arts et al., 2004).

The main limitation in using surface seismic data for reservoir monitoring is the lack of vertical resolution and the difficulty in separating the response due to fluid substitution from changes in pore-pressure. Up to now, changes in P-wave impedance have been interpreted to represent changes in either pore-pressure or saturation, which has the most dominant effect on the P-wave velocity of the reservoir. S-wave velocity has almost no effect (very little influence) on fluid changes and may be more sensitive to pore-pressure changes. Long-offset surface seismic data has been used to separate those effects incorporating some information regarding S-wave reflectivity. Methods that rely on amplitude changes with offset to discriminate pressure and saturation changes can help separate and thus simplify the interpretation of some of these effects in time-lapse AVO, as shown in Figure 2.10 (Landrø, 2001; Tura and Lumey, 1999). Figure 2.11 shows the effect of CO_2 injection under various pressures. Saturation is also examined and modelled in *Sleipner*, North Sea (Lumley et al., 2008).

a)

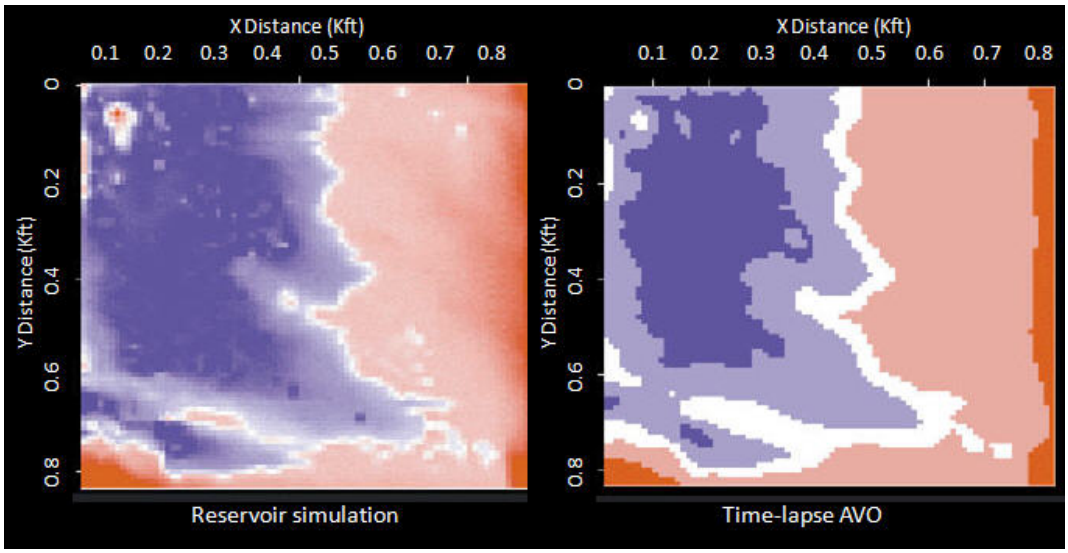

b)

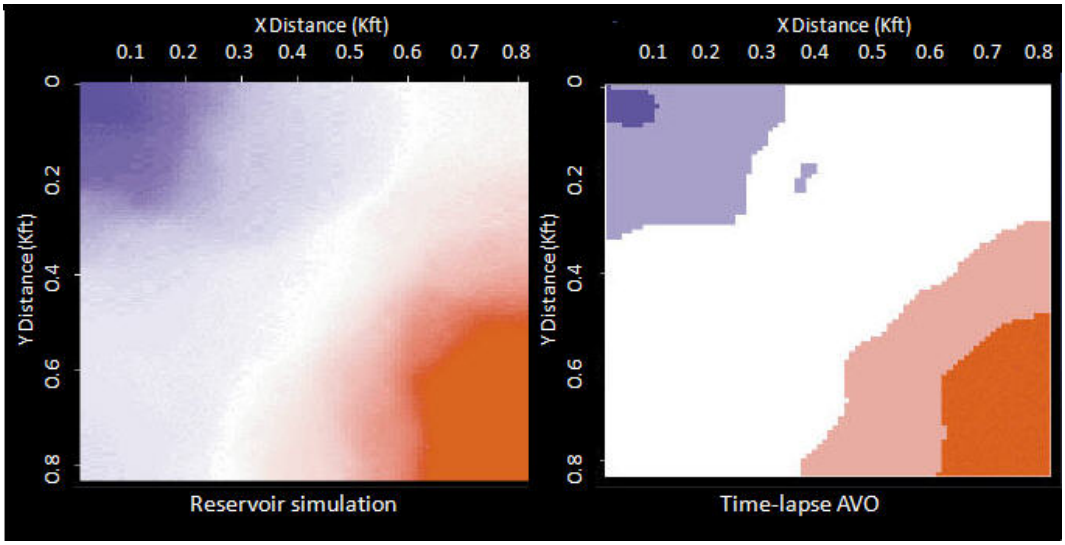

Figure 2.10 Estimation of changes in a) saturation and b) pore-pressure. The left panel in each figure is the true saturation and pressure field from a flow simulator. The right panel in each figure is the estimated saturation or pressure field using time-lapse P- and S-wave seismic data (Tura and Lumey, 1999).

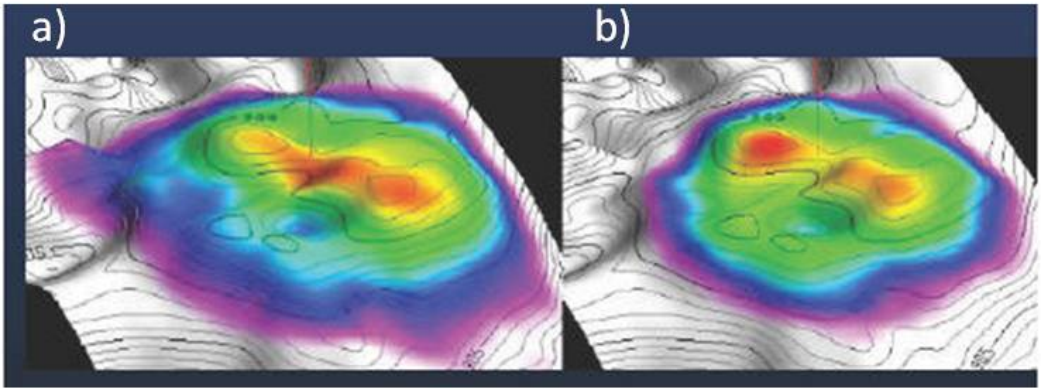

Figure 2.11 a) Pressure and b) saturation model shows the presence of CO_2 saturation of the order of less than 10% (Lumley et al., 2008).

To improve and enhance capability of surface seismic for reservoir monitoring and to differentiate pressure and saturation effects, multi-component seismic is necessary. Use of time-lapse travel-time changes in PP and PS reflectivity is the most promising way to separate saturation and pressure variations in a reservoir (Landrø et al., 2003; Lumley, 2001).

2.4.1.2 Borehole seismic monitoring

New technology such as fibre-optic sensors emplaced during drilling and completion, micro-hole drilling and other advances in sensors are likely to make borehole technology much more cost effective when used over the long run. The use of borehole seismic provides a higher resolution image than surface seismic data due to reduced attenuation (Lumley, 2001). They act as a bridge to tie seismic in time with borehole data in depth. These measurements for monitoring are of three major types; cross-well seismic/high resolution travel time, vertical seismic profile (VSP) and micro seismic (passive source). Cross-well seismic records signal between source and receiver in boreholes. It is intended to provide reflection and tomography images of reservoir properties at the meter resolution scale as it avoids harmful effect of the near surface layers. High resolution travel time method (HRTT) determines travel time changes in micro-seconds. VSP record signals between sources located at surface and receivers positioned at borehole. VSPs recorded using a range of source-receiver offsets, know as a walk-away VSP can provide some control on lateral, vertical, and azimuthally variation of reservoir properties. VSP measurement usually have higher frequency content than surface seismic, thus can improve reservoir imaging close to the well as shown in Figure 2.12 (Lumley, 2001). In other cases, time-lapse tomography and VSP imaging map P-wave velocity and impedance changes over the CO_2 plume. In contrast, S-wave velocity is insensitive to fluid changes but can suggest changes in the rock matrix which are induced by CO_2 injection (Majer et al., 2006).

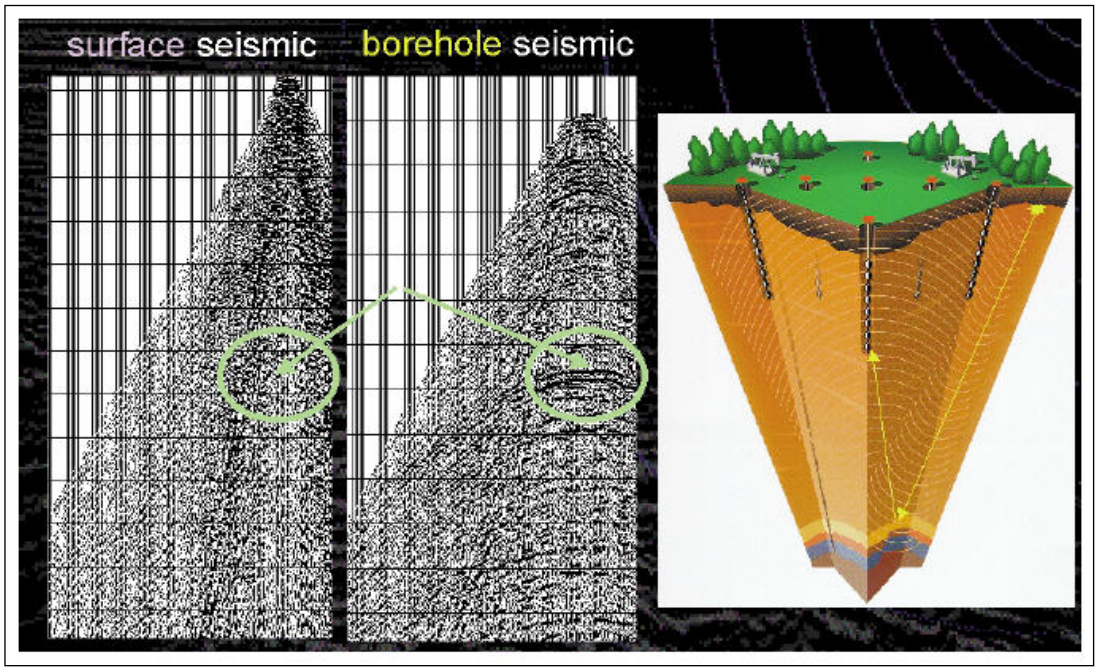

Figure 2.12 Comparison between surface seismic and borehole seismic (VSP). VSP provides higher resolution images than surface seismic (image courtesy of PGS, Exxon, and Halliburton) (Lumley, 2001).

Micro seismic (passive source) monitoring is based on global seismology where P- and S- wave arrivals are used to locate an event in x, y, z space. The activity depends on the frequency and the magnitude in Richter (Figure 2.13). Micro seismic permanently installed in borehole can effectively be deployed to monitor a range of activity at CO_2 storage sites such as cap rock integrity, illuminate sub-seismic features and early detection of fault-reactivation and generation by continuously recording events. Micro seismic should be used in conjunction with geo-mechanical modelling for optimal implementation regarding current local stress regime.

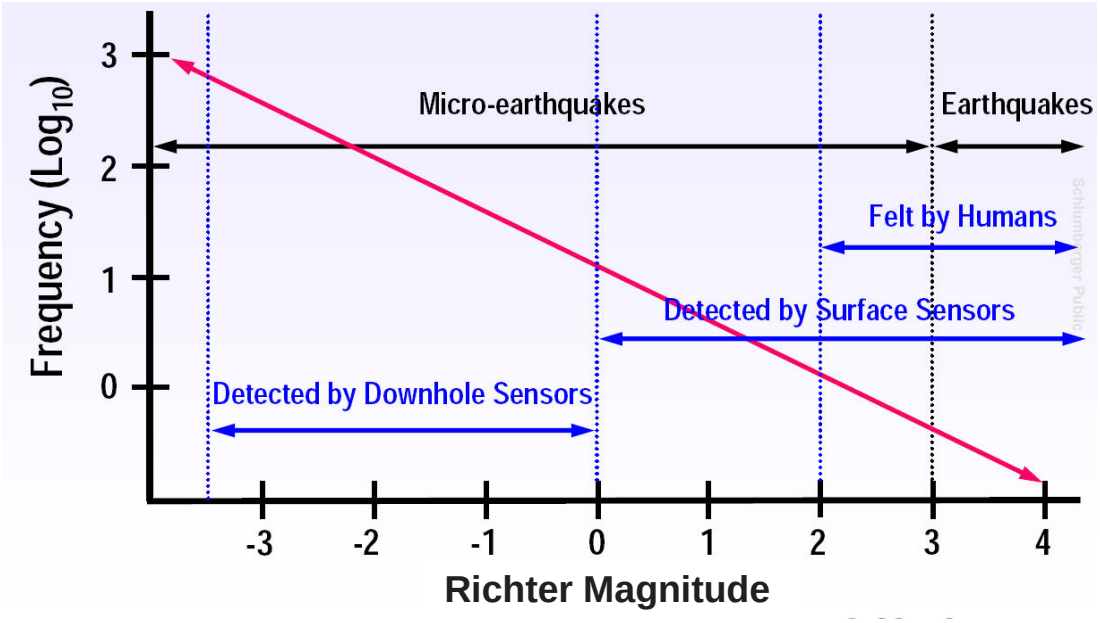

Figure 2.13 The micro seismic activity based on its magnitude and frequency (courtesy of Schlumberger Carbon Services).

We deployed combination of several seismic monitoring methods for the CO2CRC Otway Project in Figure 2.14.

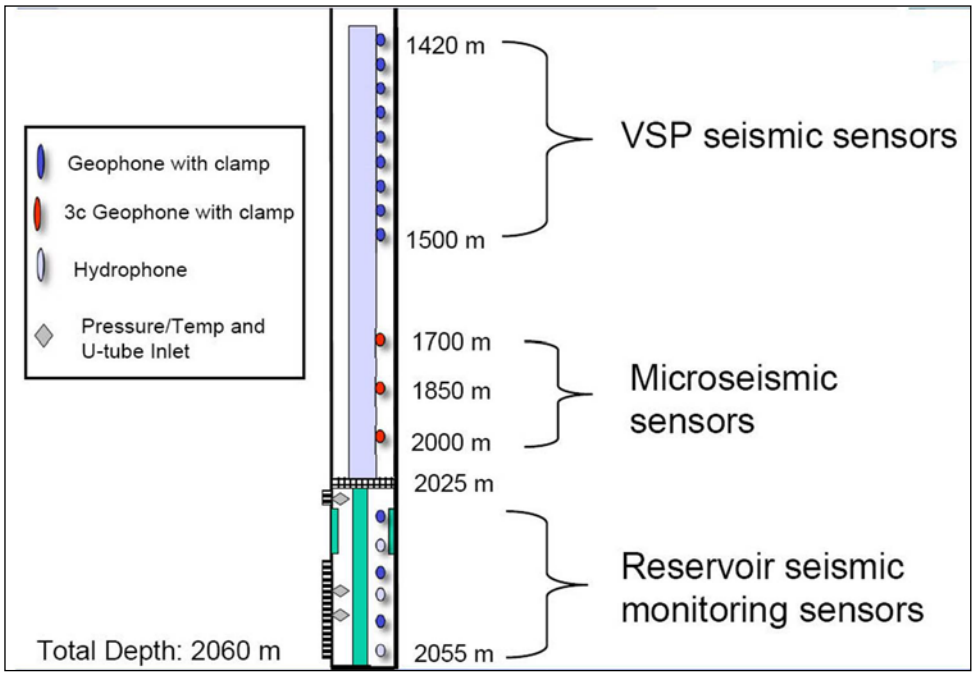

Figure 2.14 Schematic design of combination of seismic methods in Naylor-1 borehole seismic monitoring.

2.4.2 Non-seismic methods

Due to cost considerations, less expensive methods are also considered for CO_2 sequestration monitoring programs. The non-seismic methods presented below show promise as low-cost supplements to seismic monitoring, justifying further evaluation and testing under a wider range of conditions (Gasperikova and Hoversten, 2006).

2.4.2.1 Gravity

Gravity methods measure changes in earth field intensity which effectively translates to the rock density. For most of the depth interval of interest for sequestration, CO_2 is less dense and more compressible than brine or oil; hence the density contrast may produce observable gravity anomalies during the CO_2 injection. It should perform well for certain reservoir conditions such as shallow depth, large porosity and large amount of injected CO_2. To date, the gravity gradient is commonly used for improved subsurface imaging because it provides higher resolution than conventional gravity measurement. It maps anomalies of the sources by reflecting the edges and shapes rather than mass distribution (Bell et al., 1997). Gravity gradient may have "time-lapse" monitoring capability to track CO_2 movement and is deployed at for *Sleipner* CO_2 sequestration project.

2.4.2.2 Electromagnetic

Electromagnetic methods are sensitive to properties of liquid. Similarly, the phases of CO_2 when injected influence the magnitude of conductivity/resistivity of the fluid; the larger the resistivity contrast the better the resolution of the method. Therefore it is the best interest to combine this method with seismic method (Lewis and Shinn, 2001).

2.4.2.3 Well-based

Well-based systems can also be used for monitoring CO_2 sequestration. Well-based monitoring can complement surface monitoring methods by providing data that allows assessment of the physical and geochemical subsurface processes associated with CO_2 emplacement, increasing vertical resolution to observe the plume

evolution, and providing more integrity to the overall monitoring program. One of the instruments that are commonly used to monitor the changes in borehole is the RST log (Schlumberger wire-line saturation log). RST uses pulsed neutron capture to determine changes in fluid content. The parameter collected by the RST tool, Sigma (Σ), is derived from the rate of capture of thermal neutrons. The high value of Σ allows estimation of saturation of the fluid (Sakurai et al., 2006). Xue et al. (2006) estimated the CO_2 saturation using decreases in sonic velocity and increases in resistivity from repeat logging survey conducted in three observation wells. Figure 2.15 shows the RST interpretation during CO_2 injection in *Frio* Brine Pilot test.

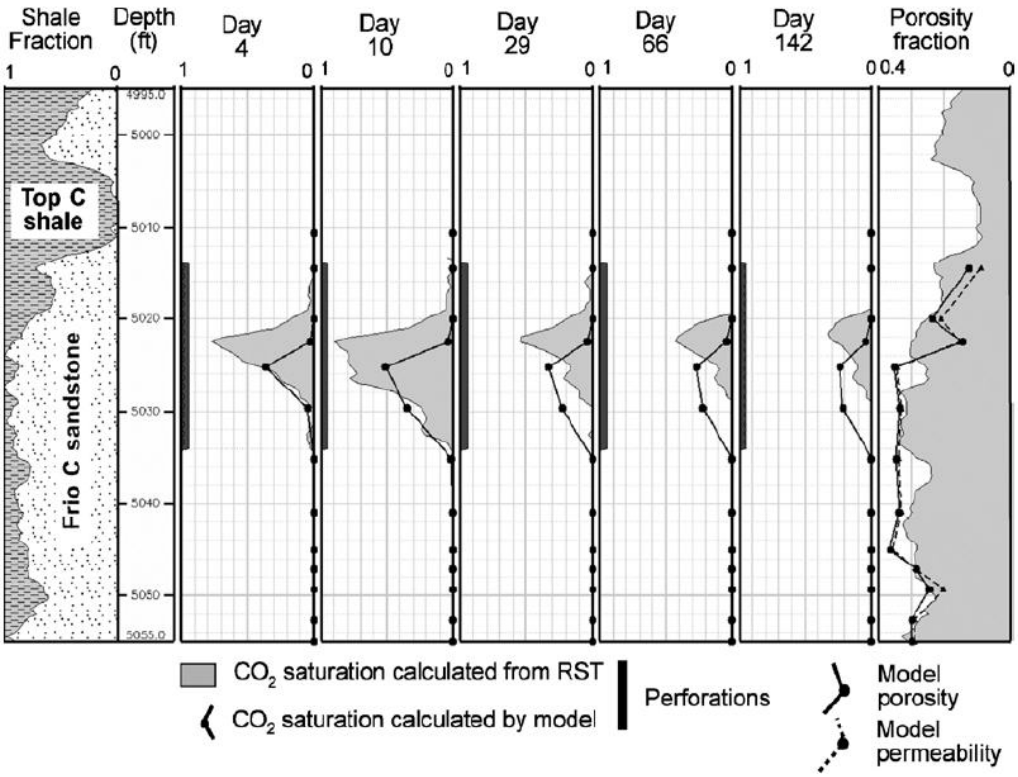

Figure 2.15 RST log collected during the Frio Brine Pilot test. CO_2 saturation at the monitoring well is compared with modelled changes in saturation layer plotted at layer midpoint. RST log shows good sensitivity and can be used to represent CO_2 saturation (Freifeld et al., 2008; Hovorka et al., 2006).

2.4.2.4 Atmospheric

Natural biological flux (emission and uptake) of CO_2 is large and variable compared to the emissions from a hypothetical leak. Local agricultural and industrial emissions can also be significant. Understanding these natural variations enables detection of CO_2 anomalies that could be related to CO_2 leakage to the atmosphere.

2.4.3 Geochemical

2.4.3.1 Hydrology and groundwater

Water levels and the chemistry of the shallow and deep aquifers are monitored to ensure early detection in the unlikely event of any injected CO_2 leaking into these freshwater aquifers. Seasonal variation, flow rate and direction of water-flows are recorded using data loggers suspended from a steel cable a few meters below the existing water level in privately and state-owned shallow and deep water bores. Groundwater sampling using a low flow pump will help identify any unusual chemical changes if the aquifer is contaminated.

2.4.3.2 Tracers

CO_2 and methane compounds of the injection stream are "tagged" using chemical tracers in order to verify the CO_2 plume behaviour. Tracers used are CD4 (*perdeuterated* methane), SF6 (CO_2 hexafluoride) and Krypton. These tracers enable us to track the movement of methane relative to CO_2, providing additional information on the long term fate of injected CO_2 and confirming that there has been no leakage to shallow aquifers, soils or the atmosphere.

2.4.3.3 Down-hole fluid sampling (U-tube)

High quality well-bore fluid and gas samples are collected at reservoir pressure from multiple levels to detect the arrival of CO_2 at the monitoring well through the identification of tracers injected at injection well in order to characterise CO_2 migration and behaviour within the reservoir and to characterise chemical changes associated with this. Samples are analysed in laboratory for their chemical and isotopic composition.

The U-tube system was developed by Lawrence Berkeley National Laboratory (LBNL) and the CO2CRC. For Otway CO_2 study it was installed in the Naylor-1 monitoring well. The U-tube system deployed at Otway consists of three tubes: one in the methane gas-cap, a second just below the current gas-water-contact (GWC) and a third in the water leg. Each U-tube consists of two ¼ inches stainless tubing lines from the surface down the monitoring well, terminating in a 'T' which opens to the formation through a check valve and a filter (Figure 2.16).

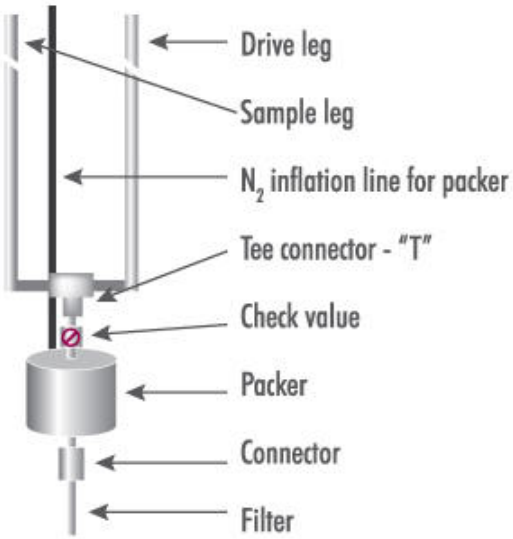

Figure 2.16 U-tube sampler.

2.5 CO_2 geological storage in Australia

CO_2 geological storage or CO_2 sequestration, also referred to as geosequestration, involves the process of injecting CO_2 into underground porous formations. In industrial sense it starts with capturing the carbon dioxide from the combustion sources then separating carbon dioxide from other gases, transporting it to the storage site and injecting it into deep geological formations where it will be trapped over the geological time frame. Geosequestration has adopted technologies commonly practiced in the oil and gas industry for many years for secondary and tertiary recovery process. However, the nature of the project and the necessity to accurately monitor CO_2 sequestration process make CO_2 sequestration unique. It requires the use of multi-disciplinary studies to ensure geosequestration is a viable and safe

option for reduction of greenhouse gas emissions and enable the combustion of fossil fuels in the future. Therefore, research and development of geosequestration projects around the world and in Australia are intended to reduce greenhouse gas emissions, maximize efficiency of the existing technologies, lower sequestration costs. Along these lines the CO2CRC Otway Project, being the only one in the world that explores the possibility of CO_2 injection into a depleted gas reservoir, is of particular interest to this research study and will be discussed throughout the text.

Chapter 3 BACKGROUND THEORY

3.1 Introduction

The seismic properties of rocks and their associated reflection characteristics can be influenced by the properties of the pore fluids contained within the rocks, influencing both compressibility and density. These fluid properties depend on composition, pressure, and temperature which are, in turn, related to source, burial depth, migration, biodegradation, and production history. Batzle and Wang (1992) examined the effects of pressure, temperature, and composition on compressibility and density of hydrocarbons (oils and gases) and brines.

Many factors that influence the seismic properties of sedimentary rocks have been studied by researchers and numerous mathematical models have been developed that describe the effects of pore fluids on seismic properties (Biot, 1956; Herawati, 2002; Robertsson et al., 2000). However, these studies tend to focus on the effects of oil and gas within the reservoirs as opposed to the effects of CO_2 accumulation and movement.

In this chapter, I discuss briefly the ideal gas laws (for comprehensive review please refer to Burcik (1979)), then the behaviour of actual gases which may deviate markedly from these laws under certain temperatures and pressures (real gas law), followed by gas properties calculations from the Otway basin as derived from gas chromatography analysis. These data are applied quantitatively using rock physics theory and analysed with regard to the seismic data and theories, providing the basis of this research project. The aim of this chapter is to present and explain the theory behind the pore fluids effects on seismic modelling used in this research. A more comprehensive description necessary for other theories is beyond the scope of this study.

3.2 Pore fluid properties

3.2.1 Ideal gas law

The effect of the pressure on the volume of the gas is expressed by Boyle's Law as follow:

$$PV = \text{Constant}, \qquad \text{or} \qquad \frac{V_1}{V_2} = \frac{P_1}{P_2}, \tag{3.1}$$

where P is the absolute pressure, and V is the volume. Equation (3.1) means that increase in pressure is inversely proportional to the change of the volume at constant temperature.

The effect of temperature on the volume of the gas is expressed by Charles's Law as follow:

$$V / T_a = \text{Constant}, \qquad \text{or} \qquad \frac{V_1}{V_2} = \frac{T_1}{T_2}, \tag{3.2}$$

where T_a is the absolute temperature expressed in Kelvin, which is equal to the centigrade temperature plus 273.

The seismic properties of pore fluids are related to primary thermodynamic properties. Thus, for gases, we start from ideal gas law which is the combination of Boyle's (eq. 3.1) and Charles's Law (eq. 3.2):

$$PV = nRT_a, \tag{3.3}$$

where R is the gas-law constant and n is the number of moles. If the number of moles is considered 1, eq. (3.3) can be rewritten as:

$$PV = RT_a, \tag{3.4}$$

this equation leads to a density, ρ of:

$$\rho = \frac{MW_{gas}}{V} = \frac{MP}{RT_a}, \tag{3.5}$$

where M is molecular weight calculated from gas composition below:

$$MW_{gas} = X_1 \cdot MW_1 + X_2 \cdot MW_2 + X_n \cdot MW_n , \tag{3.6}$$

where MW_{gas}, MW_1, MW_2, and MW_n are molecular weight of the (mixtures) gas, gas_1, gas_2 and gas_n; $X_1, X_2,$ and X_n are gas_1, gas_2 and gas_n concentration in mole fraction. Gas mixtures are characterized by a specific gravity, $S.G$, a ratio between density of gas and density of free air at a given pressure and temperature, which is also equal to the ratio of the molecular weight of gas and molecular weight of free air (molecular weight of free air is 28.97). From equation (3.6), specific gravity is defined as:

$$S.G = MW_{gas} / 28.97 . \tag{3.7}$$

The isothermal compressibility β_T is:

$$\beta_T = \frac{-1}{V}\left(\frac{\partial V}{\partial P}\right)_T , \tag{3.8}$$

where subscript T indicates isothermal conditions. If we calculate the isothermal compressional wave velocity, V_T, we find:

$$V_T^2 = \frac{1}{\beta_T \rho} = \frac{RT_a}{MW_{gas}} , \tag{3.9}$$

thus, for an ideal gas, velocity is independent of pressure and increases with temperature.

3.2.2 Real gas law

The equations given in the previous section are valid for an ideal gas at constant temperature. To overcome these restrictions, we need to consider two factors. First, when the acoustic waves travel rapidly through the fluid, the process is adiabatic, not isothermal. The difference between isothermal and adiabatic compressibility is very small in most solid materials, however for fluids and especially for gases this difference may be significant. Adiabatic compressibility is related to isothermal compressibility through ratio γ of heat capacity at constant pressure to heat capacity

at constant volume. The second factor is deviation of real gases from the ideal gas at the particular temperature and pressure. To account for this effect, the eq. (3.3) for real gases can be written as:

$$PV = ZRT\,, \tag{3.10}$$

where Z is a compressibility factor, as a function of pressure and temperature.

The gas properties highly depend on gas composition. The gas and liquid phases exist in an equilibrium state at a specific pressure and temperature. However when the pressure and temperature increase, the properties of two phases get close to each other until they merge at critical point defined by so called *pseudocritical* temperature T_{pc} and *pseudocritical* pressure P_{pc}. Figure 3.1 shows the phase diagram for carbon dioxide.

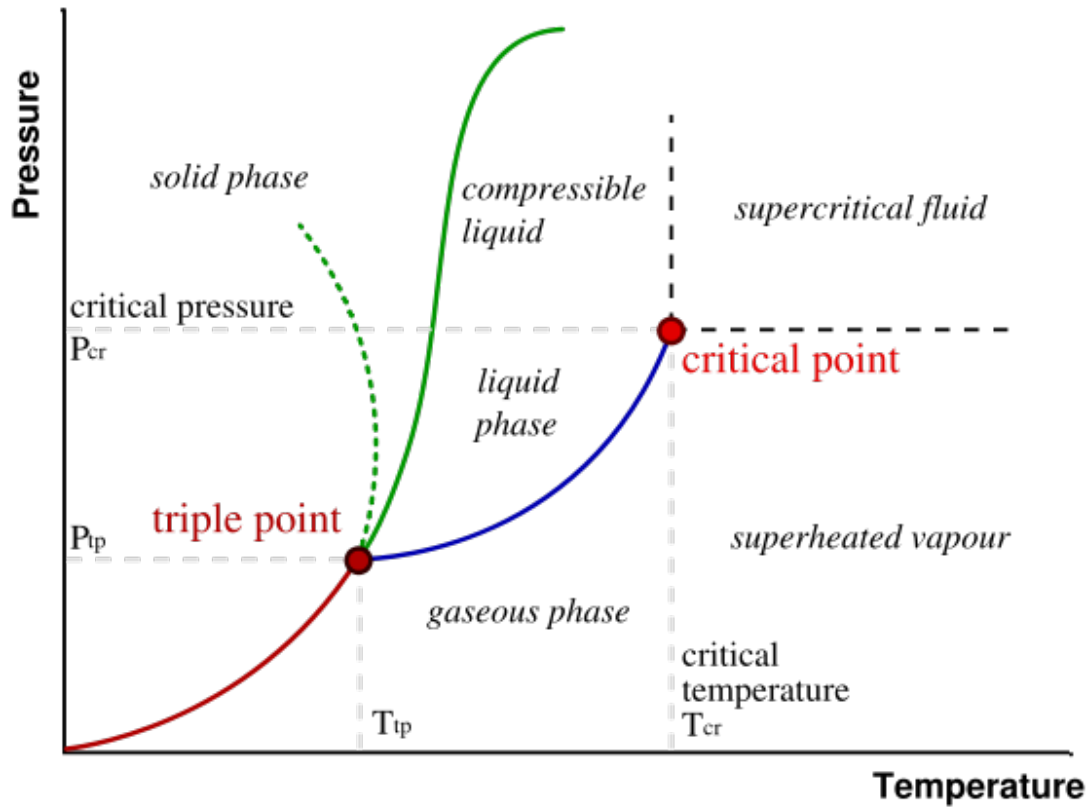

Figure 3.1 Pressure and temperature relations of different phases for carbon dioxide.

Katz (1959) developed a systematic model for properties of mixtures to determine the compressibility factor Z by normalizing or "pseudoreducing" the pressure and temperature at *pseudocritical* values. Later, Thomas et al. (1970) determined relationship between $S.G$ and the *pseudoreduced* pressure P_{pr} and *pseudoreduced* temperature T_{pr} as follows:

$$P_{pr} = P / P_{pc} = P / (4.892 - 0.4048 * S.G), \tag{3.11}$$

$$T_{pr} = T_a / T_{pc} = T_a / (94.72 + 170.75 * S.G). \tag{3.12}$$

These *pseudoreduced* pressures and temperatures can be used in the Benedict-Webb-Rubin (B-W-R) equation of state to calculate velocities for gas mixtures. This leads to the following equation for gas density ρ for the pressure and temperature typically encountered in hydrocarbon reservoirs during exploration, production and et cetera as follows:

$$\rho_g \cong \frac{28.97 * S.G * P}{Z * R * T_a}, \tag{3.13}$$

where

$$Z = \left[0.03 + 0.00527\left(3.5 - T_{pr}\right)^3\right] P_{pr} + \left(0.642 T_{pr} - 0.007 T_{pr}^4 - 0.52\right) + E, \tag{3.14}$$

and

$$E = 0.109\left(3.85 - T_{pr}\right)^2 \exp\left\{-\left[0.45 + 8\left(0.56 - 1/T_{pr}\right)^2\right] P_{pr}^{1.2} / T_{pr}\right\}. \tag{3.15}$$

The gas densities increase with pressure and decrease with the temperature as expected. Figure 3.2 shows that gas density is strongly dependent on the composition of the gases.

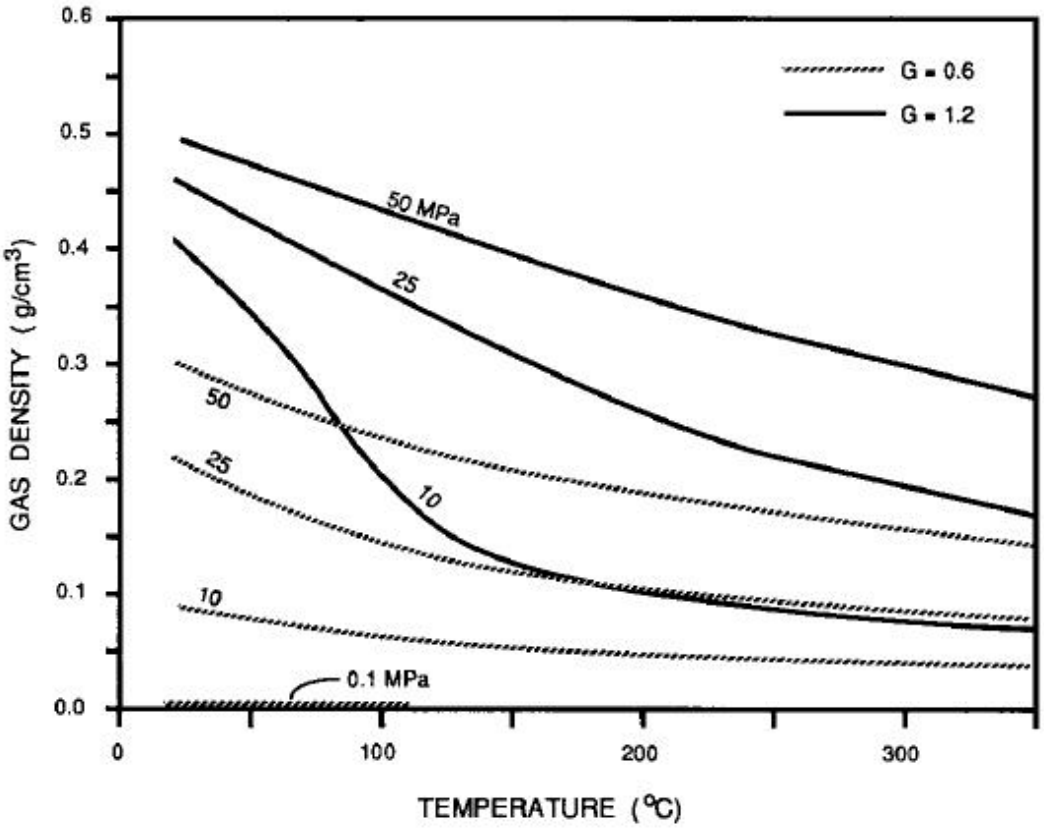

Figure 3.2 Gas densities as a function of temperature, pressure and composition. Dashed and solid line is density for light gas and heavy gas, respectively. Values for light and heavy gas coincide at 0.1 MPa (Batzle and Wang, 1992).

The adiabatic gas modulus K_s is also strongly dependent on the gas composition. Modulus increases with pressure and decreases with temperature. The approximate expression for K_s is:

$$K_s \cong \frac{P}{\left(1-\frac{P_{pr}}{Z}\frac{\partial Z}{\partial P_{pr}}\right)_T}\ \gamma_0\,, \tag{3.16}$$

where

$$\gamma_0 = 0.85+\frac{5.6}{\left(P_{pr}+2\right)}+\frac{27.1}{\left(P_{pr}+3.5\right)^2}-8.7\exp\left[-0.65\left(P_{pr}+1\right)\right]. \tag{3.17}$$

3.2.3 Fluid properties in Naylor field

3.2.3.1 Hydrocarbon gases

The gas compounds are relatively simple and easy to characterise. Hydrocarbon gases usually start from light gases (methane, ethane, etc.) up to heavy gases (which usually contain more carbon atoms in one molecule). Additionally, other gases such as water vapour, nitrogen, etc, can be present in the mixture. Here I present the hydrocarbon analysis of Naylor-1 well and CRC-1 well after production. The gas composition is used to calculate the specific gravity (S.G) and density of the gas mixture from above equations, as show in Table 3.1 a) and b).

Table 3.1 Gas chromatography analysis after production (before injection) in a) Naylor-1 and b) CRC-1 wells.

a)

No	Compounds	Mol composition %	Mol Weight	Mol Weight Gas	SG
1	N2	6.52	28.01	1.82645	0.06342
2	CO2	1.02	44.01	0.44890	0.01559
3	CH4	84.34	16.04	13.53067	0.46981
4	Ethane	4.62	30.07	1.38923	0.04824
5	Propane	2.01	44.10	0.88635	0.03078
6	I-Butane	0.41	58.12	0.23831	0.00827
7	N-Butane	0.51	58.12	0.29643	0.01029
8	I-Pentane	0.13	72.15	0.09380	0.00326
9	N-Pentane	0.11	72.15	0.07937	0.00276
10	Hexanes	0.17	86.18	0.14650	0.00509
11	Heptanes	0.10	100.21	0.10021	0.00348
12	Octanes plus	0.06	127.00	0.07620	0.00265
	TOTAL	**100.00**			**0.66363**

b)

No	Compounds	Mol composition %	Mol Weight	Mol Weight Gas	SG
1	N2	1.23	28.01	0.34456	0.01196
2	CO2	0.86	44.01	0.37849	0.01314
3	CH4	87.66	16.04	14.06329	0.48831
4	Ethane	5.00	30.07	1.50350	0.05220
5	Propane	2.44	44.10	1.07597	0.03736
6	I-Butane	0.58	58.12	0.33712	0.01171
7	N-Butane	0.72	58.12	0.41849	0.01453
8	I-Pentane	0.25	72.15	0.18038	0.00626
9	N-Pentane	0.21	72.15	0.15152	0.00526
10	Hexanes	0.33	100.00	0.33000	0.01146
11	Heptanes	0.41	107.30	0.43993	0.01528
12	Octanes	0.14	114.23	0.15992	0.00555
13	Nonaes	0.08	128.26	0.10261	0.00356
14	Decanes	0.06	141.60	0.08496	0.00295
15	Undecanes	0.02	161.10	0.03222	0.00112
16	Dodecanes+	0.01	179.60	0.01796	0.00062
	TOTAL	**100**			**0.68128**

For comprehensive review, Mavko et al. (1998) and Batzle and Wang (1992) have summarized some important properties of reservoir pore fluids.

3.2.3.2 Brine

Density of the brine depends on the salinity. The density of pure water (ρ_w) is:

$$\rho_w = 1 + 1\times10^{-6}\begin{pmatrix} -80T - 3.3T^2 + 0.00175T^3 + 489P - 2TP + 0.016T^2P \\ -1.3*10^{-5}T^3P - 0.333P^2 - 0.002TP^2 \end{pmatrix}. \quad (3.18)$$

Water with salinity S of sodium chloride, the density of brine (ρ_b) is:

$$\rho_b = \rho_w + S\left\{0.668 + 0.44S + 10^{-6}\begin{bmatrix} 300P - 2400PS \\ +T\left(80 + 3T - 3300S - 13P + 47PS\right) \end{bmatrix}\right\}, \quad (3.19)$$

in these formulas, P (pressure) is in MPa, T (temperature) is in degree Celsius, S (salinity) is the weight fraction of sodium chloride (ppm), and ρ (density of pure water - ρ_w and density of brine - ρ_b) is in g/cm^3 .

Furthermore, velocity of brine V_b can be calculated as:

$$\begin{aligned} V_b = V_w + S&\begin{pmatrix} 1170 - 9.6T + 0.055T^2 - 8.5*10^{-5}T^3 \\ +2.6P - 0.0029TP - 0.047P^2 \end{pmatrix}, \\ &+S^{1.5}\left(780 - 10P + 0.16P^2\right) - 1820S^2 \end{aligned} \quad (3.20)$$

where the velocity of pure water V_w is:

$$V_w = \sum_{i=0}^{4}\sum_{j=0}^{3} w_{ij}T^iP^j \ , \quad (3.21)$$

and the coefficients of w_{ij} are:

$$
\begin{aligned}
W_{00} &= 1402.85 & W_{02} &= 3.437*10^{-3} \\
W_{10} &= 4.871 & W_{12} &= 1.739*10^{-4} \\
W_{20} &= -0.04783 & W_{22} &= -2.135*10^{-6} \\
W_{30} &= 1.487*10^{-4} & W_{32} &= -1.455*10^{-8} \\
W_{40} &= -2.197*10^{-7} & W_{42} &= 5.230*10^{-11} \\
W_{01} &= 1.524 & W_{03} &= -1.197*10^{-5} \\
W_{11} &= -0.0111 & W_{13} &= -1.628*10^{-6} \\
W_{21} &= 2.747*10^{-4} & W_{23} &= 1.237*10^{-8} \\
W_{31} &= -6.503*10^{-7} & W_{33} &= 1.327*10^{-10} \\
W_{41} &= 7.987*10^{10} & W_{43} &= -4.614*10^{-13}
\end{aligned}
$$

For the temperatures below about 250°C, the maximum amount of gas that can go into solution can be estimated using the expression (Batzle and Wang, 1992):

$$
\begin{aligned}
Log_{10}\left(R_G\right) = Log_{10}\left\{0.712P\left|T-76.71\right|^{1.5}+3676P^{0.64}\right\}, \\
-4-7.786S\left(T+17.78\right)^{-0.306}
\end{aligned}
\qquad (3.22)
$$

where R_G is the gas-water ratio at room pressure and temperature. Then the bulk modulus of the gas-free brine K_b, and the bulk modulus of brine with gas-water ratio K_G is:

$$
K_G = \frac{K_b}{1+0.0494R_G}. \qquad (3.23)
$$

3.3 Elastic properties of heterogeneous media

Most rocks contain a number of mineral components. Therefore for accurate prediction of average grain moduli, we need to specify (1) the volume fractions of the constituents, (2) the elastic moduli for each constituent, and (3) the geometry of the constituents. If we only know the volume fractions and elastic moduli of the constituent without knowing the geometry details of it, we can only calculate upper and lower bounds for effective moduli. The separation between the bounds depends on the contrast between the constituent moduli.

3.3.1 Hashin- Shtrikman bounds

The best and narrowest bounds for estimating isotropic effective grain elastic moduli are Hashin-Shtrikman (HS) bounds. HS bounds are used to compute the estimated range of average elastic moduli for a mixture of mineral grains and to compute the upper and lower bounds for a mixture of mineral grains and pore fluids. The upper and lower Hashin-Shtrikman bounds are written as (Hashin and Shtrikman, 1963):

$$K^{HS+} = \Lambda\left(\mu_{\max}\right), \qquad K^{HS-} = \Lambda\left(\mu_{\min}\right), \tag{3.24}$$

$$\mu^{HS+} = \Gamma\left(\zeta\left(K_{\max}, \mu_{\max}\right)\right), \qquad \mu^{HS-} = \Gamma\left(\zeta\left(K_{\min}, \mu_{\min}\right)\right), \tag{3.25}$$

where

$$\Lambda\left(\mu_{\max}\right) = \left(\sum_{i=1}^{N} \frac{f_i}{K_i + \frac{4}{3}\mu_{\max}}\right)^{-1} - \frac{4}{3}\mu_{\max}, \tag{3.26}$$

$$\Lambda\left(\mu_{\min}\right) = \left(\sum_{i=1}^{N} \frac{f_i}{K_i + \frac{4}{3}\mu_{\min}}\right)^{-1} - \frac{4}{3}\mu_{\min}\ , \tag{3.27}$$

$$\Gamma = \left[\zeta\left(K_{\max}, \mu_{\max}\right)\right] = \left(\sum_{i=1}^{N} \frac{f_i}{\mu_i + \zeta\left(K_{\max}, \mu_{\max}\right)}\right)^{-1} - \zeta\left(K_{\max}, \mu_{\max}\right), \tag{3.28}$$

$$\Gamma = \left[\zeta\left(K_{\min}, \mu_{\min}\right)\right] = \left(\sum_{i=1}^{N} \frac{f_i}{\mu_i + \zeta\left(K_{\min}, \mu_{\min}\right)}\right)^{-1} - \zeta\left(K_{\min}, \mu_{\min}\right), \tag{3.29}$$

$$\zeta\left(K_{\max}, \mu_{\max}\right) = \frac{\mu_{\max}}{6}\left(\frac{9K_{\max} + 8\mu_{\max}}{K_{\max} + 2\mu_{\max}}\right), \tag{3.30}$$

$$\zeta\left(K_{\min}, \mu_{\min}\right) = \frac{\mu_{\min}}{6}\left(\frac{9K_{\min} + 8\mu_{\min}}{K_{\min} + 2\mu_{\min}}\right). \tag{3.31}$$

$\mu_{\max}$ and $\mu_{\min}$ represent maximum and minimum shear modulus of the mineral; $K_{\max}$ and $K_{\min}$ represent maximum and minimum bulk modulus of the mineral; K_i, μ_i, and f_i are bulk and shear modulus, and volume fraction of the i^{th} mineral.

Figure 3.3 shows the physical interpretation of a material whose bulk modulus would fall on one of Hashin-Shtrikman bounds. The upper bound is realized when the stiffer materials forms the shell; the lower bound, when it is in the core (Mavko et al., 1998).

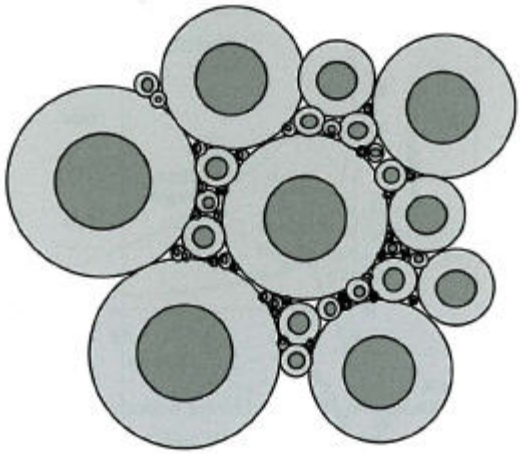

Figure 3.3 Physical interpretations of the Hashin-Shtrikman bounds for bulk modulus of a two-phase material (Mavko et al., 1998).

3.3.2 Voight and Reuss bounds

The Voight and Reuss bounds are used to give maximum and minimum of elastic moduli of mineral and pore fluid. The bounds are also used to estimate mineral modulus for a mixture of mineral grains on average. The upper bound, known as the Voight upper bound, is an arithmetic average of the mineral moduli weighted by the respective volume fractions of the constituent. It is sometimes called the isostrain average, because it gives the ratio of average stress to strain when all constituents are assumed to have the same strain (Mavko et al., 1998). The Voight upper bound (M_{Vgrain}) is:

$$M_{Vgrain} = \sum_{i=1}^{N} f_i M_i \,, \tag{3.32}$$

where M_{Vgrain} and M_i are modulus of the mixed grain and i^{th} mineral; f_i is volume fraction of the i^{th} mineral.

The lower bound, known as the Reuss lower bound, is the harmonic average of the mineral moduli weighted by the respective volume fractions of the constituent. It is sometimes called the isostress average because it gives the ratio of stress to average strain when all constituents are assumed to have the same stress (Mavko et al., 1998). The Reuss lower bound (M_{Rgrain}) is:

$$\frac{1}{M_{Rgrain}} = \sum_{i=1}^{N} \frac{f_i}{M_i} . \tag{3.33}$$

M notation in Voight and Reuss formulas can represent any modulus: K, the bulk modulus or μ , the shear modulus, E, Young's modulus, etc. It is a common practice to compute bulk modulus, $M = K$, and shear modulus, $M = \mu$, and then compute the other moduli from these.

Figure 3.4 shows schematically the bounds for elastic effective moduli, when one of the constituents is liquid or gas. Obviously, the Reuss effective elastic moduli (lower bound) give exactly the same effective elastic moduli as given by the Hashin-Shtrikman lower bound. The lower bounds correspond to suspension of the particles in the fluid and a good indicator of very soft sediments at low effective stress. In contrast, the real isotropic mixtures can never be as stiff as the Voight upper bound (except for the single phase end members).

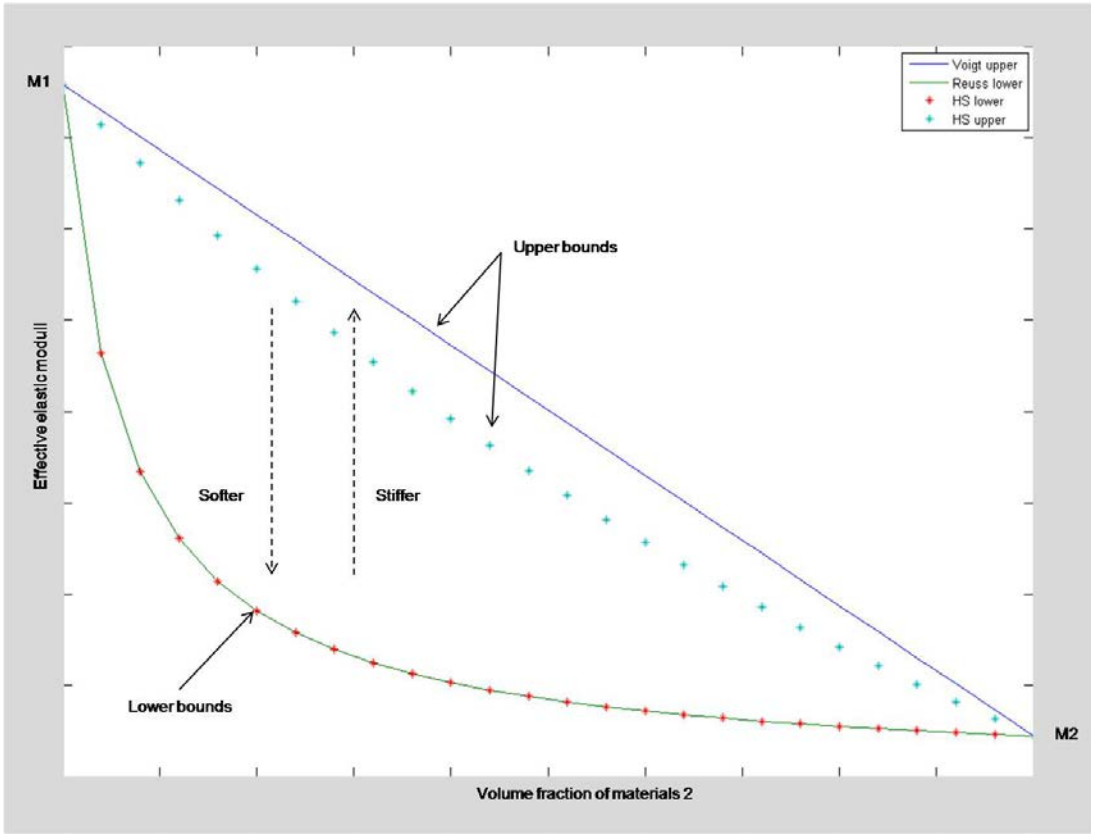

Figure 3.4 The upper and lower bounds to effective elastic modulus for a mixture of two constituents, one of them is a fluid or gas.

When one of the constituents is a liquid or gas with zero shear modulus ($\mu_{\min} = 0$), then Hashin-Sthrikman lower bound is the same as the Reuss bound as describe in Figure 3.4.

3.3.3 Wood's formula

Wood's formula is used to estimate the velocity of a fluid mixture where the heterogeneities are small compared with a wavelength. The effective bulk modulus of the fluid mixture can be calculated if the pore fluid is uniformly distributed in the pores (pressures are equal between fluids). The velocity of fluid mixture is given by Wood (1955) as follows:

$$V = \sqrt{\frac{K_R}{\rho}}, \tag{3.34}$$

where K_R is the Reuss (isostress) average of the composite:

$$\frac{1}{K_R} = \sum_i^N \frac{f_i}{K_i}, \tag{3.35}$$

and ρ is the average density defined by:

$$\rho = \sum_i^N f_i \rho_i, \tag{3.36}$$

the f_i, K_i, and ρ_i are the volume fractions, bulk moduli, and densities of the pore fluids respectively. Another form of Wood's equation to calculate bulk modulus is:

$$\frac{1}{K_f} = \frac{S_w}{K_w} + \frac{S_o}{K_o} + \frac{S_g}{K_g}, \tag{3.37}$$

where K_W, K_o, and K_g are the bulk moduli of water, oil, and gas, respectively; S_W, S_o, and S_g are water, oil and gas saturation; and $S_W + S_o + S_g = 1$.

3.3.4 Hill's equation

Hill (1952) showed that the Voight and Reuss averages can be used to estimate the effective elastic moduli a rock, K_m and G_m. This arithmetic average, later called Voight-Reuss-Hill average, is expressed as:

$$M_{VRH} = (M_V + M_R)/2 \ , \tag{3.38}$$

where

$$M_V = \sum_i^N f_i M_i, \tag{3.39}$$

$$\frac{1}{M_R} = \sum_i^N \frac{f_i}{M_i}. \tag{3.40}$$

M_{VRH} is effective grain modulus (which can be either K_m or G_m), M_V is Voight average, and M_R is Reuss average.

3.3.5 Estimating dry frame elastic moduli

For most porous medium there is a *critical porosity*, ϕ_c, which separates their mechanical and acoustic behaviour into two different domains. If the porosity is

lower than ϕ_c the grains are load-bearing, while when the porosity is greater than ϕ_c, the rock is "very soft and easily falls apart" and becomes a suspension in which the fluid phase is load-bearing. In the suspension domain, the effective elastic moduli typically follow the Reuss lower bound and in the load-bearing domain, the effective elastic moduli will lie between the upper and lower bounds of Hashin-Shtrikman (Figure 3.5). Usually the porosity of a reservoir rock is below ϕ_c. Because of this, empirical relationships have been defined that can be used to predict the dry elastic moduli of porous rocks.

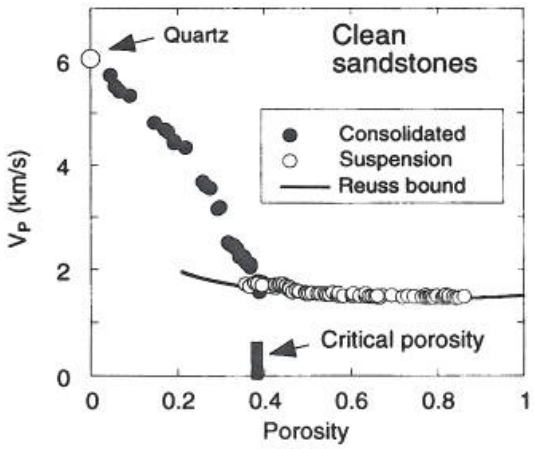

Figure 3.5 Critical porosity behaviour where in suspension domain follows Reuss lower bound (Mavko et al., 1998).

3.3.5.1 Empirical relations

Krief et al. (1990) suggested fitting a non-linear trend between the zero and critical modeled the dry rock as a porous elastic solid and calculated the dry rock modulus as:

$$K_{dry} = K_{grain}(1-\beta)\,, \tag{3.41}$$

where K_{dry} and K_{grain} are the bulk moduli of dry rock and mineral and β is Biot's coefficient (the compressibility or the pore space stiffness).

To find the relationship for β and ϕ, Krief et al. (1990) used the data of Raymer et al. (1980) as follows:

$$(1-\beta)=(1-\phi)^{m(\phi)} \text{ , where } m(\phi)=3/(1-\phi), \tag{3.42}$$

substitute eq. (3.42) into eq. (3.41) will give:

$$K_{dry}=K_{grain}(1-\phi)^{\frac{3}{(1-\phi)}} \text{ , and } \mu_{dry}=\mu_{grain}(1-\phi)^{\frac{3}{(1-\phi)}}, \tag{3.43}$$

from here, different fluid effects can be calculated using Gassmann.

Using log data (sonic and density) from field measurements, K_{dry} can also be obtained from the inverse Gassmann's equation as follows:

$$K_{dry}=\frac{K_{sat}(\frac{\phi K_m}{K_f}+1-\phi)-K_m}{\frac{\phi K_m}{K_f}+\frac{K_{sat}}{K_m}-1-\phi}. \tag{3.44}$$

3.4 Fluid effects on wave propagation

3.4.1 Biot-Gassmann's relations

The low-frequency Gassmann (1951) – (Biot, 1956) theory predicts the effect of fluid saturation on seismic properties using the dry frame properties. It allows us to predict saturated rock moduli from dry rock moduli, the changes from one fluid to another. The relationship between the dry and saturated bulk moduli of porous rocks can be written as (Mavko et al., 1998):

$$K_{sat}=K_{dry}+\eta^2 M, \tag{3.45}$$

where $$\eta=1-\frac{K_{dry}}{K_{grain}}, \tag{3.46}$$

and $$M=\frac{K_{grain}}{\eta-\phi\left[1-\frac{K_{grain}}{K_{fluid}}\right]}. \tag{3.47}$$

K_{sat} is the bulk modulus of saturated rocks, K_{dry} is the bulk modulus of the dry rock, K_{grain} is the bulk modulus of mineral grains, and K_{fluid} is he bulk modulus of the

saturated fluid. Equation (3.41) to (3.43) can be combined as follows (Mavko et al., 1998):

$$K_{sat} = K_{dry} + \frac{\left(1 - \frac{K_{dry}}{K_{grain}}\right)^2}{\frac{\phi}{K_{fluid}} + \frac{1-\phi}{K_{grain}} + \frac{K_{dry}}{K_{grain}^2}}. \tag{3.48}$$

Since shear modulus of fluid is zero, the shear modulus of saturated rock is equal to the dry shear modulus at low frequency:

$$\mu_{sat} = \mu_{dry}. \tag{3.49}$$

Estimation of K_{grain}, K_{dry}, K_{fluid}, μ_{grain} and μ_{dry} are required in order to predict the effective bulk and shear moduli for saturated rocks.

The description of saturated rock based on assumption that the fluid and solid move together during elastic wave propagation, hence the density of saturated rock (ρ_{sat}) can be expressed as the volume-weighted average of the "*m*" minerals and '*n*' fluids comprising the porous rock (Mavko et al., 1998):

$$\rho_{sat} = (1-\phi)\sum_{i=1}^{n} f_i \rho_i + \phi \sum_{j=1}^{n} f_j \rho_j, \tag{3.50}$$

where *f* is the volume fraction of the i^{th} mineral and j^{th} fluid.

Gassmann's relation assumes an isotropic porous rock, free of assumption about the pore geometry. It is valid only at sufficiently low frequencies such that the induced pore pressure as equilibrated throughout the pore space. This condition requires sufficient time for the pore fluid to flow and eliminate wave-induced pore pressure gradients as the seismic wave propagates. The limitation to low frequency explains why Gassmann's relation works best for very low frequency seismic data (less than 10^2 Hz) and may perform less well as frequencies increase toward sonic logging (approximately 10^4 Hz) and laboratory ultrasonic measurements (approximately 10^6 Hz) (Mavko et al., 1998).

3.4.2 Patchy saturation

In most Gassmann's application assumes that all fluid phases are immiscible and homogeneously distributed throughout the pore space, known as homogeneous saturation. This condition is met when the fluid is in equilibrium state over the geologic time. However this equilibrium state may be disturbed during the drilling, production, and water-flooding. Then to return to equilibrium state may require longer time frames than those encountered during the logging or time-lapse seismic survey in 4D seismic monitoring. Thus, it may cause fluids not be uniformly or homogeneously distributed throughout the pore space in reservoir or well (Gassmann, 1951). This condition may lead the inability of pore pressures to equilibrate in the time scale of wave propagation and known as patchy saturation. Inability to define the saturation type may result to incorrect model of 4D seismic response.

Knight et al. (1998) described the relationship between elastic wave velocities and water saturation in gas reservoir depend strongly on whether saturation is heterogeneous (patchy) or homogeneous. Lithologic heterogeneity in reservoir may cause heterogeneity in saturation because under conditions of capillary equilibrium, different lithologies within a reservoir can have different saturations, depending on their porosities and permeabilities. Dvorkin and Nur (1998) and Dvorkin et al. (1999) have investigated the acoustic signatures of saturation types and how to identify from well logs. I applied the workflow described in Chapter 5 and calibrated with core test results.

3.5 Elements of seismic theory

3.5.1 Elastic wave propagation

The seismic method is based upon the propagation of sound waves through the earth. The wave propagation depends on the elastic properties of the rocks through which the waves travel. The elastic properties of a rock are defined by the behaviour of the rock when subjected to various external forces. This behaviour is determined by multiple rock properties such as density and porosity and can also be affected by the fluids contained within the pore spaces of the rock units.

The size (volume) and shape of a solid body can be changed by external forces and at the same time, the change in size and shape is resisted by internal forces. As a result, when external forces are removed, the solid body tends to return to its original size and shape. In contrast, a fluid resists changes in size (volume) but not in shape. Elasticity is defined as the ability of a resisting body or fluid to return to its original undeformed condition once an external force is removed. (Aki and Richards, 1980; Sheriff and Geldart, 1995; Telford et al., 1990). Rock can be considered as a perfect elastic solid material without appreciable error, provided the deformations are small, as is the case for seismic wave (except near a seismic source where the amount of deformation may cause permanent alteration). The relations between the applied force and the deformations in elastic body are expressed in terms of stress, strain and Hooke's law. The equations of wave propagation in elastic solids are derived using Newton's second law of motion where acceleration was produced by an unbalanced force on a mass.

3.5.2 Stress, strain and Hooke's law

When seismic wave propagates through the elastic body, it induces deformation (a change in shape and volume) in the body. A measurement of the intensity of internal forces within deformable body called stress. Stress measures the force per unit area of a surface within deformable body. Figure 3.6 describes the stress components acting on the infinitesimally small volume surrounding a point within an elastic solid. The stress acting upon one of the surfaces can be decomposed into three components, one is normal to the surface (σ_{xx}), which is known as normal stress component, and two are tangential to the surface (σ_{xy}, σ_{xz}), which is known as shear stress component. A normal stress component is tensional if it is positive and compressional if it is negative. Shear stress does not apply with fluids. In fluids only one independent stress component exists which is the hydrostatic pressure.

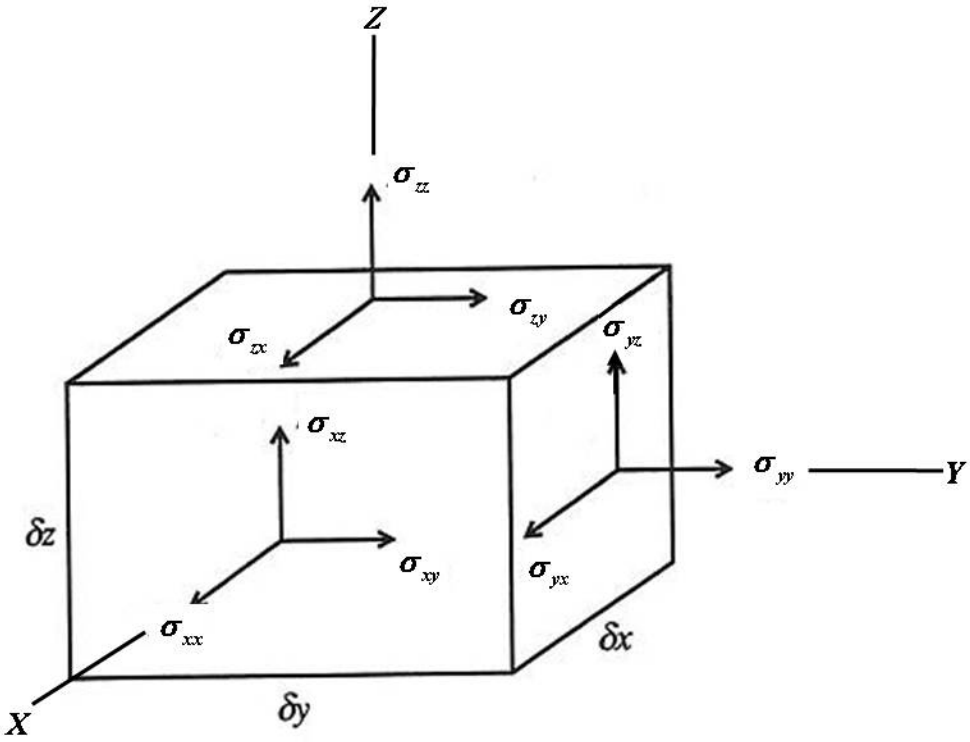

Figure 3.6 Stress components acting on an infinitesimally small volume surrounding a point within an elastic solid (Yilmaz, 2001).

To retain the solid cube requires nine stress components that make up the stress tensor which formulate the second stress tensor (Ikelle and Amundsen, 2005; Nye, 1985):

$$\sigma_{ij} = \begin{bmatrix} \sigma_{xx} & \sigma_{xy} & \sigma_{xz} \\ \sigma_{yx} & \sigma_{yy} & \sigma_{yz} \\ \sigma_{zx} & \sigma_{zy} & \sigma_{zz} \end{bmatrix} \Rightarrow \begin{bmatrix} \sigma_{xx} \\ \sigma_{yy} \\ \sigma_{zz} \\ \sigma_{yz} \\ \sigma_{zx} \\ \sigma_{xy} \end{bmatrix}. \qquad (3.51)$$

The diagonal elements are the normal stress components and the off-diagonal elements are the shear stress components. Since $\sigma_{xy} = \sigma_{yx}$, $\sigma_{xz} = \sigma_{zx}$ and $\sigma_{yz} = \sigma_{zy}$, thus there are six independent stress component instead of nine in eq. 3.51 (Ikelle and Amundsen, 2005). If the dimension of solid cube (Figure 3.5.1) are infinitesimally smaller, the sum of the moments of all surface forces about any axis must be zero (Sheriff and Geldart, 1995; Telford et al., 1990; Yilmaz, 2001). This requirement causes $\sigma_{ij} = \sigma_{ji}$ and making the stress tensor symmetrical.

The deformation in dimension or volume of elastic solid induced by stress is known as strain (Nye, 1985). Considering strain induced by seismic wave does not cause any permanent deformation on elastic solid along the propagation path because the stress field away from the typical seismic source is so small, hence strain induced by seismic wave is around 10^{-6} (Yilmaz, 2001). The relative change in dimension and shape of an elastic solid in length when the stresses applied are referred to as normal and shear strains. In addition, another form of deformation where as the elastic body is subjected to simply rotation, and a combination of the shear and rotation known as dilatation shown in Figure 3.7.

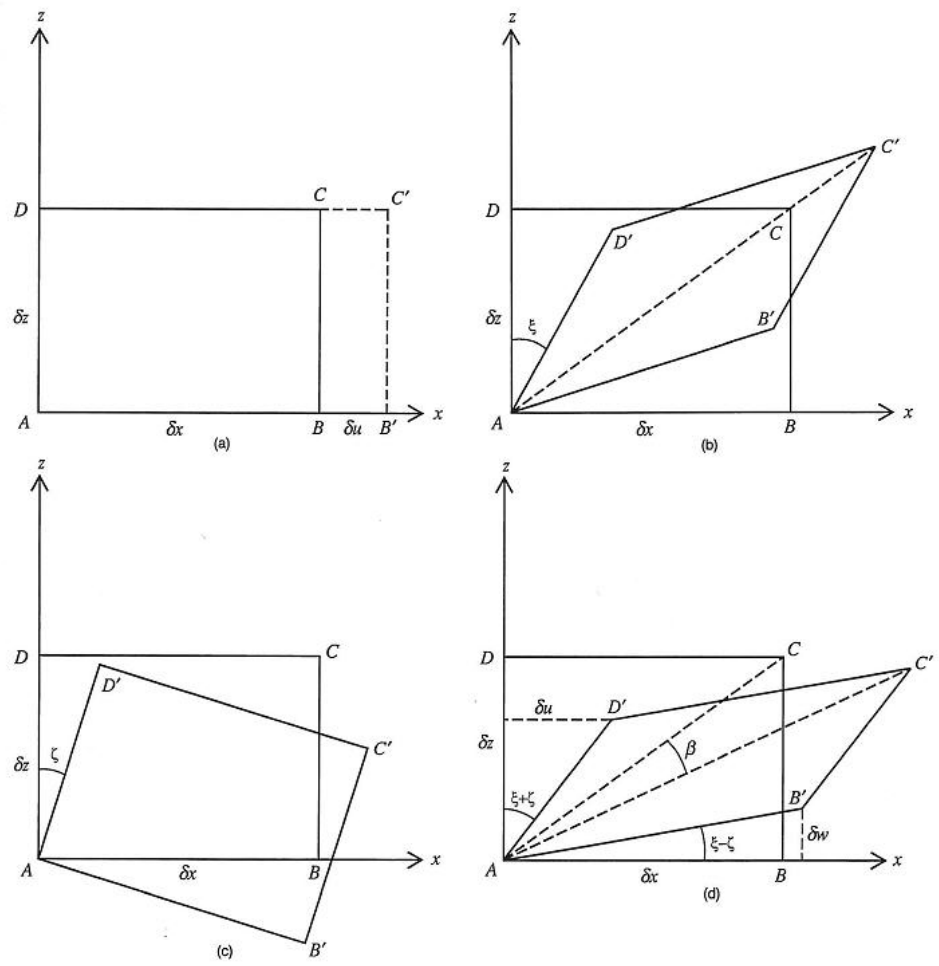

Figure 3.7 Deformations caused by stress acting on one surface of the volume a) simple extension (changing in dimension/length), b) shear (changing in shape), c) rotation and d) dilatation (changing in dimension and shape) (Yilmaz, 2001).

The strain that a unit cube undergoes in response to stress can also be expressed in components as depicted in Figure 3.7. These three dimensional components form the second order strain tensor (White, 1983):

$$\varepsilon_{ij} = \begin{bmatrix} \varepsilon_{xx} & \varepsilon_{xy} & \varepsilon_{xz} \\ \varepsilon_{yx} & \varepsilon_{yy} & \varepsilon_{yz} \\ \varepsilon_{zx} & \varepsilon_{zy} & \varepsilon_{zz} \end{bmatrix} \Rightarrow \begin{bmatrix} \dfrac{\partial u_x}{\partial x} \\ \dfrac{\partial u_y}{\partial y} \\ \dfrac{\partial u_z}{\partial z} \\ \dfrac{\partial u_z}{\partial y} + \dfrac{\partial u_y}{\partial z} \\ \dfrac{\partial u_z}{\partial x} + \dfrac{\partial u_x}{\partial z} \\ \dfrac{\partial u_y}{\partial x} + \dfrac{\partial u_x}{\partial y} \end{bmatrix}. \tag{3.52}$$

As the dimensions of the unit cube become infinitesimally small, $\varepsilon_{xy} = \varepsilon_{yx}, \varepsilon_{xz} = \varepsilon_{zx}$ and $\varepsilon_{yz} = \varepsilon_{zy}$ (Yilmaz, 2001), hence the strain tensor is defined symmetrical along the main diagonal. It implies of reducing nine independent strain components to six in eq. 3.52.

The relation between stress and strain tensor for an elastic solid was established by Hooke's law. Hooke's law states the stress component is linear proportional to the strain component (Aki and Richards, 1980; Nye, 1985; White, 1983) as shown in Figure 3.8.

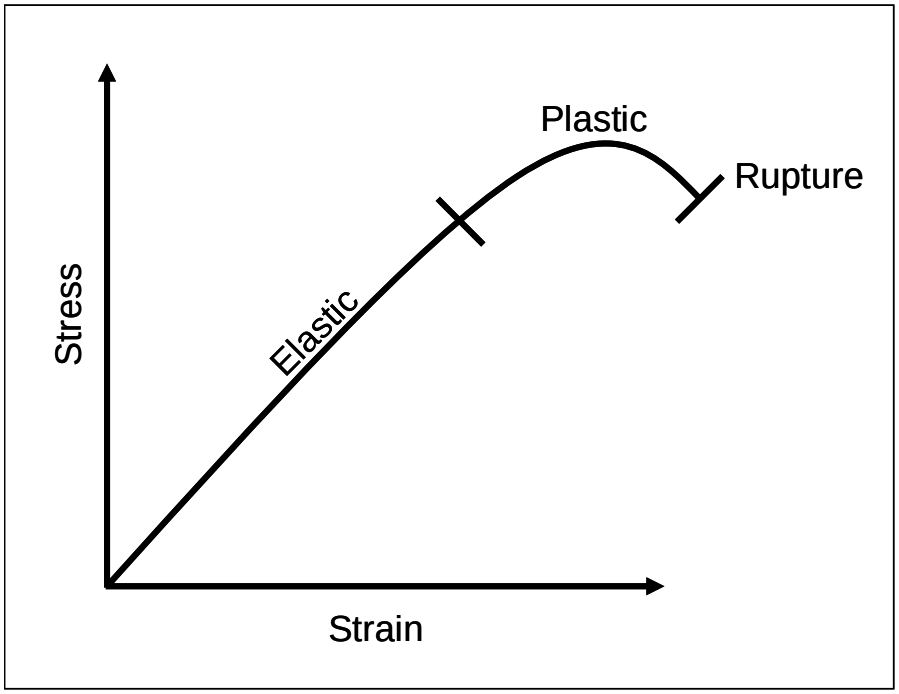

Figure 3.8 Stress and Strain relationship.

The linear stress-strain relations in isotropic and homogeneous medium which the elastic behavior has no preferred direction and for deformation that are sufficiently small (usual case for seismic wave) may be written in matrix notation (Yilmaz, 2001) as:

$$\begin{pmatrix} \sigma_{xx} \\ \sigma_{yy} \\ \sigma_{zz} \\ \sigma_{xy} \\ \sigma_{xz} \\ \sigma_{yz} \end{pmatrix} = \begin{pmatrix} \lambda+2\mu & \lambda & \lambda & 0 & 0 & 0 \\ \lambda & \lambda+2\mu & \lambda & 0 & 0 & 0 \\ \lambda & \lambda & \lambda+2\mu & 0 & 0 & 0 \\ 0 & 0 & 0 & \mu & 0 & 0 \\ 0 & 0 & 0 & 0 & \mu & 0 \\ 0 & 0 & 0 & 0 & 0 & \mu \end{pmatrix} \begin{pmatrix} \varepsilon_{xx} \\ \varepsilon_{yy} \\ \varepsilon_{zz} \\ \varepsilon_{xy} \\ \varepsilon_{xz} \\ \varepsilon_{yz} \end{pmatrix}, \tag{3.53}$$

where

$$\lambda = \frac{\nu E}{(1+\nu)(1-2\nu)}, \tag{3.54}$$

$$\mu = \frac{E}{2(1+\nu)}, \tag{3.55}$$

$$\nu = \frac{\lambda}{2(\lambda + \mu)}, \tag{3.56}$$

$$E = \frac{\mu(3\lambda + 2\mu)}{\lambda + \mu}. \tag{3.57}$$

λ and μ are Lamé's constants which is defined as the modulus of rigidity, known as shear modulus; ν is Poisson's ratio which is defined as the ratio of shear strain to principal strain, and E is Young's modulus which is defined as the ratio of principal stress to principal strain. The last four (eq. 3.54 to 3.57) are called elastic constants. Consider a medium subjected only to a hydrostatic pressure P in which all stresses are zero except σ_{xx}, we can obtain the following relations with other elastic constants as follow:

$$K = \lambda + \frac{2}{3}\mu. \tag{3.58}$$

K is bulk modulus (incompressibility), the ratio of the pressure to dilatation. In fluid, shear modulus μ=0, hence $K = \lambda$, we may call λ as bulk modulus. By eliminating different pairs of constants among the three equations (3.56 to 3.58), many different relations can be derived expressing one of the five constants in terms of two others (Sheriff, 1991; Telford et al., 1990). The simple form outlines the relationship among elastic constants in an isotropic media is summarized by Mavko et al. (1998) from original table by Birch (1961) as shown in Table 3.2. Note that all elastic constants have the same units as stress (force/area) except for Poisson's ratio ν which is dimensionless. When the stress is increased beyond elastic limit, Hooke's law no longer holds. Obviously, one should suspect experimental errors or that the material is not isotropic (Mavko et al., 1998). The condition is given by

$$\lambda + \frac{2\mu}{3} \geq 0; \mu \geq 0; \tag{3.59}$$

or

$$-1 < \nu \leq \frac{1}{2}; E \geq 0. \tag{3.60}$$

Table 3.2 Relations among elastic constants in an isotropic material (after Birch, 1961).

K	E	λ	ν	M	μ
$\lambda + 2\mu/3$	$\mu\frac{3\lambda+2\mu}{\lambda+\mu}$	—	$\frac{\lambda}{2(\lambda+\mu)}$	$\lambda + 2\mu$	—
—	$9K\frac{K-\lambda}{3K-\lambda}$	—	$\frac{\lambda}{3K-\lambda}$	$3K - 2\lambda$	$3(K-\lambda)/2$
—	$\frac{9K\mu}{3K+\mu}$	$K - 2\mu/3$	$\frac{3K-2\mu}{2(3K+\mu)}$	$K + 4\mu/3$	—
$\frac{E\mu}{3(3\mu-E)}$	—	$\mu\frac{E-2\mu}{(3\mu-E)}$	$E/(2\mu) - 1$	$\mu\frac{4\mu-E}{3\mu-E}$	—
—	—	$3K\frac{3K-E}{9K-E}$	$\frac{3K-E}{6K}$	$3K\frac{3K+E}{9K-E}$	$\frac{3KE}{9K-E}$
$\lambda\frac{1+\nu}{3\nu}$	$\lambda\frac{(1+\nu)(1-2\nu)}{\nu}$	—	—	$\lambda\frac{1-\nu}{\nu}$	$\lambda\frac{1-2\nu}{2\nu}$
$\mu\frac{2(1+\nu)}{3(1-2\nu)}$	$2\mu(1+\nu)$	$\mu\frac{2\nu}{1-2\nu}$	—	$\mu\frac{2-2\nu}{1-2\nu}$	—
—	$3K(1-2\nu)$	$3K\frac{\nu}{1+\nu}$	—	$3K\frac{1-\nu}{1+\nu}$	$3K\frac{1-2\nu}{2+2\nu}$
$\frac{E}{3(1-2\nu)}$	—	$\frac{E\nu}{(1+\nu)(1-2\nu)}$	—	$\frac{E(1-\nu)}{(1+\nu)(1-2\nu)}$	$\frac{E}{2+2\nu}$

The generalized form of Hooke's Law for anisotropic in linear elastic solid may therefore be written as (Nye, 1985):

$$\sigma_{ij} = C_{ijkl}\varepsilon_{kl}; \varepsilon_{ij} = S_{ijkl}\sigma_{kl}, \tag{3.61}$$

where the C_{ijkl} and S_{ijkl} are the components of fourth-rank elastic tensors. The C_{ijkl} are the elastic stiffnesses and the S_{ijkl} are the elastic compliances. In practice, we cannot measure strains however we can relate stress to displacement (u) rather than strain by:

$$\sigma_{ij} = C_{ijkl}\frac{\partial u_k}{\partial x_l}, \tag{3.62}$$

Since $\sigma_{ij} = \sigma_{ji}$ and $\varepsilon_{ij} = \varepsilon_{ji}$ in these equations are the symmetry parts of stress and strain tensors, thus $C_{ijkl} = C_{jikl} = C_{ijlk} = C_{jilk}$ and $S_{ijkl} = S_{jikl} = S_{ijlk} = S_{jilk}$. These relations reduce the number of independent constant from eighty one to thirty six furthermore to twenty one, the maximum number of elastic constants that medium can have

(Mavko et al., 1998). In matrix notation may be expressed as (Nye, 1985; White, 1983)

$$\begin{bmatrix} \sigma_{xx} \\ \sigma_{yy} \\ \sigma_{zz} \\ \sigma_{xy} \\ \sigma_{yz} \\ \sigma_{xz} \end{bmatrix} = \begin{bmatrix} C_{11} & C_{21} & C_{31} & C_{41} & C_{51} & C_{61} \\ C_{12} & C_{22} & C_{32} & C_{42} & C_{52} & C_{62} \\ C_{13} & C_{23} & C_{33} & C_{43} & C_{53} & C_{63} \\ C_{14} & C_{24} & C_{34} & C_{44} & C_{54} & C_{64} \\ C_{15} & C_{25} & C_{35} & C_{45} & C_{55} & C_{65} \\ C_{16} & C_{26} & C_{36} & C_{46} & C_{56} & C_{66} \end{bmatrix} \begin{bmatrix} \frac{\partial u_x}{\partial x} \\ \frac{\partial u_y}{\partial x} \\ \frac{\partial u_z}{\partial x} \\ \left(\frac{\partial u_y}{\partial z} + \frac{\partial u_z}{\partial y} \right) \\ \left(\frac{\partial u_z}{\partial x} + \frac{\partial u_x}{\partial z} \right) \\ \left(\frac{\partial u_x}{\partial y} + \frac{\partial u_y}{\partial x} \right) \end{bmatrix}. \tag{3.63}$$

3.5.3 Elastic wave equation

To examine how stress field are propagated through an elastic solid, Newton's second law of motion states the sum of all force (f) acting upon a body in an arbitrary direction i, is equal to the product of mass (m) and acceleration (a) of the body:

$$f_i = ma. \tag{3.64}$$

Figure 3.9 shows the force applied to the volume can be expressed in term of applied stress:

$$f_i = \frac{\partial \sigma_{ij}}{\partial x_j}. \tag{3.65}$$

We can also describe the Newton's second law of motion in term of displacement (u) of the volume:

$$f_i = \rho \frac{\partial^2 u_x}{\partial t^2}. \tag{3.66}$$

where ρ is the density of the volume and t is the time. Hence, combining eq. (3.64) and (3.65) allows Newton's second law of motion to be expressed in term of applied stress and displacement:

$$\rho \frac{\partial^2 u_x}{\partial t^2} = \frac{\partial \sigma_{ij}}{\partial x_j} \ . \tag{3.67}$$

Substituting eq. (3.61) into eq. (3.66) we arrive at the following system of wave equations:

$$\rho \frac{\partial^2 u_i}{\partial t^2} = \frac{\partial}{\partial x_j}\left(C_{ijkl} \frac{\partial u_k}{\partial x_l} \right) = C_{ijkl} \frac{\partial^2 u_k}{\partial x_j \partial x_l} \ . \tag{3.68}$$

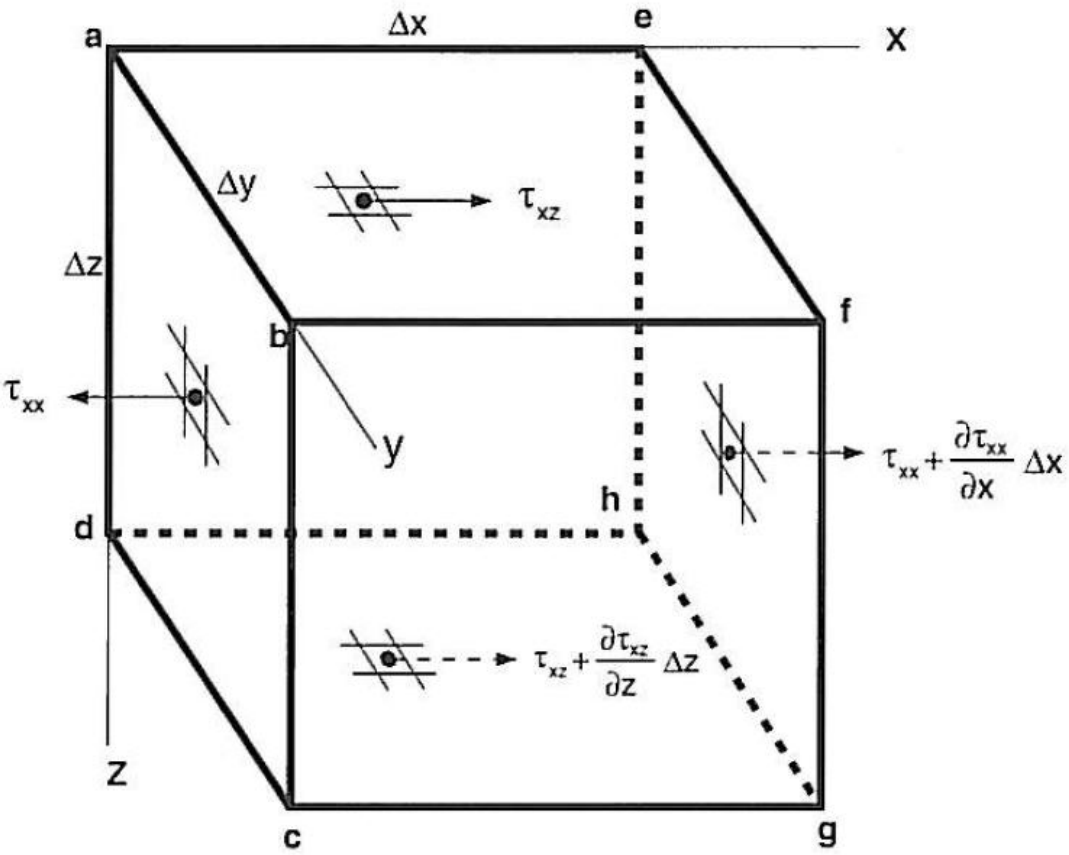

Figure 3.9 Illustration of stress components in the x-direction, on opposite faces of the volume (Ikelle and Amundsen, 2005).

3.5.4 Isotropic medium

The wave equation (eq. 3.68) describes the various types of elastic waves travelling through the earth body. We shall derive two types of elastic waves that are of interest in exploration seismology and are related to my research project. In homogenous, isotropic, and linearly elastic medium which have the maximum symmetry, are

completely characterized by two independent constants (Mavko et al., 1998). This simplifies the elastic stiffness and compliance tensors as each pair of indices $ij(kl)$ is replaced by one index $I(J)$, therefore the relation becomes $C_{ijkl} = C_{IJ}$ and $S_{ijkl} = S_{IJ}$.

$$C_{IJ} = \begin{bmatrix} C_{11} & C_{12} & C_{12} & 0 & 0 & 0 \\ C_{12} & C_{11} & C_{12} & 0 & 0 & 0 \\ C_{12} & C_{12} & C_{11} & 0 & 0 & 0 \\ 0 & 0 & 0 & C_{44} & 0 & 0 \\ 0 & 0 & 0 & 0 & C_{44} & 0 \\ 0 & 0 & 0 & 0 & 0 & C_{44} \end{bmatrix}, \qquad C_{12} = C_{11} - 2C_{44}, \tag{3.69}$$

We can relate the two independent constants, C_{11} and C_{44} to bulk modulus (K) and shear modulus (μ) of the rock as follow (Mavko et al., 1998):

$$C_{11} = \lambda + 2\mu, C_{12} = \lambda, C_{44} = \mu \ , \tag{3.70}$$

As a result, for compressional wave (P-wave) propagates along the x-axis, where the motion is parallel to the direction of wave propagation. The equation becomes:

$$\rho \frac{\partial^2 u_x}{\partial t^2} = \left(K + \frac{4}{3}\mu \right) \frac{\partial^2 u_x}{\partial x_x}, \tag{3.71}$$

Rearrangement gives the P-wave velocity (V_P) for a seismic wave travelling in an isotropic medium as:

$$\frac{\partial u_x}{\partial t} = \sqrt{\frac{K + \frac{4}{3}\mu}{\rho}}, \tag{3.72}$$

For shear wave (S-wave) propagates along the x-axis, where the displacement is perpendicular to the direction of wave propagation. The equation becomes:

$$\rho \frac{\partial^2 u_x}{\partial t^2} = \mu \frac{\partial^2 u_x}{\partial x_x} \quad , \tag{3.73}$$

Rearrangement gives the S-wave velocity (Vs) for a seismic wave travelling in an isotropic medium as:

$$\frac{\partial u_x}{\partial t} = \sqrt{\frac{\mu}{\rho}}, \tag{3.74}$$

Therefore, to predict P- and S- wave velocity requires the knowledge of bulk modulus (K), shear modulus (μ) and density (ρ). If the medium is fluid, then S-wave velocity is equal to zero and P-wave velocity would be the speed of sound waves in fluid (Ikelle and Amundsen, 2005).

3.5.5 Anisotropic medium

A medium is considered to be anisotropic if its elastic properties vary with direction (Crampin, 1989; Winterstein, 1990). The common interpretation of seismic anisotropy or velocity anisotropy relates to variation of wave speed (seismic velocity) with direction of wave travel (Crampin, 1989; Sheriff and Geldart, 1995). Obviously, anisotropy effect is large in S-wave data and it influences data interpretation.

3.5.5.1 Tranverse Isotropy

The simplest realistic form of seismic anisotropy is transverse isotropy (Ikelle and Amundsen, 2005; Thompson, 2002). Transverse isotropy possesses a velocity having the same value when measured within a plane, but a different value when measured perpendicular to the plane or along the symmetry axis. Transverse anisotropy can be in the two forms within the subsurface based on their symmetry axis as shown in Figure 3.10. It is usually oriented with gravity or regional stress. If gravity is the dominant factor, the symmetry axis direction will be vertical, and we get VTI (Vertical Transverse Isotropy), which is a layered rock having physical properties not varying in horizontal direction but varying in the vertical axis. If regional stress is dominant factor, the symmetry axis direction will be horizontal, and we get HTI (Horizontal Transverse Isotropy), which is a layered rock having physical properties not varying in vertical direction but varying in the horizontal axis. Vertical fractures can cause this form of anisotropy in the subsurface. When the axis of symmetry is neither horizontal nor vertical, but tilted in some arbitrary direction, seismic velocities depends on azimuthal direction. This type of anisotropy is referred to as azimuthal or titled transverse anisotropy (TTI) (Ikelle and Amundsen, 2005; Thompson, 2002).

a)

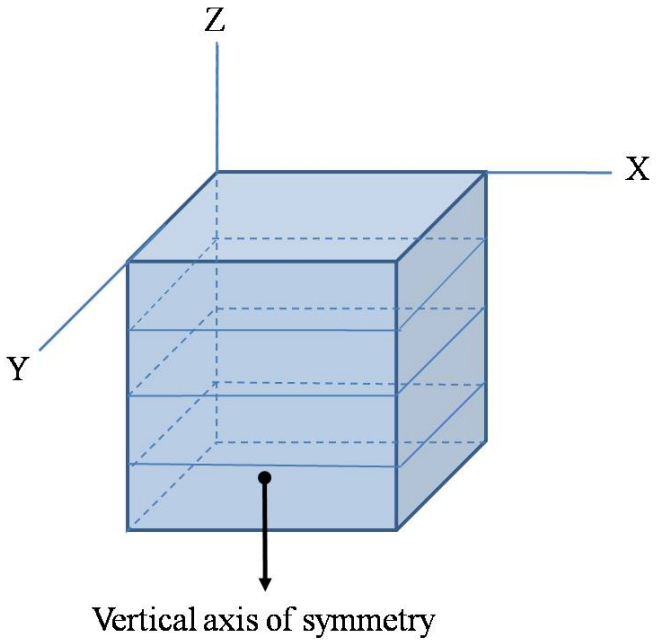

b)

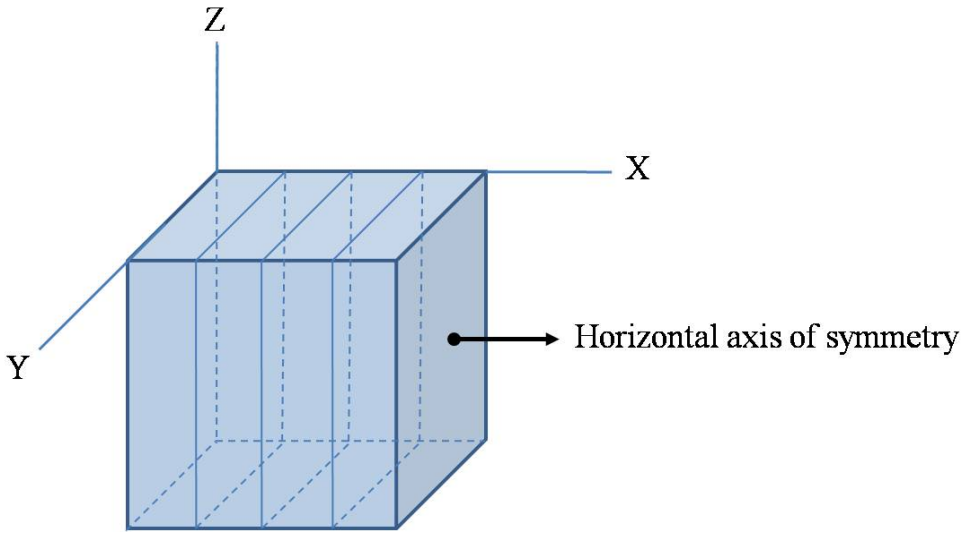

Figure 3.10 Diagram of two general forms of anisotropy exist in the subsurface. a) vertical transverse isotropy (VTI) describes seismic velocity not varying horizontally along bedding plane, but vary vertically along symmetry axis. b) horizontal transverse isotropy (HTI) describes seismic velocity not varying vertically along bedding plane, but vary horizontally along symmetry axis.

Rock formations with VTI and HTI are described by five independent elastic constants. The stiffness tensor of a VTI medium is (Ikelle and Amundsen, 2005)

$$C_{ij} = \begin{bmatrix} C_{11} & C_{11}-2C_{66} & C_{13} & 0 & 0 & 0 \\ C_{11}-2C_{66} & C_{11} & C_{13} & 0 & 0 & 0 \\ C_{13} & C_{13} & C_{13} & 0 & 0 & 0 \\ 0 & 0 & 0 & C_{44} & 0 & 0 \\ 0 & 0 & 0 & 0 & C_{44} & 0 \\ 0 & 0 & 0 & 0 & 0 & C_{66} \end{bmatrix} \tag{3.75}$$

The stiffness tensor of a HTI medium is (Ikelle and Amundsen, 2005)

$$C_{ij} = \begin{bmatrix} C_{11} & C_{13} & C_{13} & 0 & 0 & 0 \\ C_{13} & C_{33} & C_{33}-2C_{44} & 0 & 0 & 0 \\ C_{13} & C_{33}-2C_{44} & C_{33} & 0 & 0 & 0 \\ 0 & 0 & 0 & C_{44} & 0 & 0 \\ 0 & 0 & 0 & 0 & C_{66} & 0 \\ 0 & 0 & 0 & 0 & 0 & C_{66} \end{bmatrix} \tag{3.76}$$

One manifestation of azimuthal anisotropy in seismic data is shear-wave splitting. They split into two types of shear-waves when entering an anisotropic medium, fast and slow (Crampin, 1989). These two shear waves are perpendicular to each other. The fast shear wave is polarized parallel to the direction of maximum horizontal stress, and the slow shear wave is polarized parallel to the direction of minimum horizontal stress. Figure 3.11 shows an example of a shear wave splitting in application of seismic survey. In medium with vertical fractures, the fast shear wave will be polarized parallel to the fractures alignment, whereas the slow shear wave will be polarized perpendicular to the fractures alignment. The common notation for fast shear wave is V_{SH} and slow shear wave is V_{SV} .

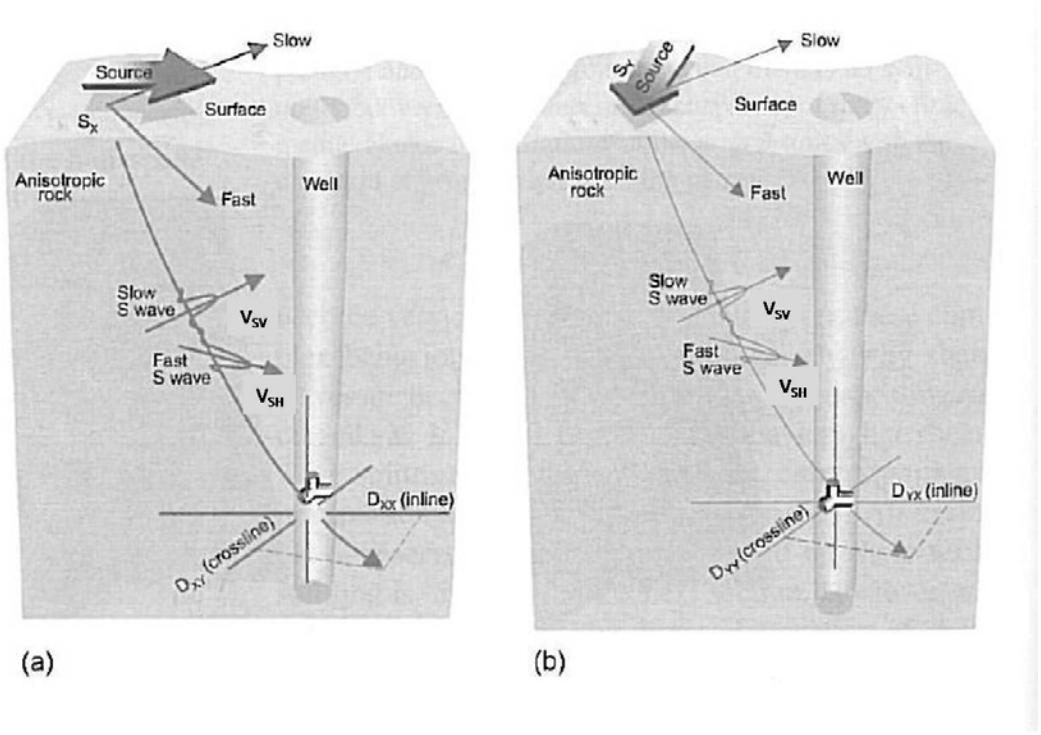

Figure 3.11 An example of two types of shear wave splitting from seismic measurement. A) Using source along the x-axis; b) Using source along the y-axis. Both sources cause shear wave splitting when the velocities travel in anisotropic rock (Ikelle and Amundsen, 2005).

3.6 Seismic inversion

Inversion can be explained as a process of inverting seismic reflection data into physical properties of the layer, density and velocity. The goal is to estimate model parameters from observed data within some error. For this research purpose, the inversion is limited to acoustic impedance due to availability of only post-stack seismic data. The method used here is model based inversion.

3.6.1 Convolution model

Model based inversion starts with convolution model. Convolution is a mathematical operation defined as "a change in wave shape as a result of passing through a linear filter" (Sheriff, 1991). In 1D inversion, the seismic trace *s(t)* is modelled as a convolution of the normal-incidence reflectivity series *r(t)* with the wavelet *w(t)* and the addition of a random noise component as shown in eq. 3.77.

$$s(t) = w(t) \otimes r(t) + noise \quad , \tag{3.77}$$

The normal-incidence reflectivity is defined in terms of the contrast in the seismic impedance between two homogeneous layers as (Russell and Hampson, 2006):

$$R_{pi} = \frac{Z_{pi+1} - Z_i}{Z_{pi+1} + Z_i}, \tag{3.78}$$

where the subscript r_{pi} is the zero-offset P-wave reflection coefficient at the i^{th} interface of a stack of N layer and $Z_{pi}=\rho iVi$ is the i^{th} ρ-impedance of the i^{th} layer, where ρ is density, V_P is P-wave velocity and $\otimes$ denotes convolution. If we assume that recorded seismic trace is a given in eq. (3.78), the we can invert this equation to recover the P-impedance using the recursive equation given by Lindseth (1979):

$$Z_{pi} = Z_{pi}\left[\frac{1+r_{pi}}{1-r_{pi}}\right]. \tag{3.79}$$

Theoretically, by applying eq. (3.79) to a seismic trace, we can invert reflection data to P-impedance (Russell and Hampson, 2006). However, since the seismic trace is a band-limited version of the reflectivity given in eq. (3.77), with typical frequency range of 10-60Hz, consequently the information of low frequency component of the reflectivity data is removed (Lindseth, 1979; Oldenburg et al., 1983).

3.6.2 Low frequency model

All inversion algorithms suffer from non-uniqueness problem that could produce many possible solutions, in other words, there is more than one possible geological model consistent with seismic data (Hampson-Russell., 2010; Oldenburg et al., 1983). In order to restrict possible solutions, a priori low-frequency information is added (Herawati and Davis, 2003). Low frequency component can be estimated from well log data (sonic and density logs) or RMS velocity estimates from seismic data (Avseth et al., 2005; Oldenburg et al., 1983; Russell and Hampson, 2006). The model is constrained and guided by horizons interpretation. Later the low frequency model is used as constrain to the upper and lower limit of impedance result.

3.6.3 Model-based inversion

STRATA program (Hampson-Russell., 2010) is used to generate model based inversion. The program is based on a generalized linear inversion method (GLI), described by Cooke and Schneider (1983); Russell (1988). The objective of this method is to perturb the low frequency model until we obtain a good fit between the seismic data and a synthetic trace computed by applying eq. (3.77) and (3.78) within some error (minimum).

The model is built based on the assumption as follow:

- Seismic trace and a good estimate of seismic wavelet are known.
- 1-D earth model, consist of a series of number layer.
- An earth model is characterised by a blocky impedance profile from well logs (average value).

The generalized linear inversion algorithm is based on utilizing Taylor series expansion:

$$F\left(M\right)=F\left(M_0\right)+\frac{\partial F\left(M_0\right)}{\partial M}\Delta M+...., \tag{3.79}$$

where M_0, M, ΔM, $F(M)$, and $F(M_0)$ are is initial model, true model, change in model parameters, observed seismic, and synthetic seismic from initial model, respectively.

To solve ΔM, eq. (3.74) can be reordered as follow:

$$F\left(M\right)-F\left(M_0\right)=\frac{\partial F\left(M_0\right)}{\partial M}\Delta M, \tag{3.80}$$

The error between the real and synthetic seismic data is defined as:

$$\Delta F=F\left(M\right)-F\left(M_0\right)=\frac{\partial F\left(M_0\right)}{\partial M}\Delta M=A\Delta M, \tag{3.81}$$

where A is matrix of derivative.

The solution can be written as follow:

$$\Delta M = \left(A^T A\right)^{-1} A^T \Delta F. \tag{3.82}$$

Equation (3.82) assumes a stable inverse but it may not always be the case because of the noise and the non-unique model parameters problem (Herawati and Davis, 2003). Cooke (1981) introduced the damping parameter (λ) or pre-whitening factor to stabilize the inverse solution. Thus eq. (3.82) can be rewritten as:

$$\Delta M = \left(A^T A + \lambda I\right)^{-1} A^T \Delta F. \tag{3.83}$$

where *I* is identity matrix.

In the GLI method each block is assigned a starting impedance value, impedance changes within the block, and thickness in time (Cooke and Schneider, 1983). Initial guess model in GLI method is impedance log that has been constrained by the horizon interpretation. Thus, low frequency model has been incorporated in the process.

Equation (3.77) relates the model to the observation is the convolution model. The model is characterized by the reflection coefficients and the observation is the recorded seismic trace. The impedance within the layer is computed using the definition of reflection coefficient in eq. (3.78). By knowing the reflection coefficient between two layers and the acoustic impedance of the upper layer, the acoustic impedance of the below layer can be calculated. The acoustic impedance of upper layer is estimated from the initial model. Hence, the general equation of the impedance for *i* layer is defined by:

$$I(i) = I(1)\prod_{j=2}^{i}\left[\frac{1+r(j)}{1-r(j)}\right]. \tag{3.84}$$

3.7 Seismic imaging

As we gain more understanding of rock physics and seismic theory, we are now able to quantify interpretation of seismic data and relate them to the rock properties. The use of reflection seismic amplitudes to derive various seismic attributes are presented here especially the attributes used to image the changes in the elastic properties of the Waarre-C formation before and after CO_2 injection. However, I begin a discussion on the limits of the resolution of seismic data.

3.7.1 Seismic resolution

Seismic resolution relates to the magnitude of the image that can be observed within seismic data. Yilmaz (2001) defines resolution as how close two points can be, yet still be distinguished from one another. Seismic resolution is generally considered in terms of being able to distinguish and separate between the top and the bottom of a layer and is limited by the thickness of the layer itself (vertical resolution), or between two reflecting points horizontally (horizontal resolution). Both depend on signal bandwidth content. The vertical resolution is dependent on the dominant frequency while the horizontal resolution is dependent on the size of the Fresnal zone. Seismic resolution is the key to extraction of stratigraphic detail from seismic data and this has become more important for quantitative seismic interpretation.

3.7.1.1 Vertical resolution

The dominant wavelength of seismic waves is given by

$$\lambda = \frac{v}{f} \ . \tag{3.85}$$

where v is velocity and f is dominant frequency. Seismic wave velocities in the subsurface range between 2000 to 5000 m/s and generally increase in depth. The dominant frequency of the seismic signal typically varies between 20 to 50 Hz and decrease in depth. Typical seismic wavelengths range from 40 to 250 m and generally increase in depth due to increase in velocity and greater frequency attenuation.

Seismic resolution has been examined intensively by a number of researchers using both physical and numerical modelling. Rayleigh (1945) established the criterion for seismic resolution and determined that the limit of vertical resolution occurs when two points are separated in time by the peak-to-trough interval of wave propagation, that is one half wavelength as shown in Figure 3.12 (Kallweit and Wood, 1982). The next criterion developed by Ricker (1955) who studied the composite waveform reflected from the thin bed. He noticed as the thickness of the bed decreased, the separation of the two wavelets decreased and that the two peaks merged into one central maximum before becoming one single major peak. Ricker defined the limit of vertical resolution as occurring when two spikes are separated by an interval equal to the separation between inflection point on the central maximum of the waveform which produced the flat-spot or zero-curvature (Figure 3.12). Similarly, (Widess, 1973) studied the limit of vertical resolution by examining physical a wedge model using amplitude reflection. He found that if the bed thickness is greater than the length of the wavelength; the two distinct wavelets can be separable and recorded from the top (trough) and the base (peak) of the bed, as shown in Figure 3.13. As the thickness decreases, the two distinct wavelets cannot be separated from the top and the base of the bed and become one single wavelet. The only characteristic of seismic response observable is the change in amplitude of the waveform to the maximum when the bed thickness is equal to 1/4 of a wavelength. This condition is known as tuning and at this point it is possible to calculate the tuning thickness. After this point, the amplitude of the wavelet decreases as well as trough-to-peak time decreases. When the bed thickness is reached 1/8 of a wavelength, there is negligible change in the observable peak-to-trough time. Thus, Widess considered 1/8 of a wavelength as the limit of vertical resolution (resolvable limit). Wedge model generates a reflection even where bed thickness is much smaller than resolvable, the minimum thickness for a layer to give a reflection is known as detectable limit in the order of 1/30 wavelength. There is nearly a 10:1 ratio between wavelengths shallow and deep in the earth. In practice, the limit of vertical resolution is influenced by signal-to-noise ratio as well as the interpreter's perspective.

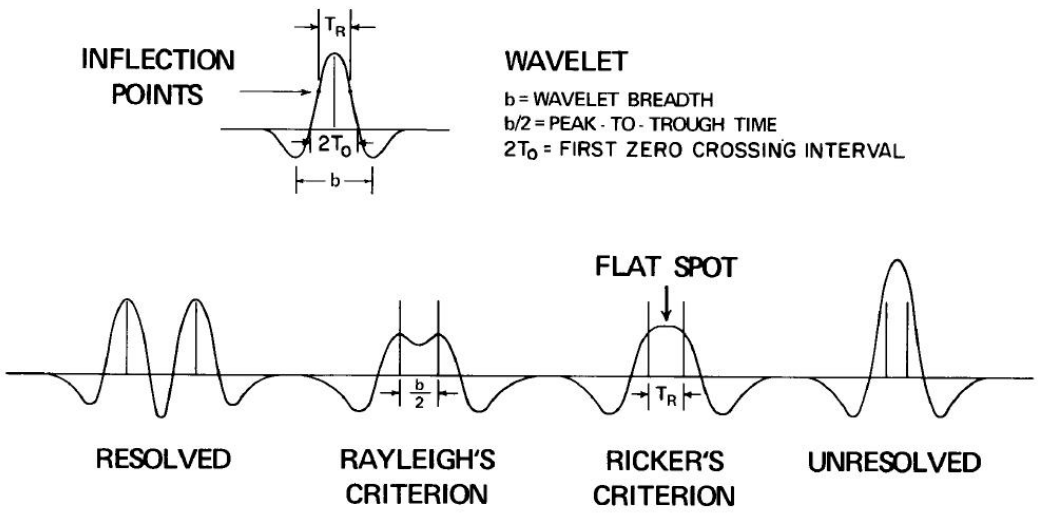

Figure 3.12 Criterion comparisons between the limit of vertical resolution defined by Rayleigh (1945) and Ricker (1953). Rayleigh's limit occurs when two points are separated in time by the peak-to-trough interval of wave propagation, which are one half wavelengths. Ricker's limit occurs when two spikes are separated by an interval equal to the separation between inflection points on the central maximum of the waveform (after Kallweit and Wood, 1982).

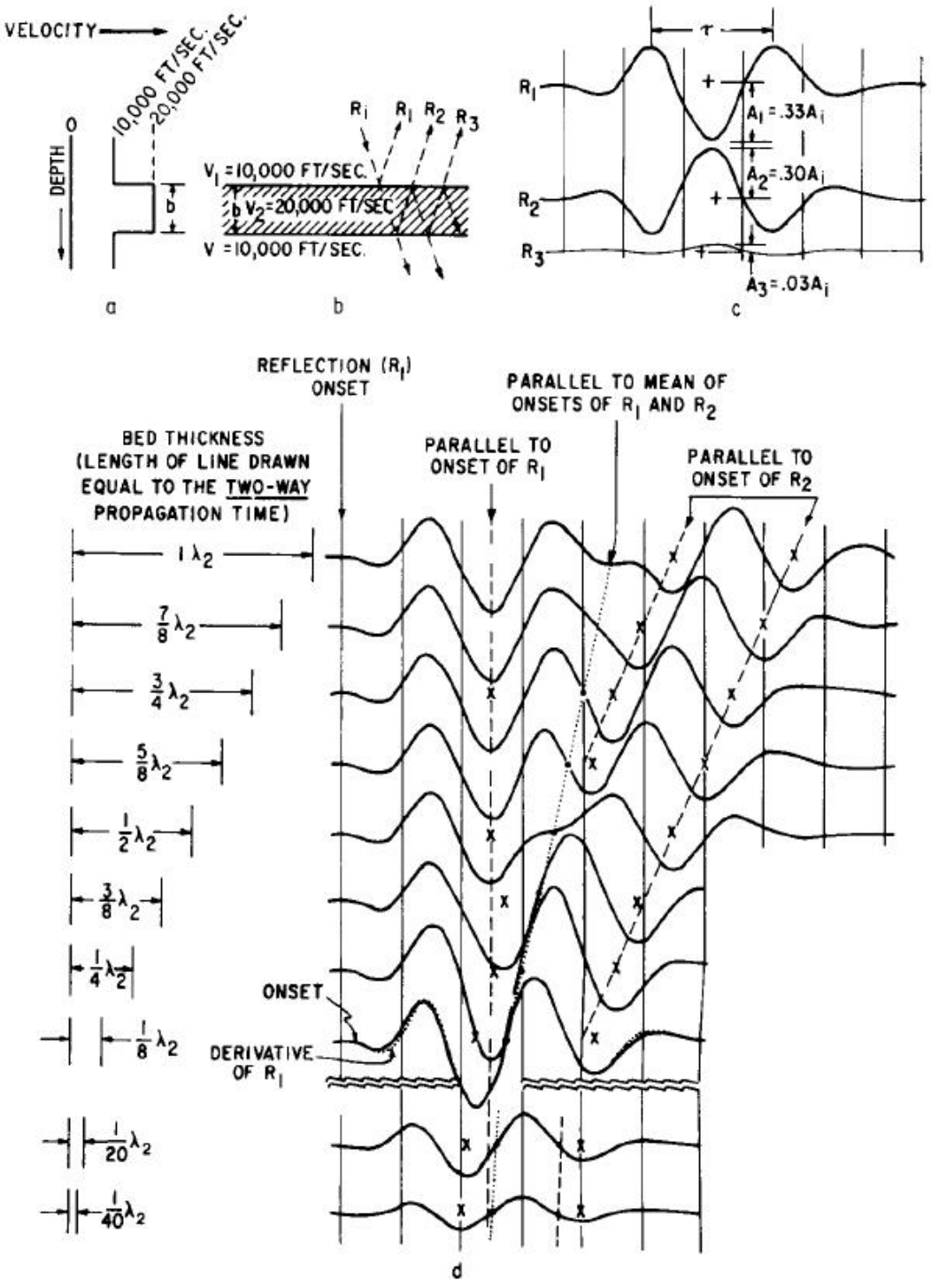

Figure 3.13 Widess (1973) defined the limit of vertical resolution and their effect on bed thickness. a) Velocity diagram, b) reflection of two interfaces diagram, c) Synthetic trace from b, and d) Form and relative timing of composite reflection as a function of bed thickness.

3.7.1.2 Horizontal resolution

Horizontal resolution is also an important consideration when evaluating seismic data. The seismic source produces a spherical wavefront which reflects from the horizontal reflector rather than from a point, as shown in Figure 3.14. The portion of a reflector from which reflected energy can reach a detector within one-half wavelength of the first reflected energy is called first Fresnal zone (Sheriff, 1991). Two reflecting points that fall within first Fresnal zone generally are considered indistinguishable as observed from the earth's surface. Since the limit of horizontal resolution depends on the size of Fresnal zone and Fresnal zone depends on wavelength and frequency, in other word, the shallower the event, the higher the frequency, and the smaller the Fresnal zone. Thus the easier it is to differentiate between two reflecting point (Yilmaz, 2001).

The radius of Fresnal zone (r) depends on the depth of reflecting interface (z) and the dominant seismic wavelength (λ) (Yilmaz, 2001)

$$r = \sqrt{\frac{z_0 \lambda}{2}} . \tag{3.86}$$

Threshold for lateral resolution implies that the radius of first Fresnal zone decreases with increasing dominant frequency of seismic wavelength.

$$r = \frac{v}{2}\sqrt{\frac{t_0}{f}} . \tag{3.87}$$

where $t_0 = 2z_0 / v$, the travel time of seismic energy. The Fresnal zone generally increases with depth, as a result, the horizontal resolution become poor.

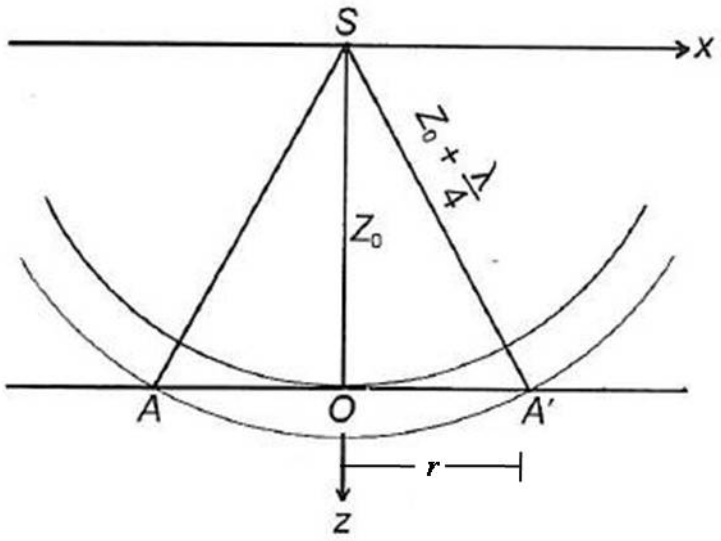

Figure 3.14 Schematic presentation of Fresnel zone. Seismic source produces a spherical wavefront that impinges on the horizon planar reflector AA'. The AA' interface is known as the first Fresnel zone by Sheriff (1991). Two reflecting points that fall within this zone generally are considered indistinguishable as observed from the surface (Yilmaz, 2001).

3.7.2 Seismic reflectivity

When seismic waves propagates in the earth, they will encounter layer boundaries with different physical properties, thus the energy of incident wave at each boundary is partitioned. For example, P-wave and S-wave velocity can be either reflected and/or transmitted at the boundary interface as shown in Figure 3.7.4 (Yilmaz, 2001). Therefore the types of partitioning of incident waves depend upon the angle of incident, the angle between the incident wave and the normal to the boundary. When seismic wave impinges at normal incidence upon a layer boundary, the reflection coefficient (RC) is given by:

$$RC = \frac{\rho_2 V_2 - \rho_1 V_1}{\rho_2 V_2 + \rho_1 V_1} = \frac{Z_2 - Z_1}{Z_2 + Z_1} = \frac{\Delta AI}{2AI}, \qquad (3.88)$$

ρ_1, ρ_2 and V_1, V_2 are the densities and velocities of upper and lower layers, respectively. The product of velocity (V) and density (ρ) is impedance (Z), if there is a different between impedance of the upper and lower layer, then a reflection occurs at the interface name acoustic impedance or zero-offset reflectivity (AI).

Snell's Law established the relationship between the angle of incident, and others when seismic waves passing through a boundary of two different physical properties. Thus, the general form of Snell's law as described in Figure 3.7.4 is:

$$\frac{\sin\varphi_0}{V_{p1}} = \frac{\sin\varphi_1}{V_{p1}} = \frac{\sin\varphi_2}{V_{p2}} = \frac{\sin\psi_1}{V_{s1}} = \frac{\sin\psi_2}{V_{s2}}. \tag{3.89}$$

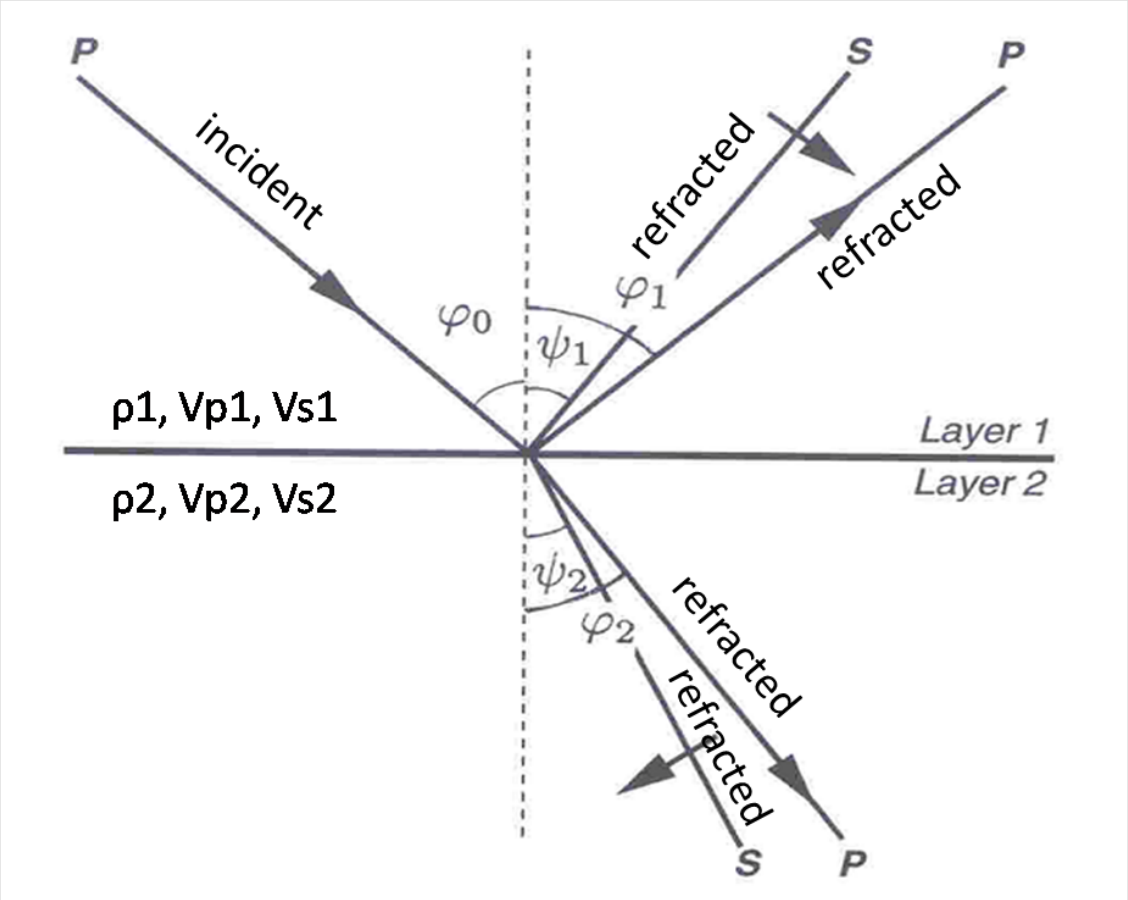

Figure 3.15 Partitioning of an incident P-wave at an interface. At non-zero angles of incidence, both P- and mode converted S-wave energy are reflected from and transmitted across the interface (Yilmaz, 2001).

Zoeppritz (1919) related the P- (reflected) and S- (transmitted) waves to the physical properties of two layers as a function of angle of incident. In matrix notation, Zoeppritz's equation can be expressed as follows (Yilmaz, 2001):

$$\begin{bmatrix} R_p \\ R_s \\ T_p \\ T_s \end{bmatrix} = \begin{bmatrix} \cos\varphi_1 & \frac{V_{p1}}{V_{s1}}\sin\psi_1 & \frac{V_{p1}}{V_{p2}}\cos\varphi 2 & -\frac{V_{p1}}{V_{s2}}\sin\psi_2 \\ -\sin\varphi_1 & \frac{V_{p1}}{V_{s1}}\cos\psi_1 & \frac{V_{p1}}{V_{p2}}\sin\varphi 2 & \frac{V_{p1}}{V_{s2}}\cos\psi_2 \\ -\cos 2\psi_1 & -\sin 2\psi_1 & \frac{\rho_2}{\rho_1}\cos 2\psi_2 & -\frac{\rho_2}{\rho_1}\sin 2\psi_2 \\ \sin 2\varphi_1 & -\frac{V_{p1}^2}{V_{s1}^2}\cos 2\psi_1 & \frac{\rho_2 V_{p1}^2 V_{s2}^2}{\rho_1 V_{p2}^2 V_{s1}^2}\sin 2\varphi_2 & \frac{\rho_2 V_{p1}^2}{\rho_1 V_{s1}^2}\cos 2\psi_2 \end{bmatrix} \begin{bmatrix} \cos\varphi_1 \\ \sin\varphi_1 \\ \cos 2\psi_1 \\ \sin 2\varphi_1 \end{bmatrix} \quad (3.90)$$

R and *T* are defined as reflected and transmitted coefficient with subscript *p* and *r* are P- and S-waves, respectively.

To better understand the relationship between the coefficients and the physical parameters at the given angle of incidence, Aki and Richards (1980) derived the exact Zoeppritz's equation for small elastic properties changes with the incidence angle less than critical angle by linear approximation as follows:

$$R(\varphi_0) = R_p + G\sin^2\varphi_0 + C\tan^2\varphi_0\sin^2\varphi_0, \quad (3.91)$$

where

$$R_p = \frac{1}{2}\left[\frac{\Delta V_p}{V_p} + \frac{\Delta\rho}{\rho}\right], \quad (3.92)$$

$$G = \frac{1}{2}\frac{\Delta V_p}{V_p} - 4\left[\frac{V_s}{V_p}\right]^2\frac{\Delta V_s}{V_s} - 2\left[\frac{V_s}{V_p}\right]^2\frac{\Delta\rho}{\rho}, \quad (3.93)$$

$$C = \frac{1}{2}\frac{\Delta V_p}{V_p}. \quad (3.94)$$

Aki-Richards equation uses average density and velocities across the layer boundary and the different between upper and lower layer as follows:

$$V_p = \frac{V_{p2} + V_{p1}}{2}, \tag{3.95}$$

$$V_s = \frac{V_{s2} + V_{s1}}{2}, \tag{3.96}$$

$$\rho = \frac{\rho_2 + \rho_1}{2}, \tag{3.97}$$

$$\Delta V_s = V_{s2} - V_{s1}, \tag{3.98}$$

$$\Delta\rho = \rho_2 - \rho_1 . \tag{3.99}$$

R_p represents the first term of an approximation of zero-offset reflection coefficient known as the intercept and can be used to derive the acoustic impedance attribute, which is indirectly related to porosity in reservoir rocks. *G* represents the second term of the biggest effect on amplitude as a function of offset known as gradient. Gradient depends on changes in P- and S-wave velocities and density and corresponds to the small angles, typical less than 30^0 (critical angle). In term of interpretation, *G* is directly related to change in Poisson's ratio $\Delta\sigma$, which in turn, is directly related to fluid saturation in reservoir rocks. *C* represents the third term dependence on changes in P-wave only. The third term corresponds to the large angle, greater than 30^0 (critical angle). This approximation leads us to estimate the elastic parameters of reservoir rocks from reflection amplitude and relates these parameters to reservoir fluids.

3.7.3 Seismic trace attributes

Attributes are simply defined as information extracted from seismic data. The usefulness and quality of the attribute analysis depends on a combination of reservoir characterization, the availability and quality of the data, and interpreter experience. If these factors are of sufficient quality, it is possible to significantly improve estimates of rock properties, depositional environment and interpreting seismic facies.

Several of the attributes classification are derivative from complex trace attributes analysis (Taner et al., 1979). The complex trace seismic analysis was first introduced in 1976 and is based on attributes measurements which are derived from an analytic signal as shown in Figure 3.16 and can be defined as:

$$F(t) = f(t) + if^*(t) = A^{i\theta}, \tag{3.100}$$

where $f(t)$ is the real part of the complex trace, $f^*(t)$ is the imaginary part of the complex trace, A is the reflection strength or instantaneous amplitude and θ is the instantaneous phase. The real part $f(t)$ is the recorded signal and could be thought as a measure of kinetic energy (Taner and Sheriff, 1977). The imaginary part $f^*(t)$ is called the quadrature trace and it implies applying a 90^0 phase shift of seismic trace using Hilbert transform (Bracewell and Kahn, 1966). The quadrature trace can be thought of as a measure of potential energy. The Complex trace equation describes the energy transfer back and forth between kinematic and potential forms as a particle moves in response to the passage of the seismic wave through the medium. The use of complex trace $f(t)$ makes it possible to define instantaneous amplitude, phase, frequency and later, its derivatives (Barnes, 1998; Barnes, 2007; Taner et al., 1979). The instantaneous measurements are associated with an instant time rather than an average over a time interval. Thus to infer any stratigraphic meaning from instantaneous attributes, the amplitude and frequency content of the seismic signal must be preserved in each processing step prior to estimating the instantaneous parameters. Any variations in the shape of the basic waveform that is not attributable to the subsurface geology must be eliminated. Multiples and all types of random noise limit the reliability of the results (Yilmaz, 2001).

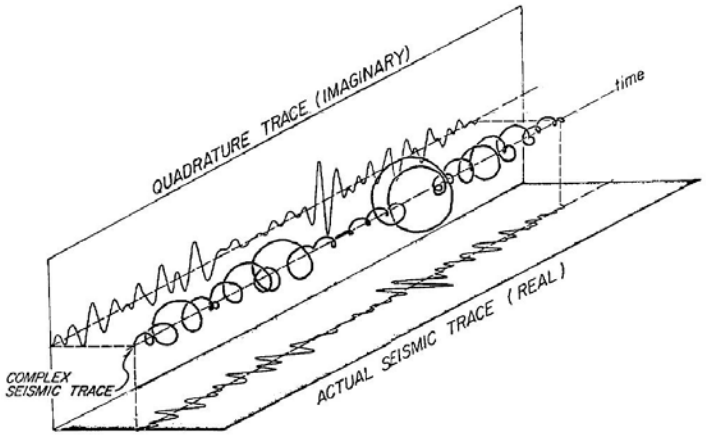

Figure 3.16 Isometric diagram of a complex seismic trace show the actual seismic trace and imaginary trace (after (Taner and Sheriff, 1977).

3.7.3.1 Reflection strength or envelope amplitude

Reflection strength can be thought of as amplitude independent of phase. It is the envelope of the seismic trace. Reflection strength is defined as (Taner et al., 1979):

$$A(t) = \sqrt{f^2(t) + f^{*2}(t)} \tag{3.101}$$

The reflection strength is an effective tool to identify bright and dim spots (Yilmaz, 2001). It provides information about contrast in acoustic impedance. Lateral changes in reflection strength are often associated with major lithologic changes or with hydrocarbon accumulations. Sharp local changes may also indicate faulting (Taner et al., 1979). Gas reservoirs, in particular, frequently appear as high-amplitude "bright-spot" reflections. Reflection strength also provides a means of detecting and calibrating thin-bed tuning effects which may result from the constructive and destructive interference of reflector wavelet.

3.7.3.2 Instantaneous phase

Instantaneous phase is a measure of the continuity of events on a seismic trace. Phase describe the angle between the phasor (a rotating vector formed by the real and imaginary components of the time series) and the real axis as a function of time. It looks like the following:

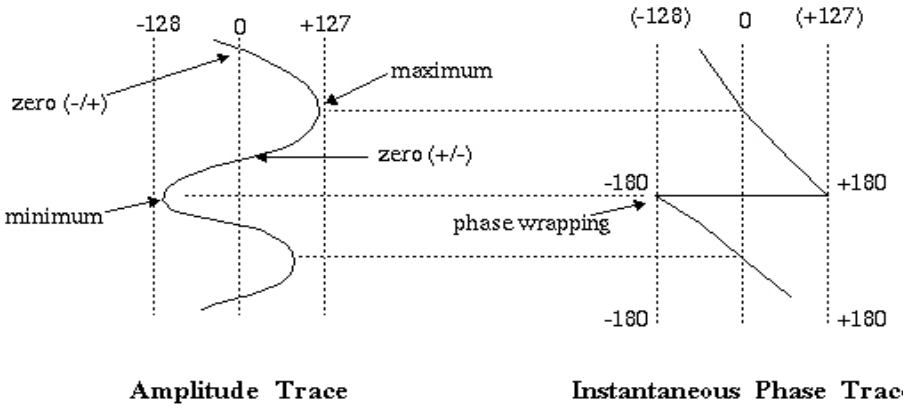

Figure 3.17 The comparison between amplitude trace and instantaneous phase trace (Landmark, 2003).

For this research purpose, I used amplitude attribute analyses which taking attribute extraction at the time window centred about a single horizon, maximum peak and RMS amplitudes. Qualitatively, amplitude-based map can be useful in identifying gas and fluid accumulation, lithology, channel features, tuning effects, etc. Barnes (2007), and Brown (2004) provide a good overview of the value of amplitude statistics. Rijks (1991) describes the use of amplitude and other attributes extraction workflow. A review of maximum peak and RMS amplitude computation is illustrated in Figures 3.18 and 3.19.

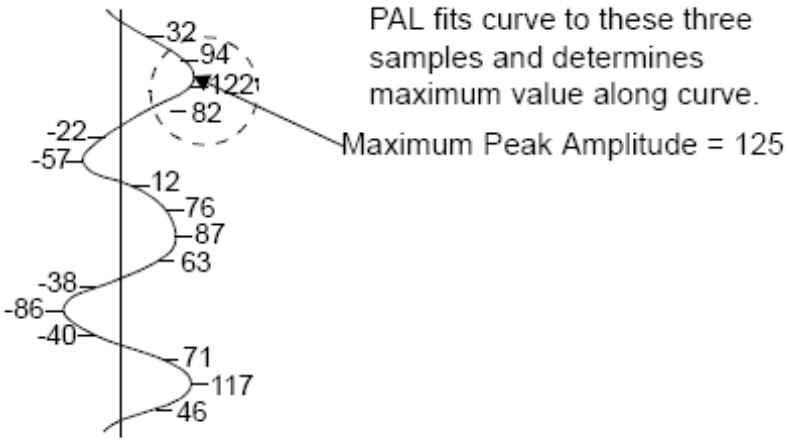

Figure 3.18 Maximum Peak Amplitude computation. For each trace, the computation does parabolic fit through the maximum positive amplitude in the analysis window and the two samples on either side of it and the maximum value along that curve is interpolated (Landmark, 2003).

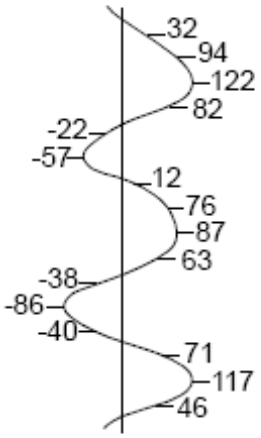

$$RMS = \sqrt{\frac{1}{N}\sum_{i=1}^{N} a_i^2}$$

$$= \frac{1}{16}(32^2 + 94^2 \ldots + 117^2 + 46^2)$$

$$= \sqrt{\frac{1}{16}(83945)}$$

$$= \sqrt{5246.56}$$

$$= 72.43$$

Figure 3.19 RMS (Root-Mean-Square) amplitude computation. Because amplitudes are squared before averaging, thus the RMS computation is very sensitive to extreme amplitude values. For example bright spot, flat spot (Landmark, 2003).

I have reviewed some fundamental rock physics and seismic theory in this chapter that support my analysis of the seismic and well data acquired at Naylor field to monitor CO_2 storage in the Waarre-C sand reservoir. I will provide an overview of Otway Basin, some background information supporting the study, how the data has been collected and selected during the research project including recent reservoir characterization work and the challenge I am facing toward the completion of my research project as a starting point of all my work in the next chapter.

Chapter 4 THE CO2CRC OTWAY PROJECT

4.1 Introduction

The CO2CRC Otway Project is Australia's first and the world's largest demonstration project of CO_2 geosequestration. Its aim is to capture, compress, and transport, inject and store CO_2 in the geological subsurface. The objective is to demonstrate that CO_2 capture and storage is a viable, safe and secure option for greenhouse gas abatement in Australia. This will be achieved through a carefully designed monitoring program which will incorporate a variety of scientific methodologies to verify the capture and storage process.

In this chapter, I will briefly review previous work, the regional geology and concept of the CO_2 geological storage site, what kind of data was used to support my research, and how the data was collected selected, and conditioned. This will be followed by a description of the reservoir characterization which was a collaboration of many disciplines and expertise to interpret build and validate the static model subsequently used for dynamic simulation to investigate the expected flow of CO_2 and minimize the risk before and after injection. I conclude this chapter with discussions and conclusions.

4.2 Naylor field

The Naylor gas field is a small fault bounded field (~1km^2) with a single production well, Naylor-1. The field is situated in the Port Campbell Embayment in the onshore portion of the Otway Basin in south-western Victoria, Australia. It is located off the Great Ocean Road, around 40 km from the town of Warrnambool (Figure 4.1). The Naylor-1 well was drilled by Santos in 2002 on the basis of a strong gas effect (DHI) on seismic at the Waarre Formation unit C level (Waarre-C). The field was produced until October 2003, and suspended due to high water cut. The CO2CRC then identified the depleted gas field as a suitable site for CO_2 geological storage. The Naylor-1 well was modified to perform as a monitoring well while about 300 m down-dip of Naylor-1, the CRC-1 well was drilled as the current injection well. The

CO_2 is produced from the Buttress field to the North, transported 2 km via pipeline, and then injected into the Waarre-C reservoir (Fig.4.2)

Figure 4.1 The location of the Naylor field. The red solid line is the seismic cross section across the area of interest. Naylor-1 and CRC-1 wells are act as monitoring and injection wells, respectively. Buttress-1 well is the CO_2 source (CO2CRC, 2008).

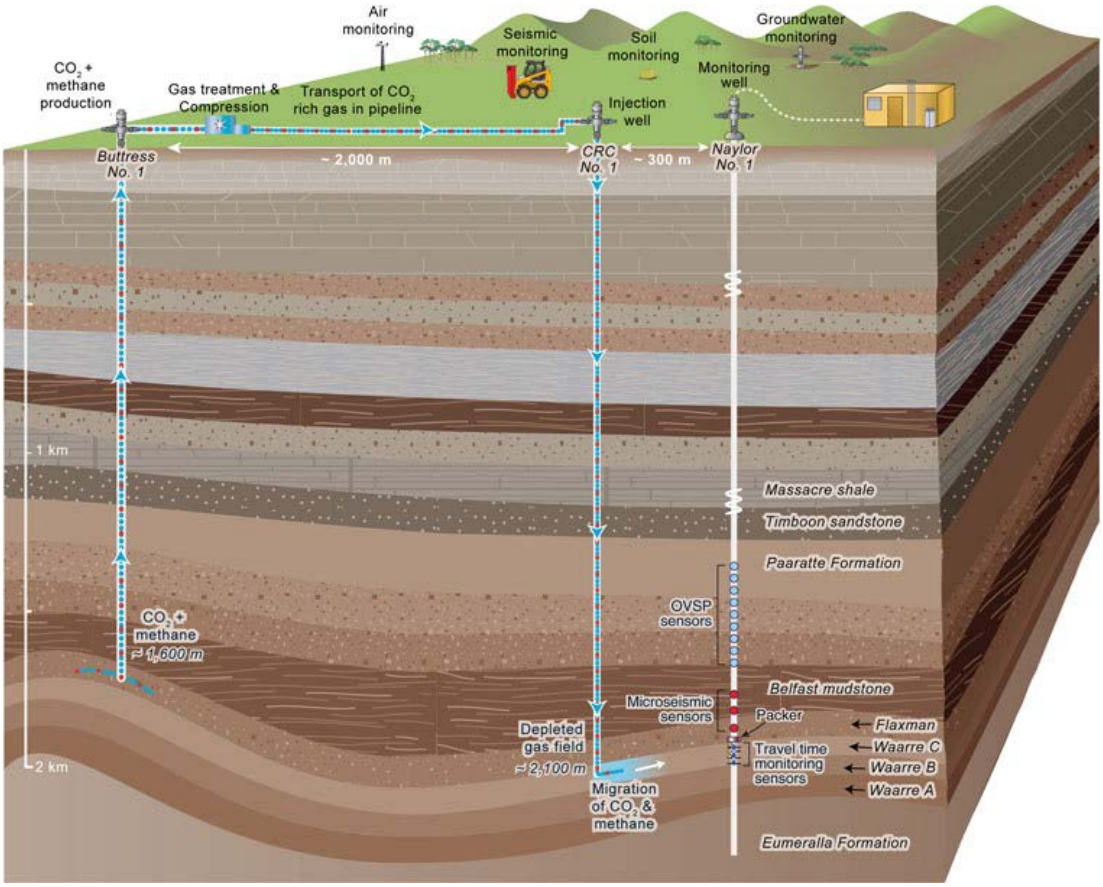

Figure 4.2 The injection scenario shows the Buttress-1 well as a source of CO_2 with CRC-1 injection well and Naylor-1 monitoring well (courtesy of CO2CRC).

4.2.1 Previous works

The first seismic survey (pre-production), named Curdie Vale 3D, was acquired by Geco Prakla in March 2000, and subsequently processed by CGG focusing on the Waarre and Belfast formations. It led to the subsequent discovery of Naylor gas field by Santos in 2001. The production of Waarre-C sand with Naylor-1 well finished in 2003. Wisman et al. (2005) reassessed these data for structural and attributes variations to further refine reservoir characterization. A complete and comprehensive reservoir characterisation has been previously done by Spencer and Pedalina (2006) prior to CRC-1 drilling. Further reservoir characterisation and core analysis has been performed by Dance and Vakarelov (2007) after CRC-1 was drilled.

In 2005, Wisman investigated the site using existing pre-production seismic and well data. The main objective was to reassess pre-production seismic data recorded in the

Otway basin to help design a new seismic program for monitoring the CO_2 sequestration process. The 3D seismic data and well data used for calibration were subjected to a detailed analysis. Various seismic attributes were generated to investigate the presence of hazardous zones that could provide leak points through the sealing shale unit. Li et al. (2006) built an initial fluid substitution modelling (FSM) application and predicted the time-lapse seismic response for the CO2CRC Otway Project. However, that model was based on a crude history match. The revised model from updated history matching (Xu, 2006) showed only 1-3% changes in elastic properties could be expected. This subtle change was deemed impossible to detect by conventional seismic methods.

Reservoir simulation and history matching by Xu (2007) were conducted to model the uncertainty risk, time of CO_2 breakthrough at the Naylor-1 well (monitoring well), predict the likely flow behaviour of injected CO_2 and obtain the best scenario for CO_2 injection location. The input from reservoir simulation and history matching were then used by Wisman and Urosevic (2007) as an input to model the time-lapse seismic response for accurate prediction of elastic properties changes before, during and after CO_2 injection.

Spencer and Pedalina (2006) performed a complete and comprehensive reservoir characterization of the CO2CRC Otway Project with help from other researchers and specialised consultants. The work included stratigraphic correlation, structural modelling, depth conversion sensitivity, sub-seismic fault distribution and impact on flow, depositional environment model, Waarre-C shale and sand characterisation, and the extraction of facies and/or depositional trends based on the 3D seismic. The Waarre-C reservoir is interpreted as a thin layer bounded by poorly defined sequence stratigraphic boundaries. Three structural horizons were created, based on the seismic interpretation of reflectors associated with the top and base of the Waarre-C unit. The seismic time depth conversion from three structural models showed the most likely maximum depth conversion error of $\pm$ 25m at the furthest distance away from the well control. Sub-seismic faulting is believed to have no significance for this particular reservoir as well as down-dip porosity/permeability loss. The core and regional assessment work has determined the most likely depositional model is the

regressive low sinuosity braided fluvial (Faulkner, 2000). Figure 4.3 shows the example of low sinuosity braided fluvial in Fairbank, Alaska, a potential analogue for Otway basin. Analysis of the depositional model and the effect on the flow, while not in the scope of this research, are important when studying seismic time-lapse effects.

The result of the reservoir simulation and history matching suggested the original (pre-production) gas-water-contact was at 2066.1 mD, while current gas-water-contact is at 2040mD in Naylor-1 (Figure 4.4). While this result agrees with the reservoir characterisation study it spells out a great challenge for the application of seismic methods for monitoring of CO_2 injection into Waarre-C sand.

Figure 4.3 Fluvial braided system in Fairbanks, Alaska.

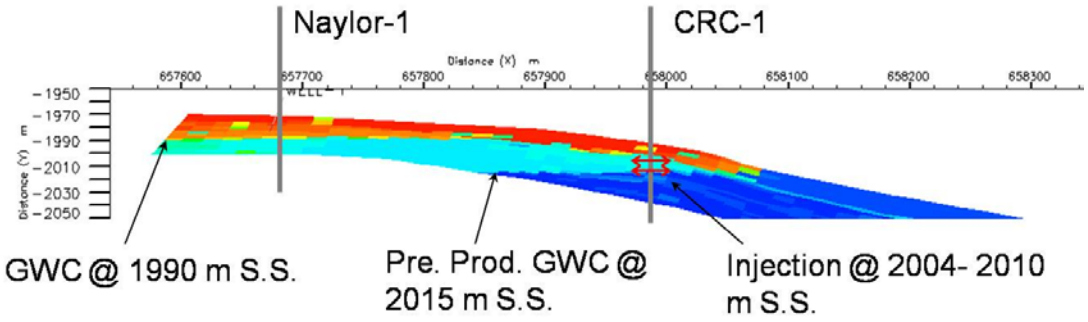

Figure 4.4 Initial condition for injection with predicted gas-water-contact (Xu, 2007).

4.2.2 Regional geology

The Otway Basin is one of several extensional and transitional sedimentary basins along the margin of the Australian continent. The Otway Basin was developed during the Late Jurassic and was extending west-northwest ward for over 500 kilometres along the southern margin of eastern Australian mainland coast. It is both located onshore and offshore south-western Victoria and south-eastern South Australia (Lang et al., 1989). The Otway Basin consists of a series of superimposed sedimentary sequences, each deposited during different phases of the breakup and separation of Australia from Antarctica. The Otway Group (intra-cratonic basin) was the first sequence deposited during Late Jurassic to Early Cretaceous rifting, and then overlain by the Sherbrook Group (marginal marine basin) during Late Cretaceous, followed by the Wangerrip (deltaic sequence), Nirranda (marine sandstone) and Heytesbury (marine carbonates) Groups during the Lower and Upper Tertiary (Lang et al., 1989). The Waarre Formation is the lower part of the Sherbrook Group (Figure 4.2) within the Otway Basin. The Waarre Formation traditionally represents the primary reservoir of the Otway Basin, with hydrocarbons and CO_2 occurring in both the onshore and offshore.

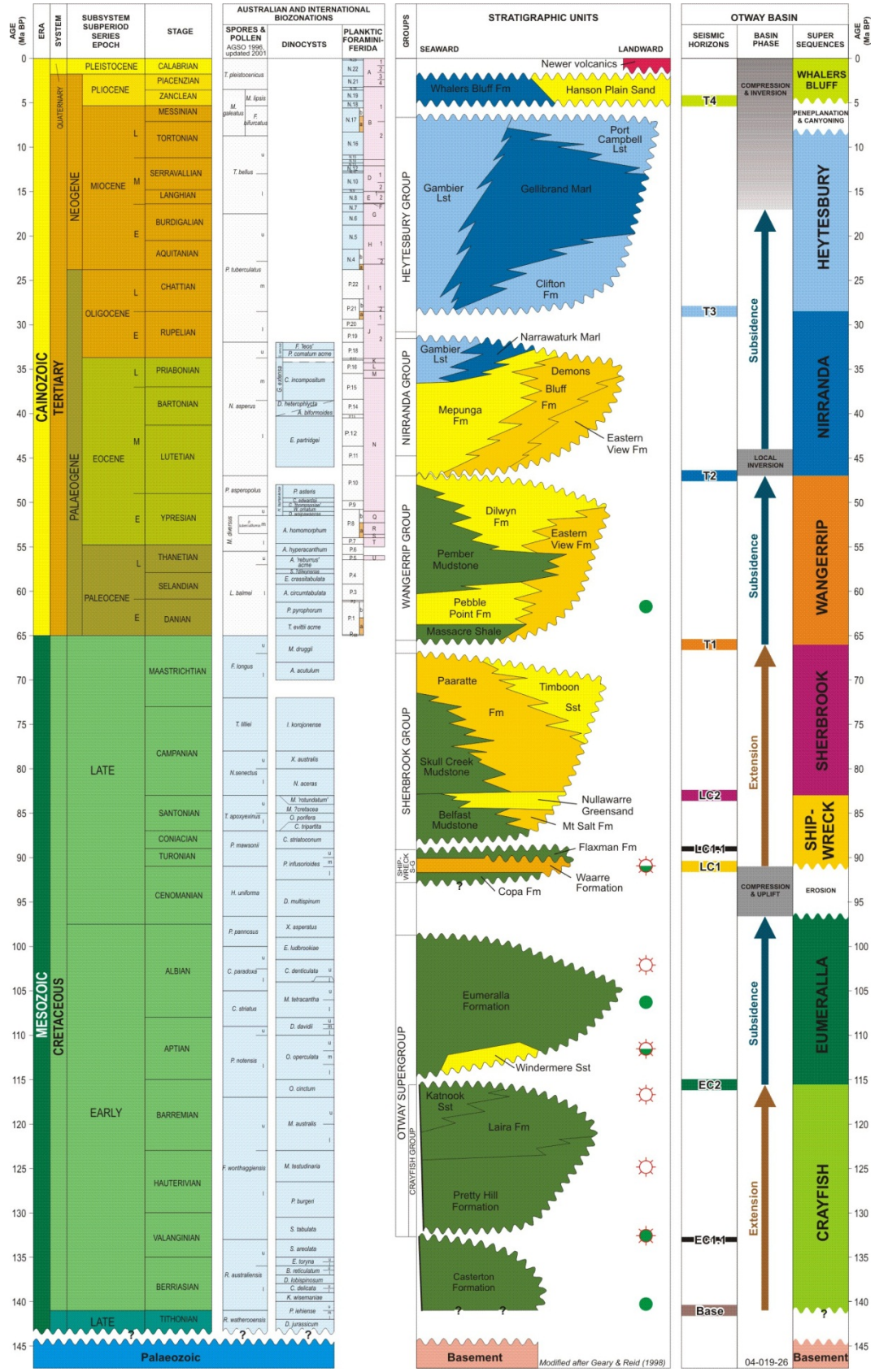

Figure 4.5 Regional Chronostratigraphic Chart – Otway Basin (Geoscience Australia, 2008).

4.2.3 Stratigraphy

The Waarre Formation is recognised as the principal reservoir unit throughout the Port Campbell Embayment, where small gas fields (less than 10 MMCFD) were discovered in the late 1970s and the early and mid 1980s (Buffin, 1989; Lang et al., 1989). The Waarre Formation is comprised of four sub-units lying between the Mid Cretaceous unconformity and a major Upper Cretaceous transgression. These were first described by Buffin (1989) as A, B, C and D units respectively; although it is only the C unit that is of immediate interest here (primary gas reservoir). Later, unit D in this system was elevated to a separate formation, the Flaxmans Formation, by Partridge (2001) who incorporated it into a new stratigraphic scheme (Figure 4.3). Faulkner (2000) has established a framework for the sequence stratigraphy of the Sherbrook Group in the Shipwreck Trough and Port Campbell Embayment using the same biostratigraphic zones (Figure 4.5). He interpreted the Waarre-C as being developed during a Low Stand to Transgressive System Tract. Figure 4.4 shows the Naylor field location map with well cross-sections. With newly acquired data, Dance et al. (2009) recompiled and reinterpreted in detail the depositional environment for the Waarre-C using this stratigraphic framework at the Naylor field as shown in Figure 4.6. The depositional model is now proposed as a stacked sequence of fluvial dominated low sinuosity channels frequently influenced by tidal processes and marine storm surges.

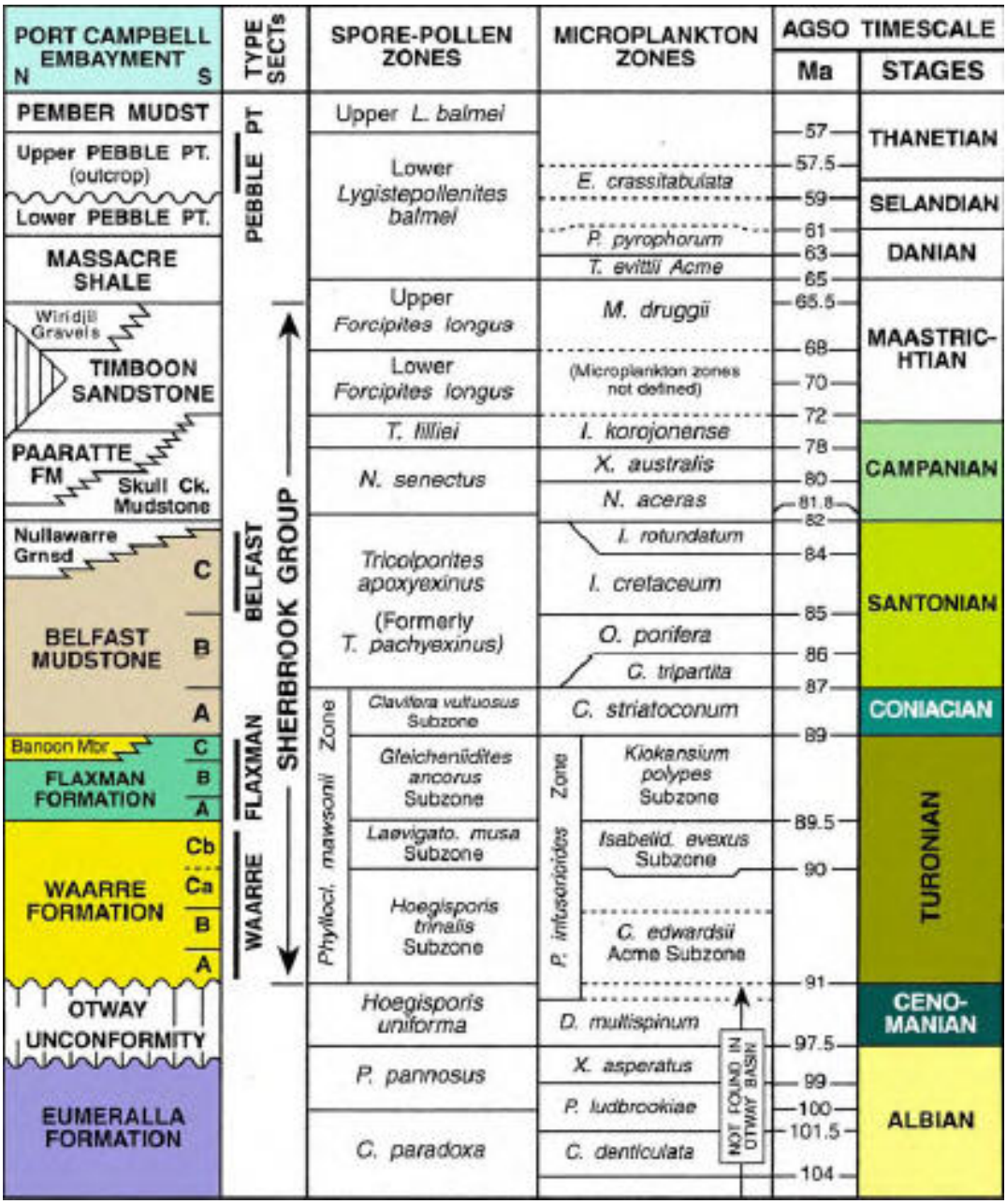

Figure 4.6 Detailed stratigraphic chart of the Sherbrook Group sediments (Partridge, 2001).

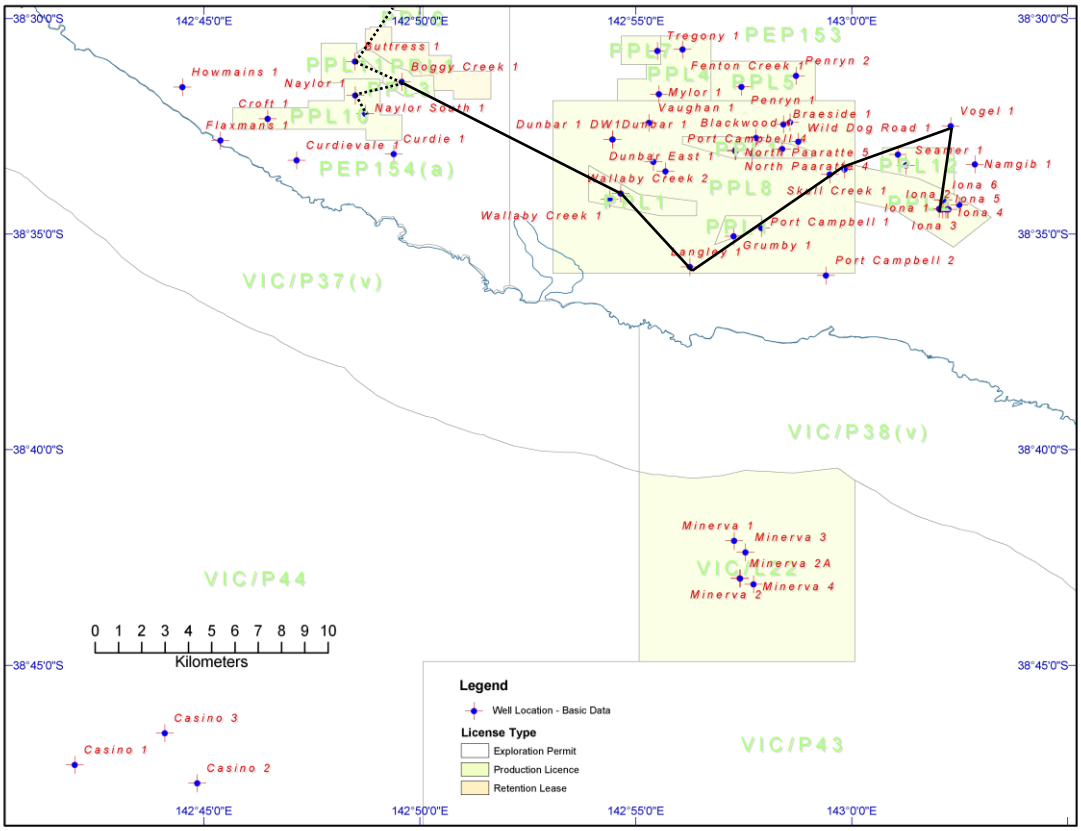

Figure 4.7 The Naylor field location map. The black lines show the location of stratigraphy cross section from Faulkner (2000); the black dashed lines show the location of seismic cross section from Spencer et al. (2006).

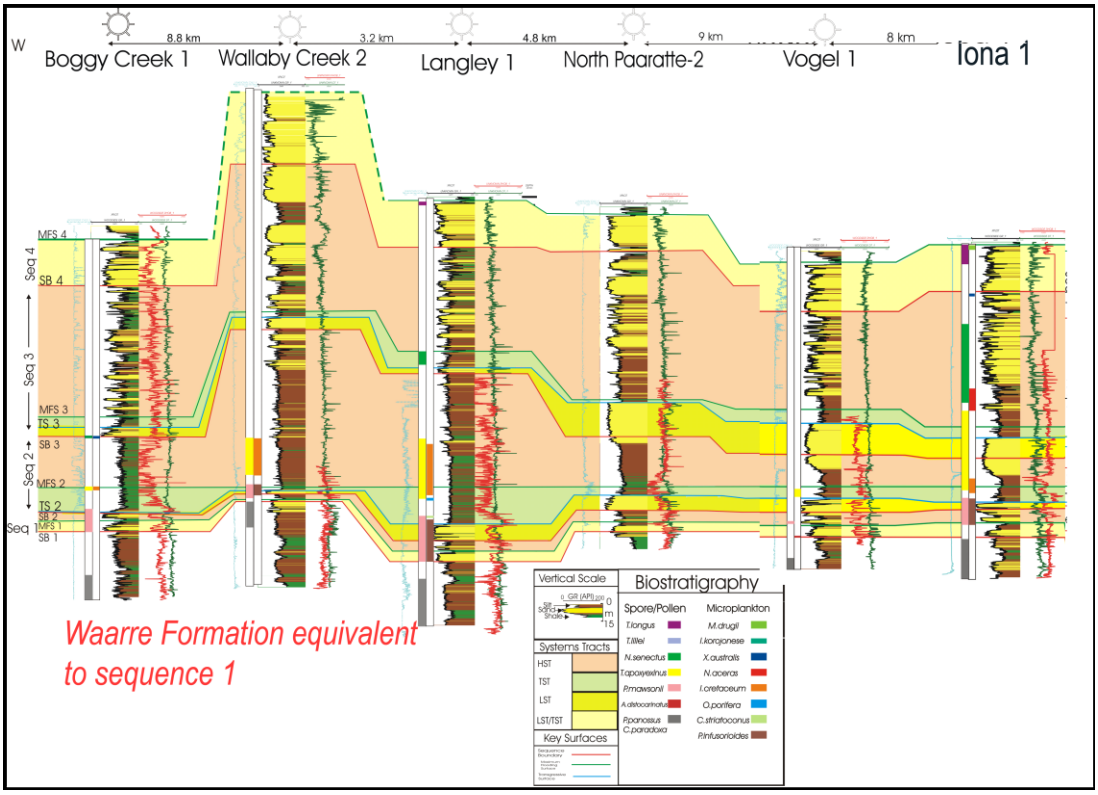

Figure 4.8 Regional stratigraphic cross-section of Waarre Formation at the north of the main ESE trending fault shows a fairly uniform Waarre-C thickness (10-20m). Boggy Creek-1, Langley-1 and Iona-1 are the key wells. Location of the cross-section is shown by the black line in Figure 4.4. It provides a sequence stratigraphic correlation of the Port Campbell Embayment and immediate offshore Shipwreck Trough. Waarre-C formation is equivalent to sequence 1 (Faulkner, 2000).

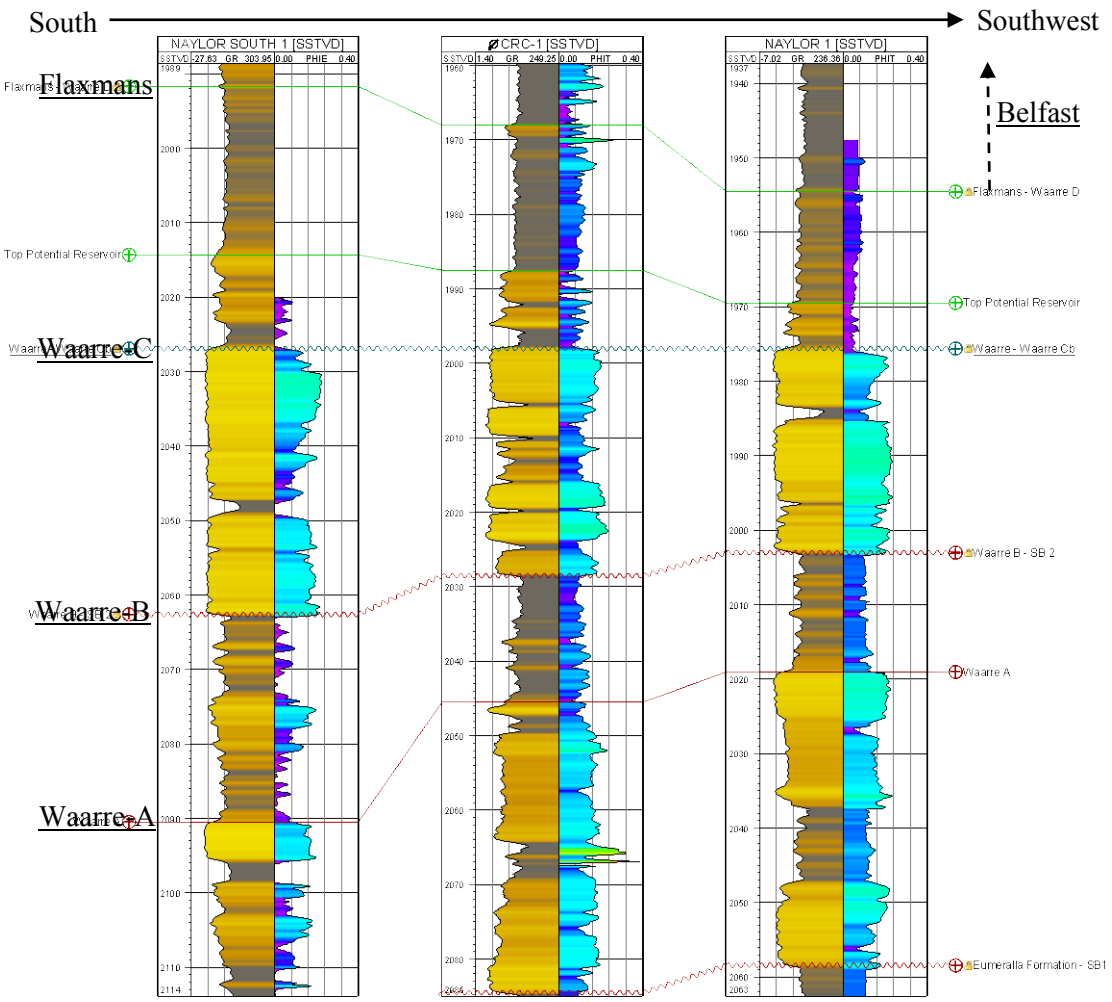

Figure 4.9 The well cross-section from South to Southwest shows the thinning of Waarre-C (Wisman et al., 2008). The location of cross-section is shown in Figure 4.8 (solid red line).

The Waarre Formation is overlain by the Flaxmans Formation, an intermediate seal, and the Belfast Mudstone. The Belfast Mudstone is a proven seal over the Naylor field as evidenced by the fact that it has provided containment of the methane in the field over geologic time.

4.2.4 Structure

The Otway Basin is structurally complex as a result of the superposition of a number of tectonic events which occurred both during and after the development of the basin (Lang et al., 1989). The major faults in the Otway Basin are interpreted as normal trending northeast-southwest in the western part of the basin and more north-westerly toward the eastern end of the basin. There are three major faults bounding the Naylor

structure at the each side of Naylor-1 well and the southern part of Naylor South-1 well. Figure 4.7 illustrates the complex fault zones around Naylor field (Spencer and Pedalina, 2006). Deposition of the Waarre-C Formation was likely affected by synchronous structural control which would have had an important influence over the position of feeder systems and valley incision. The stacked nature of incised valleys interpreted from core observations can be related to river courses forced to conform to topographic troughs related to underlying tectonic and structural control. Continued growth of these faults through to the Tertiary, and local inversion results in the juxtaposition of the Belfast Mudstone against the Waarre-C Formation at the Naylor field. All fields in the area have some fault control of either structural closure and/or spill-point. Further discussion on the Naylor field faults is in the reservoir characterisation section.

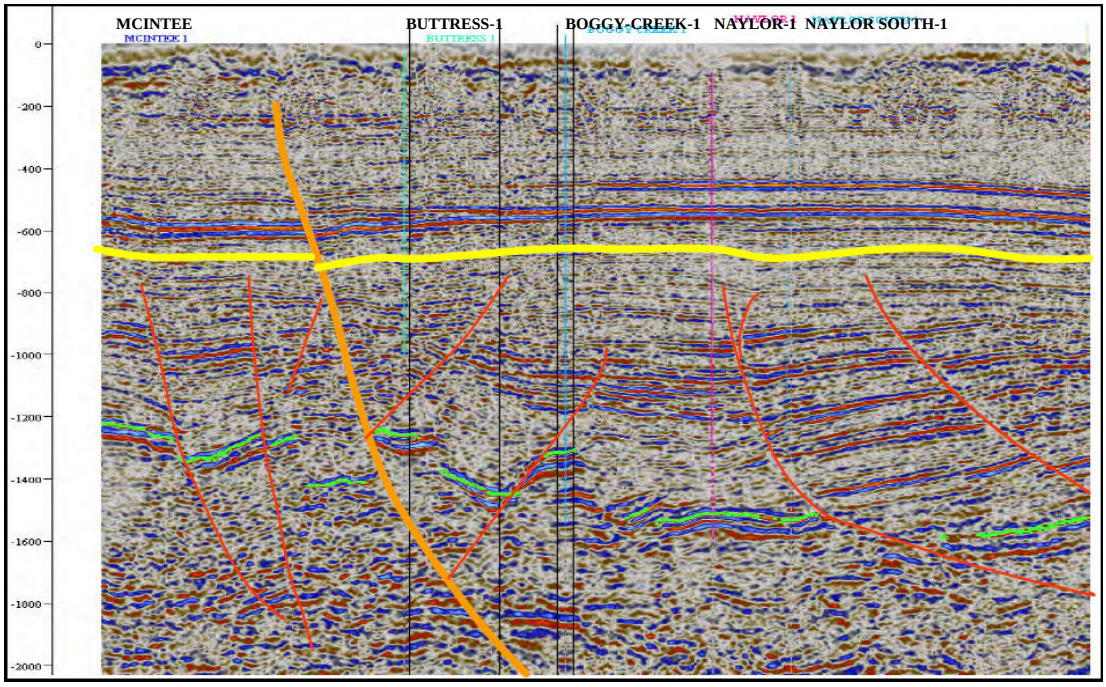

Figure 4.10 Seismic cross-section from North to South of Naylor field. The green marker represents top of Waarre-C. The Flaxmans Formation and Belfast Mudstone are the relatively featureless sections above it. Red faults mostly die out at the top of the Sherbrook Group (the yellow marker) and a few faults (orange) were reactivated by Miocene to recent compression (Spencer and Pedalina, 2006). The location of cross-section is shown in Figure 4.4 (black dashed line).

In summary, Figure 4.8 shows the location of cross section in Figure 4.6 and 4.7, respectively.

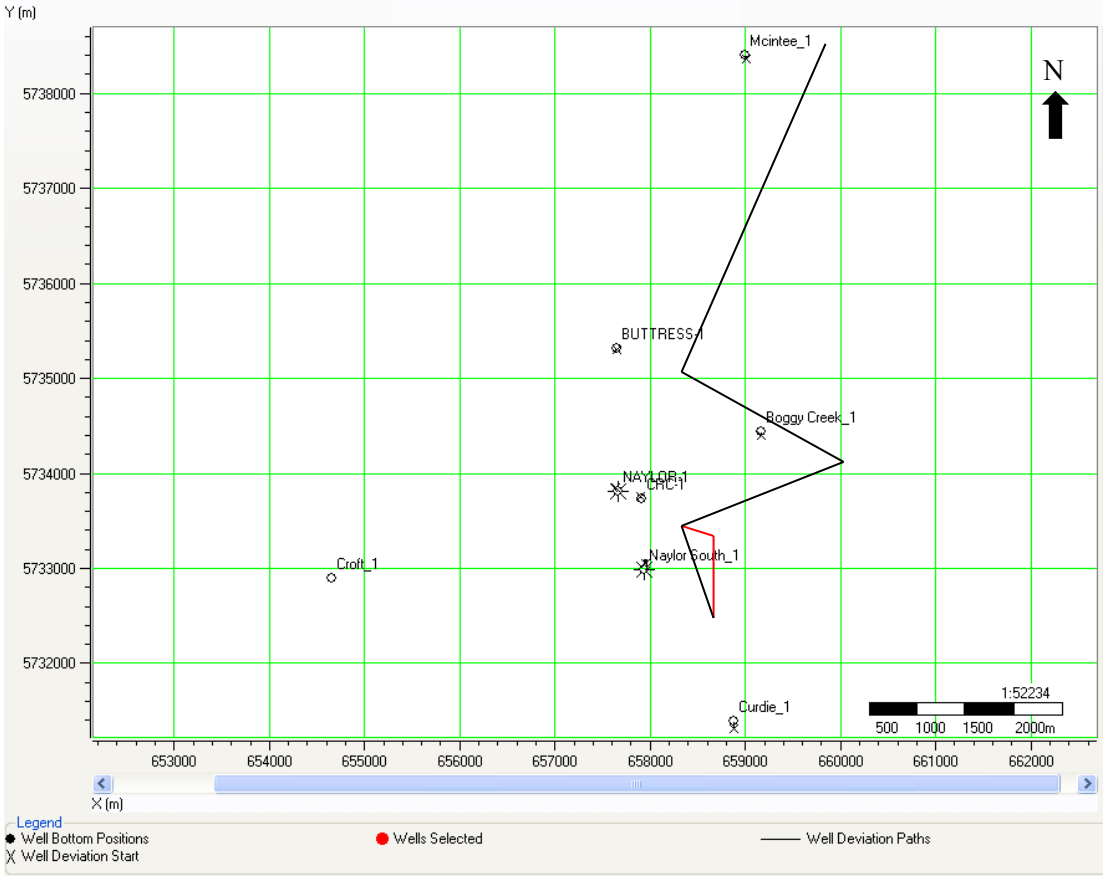

Figure 4.11 The location of the cross section of Figures 4.6 (red lines) and 4.7 (black lines).

4.3 Data collection and conditioning

4.3.1 Seismic data

A 3D seismic survey on a 20m x 20m grid was acquired by Geco-Prakla and then processed by Compagnie Générale de Géophysique (CGG) for Santos in 2000. The primary objective was to accurately map the Waarre-C and Belfast formations (CGG, 2000). In 2005, two seismic volumes of the pre-production data, migration and pre-stack time migration (PSTM), were used for detailed re-interpretation of the Naylor field. Polarity followed the SEG normal convention (European polarity) where an increase in impedance is represented by a trough. Thus, a strong peak represents

Waarre-C gas sands. Relative amplitude processing was required to maintain relative amplitude between bright and dim spots across the field.

In December 2007, a new 3D seismic survey was acquired to serve as a baseline survey. This provided a picture of the reservoir post production and prior to CO_2 injection. A repeat 3D survey was conducted in January 2009 close to the end of injection to serve as a monitoring survey for time-lapse monitoring of CO_2 injection. It was anticipated that differences in the data between two surveys will indicate the distribution of the CO_2 plume within the subsurface. However, due to differences of the acquisition and processing parameters, it was necessary to cross-equalize the data to gain a better understanding of the subtle response expected from the injection of CO_2. (Efthymiou, 2008) studied the time-lapse of pre-production seismic (2000) and post-production/pre-injection (baseline) seismic (2007). He concluded the cross-equalized technique was successful in eliminating many errors due to different acquisition, and processing process. Comparisons of the two cross-equalised data sets show the observed amplitude anomaly as shown in amplitude volume. Pevzner and Shulakova (2009) performed reprocessing of the 2009 3D seismic data with particular attention to recover true amplitude at Waarre-C level between Naylor-1 and CRC-1 wells during CO_2 injection.. They were able to resolve subtle changes in amplitude between the two surveys related to the injected CO_2. This seismic data is fundamental to verification and confirmation of the rock physics model used in the seismic modelling.

Figure 4.9 shows the strong affect of gas can be seen in 2000 3D seismic data. Table 4.1 shows the summary of seismic time-lapse acquisition in Naylor field.

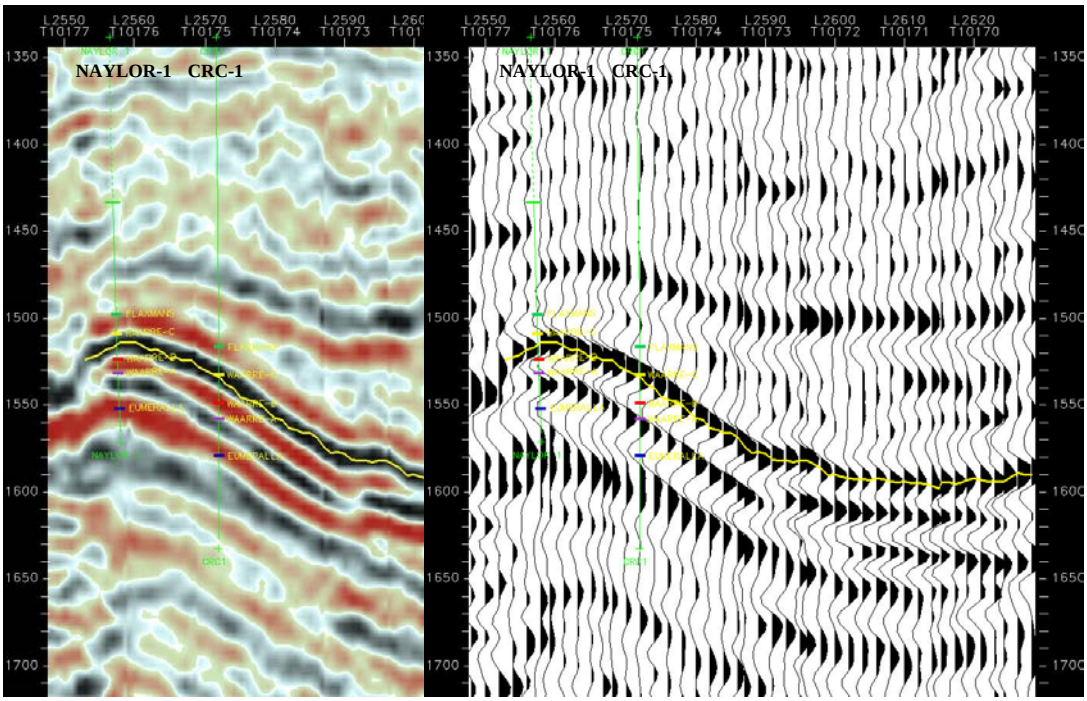

Figure 4.12 2000 3D seismic migration volume (pre-production). Yellow line represents top Waarre-C which shows strong amplitude anomaly caused by the presence of the gas.

Table 4.1 Seismic time-lapse acquisition in Naylor field.

Acquisition type	Year		
	2000	2007	2009
3D Seismic	Pre-production	After production/Pre-injection	Post injection

4.3.2 Well data

The Naylor-1 well, which has been converted to the monitoring well, had a limited database consisting of basic wire-line log suite and no conventional core. The CO2CRC re-logged the hole in 2006 to determine the post production gas-water contact and improve the calculated petrophysical logs. There was uncertainty in the location of the original gas-water contact (pre-production GWC/OGWC) and it was estimated from spill point analysis of the depth structure maps to be ~2015m SS,

down dip of Naylor-1. Zero-offset VSP data was acquired in 2007 and constrained the time-depth relationship and well to seismic tie.

CRC-1 was drilled in 2007 after production in the Naylor field was completed and located about 300 m down-dip from Naylor-1 well. Well data are available in the form of geophysical (wire-line logs) and petrophysics logs. Zero-offset VSP has been acquired and served as a time-depth pairs and for well-tie.

I used Naylor-1 logs (pre-production) to obtain pre-injection and post-injection logs as well as CRC-1 logs (pre-injection) to create post-injection logs through Gassmann's fluid substitution methodology. Together with 3D seismic pre-production, post-production/pre-injection and post-injection, I modelled the time-lapse seismic response likely caused by CO_2 injection.

Prior to that, conditioning the logs has been done through the following step:

1. Blocking – simplify log responses for inversion process (the interface is clearly seen). Backus averaging was used. I blocked the log every 1 meter sample (the smaller the defined average block size, the better the blocked description of the logs)
2. Synthetic seismogram – to tie the well to seismic event, match the well and seismic frequency.

Vertical seismic profiles (VSP) have been recorded in both wells. I used zero offset VSP to obtain accurate time/depth pair in order to calibrate the log (depth domain) to seismic event (time domain). Other VSP's method have been recorded in CRC-1 however further details of the analysis of VSP's data for this project are beyond the scope of my research interest.

Log conditioning provided a good tie between the log and seismic responses. This step is essential for quantitative time-lapse analysis and in creating a stable wavelet for inversion and seismic modelling. Table 4.2 shows the available well data from both wells.

Table 4.2 Summary of Naylor-1 and CRC-1 wells data.

			PRE-PRODUCTION		POST-PRODUCTION / PRE-INJECTION	
			NAYLOR-1		CRC-1	
Well information			X (m)	Y (m)	X (m)	Y (m)
	Coordinates				657899	5733759
	Time-Depth	Checkshot, ZVSP	X		X	
	Deviated	Deviation survey	X		X	
	Core samples	Belfast, Flaxman, Waarre-C	---		X	
	Kelly Bushing/Drilling Floor	KB/DF	51.1 (m)		50 (m)	
	Ground Level	GL			44.5 (m aMSL)	
Logs	P-wave velocity	Vp	X		X	
	S-wave velocity (fast and slow)	Vs	---		X	
	Density	ρ, Rho	X		X	
	Caliper	CALI	X		X	
	Gamma Ray	GR	X		X	
	Porosity	ϕ, PHIT, PHIE	X		X	
	Permeability	Perm, KECHOCalL, KECHO_HR, KTIM, KAIR, KINF	---		X	
	Water saturation	SWT, SXOT, SW, SXO	X		X	
	Resistivity	LLD, LLS, MLL	X		X	
	Clay volume	VCL, VWCL, VDCL	X		X	
	Spontaneous potential	SP	X		X	
	Neutron Porosity	NPHI	X		X	
Top formations			MD (m)	TVDSS (m)	MD (m)	TVDSS (m)
	Belfast		1773.29	1722.19	1728.00	1678.00
	Flaxman		2007.00	1955.90	2022.50	1972.50
	Top Potential Reservoir		2022.04	1970.94	2041.98	1991.98
	War-C		2028.23	1977.13	2052.50	2002.50
	War-B		2055.86	2004.76	2083.00	2033.00
	War-A		2072.00	2020.90	2100.00	2050.00
	Eumeralla		2111.61	2060.51	2139.00	2089.00

4.3.3 Core data

During the drilling of CRC-1 well, 42m of core was recovered through seal and reservoir formations. The primary target formations were the Waarre Formation and the interface between the reservoir and seal, the Flaxmans Formation, as well as secondary targets in the formations above. The purpose was to evaluate the characteristic of Waarre-C sand as an injection interval and the sealing capacity of the Belfast Mudstone including any potential for geochemical reactions. Core number 6 was recovered from 2051m-2075.5 m measured depth with 96% recovery (23.53m). Cores were approximately 3 inches in diameter and were in a good condition. One quarter of core was slabbed to expose a flat face for GR scan and high resolution photography. Dance and Vakarelov (2007) conduct detailed sedimentological analysis at Core Laboratories in Perth. The GR log was used to correct and correlate depths down-hole with core samples. After this correction and

adjustment, depths were reported in corrected measured depth from RT (Rotary Table). The result of the sedimentological analysis of the cores suggested complex stratigraphy that included the presence of incised valley fill deposits within the Waarre Formation, overlain by transgressive to offshore open marine deposits in the Flaxman Formation. Figure 4.10 shows the facies interpretation of the Waarre-C core samples. Comprehensive analysis of Waarre-C core can be found at Dance and Vakarelov (2007)'s report.

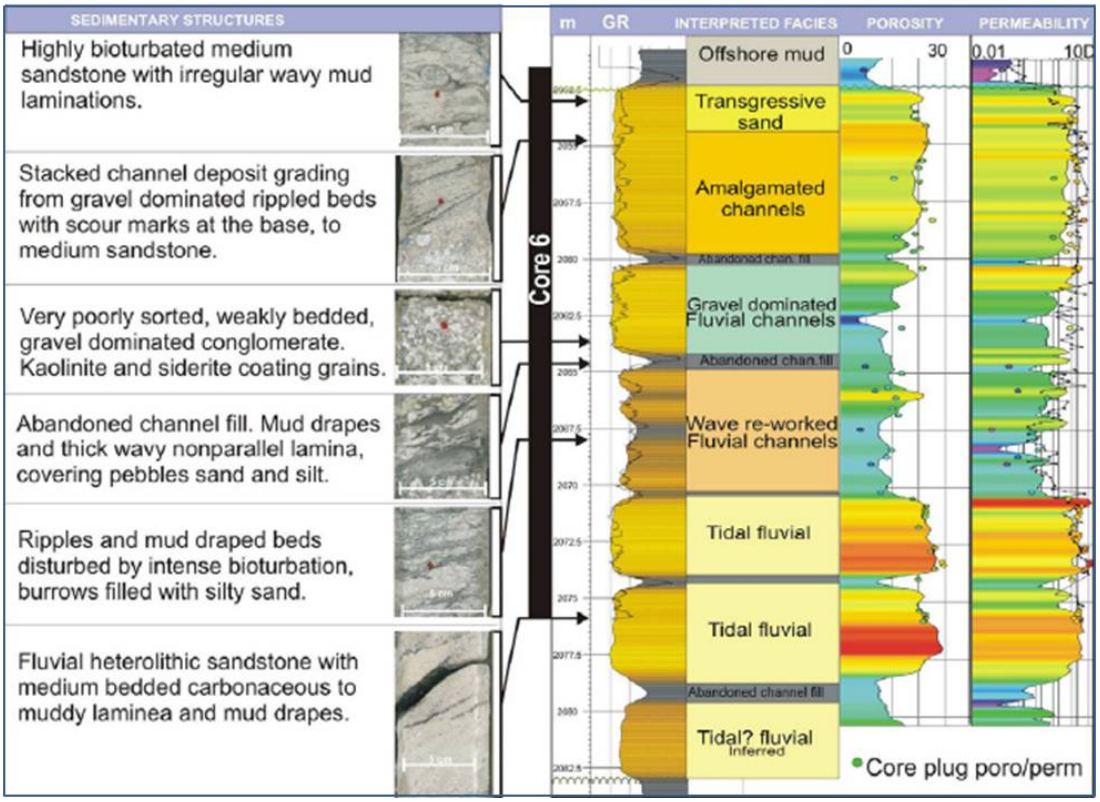

Figure 4.13 CRC-1 core photographs and descriptions compared to the well composite. Left to right core GR matched over the down-hole GR log, interpreted facies, core porosity measurements over the Phi log, core permeability-Klinkenberg corrected and mini-perm profile (dotted) showing good agreement with down-hole permeability log (Dance and Vakarelov, 2007).

Samples for ultrasonic core measurement were chosen on the basis of availability and the condition of the samples, especially within sand intervals. Each sample represents one facies classification. The thickness of each facies within Waarre-C, excluding the shale zone, is approximately 2.5 to 5 meters therefore one ultrasonic core

measurement for each facies can be considered representative. Only 3 samples from the sand interval were consolidated enough to undergo ultrasonic core measurements. We excluded core samples for analyses at the depth of 2064.67 to 2070.5 m which is a shale zone. Another fluid substitution methodology was devised for this interval.

4.3.4 Petrology

In total 34 samples from the Waarre-C core were plugged for petrological analysis. Various petrological analyses, including X-ray diffraction (XRD) and scanning electron microscopy were performed on these samples. In general, the petrographic analyses in this study focused on the mineral content and textural relationships of the rocks and are described in detail (Schacht, 2008). Table 4.3 shows a list of core samples from Waarre-C at CRC-1 well. Some samples were excluded from petrographic analyses because they either had the same lithofacies classification or the core samples were soft or brittle/fragile/lost. Some samples from the same lithofacies were examined for different purposes.

Table 4.3 List of core samples and associated analyses from CRC-1 well. Color represents facies classification (orange = transgressive sand, yellow = amalgamated sand, purple = gravel dominated and green = tidal fluvial). The injection interval is yellow color (modified after Schacht, 2008).

Depth (m)	Plug No	Thin Section	XRF Quant	XRD Bulk Quant	Microprobe	SEM	Ultrasonic measurement
2053.65	128	x	x	x	x	x	
2053.90	127	x	x	x			
2054.90	125	x				x	
2055.00							x
2055.75	123	x	x	x	x	x	
2056.80	120	x				x	
2057.00							x
2058.55	118	x	x	x	x	x	
2059.15	116	x				x	
2060.45	115	x	x	x			
2060.95	114	x	x	x	x	x	
2063.00	112	x			x	x	
2071.50	152						x
2072.60	94	x	x	x		x	
2074.00	92	x			x	x	

4.4 Reservoir characterisation

The primary objective of this study is to assess the existing seismic data recorded in Naylor field to help design a seismic program which is strictly aimed for monitoring of CO_2 sequestration. For this purpose I conducted a detailed analysis of the 3D seismic data and used borehole data sets for calibration. The interpretation was done on 2000, 2008 and 2009 vintage 3D seismic data, pre-production well data (Naylor-1 well) with some extension to post production/pre-injection well data (CRC-1 well). Various structural enhancements and seismic attribute maps are computed to investigate the presence of hazardous zones that could potentially provide paths for upward CO_2 migration through the existing sealing shale unit and to determine the presence of the gas in sand bodies (geometrically). Interpretation of pre- and post production gas-water-contacts are also needed to avoid injecting CO_2 into residual gas zones (difficult to monitor) and to effectively locate the injection well. The output from reservoir characterization was used as an input to build the Waarre-C geological model – dynamic simulation. This work was done prior to acquiring the seismic baseline. Therefore, reassessment of the existing data is required to make sure all the data are consolidated and consistent. The results are shown and discussed in this chapter.

4.4.1 Geophysical challenging

The Naylor field has many advantages for an injection study site such as a long history of production with a proven seal, availability of data from an existing well and seismic, well-established infrastructure, and accessible (permits). Challenges include the relatively deep depth to the reservoir level, the small size of the field and the presence of residual gas present within the reservoir. Also, faulting within the field is complex and there are thin sand bodies with clay intercalations and uncertainty of the gas-water-contact.

The proposed data analyses flow of Naylor field as shown in Figure 4.11 is as follows:

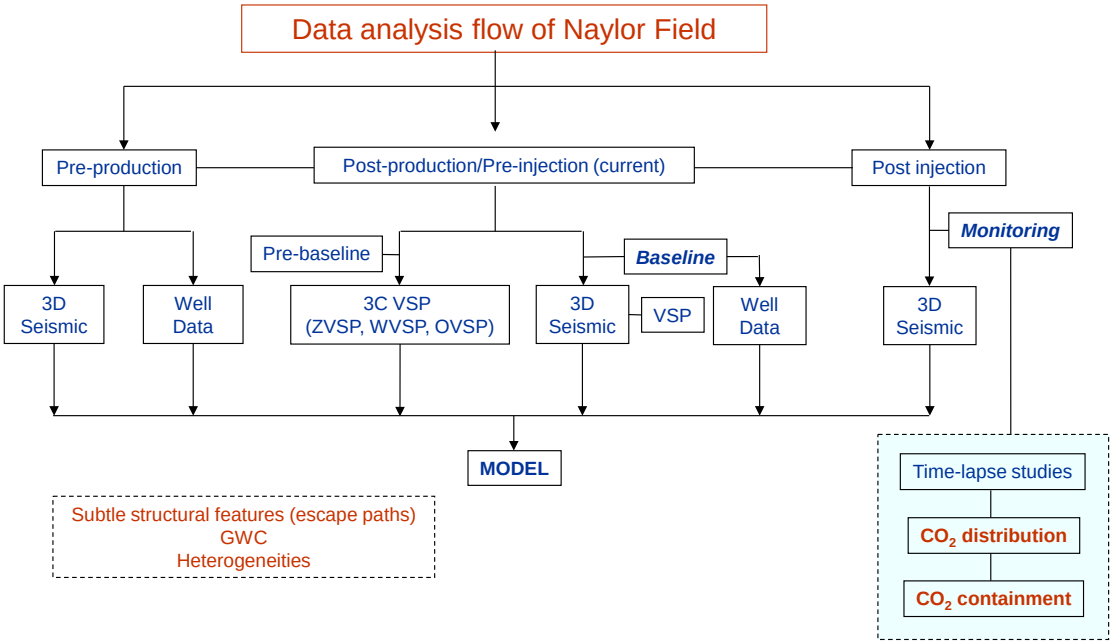

Figure 4.14 Schematic workflow of Naylor field reservoir characterisation.

4.4.2 Seismic horizons, faults and attributes

Six key horizons were interpreted in the time domain, tied to the well tops. All of the key horizons were picked on the 2000 vintage 3D seismic data:

1. Belfast : Regional seal above the reservoir.
2. Flaxman : Local seal directly above the reservoir.
3. Waarre-C : Main input geological horizon and Top of Waarre formation unit C sandstones.
4. Waarre-B : Base of Waarre C and top of Waarre B shale.
5. Waarre-A : Base of Waarre B and top of Waarre A sandstones.
6. Eumeralla : Base of Waarre A (Waarre Formation) and top Eumeralla Formations.

Early interpretation was conducted by Santos. Initial interpretation of the project was done by Lynton Spencer and Frank La Pedalina from Geoscience Australia. I used the initial interpretation to extend and interpolate the horizon and constrain the tie to

CRC-1 and 2007 3D seismic volume. These interpretations were then used to create a new 3D model. The revised horizons are shown in Figure 4.12.

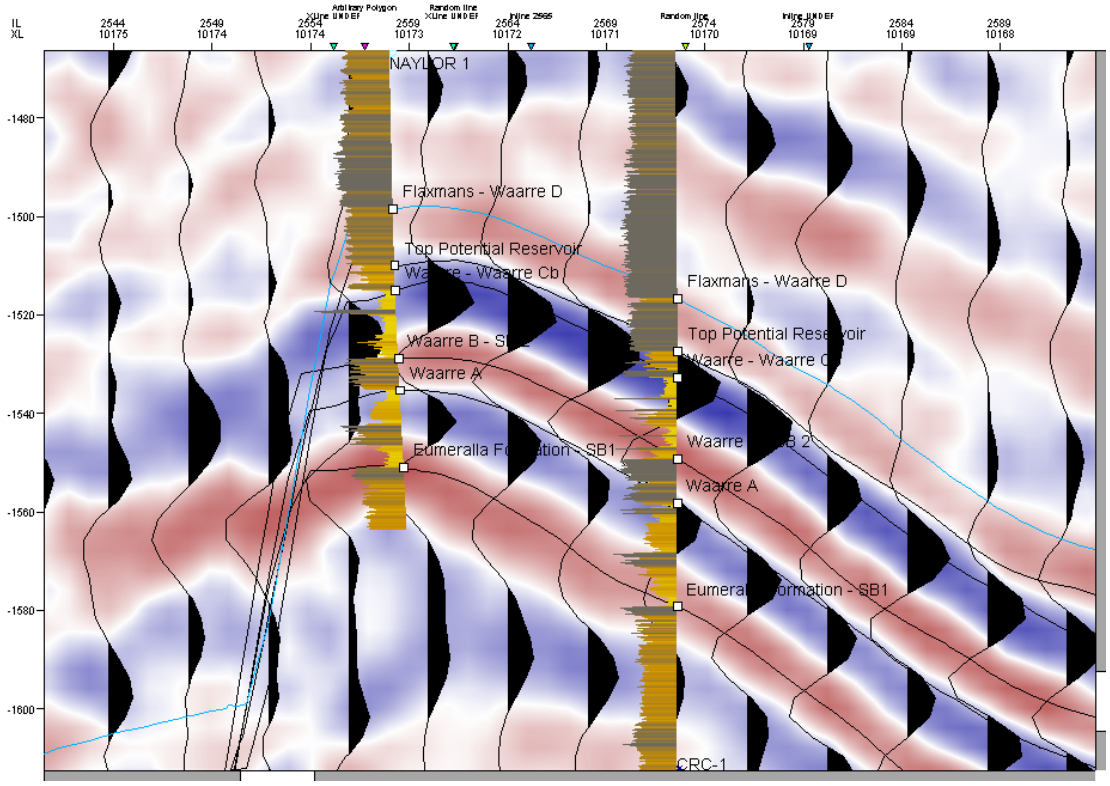

Figure 4.15 Seismic section across Naylor-1 and CRC-1 showing the revised horizons, Waarre-C, -B, -A and Eumeralla. The target horizon is Waarre-C which associated with black peak.

Analysis of stratigraphic features of the 2000 vintage 3D seismic involves the extraction of several complex trace attributes such an amplitude envelopes, spectral balancing and RMS. The predicted gas-water-contact is hard to see in the migration volume; however it is easily distinguished using an amplitude extraction envelope with a time window of 10 ms above and 20 ms below the Waarre-C horizon. The red colour shows the very high amplitude anomaly and low frequency content associated with a gas reservoir. It also suggests that the reservoir edge could be associated with pre-production gas-water-contact (Figure 4.13).

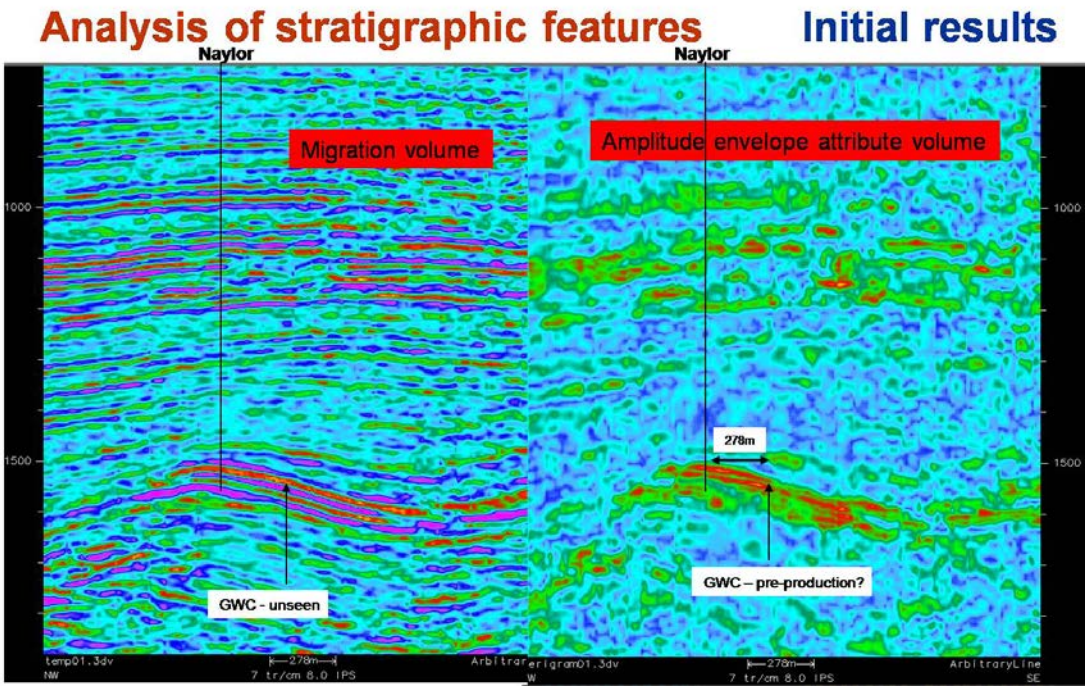

Figure 4.16 The envelope amplitude volume indicates the existence of pre-production gas-water-contact in conjunction with the fault at the edge of gas sand (red colour represents high amplitude).

Figure 4.14 shows a horizon slice of the Waarre-C where the high amplitude anomaly is caused by the gas effect. RMS amplitude extraction can also distinguish a similar feature, and the edge of the closure is coincident with the prediction of the gas-water-contact (Figure 4.15).

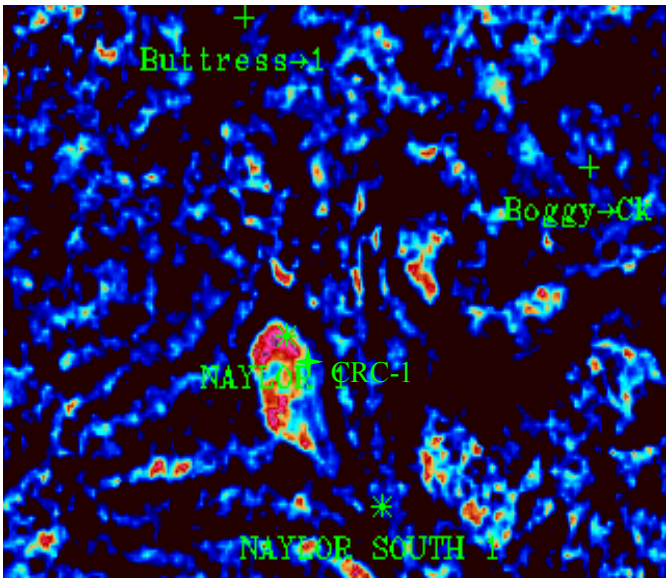

Figure 4.17 Horizon slice of spectral balance (peak amplitude) of top Waarre-C showing the reservoir body with high amplitude anomaly (red color). The edge of the closure is coincident with prediction of the gas-water-contact.

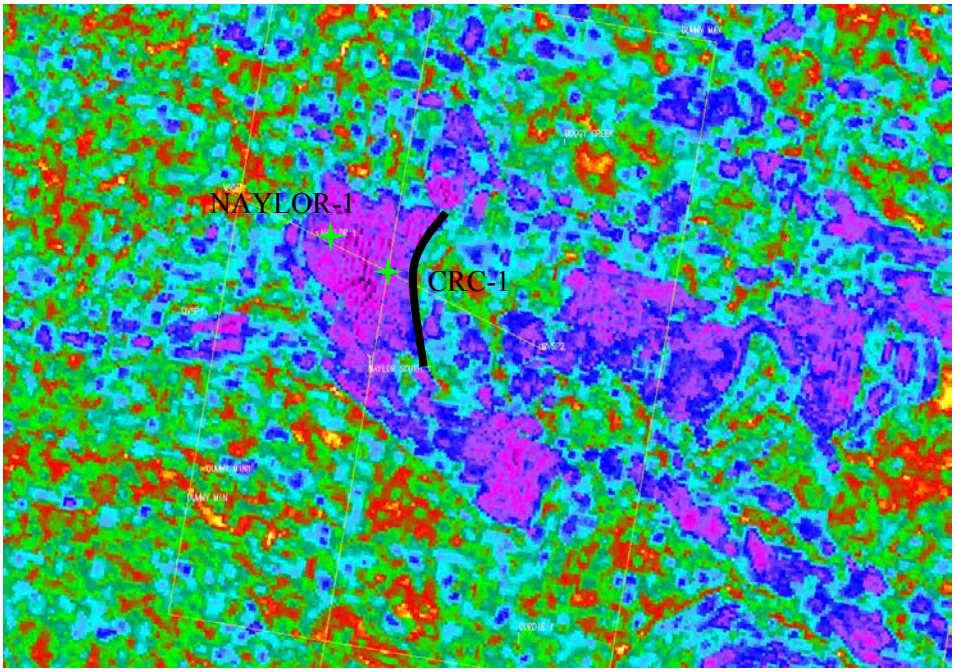

Figure 4.18 RMS amplitude suggested the edge of reservoir body is coincident with prediction of gas-water-contact.

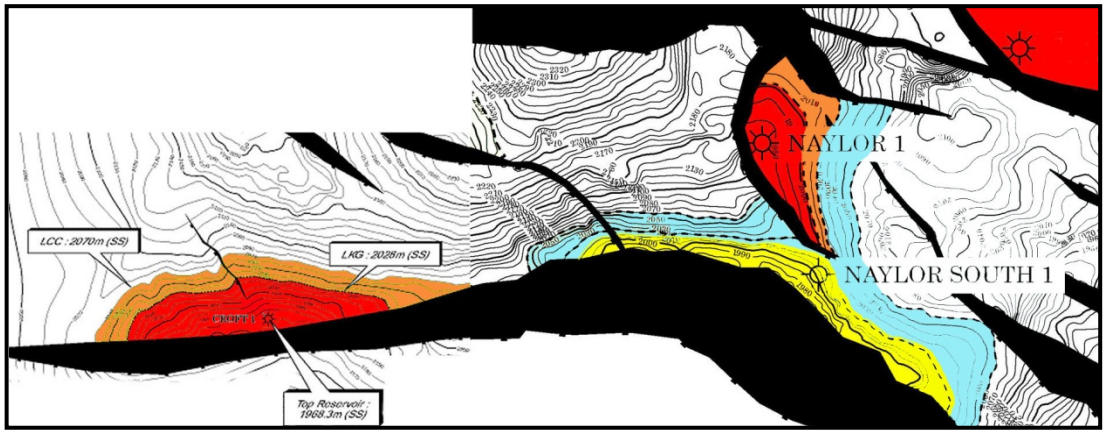

Figure 4.19 Regional structure map of the Naylor field (Spencer et al., 2006). Red closure in Naylor-1 well is the gas accumulation before production. The blue is the closure (the spill point), known to be water wet. The gas-water-contact has been estimated being at 2015mSS, and was coincident with the edge of the amplitude anomaly which is shown in Figure 4.14 and 4.15.

Sub-seismic faults exist within the Naylor structure and could potentially provided barriers and compartmentalization within the reservoir and affect the flow of CO_2. The geophysical attributes from 2000 vintage 3D seismic data were analysed with regard to seismic fault interpretation. The result suggested:

- Sub-seismic faults are hard to positively identify in pre-production 3D seismic data due to low spatial resolution (20x20 m bins).
- Seismic attribute analysis was employed to enhance structural imaging.
- Between Naylor-1 and CRC-1 wells, sub seismic faults could not be interpreted with high confidence. However, the occurrence of a small fault is most likely on the eastern side of CRC-1 well, located around 300 meters from Naylor-1 well.
- This sub-seismic fault could be identified on 10 -11 dip lines (in-lines), which correspond approximately to 200-220 m in length.
- Some of attributes show acquisition footprint around Naylor-1 and CRC-1 wells that could mask the sub-seismic fault and increase uncertainty of sub-seismic fault interpretation between Naylor-1 and CRC-1 wells from surface seismic data. Revisited seismic and VSP interpretation will help to reduce uncertainty.

- The attribute interpretation also highlighted possible variations in lithology within the reservoir sands. Other, frequency based attributes such as spectral decomposition, showed some potential for mapping fluid distribution across the field.
- A sub-seismic fault between Naylor-1 and the proposed location of CRC-1 wells was detected on VSP acquired in Naylor-1. However, it is not believed to be of significant length and offset to impede CO_2 flow.

4.4.3 Estimating pre- and post production gas-water-contact

The original gas-water-contact in the Naylor field could not be determined from the Naylor-1 well. There was no evidence in the well data that the GWC was intersected by the well and, no indications from the basic wire-line logs of a GWC. It was also impossible to establish a local water gradient from which to make a reliable estimate. To overcome this issue, the original GWC was interpreted from seismic amplitude mapping of 2000 vintage 3D seismic data. Amplitudes were extracted on the top of the Waarre-C as well as over a time window. Amplitude attributes analyses at the top of Waarre-C and over the time window was found to give the best results. From the amplitude map created, a seismic amplitude cut-off was established, marking the edge of the gas effect within the top of Waarre-C. This edge is also coincident with the mapped termination of the Naylor Field bounding fault. This suggests that the Naylor field bounding fault is sealing and capable of withholding a gas column the size of the structure (Spencer et al., 2006). The predicted original GWC was 2015mSS after depth conversion of the geological model as shown in Figure 4.17.

History matching of the production data from the field also suggested that the original gas-water-contact was 2015mSS, supporting the interpretation of the predicted original GWC from seismic amplitude. The current GWC is 1996mSS, interpreted from the Naylor-1 RST log. The log was acquired in 2006. Figure 4.18 displays the predicted GWC from history matching and Figure 4.20 shows the interpretation of the current (post-production) GWC after verification by the RST log.

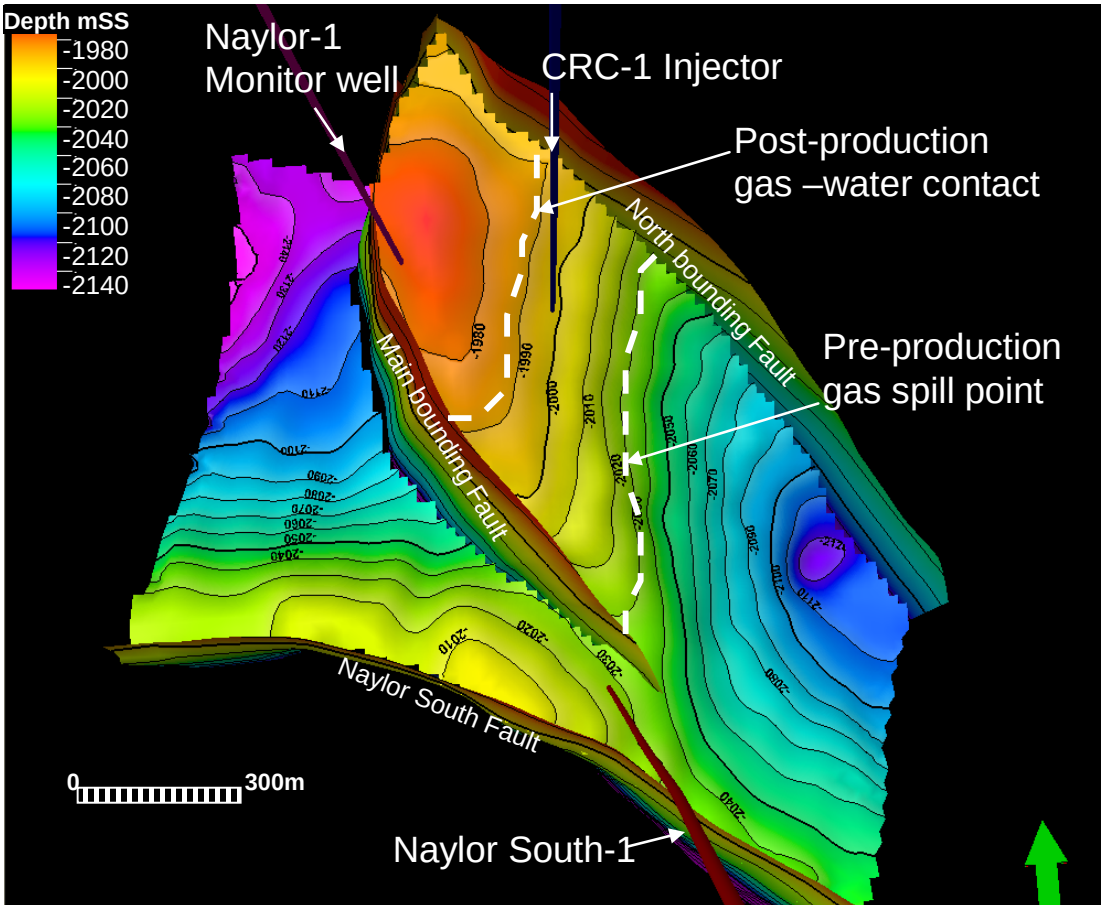

Figure 4.20 Geological model confirmed the original (pre-production) and current (post-production) gas-water-contact at 2015mSS and 1990mSS (Dance et al., 2009).

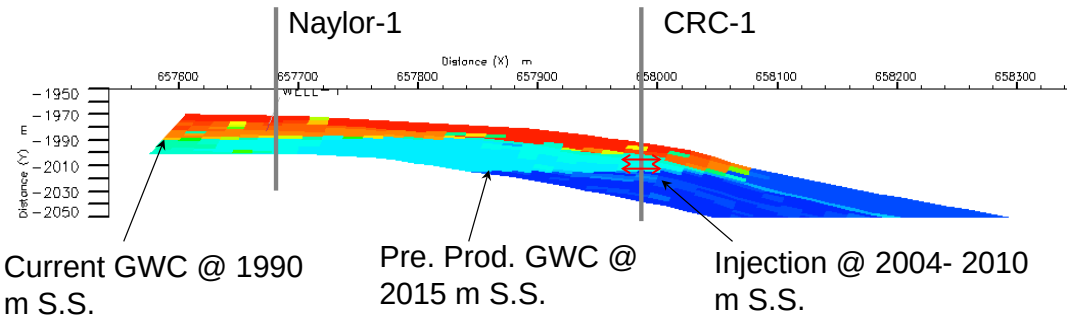

Figure 4.21 Prediction of GWC based on history matching (Xu, 2007).

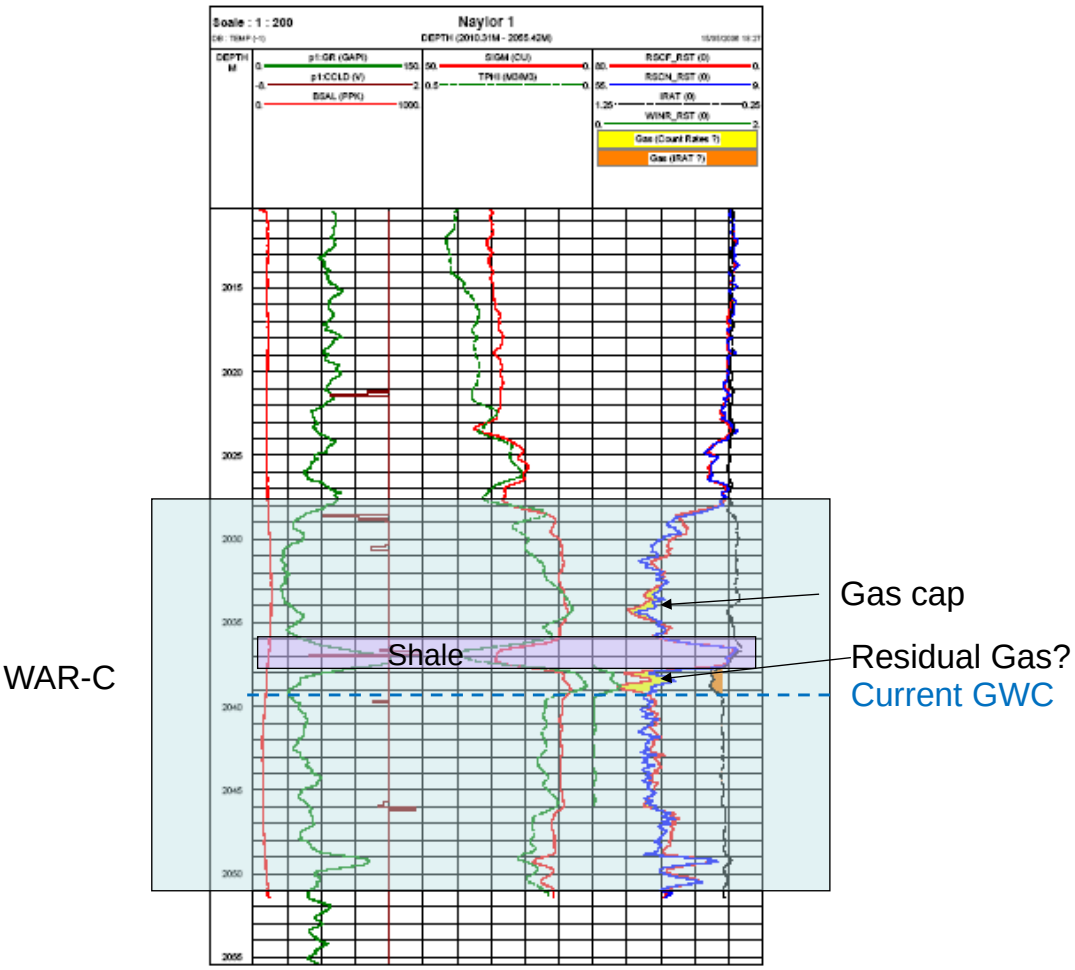

Figure 4.22 The RST log of Naylor-1 well. Current gas-water-contact is 1990mSS.

4.4.4 Well seismic tie

The zero offset Vertical Seismic Profile (VSP) was used to correlate the well data with the seismic data. Figure 4.20 shows the synthetics seismogram correlated with the zero offset VSP. The correlation coefficient is quite high with respect to the key horizon at reservoir interval.

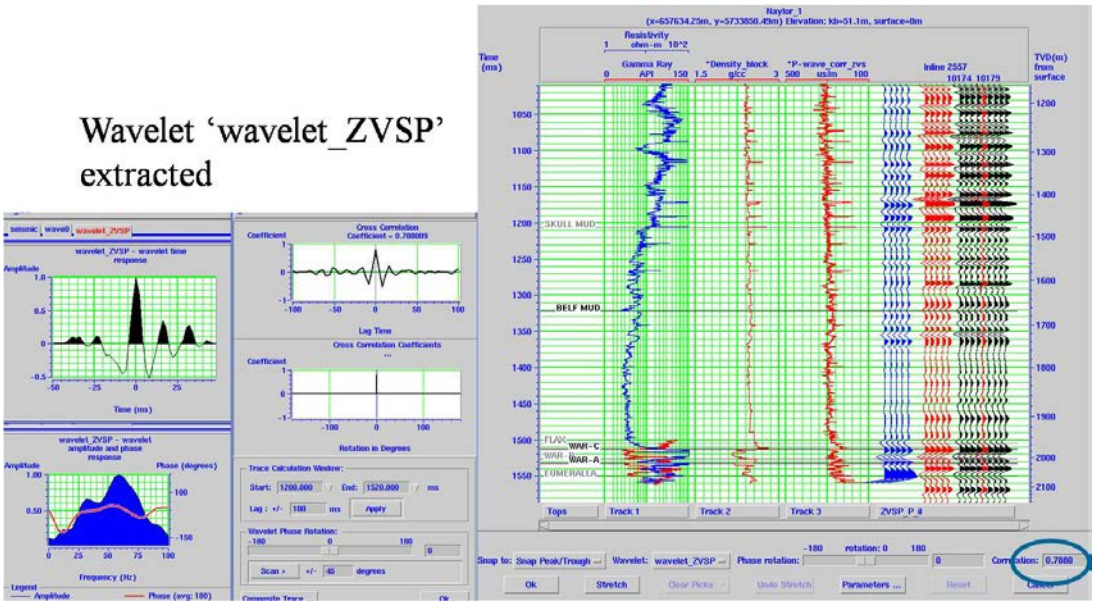

Figure 4.23 Synthetic seismogram after applying ZVSP shows good correlation between seismic and Naylor-1 well.

4.5 Dynamic Simulation

Four geo-model cases were created in the PETREL geo-modelling package (Spencer et al., 2006). The models cases were generated using the geological and geophysical data from Naylor Field and the surrounding areas. Multiple models were generated on the Waarre-C interval to test sensitivities in variations in the geologic parameters. The results suggested that a regressive braided fluvial model was the most likely geological model of Waarre-C (Figure 4.21). Dance et al. (2009) has revised the model with the new input data (logs and core samples analyses) from CRC-1 well (Figure 4.22). The most likely geological model was then upscale to a dynamic simulation model. Xu (2007) built the dynamic simulation model of Waarre-C using the ECLIPSE software package. The aim of the dynamic simulation was to assess the sensitivities to variations in reservoir properties and to be able to locate the injection well optimally and assess the risk in estimating the time to breakthrough of CO_2 at the Naylor-1 monitoring well (Figure 4.23). Modelling suggested that the breakthrough would occur between four and nine months from the commencement of injection.

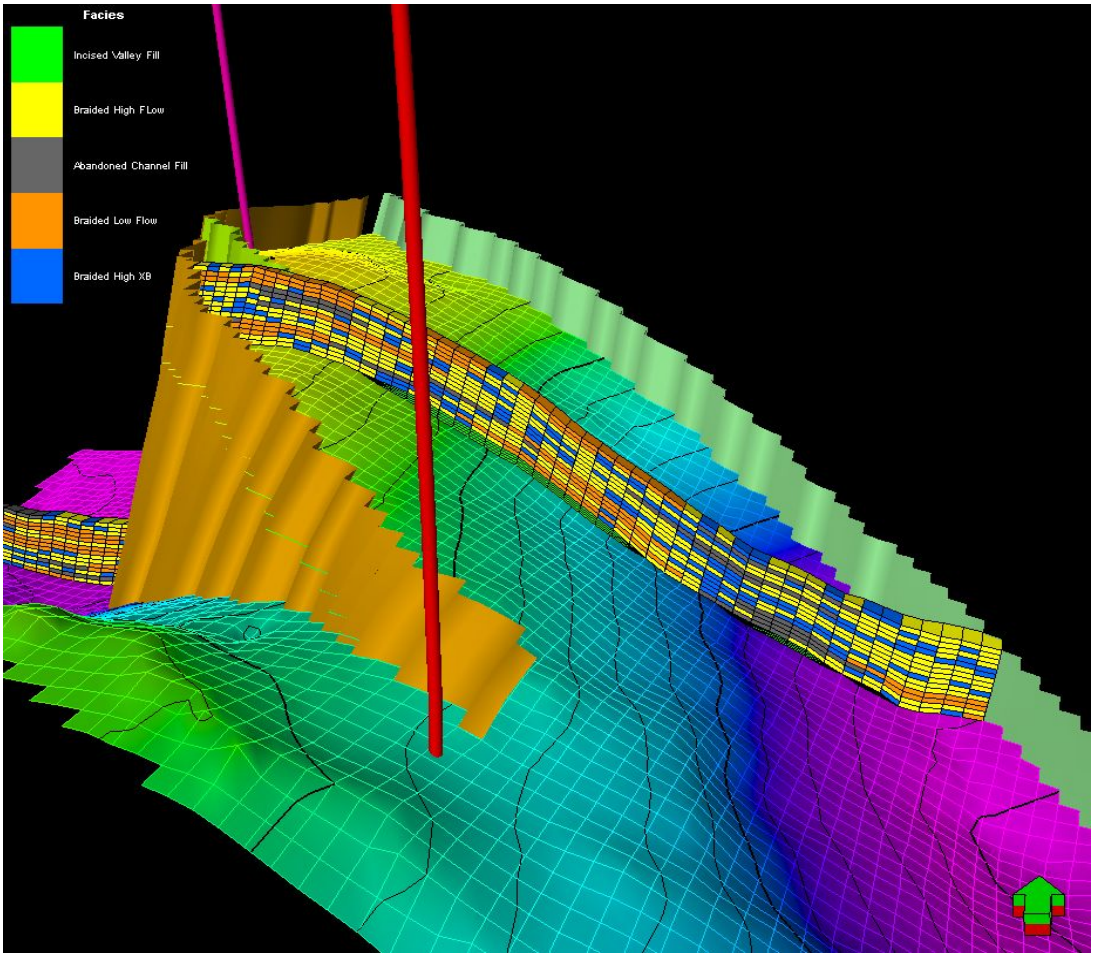

Figure 4.24 Regressive Braided Fluvial model shows the most likely interpret facies in Naylor field (Spencer and Pedalina, 2006).

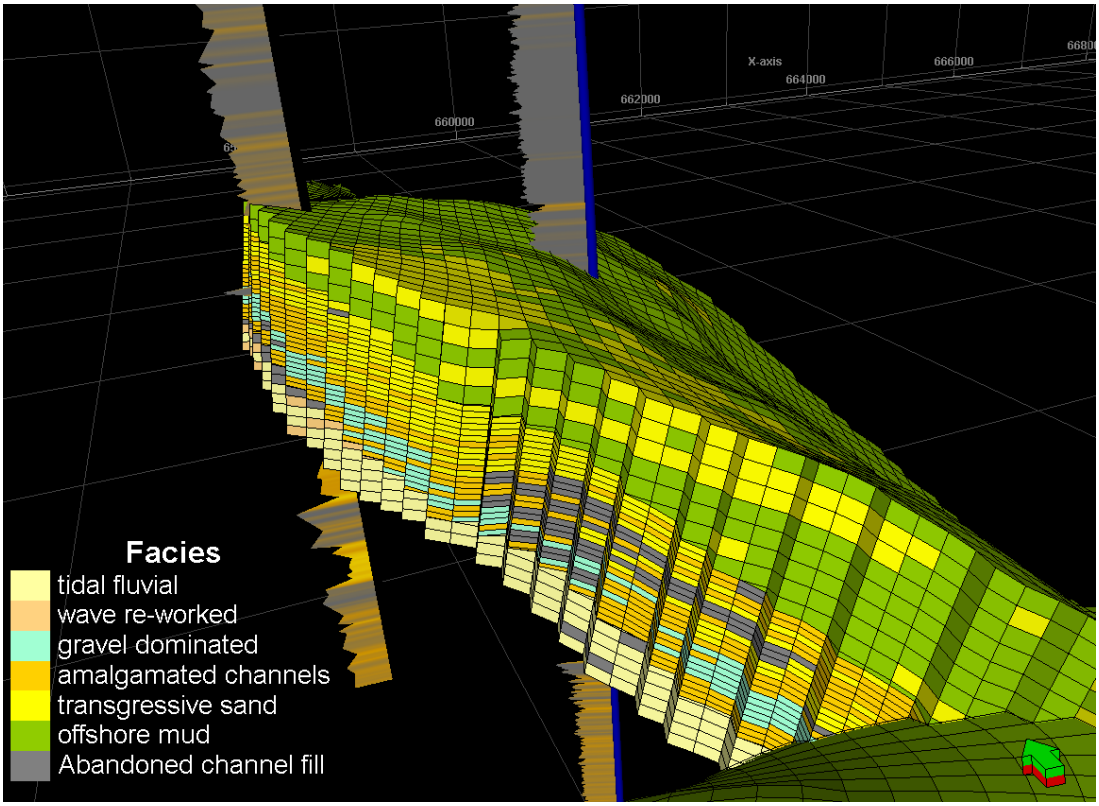

Figure 4.25 3D facies model. The depositional facies were populated into the 3D static geological model and used to constrain the distribution of reservoir properties (poro/perm) away from the wells. This model formed the basis for the dynamic simulations (Dance et al., 2009).

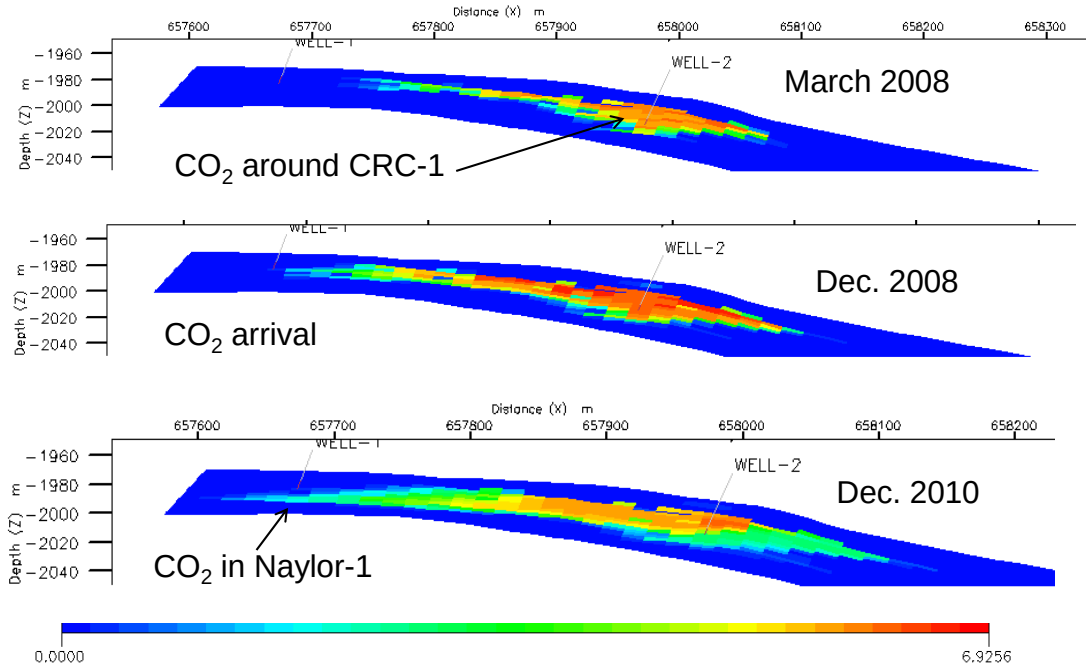

Figure 4.26 CO_2 migration in cross-sectional view. The breakthrough is expected within 4 to 9 months of the commencement of CO_2 injection (Xu, 2007).

The predicted gas-water contact, gas saturation, pore pressure, and temperature during CO_2 injection from reservoir simulation/history matching was used as input for the rock physics model as shown in Table 4.4.

Table 4.4 History matching parameters for Naylor-1 and CRC-1 wells.

History matching	NAYLOR-1		CRC-1	
	Avg. pore pressure MPa	Avg. gas saturation (mix gases)	Avg. pore pressure MPa	Avg. gas saturation (mix gases)
Pre-production	19.30	0.90		
Post-production/pre-injection (0 month - *baseline*)	17.60	0.20	17.60	0.20
Post injection (12 months - *monitoring*)	20.00	0.80	20.00	0.80

4.6 Discussion and conclusions

The CO2CRC Otway Project - the first CO_2 storage in Australia - aims to demonstrate that CO_2 can be safely stored in a depleted gas field and that an appropriate monitoring strategy can be deployed to verify its containment. The CO2CRC Otway Project involves many disciplines and expertise from research organizations, universities/institutes, government bodies and industries around the world working toward of the shared goal of reducing greenhouse gas emissions to the atmosphere.

A depleted gas field, the Naylor field was selected as a test site for a CO_2 geosequestration project. The field was chosen because of its high porosity and permeability reservoir, the presence of a proven seal over the field, and it had pre-existing data that covered the field and could be used to characterize the reservoir and monitor the CO_2 injection. In addition, the field was located close to the source of the CO_2 and had well-established infrastructure. The Naylor-1 well was selected as a monitoring well. In April 2007, the CRC-1 well was drilled 300 m down-dip of Naylor-1 well to a total depth of 2250 m. This well was drilled as an injection well. The new set of data were logged and sampled and used in the reservoir characterization of the Naylor field.

There are several limitations and disadvantages to the Naylor field as a test site for geosequestration. Because of the small size of the reservoir and its relatively deep depth below the surface, storage capacity is limited and it is more expensive to drill disposal wells. Also, since the field is a depleted gas reservoir, existing residual gas have the potential to mask the changes in seismic response associated with the injection of CO_2 into the reservoir, making it more difficult to detect the replacement of gas with CO_2. Uncertainties about the original gas-water contact of the field were another complication that had to be addressed prior to placing the injection well. As with all subsurface reservoirs, there was also the possibility of sub seismic faults which could potentially lead to leaking of the injected gasses. Because of these issues, it was important to carefully design the monitoring program to mitigate their effects.

This study reflects the result of several years of work on reservoir characterization of the Naylor field, involving multiple lines of study. The data has been integrated and interpreted to produce a full geologic and geophysical characterization, then dynamically modelled through a production/injection history match to predict the behaviour of the gas injection program. This simulation work was also used to determine the validity of the geological model.

Geologic characterization of the Naylor field was primarily based upon the analysis of the Naylor-1 and CRC-1 wells, integrated with the seismic data analysis. Geological modelling has suggested that a regressive braided fluvial model is the most likely case of depositional environment (Dance and Vakarelov, 2007; Faulkner, 2000; Spencer and Pedalina, 2006).

Geophysical characterization of Naylor field involved mapping of the structural aspects of the field and attribute analysis to determine stratigraphic detail and variations within the reservoir interval. The well data were used to model the synthetic seismic response using different rock physics properties to compare to the 3D seismic response. These synthetic matches were then used to define the limitations of the data and to determine the expectations within the data of the seismic changes associated with the various stages of the life of the field (pre-production /pre-baseline and baseline).

Seismic attribute extractions were also used to detect the presence of faults and other features within the injection study area that could either impede or alter the flow of CO_2 through the reservoir or provide a leak pathway. A fault-liked feature located between the injector and monitoring well is not considered large enough to pose a potential impact on CO_2 arrival times at Naylor-1. Subtle faulting within the reservoir was better defined by the study.

The Naylor-1 well did not cross the original gas-water contact for the Naylor field. Seismic attributes were used to determine (based on amplitude) the most likely extent of the Naylor field gas column. Using ZVSP velocity information from the wells to depth convert the seismic horizons, the original GWC for Naylor-1 field was estimated. The initial gas-water-contact (before production) has been established in

the geological model at 2015mSS. The current gas-water-contact is established and confirmed by RST log at 1990mSS.

Variations in lithology and fluid suggested by several seismic attributes agree in general with the modelled geology and pre-production gas water contact. It was therefore concluded that the geophysical attribute analysis did not identify any significant features that would warrant review of the proposed location of CRC-1.

The Naylor-1 production history and the post-production pressure response were history matched as part of the aquifer characterisation. This, combined with the result of the other studies on the field (geologic reservoir characterisation, CRC-1 well data and core laboratory tests, seismic attributes, etc), has reduced and constrained many of the previous uncertainties in the field (i.e. depositional environment, heterogeneity, reservoir properties). The new geological model is therefore considered as the most likely case. The only remaining significant uncertainty is the hydro-geological effect from the aquifer system which is beyond the scope of this research.

Dynamic simulation, of the geologic model showed that the breakthrough time at the monitoring well was expected to be in the range of 4-9 months. The model suggested that the breakthrough would occur in the middle section of the Naylor-1 monitoring well, slightly below the current GWC. This would be reached using an injection rate of 85,020 m3/d (3 MMscfd) with a maximum pore pressure of about 20 MPa at the end of the injection.

CO_2 injection was commenced in April 2008 and CO_2 (tracer) breakthrough was first detected at Naylor -1 well on July 17, 2008 through the monitoring string consist of 3 U-tubes and other instruments (geophones, etc.). A total of 65,000 tonnes of CO_2 was injected into the Waarre-C in Naylor field over the course of this study. The CO_2 injection was ceased in August 2009.

In conclusion, the Waarre-C reservoir in Naylor field is known to be well sealed and of a good reservoir quality. It is good reservoir for short term CO_2 injection and subsequent long term CO_2 storage.

Chapter 5 ROCK PHYSICS MODEL OF WAARRE-C SANDSTONES

5.1 Introduction

Naylor-1 well was drilled in 2001 on the basis of direct hydrocarbon indicator at the level of Waarre Formation. The Waarre Formation is the main reservoir unit within the Port Campbell Embayment (PCE) in Otway Basin. There are several depleted and producing hydrocarbon fields and a producing CO_2 field throughout the Otway Basin at Waarre Formation level. However the main production is from gas drive. Up to 3.965 BCF gas methane has been produced in Naylor-1 well since 2002 and in 2004 was shut-in due to the water influx (Spencer and Pedalina, 2006). Because the field was small, the cost of water handling was not considered economical. Therefore Naylor-1 well was abandoned and proposed to be used as a CO_2 storage site. In 2007, CRC-1 well was drilled down-dip of Naylor-1 well and acts as an injection well while Naylor-1 well acts as monitoring well. The supercritical CO_2 was injected at the level of Waarre-C formation in 2008 and was expected to mix and/or replace existing residual gas methane in the reservoir. As of August 2009, 65,000 tonnes of supercritical CO_2 has been injected. To implement seismic monitoring at Otway, but also at any other CO_2 sequestration site it is necessary to predict, as accurate as possible, changes in seismic response to varying quantities of CO_2 injected into a reservoir rock.

5.2 Elastic properties of porous rocks

A successful application of a time-lapse seismic technology for monitoring a reservoir dynamic depends on the magnitude of the change in the elastic properties of the reservoir over time. Since this seismic technology may not be applicable for all CO_2 storage projects, a feasibility assessment must be conducted prior to project commencement to ensure success. In the case of Otway Basin, the injection of CO_2 into the Waarre-C sand will alter the elastic properties of the reservoir given its high porosity and weak skeletal frame. Whether such changes can be detected by time-lapse seismic methodologies remains unknown unless a detail rock physics model is developed. Subsequent numerical simulation of seismic response to long-term CO_2

storage will determine the magnitude of elastic property changes and if conditions for the application of seismic monitoring are met. It requires mathematical model that can predict the effect of pore fluids, minerals, porosity and effective pressure on the seismic properties of the reservoir. This model can be established through the application of rock physics and fluid substitution methodology and result verification against wire-line logs and core samples measurements. All of this is aimed at devising the best strategy for the long-term CO_2 storage monitoring within the CO2CRC Otway Project, as addressed in this chapter.

Injection of CO_2 into the formation will cause a change of seismic response in two main ways: by changing the properties of the pore fluid, and by changing the rock matrix through change of pressure. Hence to assess seismic response we first need to understand how is the pore fluid affected by variable CO_2 saturation. Pore fluids have properties which depend on composition, pressure and temperature and strongly influence the seismic properties of the rocks.

Of particular interest to seismic monitoring is to examine how different fluids and fluids mixtures affect rock elasticity. For that reason I calculated elastic properties of methane, CO_2 and their mixtures, and water. I used *in-situ* gas composition, pressure and saturation and combined it with the pressure and saturation prediction from flow simulations to derive the fluid properties.

5.2.1 Methane (CH_4)

Gases are characterized by a specific gravity, G, the ratio of the gas density to air density at 15.6^{o}C and atmospheric pressure. G can be defined as well as the ratio of molecular weight of the gas (gas mixture) to that of air (28.97). Typical hydrocarbon gases have G value from 0.56 for pure methane (lighter) to greater than 1.8 for gases with higher carbon number (heavier). Methane is extremely compressible compared to heavier gases with bulk modulus from 0.01 to 0.2 GPa (Batzle and Wang, 1992).

Figure 5.1 shows the velocity, density and bulk modulus of methane-water mixture at temperature 85^{o}C (*in-situ*) and varying pressure (*in-situ* and prediction). The equation 3.10 to 3.14 for calculation of gas properties are described in Chapter 3.

a)

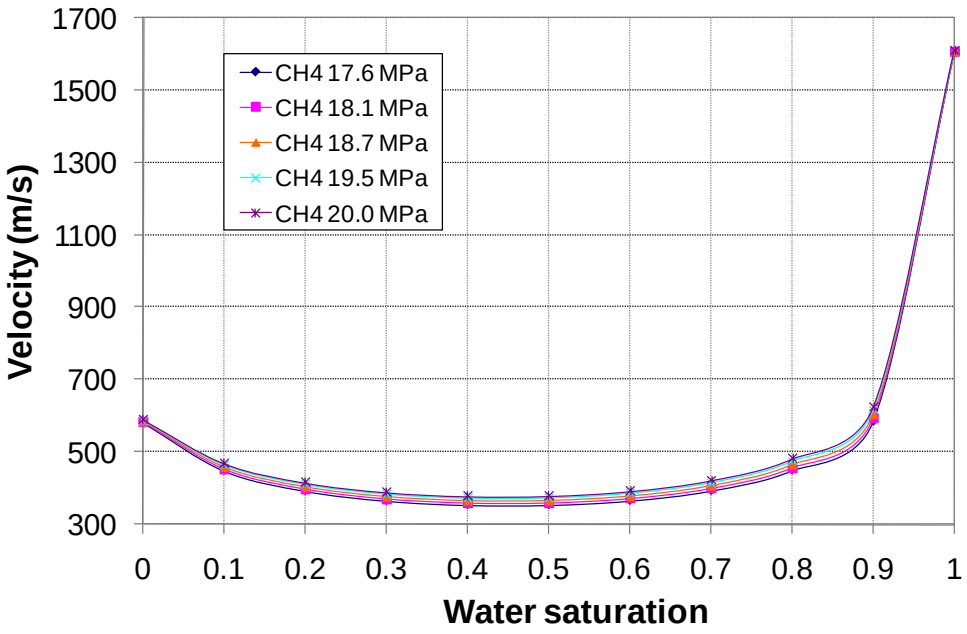
1700
1500
1300
1100
900
700
500
300
Velocity (m/s)
CH4 17.6 MPa
CH4 18.1 MPa
CH4 18.7 MPa
CH4 19.5 MPa
CH4 20.0 MPa
0
0.1
0.2
0.3
0.4
0.5
0.6
0.7
0.8
0.9
1
Water saturation

b)

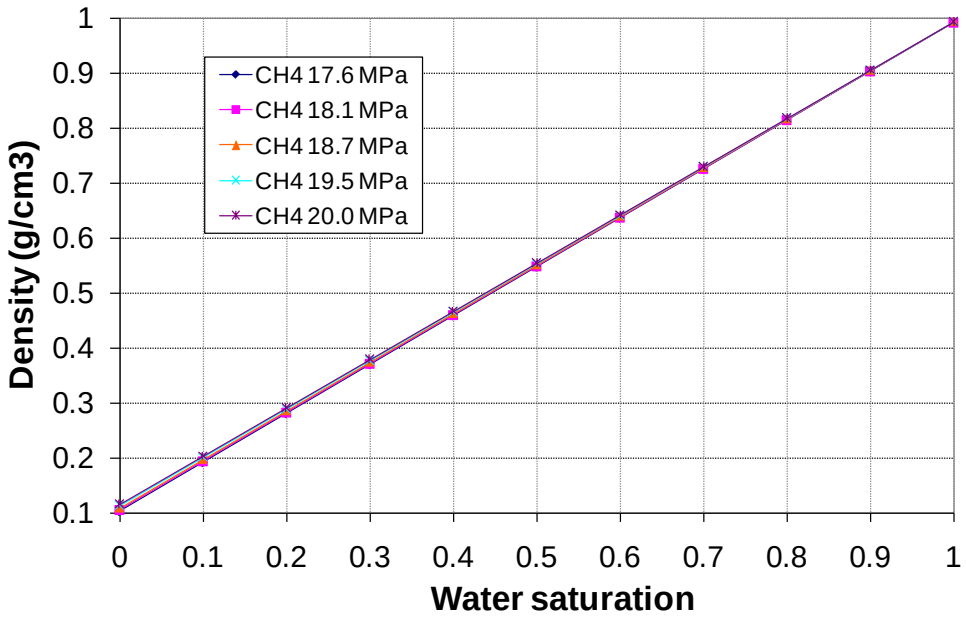
1
0.9
0.8
0.7
0.6
0.5
0.4
0.3
0.2
0.1
Density (g/cm3)
CH4 17.6 MPa
CH4 18.1 MPa
CH4 18.7 MPa
CH4 19.5 MPa
CH4 20.0 MPa
0
0.1
0.2
0.3
0.4
0.5
0.6
0.7
0.8
0.9
1
Water saturation

c)

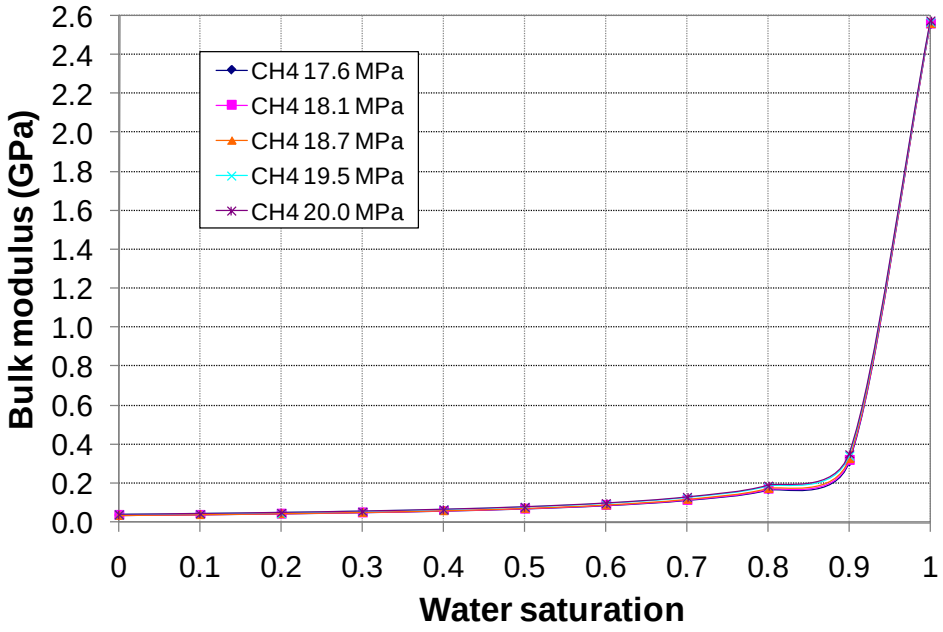

Figure 5.1 Elastic properties of methane and water mixture: a) velocity, b) density, and c) bulk modulus versus pressure and saturation.

The velocity and bulk modulus decrease rapidly when small amount of methane is introduced into water. However both velocity and bulk modulus are only weakly dependent on saturation below 90% water saturation. The density is less influenced by pressure changes and more by saturation. The effect of methane on seismic response is thus easy to predict. The situation with CO_2 or gas mixes is different.

5.2.2 Carbon dioxide (CO_2)

CO_2 can exist in the form of gas, liquid or in supercritical phase. The critical pressure and temperature of CO_2 are 7.3773 MPa and 30.9782^{o}C, respectively. Once it is injected, CO_2 can exist as free gas or as a dissolved constituent in the already existing pore fluid (Carcione et al., 2006). If CO_2 is in the supercritical phase, then the gas compressibility is lower than in the gas phase. The density of supercritical CO_2 is heavier than in the gas phase, closer to the oil/water, but the bulk modulus of supercritical CO_2 is closer to the gas phase. Thus monitoring CO_2 injection is challenging because the differences in seismic properties become smaller between methane-water mixture (*in-situ* pore fluids) and supercritical CO_2. Seismic

monitoring can be used to monitor injected CO_2 and its displacement process only if the injected CO_2 causes sufficient changes in seismic properties of the formation rock. Therefore it is crucial to derive CO_2 properties at the given depth, pressure and temperature. Figures 5.2 a), b), and c) show CO_2 properties calculated using equation 3.10 to 3.14 in Chapter-3 at temperature of 85^{o}C (*in-situ*) with varying pressure *(in-situ* and as predicted by flow simulators). It is clear that the behaviour of CO_2 is significantly different from the one of the pure gas.

a)

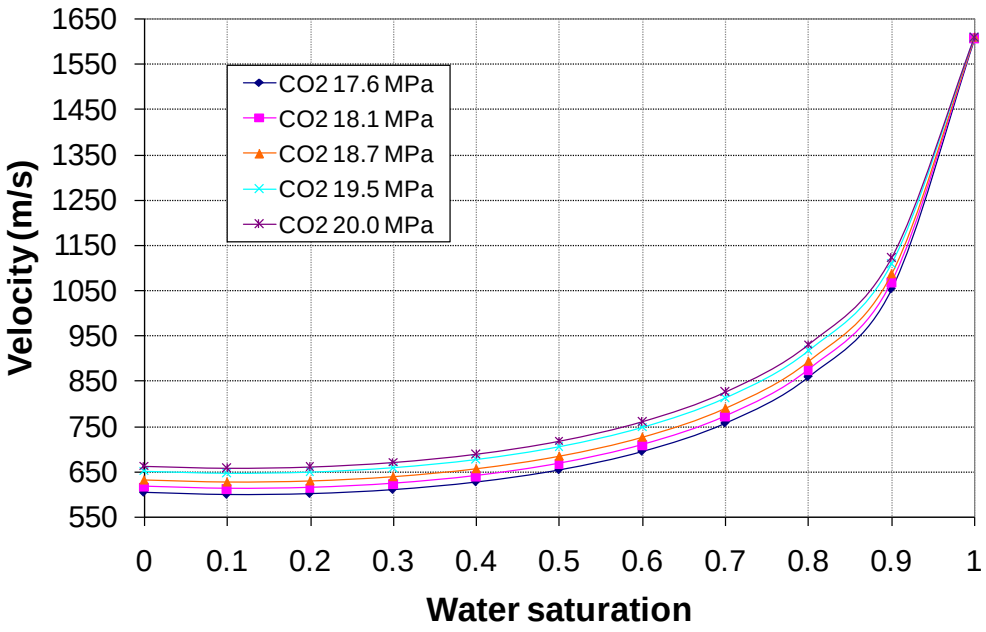

b)

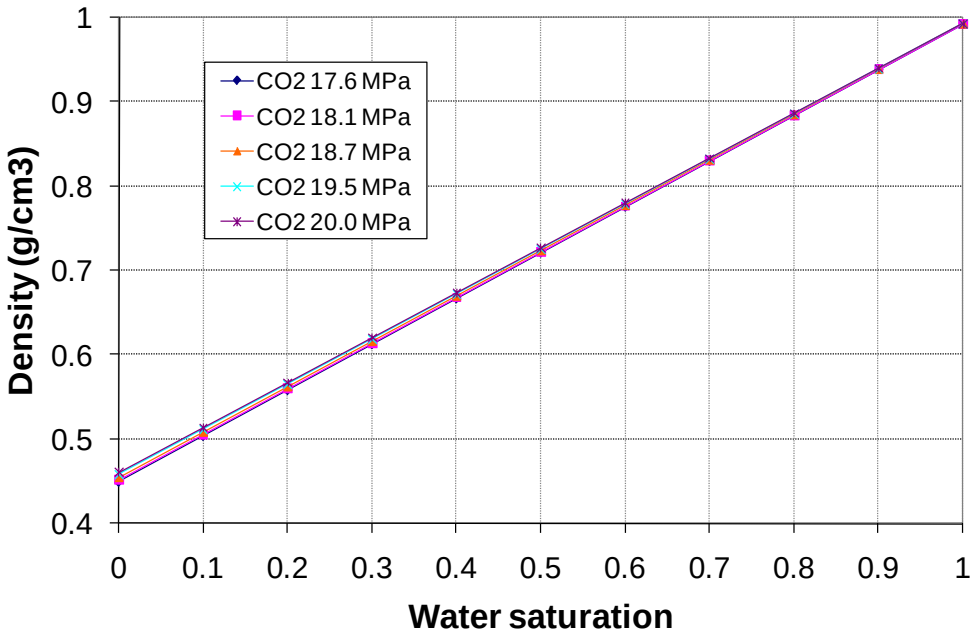

c)

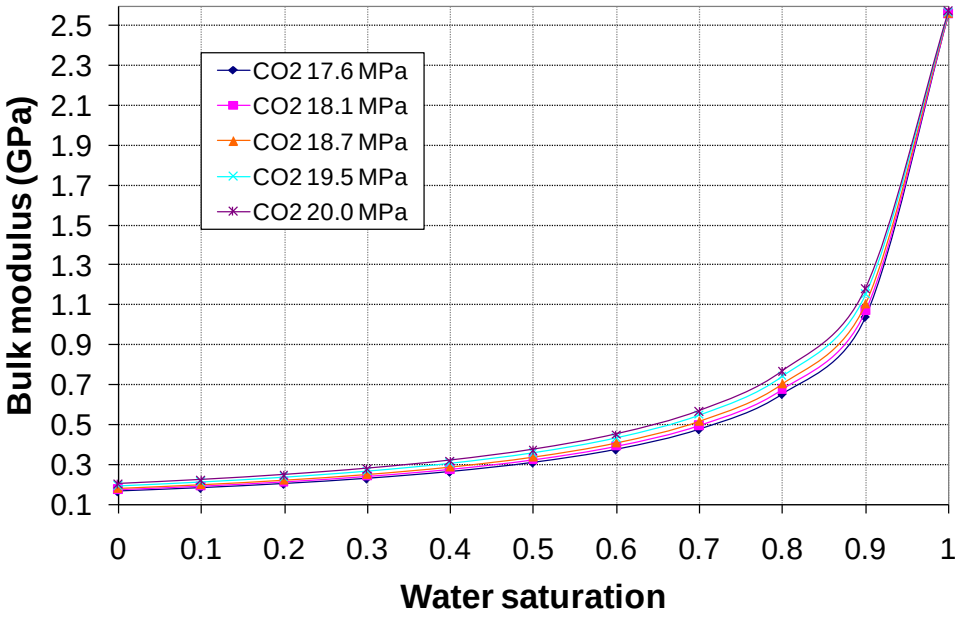

Figure 5.2 Elastic properties of mixture of carbon dioxide and water: a) velocity, b) density, and c) bulk modulus versus pressure and saturation.

The velocity and bulk modulus decrease gently as CO_2 saturation increases. This can be observed across the entire water saturation range. It suggests that introducing CO_2 gives less ambiguity in estimation of the elastic properties compared to methane (CH_4) since both velocity and bulk modulus are dependent on saturation below 90% water saturation. The density is more influenced by saturation changes.

5.2.3 Brine

The most common pore fluid is brine. Properties of brine depend on salinity (which ranges from pure water (zero salinity) to saturated saline solutions), pressure and temperature. Increasing the salinity increases the density of brine. Batzle and Wang (1992) provide a series of useful empirical relations between the state variables and velocity and density of the brine. Brine properties are calculated using equation 3.19 to 3.24 in Chapter-3.

5.2.4 Gas mixtures

In the CO2CRC Otway Project, a mixture of CO_2 with other gases, mainly methane, is injected into Waarre-C sand. I used ideal gas law and equation of state (EOS) as described in Chapter 3 to compute properties of such gas mixture at temperature 85^{o}C with varying pressure and saturation. This simulates pre-injection (gas mixture @17.6 MPa – CH_4 dominant) and post injection case (gas mixture @20MPa – CO_2 dominant) as shown in Figure 5.3 a), b) and c). Pressure and gas saturation from reservoir simulation for CO_2 geological storage is shown in Table 5.1 (Xu, 2007). Gas compositions for Naylor-1 (monitoring), CRC-1 (injection) and Buttress-1 (source of CO_2) are shown in Table 5.2. In Figure 5.4, I illustrated the most likely phase of CO_2 injected in the CO2CRC Otway Project.

Table 5.1 Pressure and gas saturation from the reservoir simulation.

	NAYLOR-1		CRC-1	
Stage/time (months from injection)	Avg. pore pressure MPa	Avg. gas saturation (mix gases)	Avg. pore pressure MPa	Avg. gas saturation (mix gases)
Before production	19.30	0.90		
After production/pre-injection (0 month - *baseline*)	17.60	0.20	17.60	0.20
Post injection (12 months - *monitor*)	20.00	0.80	20.00	0.80

The amount of injected CO_2 is 100,000 tonnes.

Table 5.2 *In-situ* gas compounds from Naylor-1 and CRC-1 wells before and after production/pre-injection, and most likely post-injection.

NAYLOR-1 *in-situ* gas compounds (before production)		NAYLOR-1 *in-situ* gas compounds after production (pre injection)	
Compounds	**Mol composition %**	**Compounds**	**Mol composition %**
N2	6.52	N2	4.19
CO2	1.02	CO2	0.09
CH4	84.34	CH4	86.63
Ethane	4.62	Ethane	4.97
Propane	2.01	Propane	2.21
I-Butane	0.41	I-Butane	0.41
N-Butane	0.51	N-Butane	0.51
I-Pentane	0.13	I-Pentane	0.13
N-Pentane	0.11	N-Pentane	0.11
Hexanes	0.17	Hexanes	0.17
Heptanes	0.10	Heptanes	0.10
Octanes plus	0.06	Octanes plus	0.48
CRC-1 *in-situ* gas compounds (pre-injection)		**CRC-1/NAYLOR-1 *in-situ* gas compounds (post-injection)**	
Compounds	**Mol composition %**	**Compounds**	**Mol composition %**
N2	1.23	N2	1.38
CO2	0.86	CO2	78.7
CH4	87.66	CH4	18.9
Ethane	5.00	Ethane	0.52
Propane	2.44	Propane	0.23
I-Butane	0.58	I-Butane	0.05
N-Butane	0.72	N-Butane	0.05
I-Pentane	0.25	I-Pentane	0.01
N-Pentane	0.21	N-Pentane	0.01
Hexanes	0.33	Hexanes	0.03
Heptanes	0.41	Heptanes	0.03
Octanes	0.14	Octanes	0.02
Nonaes	0.08	Nonaes	0.02
Decanes	0.06	Decanes	0.03
Undecanes	0.02	Undecanes	0.02
Dodecanes+	0.01		

The source of CO_2 for injection was from the Buttress-1 well. It was used to predict most likely post-injection gas composition in Naylor-1 and CRC-1 wells.

a)

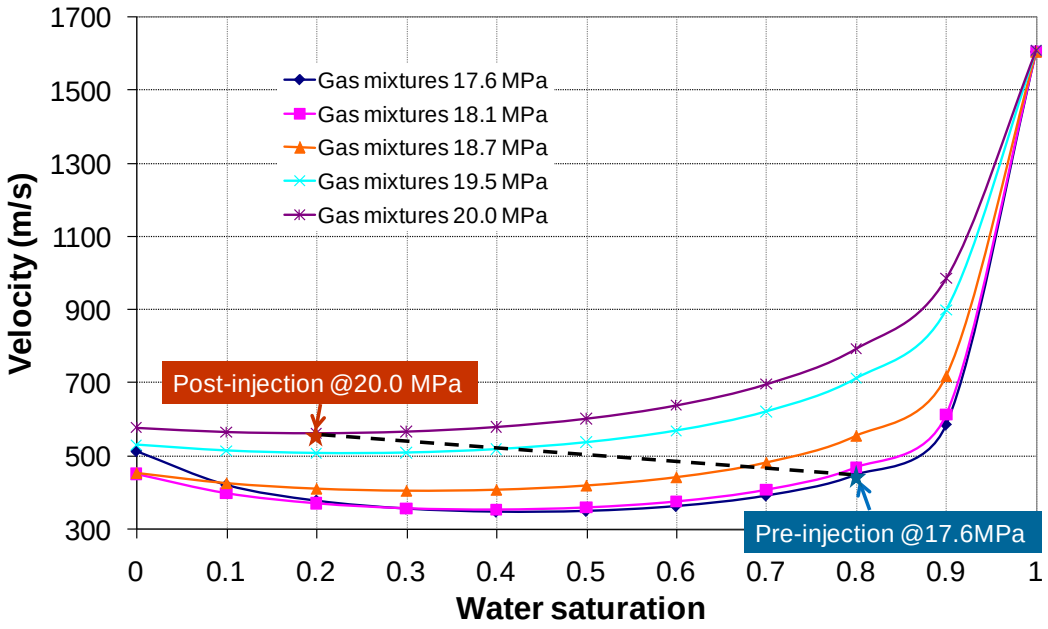
Velocity (m/s)
1700
1500
1300
1100
900
700
500
300
0
0.1
0.2
0.3
0.4
0.5
0.6
0.7
0.8
0.9
1
Water saturation
Gas mixtures 17.6 MPa
Gas mixtures 18.1 MPa
Gas mixtures 18.7 MPa
Gas mixtures 19.5 MPa
Gas mixtures 20.0 MPa
Post-injection @20.0 MPa
Pre-injection @17.6MPa

b)

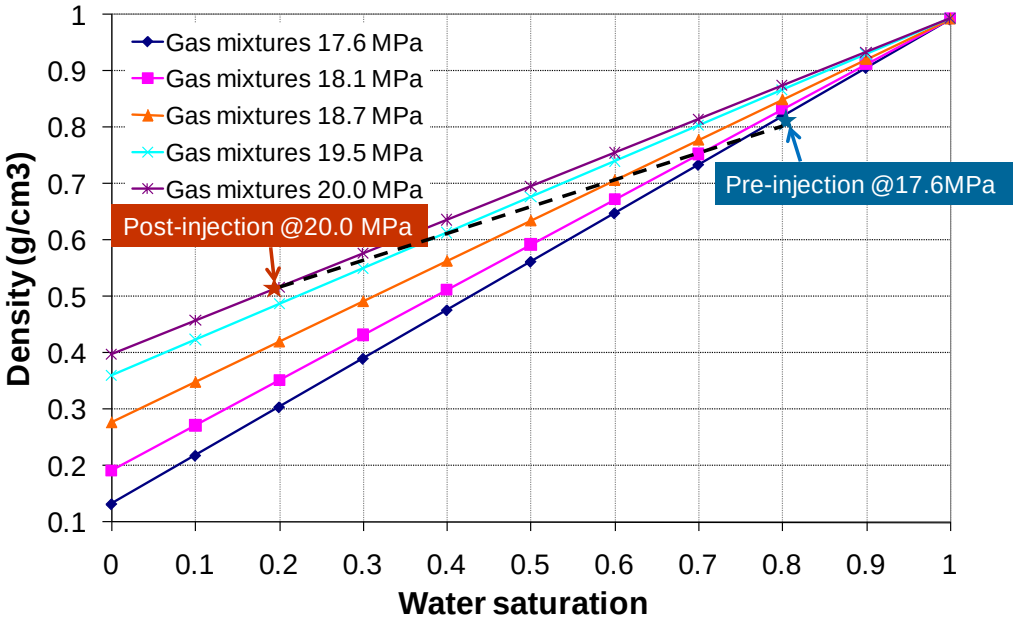
Density (g/cm3)
1
0.9
0.8
0.7
0.6
0.5
0.4
0.3
0.2
0.1
0
0.1
0.2
0.3
0.4
0.5
0.6
0.7
0.8
0.9
1
Water saturation
Gas mixtures 17.6 MPa
Gas mixtures 18.1 MPa
Gas mixtures 18.7 MPa
Gas mixtures 19.5 MPa
Gas mixtures 20.0 MPa
Post-injection @20.0 MPa
Pre-injection @17.6MPa

c)

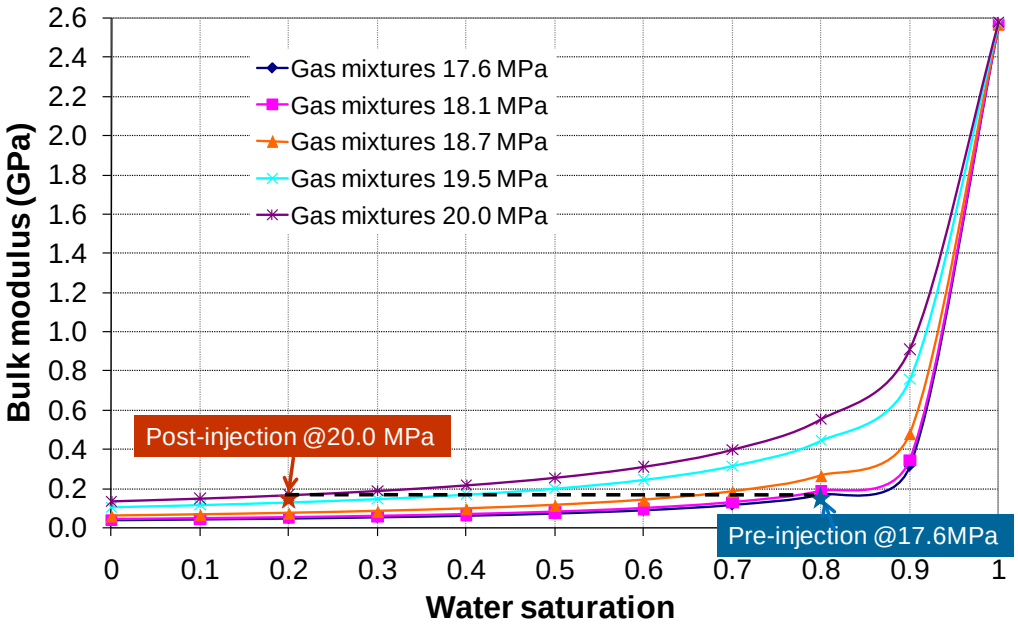

Figure 5.3 Predicted elastic properties of CH_4-CO_2 mixtures and water: a) velocity, b) density and c) bulk modulus versus pressure and water saturation.

The velocity of the fluid mixture depends on saturation, gas composition and pressure. It makes the velocity of the pore fluid post-injection, where the CO_2 is dominant, higher than pre-injection, where the CH_4 is dominant. The pore pressure increase during the injection causes an increase in the bulk modulus of the CH_4- CO_2 mixture and water with respect to initial state. Dissolution of CO_2 into water increases the overall acoustic velocity of gas mixtures. Hence the velocity of gas mixtures after 12 months of injection (post-injection) will slightly increase with respect to the initial state.

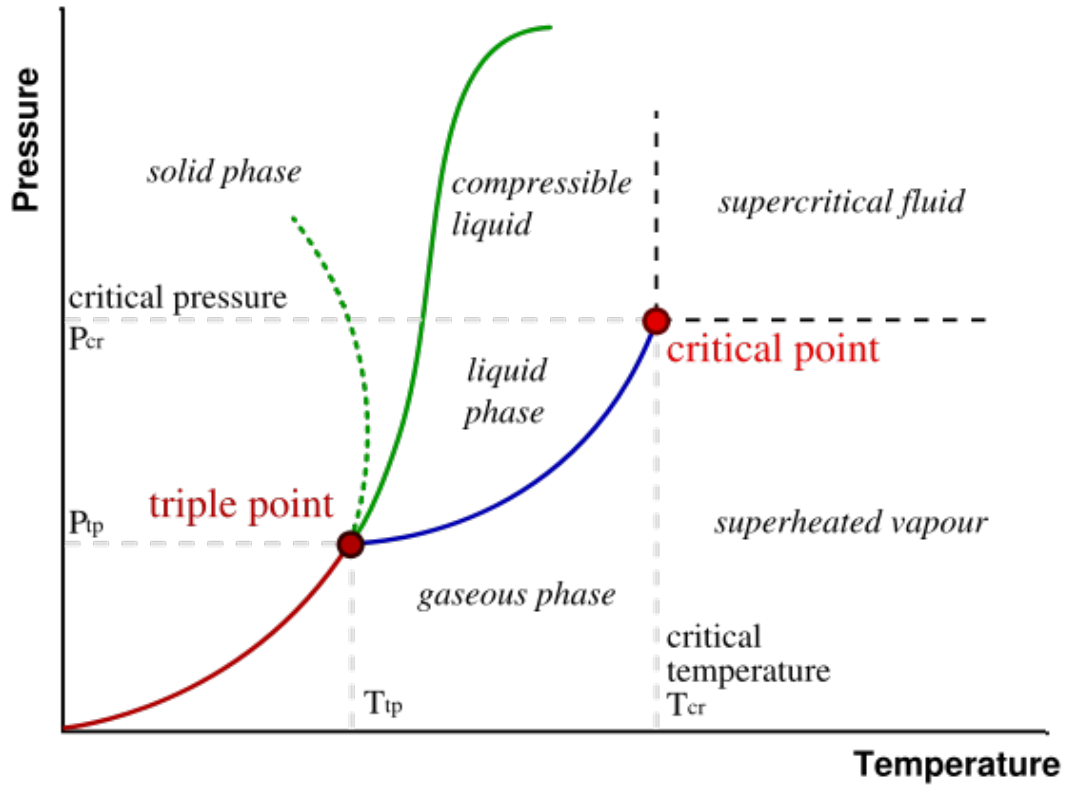

Figure 5.4 Phase diagram of pressure and temperature of pure CO_2. Supercritical CO_2 is injected into Waarre-C sand.

As the critical point is approached, the properties of the gas and liquid phases approach one another, resulting in only one phase which is called a supercritical fluid. At and above the supercritical point, the compressibility of the fluid is close to of a gas, while the density is close to that of a liquid. At the time of injection the Waarre-C reservoir has an *in-situ* pressure and temperature above the critical point of CO_2. Thus in the reservoir the injected CO_2 will be in the form of a supercritical fluid.

5.2.5 Fluid mixtures

Optimal depth interval for CO_2 storage is 1.5-3 km. In this range, CO_2 is in supercritical stage and large quantities of CO_2 can be stored in relatively small volumes. Hence this depth interval is of main interest for the calculation of thermodynamic properties. There are many existing mixture models with particular

utilisation of the equation of state. One of them, the cubic equation of state of Peng and Robinson (1976), is widely used for calculation of the physical properties of gas mixtures. This equation is explicit in pressure. The calculation of vapour pressure and equilibrium phase of mixtures, and for the evaluation of corresponding experimental data, the use of cubic equations of state is quite functional as they yield fairly accurate results (Klimeck, 2000; Klimeck et al., 1999) . A recently new equation of state called GERG-2004 has been developed to enable calculation of thermodynamic properties for a wide range of different mixtures and operating conditions. Homogeneous gas, liquid, and supercritical region, and also vapour-liquid equilibrium states (O.Kunz et al., 2007) are computed with these equations. I used GERG-2004 and Batzle and Wang equations to calculate density, velocity and bulk modulus for gas and fluid mixtures. This is shown in Table 5.3 a) and b). In initial calculations I assumed quartz as a matrix, porosity of 21.1%, brine-gas saturation level at 80/20 % for pre-injection and 20/80 % for post-injection with salinity of 21000 ppm. The reservoir pressure was 17.6 and 20 MPa for pre- and post-injection, respectively, while the temperature was kept constant at 85^{o}C. These parameters were input into Gassmann's equations to compute saturated bulk modulus and corresponding body wave speeds. Table 5.4 shows the computed values.

Table 5.3 a) Gas and b) Fluid mixtures properties calculation.

a) Gas properties

			Gas Properties		
			Density (g/cm^3)	*Sound of speed (m/s)*	*Bulk modulus (MPa)*
GERG-2004	Pre-injection	*Pure methane (CH4)*	0.10198	526.896	28.312
		Gas mixtures (in-situ CRC-1)	0.11102	506.021	28.427
		Brine - RokDoc (gas free)	0.992	1605.37	2557
		Brine - RokDoc (average gas)	0.992	1566.2	2434
	Post-injection	*CO2 (80%), CH4 (20%)*	0.39602	334.436	44.295
		Gas mixtures (most-likely predicted based on BUTTRESS-1 gas composition)	0.39183	334.507	43.844
		Brine - RokDoc (gas free)	0.993	1610.35	2575
		Brine - RokDoc (average gas)	0.993	1567.94	2442
Batzle and Wang	Pre-injection	*Pure methane (CH4)*	0.10231	582.35624	34.699
		Gas mixtures (in-situ CRC-1)	0.13243	513.4	34.91
		Brine (gas free)	0.992	1610.35156	2572.99463
	Post-injection	*CO2 (80%), CH4 (20%)*	0.396363	576.66195	131.806
		Gas mixtures (most-likely predicted based on BUTTRESS-1 gas composition)	0.39807	578.46	133.2
		Brine (gas free)	0.993	1610.35088	2575.42905

b) Fluid properties

			Fluid Mixtures Properties		
			Density (g/cm^3)	*Sound of speed (m/s)*	*Bulk modulus (MPa)*
GERG-2004	Pre-injection	*Pure methane (CH4) 20%, brine 80%*	0.81415	408.04000	135.56
		Gas mixtures (in-situ CRC-1) 20%, brine 80%	0.81596	408.38	136.08
	Post-injection	*CO2 (80%), CH4 (20%) - gas mixtures 80%, brine 20%*	0.51542	327.06	55.13
		Gas mixtures (most-likely predicted based on BUTTRESS-1 gas composition) 80%, brine 20%	0.51206	326.46	54.57
Batzle and Wang	Pre-injection	*Pure methane (CH4) 20%, brine 80%*	0.81422	449.64	164.62
		Gas mixtures (in-situ CRC-1) 20%, brine 80%	0.82024	449.25	165.55
	Post-injection	*CO2 (80%), CH4 (20%) - gas mixtures 80%, brine 20%*	0.51572	561.64	162.68
		Gas mixtures (most-likely predicted based on BUTTRESS-1 gas composition) 80%, brine 20%	0.51708	563.81	164.37

Table 5.4 Rock saturated properties calculations.

			Rock Saturated Properties		
			Density of rock saturated (g/cm^3)	*Velocity of rock saturated (m/s)*	*Bulk modulus of rock saturated (MPa)*
GERG-2004	Pre-injection	*Pure methane (CH4) 20%, brine 80%*	2.255535245	3487.66214	12498.15
		Gas mixtures (in-situ CRC-1) 20%, brine 80%	2.255916733	3487.42049	12498.98
	Post-injection	*CO2 (80%), CH4 (20%) - gas mixtures 80%, brine 20%*	2.192501776	3498.965048	12284.97
		Gas mixtures (most-likely predicted based on BUTTRESS-1 gas composition) 80%, brine 20%	2.191794504	3499.469308	12284.05
Batzle and Wang	Pre-injection	*Pure methane (CH4) 20%, brine 80%*	2.255549387	3490.570672	12544.1
		Gas mixtures (in-situ CRC-1) 20%, brine 80%	2.256820235	3489.680829	12545.56
	Post-injection	*CO2 (80%), CH4 (20%) - gas mixtures 80%, brine 20%*	2.192565322	3510.25612	12459.27
		Gas mixtures (most-likely predicted based on BUTTRESS-1 gas composition) 80%, brine 20%	2.19285345	3510.200579	12461.97

Corresponding time-lapse differences are shown in Table 5.5. Although the bulk modulus of gas and fluid were very different and varieties for different stages, the computed differences are small (less than 2%), as expected. Therefore, Batzle and Wang (1992) equations appear to produce reasonable results and could be used to predict time-lapse properties of gas/fluid mixtures.

Table 5.5 Saturated rock properties differences.

	Rock Saturated Properties Difference (%)		
Gas mixtures	*Density of rock saturated (g/cm^3)*	*Velocity of rock saturated (m/s)*	*Bulk modulus of rock saturated (MPa)*
Pre-injection	*0.04*	*0.06*	*0.06*
Post-injection	*0.05*	*0.31*	*1.44*

5.3 Fluid properties at Naylor field

Quantitative interpretation at Naylor requires a detailed knowledge of how CO_2 saturation affects properties of the pore fluid and hence elasticity of a reservoir rock. Properties of fluids mixtures containing CO_2 depend on the depth of storage, pressure and temperature. At the greater depth, such as in the case of the Waarre-C reservoir, where pore pressure exceeds 6 MPa; the CO_2 behaves as a "zero-viscosity" liquid while the bulk modulus is closer to that of a gas.

I calculated fluid properties from gas composition taken from the Naylor-1, CRC-1 and Buttress-1 wells. I then computed properties of water mixed with pure CO_2, pure CH_4 and with gas mixtures (CO_2, CH_4 and other gases as calculated for *in-situ* gas reservoir using gas chromatography). Gas-water mixture at each pressure has different average gas saturation and composition (pre-injection CH_4 is dominant and post-injection CO_2 is dominant). I calculated the effect of gas saturation based on the results of reservoir simulation as given in Table 5.2 and shown in Figure 5.5 a) to e).

a) Pore pressure at 17.6 MPa

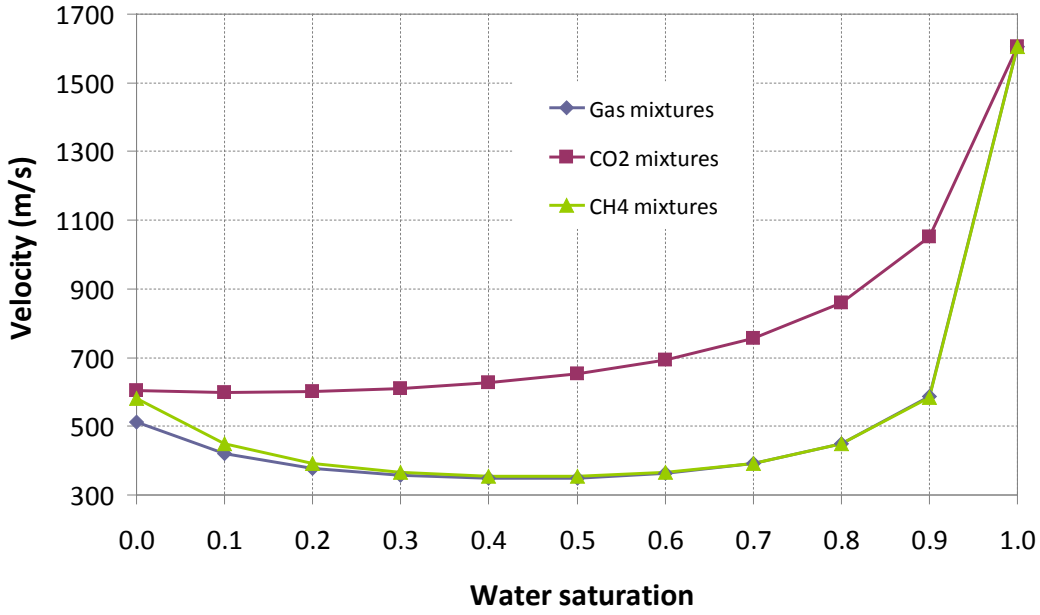

b) Pore pressure at 18.1 MPa

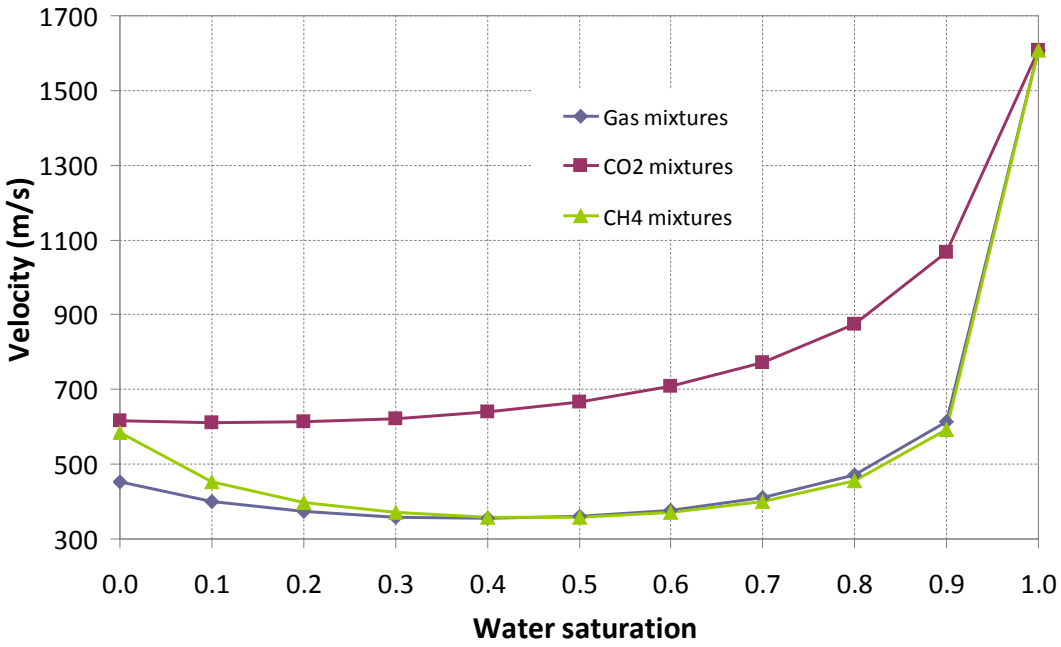

c) Pore pressure at 18.7 MPa

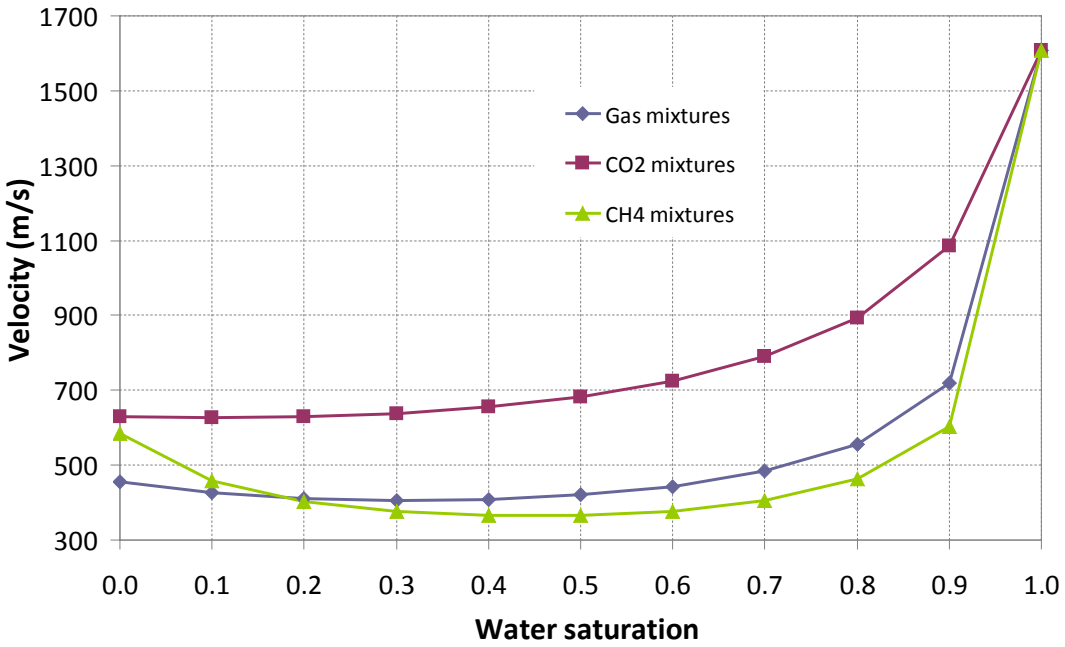

d) Pore pressure at 19.5 MPa

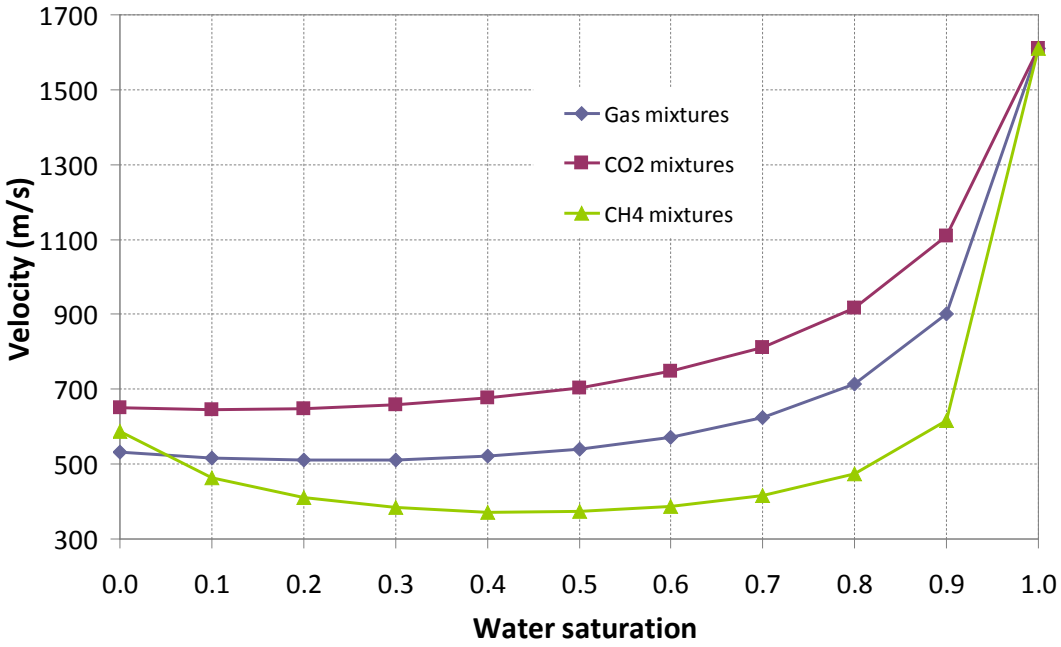

e) Pore pressure at 20 MPa

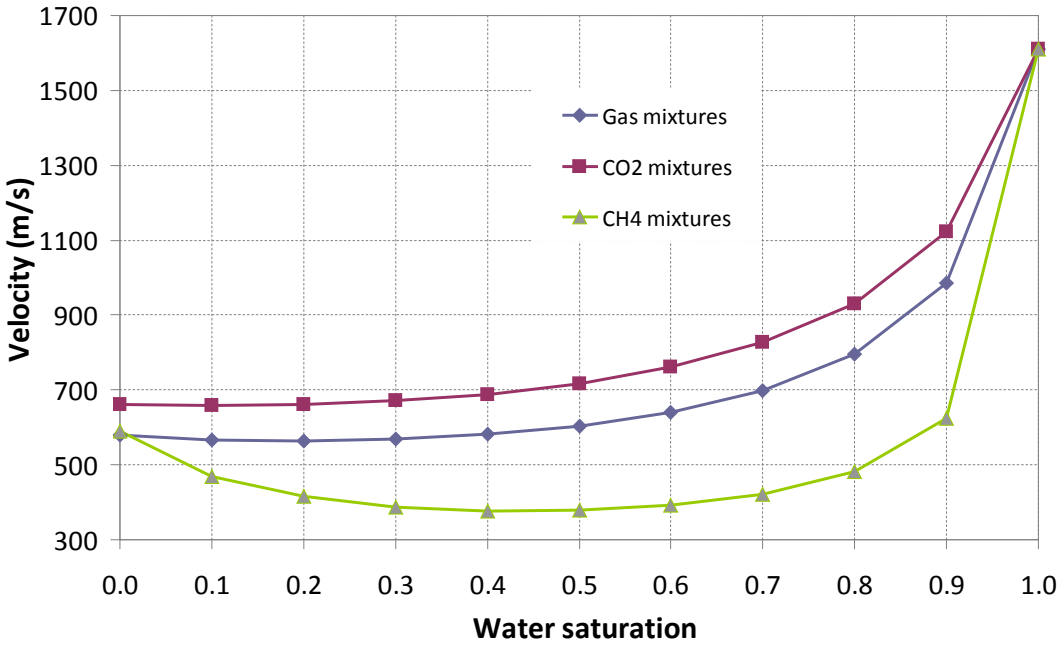

Figure 5.5 The effect of CO_2 saturation on velocity at different pore pressure for Waarre- C reservoir. a) Pore pressure at 17.6 MPa, b) pore pressure at 18.1 MPa, c) pore pressure at 18.7 MPa, d) pore pressure at 19.5 MPa and e) pore pressure at 20 MPa.

CO_2 and CH_4 are pure substance; gas mixtures compositions are derived from gas chromatography for *in-situ* conditions. In this case, the CO_2 content in gas mixtures increased to 80% at 20 MPa. CO_2 and gas mixtures velocities are constant for below 90% water saturation at 20 MPa. It also suggests that the density effect is similar. Therefore, estimation of saturation from elastic properties shows less ambiguity for CO_2 – water mixture than for CH_4-water mixture (Figure 5.5).

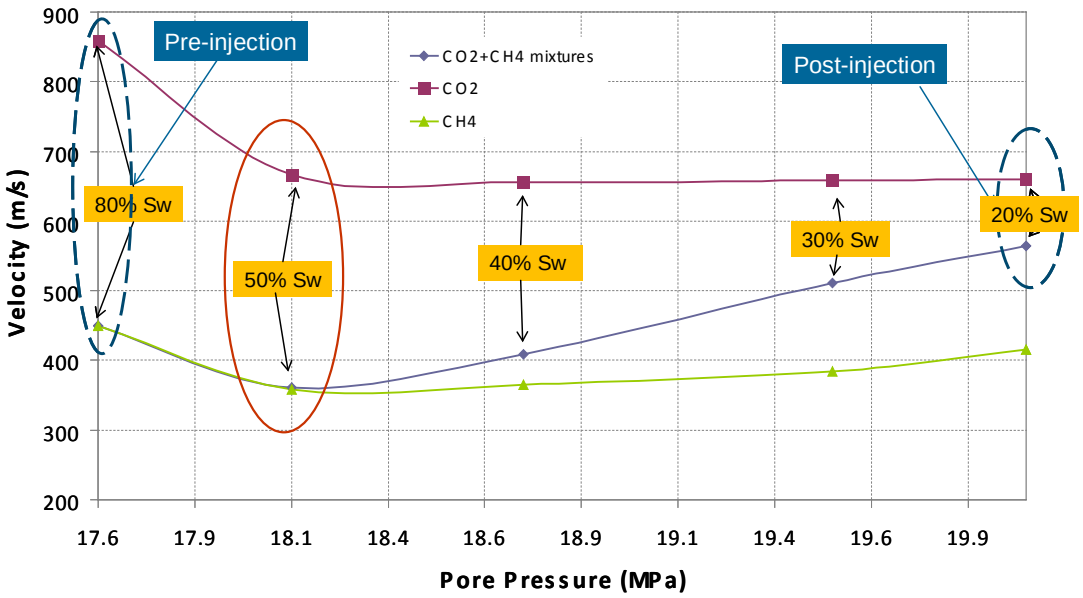

Figure 5.6 Predicted velocity for gases and their mixtures for varying saturation and pressure.

The velocity of CO_2 + CH_4 mixtures suddenly jump due to an increase in CO_2 saturation around S_W~0.5. It appears that saturation changes produce more effect than pressure with respect to velocity differences. However the velocity differences become smaller when the pressure is higher. That would suggest that monitoring is needed to be conducted in short time intervals to capture the largest differences point of fluid properties changes as suggested in Figure 5.6.

5.4 Time-lapse elastic properties of reservoir rocks

5.4.1 Ultrasonic core measurements

Prediction of time-lapse seismic response requires knowledge of the effect of saturation and pressure on seismic velocities which can be obtained by laboratory measurement using core samples (ultrasonic core measurement). The measurements use dry condition to avoid the effects associated with the dispersion between sonic and ultrasonic frequencies, which can be large for fluid-saturated samples (Batzle et al., 2006; Mavko and Jizba, 1991). 42m of cores from CRC-1 well were recovered through reservoir and seal intervals. The area of interest was Waarre sandstone formation unit- C (Waarre-C, core #6). The interval from 2051-2075.5m was recovered with 96% success (23.53m). The deepest core penetrated approximately 1m through the base of the Flaxman and then 22.5m of the Waarre-C (Dance and Vakarelov, 2007). Diameter of the core was approximately 3 inches and in general in a good condition. Several cores (sand interval) were selected for ultrasonic measurement. Three high quality cores taken at depth of 2055, 2057, and 2071.5 mRT within Waarre-C sandstone were selected for further analysis. These cores have high permeability and porosity values (Figure 5.7). The equipment used for measurement comprises a high-stiffness load frame, a triaxial pressure cell and systems for cell and pore pressure control as shown in Figure 5.8. The core was mounted between top and base platens vertically (P-and S-waves) with 38 mm in diameter (Siggins, 2006; Siggins et al., 2009).

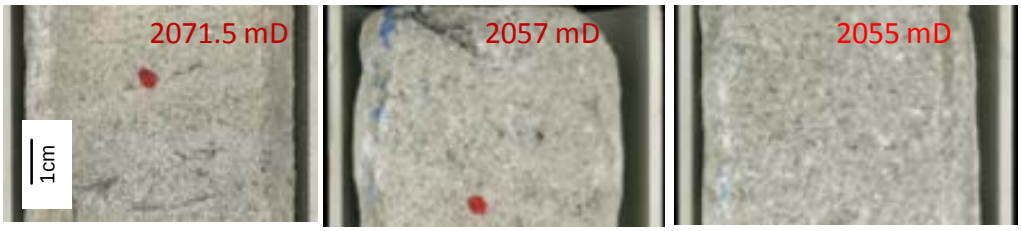

Figure 5.7 Representative core sample of Waarre Sandstone unit C at a) 2071.5, b) 2057 and c) 2055 meters depth, with fine to coarse grained massive, quartz dominant and good porosity and permeability.

Figure 5.8 Computer-controlled triaxial pressure cell with independent control of pore pressure with the pore fluid maintained in both gaseous and liquid phases as required.

The measurements of dry ultrasonic P- and S-wave velocities, as a function of confining pressure, were carried on core samples at "room-dried" conditions, with confining pressures varied from 5 MPa up to 55 MPa in steps of 5 MPa. The Gassmann's equation was then applied to compute the properties of the saturated samples (Mavko et al., 1998), which is expected to give the static limit of the elastic properties. Of particular interest of course was to compare elastic properties of saturated core samples with field measurements.

5.4.2 Estimating reservoir effective pressure

To estimate the effective pressure P_{eff} , I used the following formula (Biot, 1957):

$$P_{eff} = P_{ob} - \eta P_p \tag{5.1}$$

where P_p is the pore pressure, η is the effective pressure coefficient, and P_{ob} is the overburden pressure given as:

$$P_{ob}(z) = P_0 + g\int_0^z \rho(z)\,dz \tag{5.2}$$

where $\rho(z)$ is the density of the overlying rock at depth z (sum of density log at given depth) and g is the acceleration due to gravity (9.80665 m/s^2 or 9.80665 N/kg) and P_0 is the pressure at surface (datum pressure). Pore pressure was obtained from RFT and MDT tests as well as from production history report. The effective pressure coefficient η was assumed to be one (Gurevich, 2004). This assumption based on the sensitivity of the elastic properties to pressure in this pressure regime is relatively weak and unlikely to influence the results. Pore pressure was defined as 19.3 MPa before production and 17.6 MPa after production before CO_2 injection; overburden pressure at the depth of 2052 mD was approximately 44.85 MPa, as a result the current effective pressure within reservoir interval was approximately 27.25 MPa.

5.4.3 Methodology

The potential error in computation of bulk moduli in the case of CRC-1 reservoir with only logs is high unless calibrated with core sample tests. Therefore, to obtain elastic properties of reservoir rock I did the following:

1. Perform dry core measurements to obtain the relationship between effective pressure and velocities.
2. Calculate K_{dry} from dry core measurements.
3. Derive K_{grain} using inverse Krief since porosity and grain density are measured or known.
4. Apply Gassmann's equation to compute core saturated velocities from the dry core measurements at *in-situ* reservoir condition (S_w= 98.53%).
5. Apply Gassmann's equation to compute bulk modulus of saturated porous rock (K_{sat}) from log measurements.

6. Compare the calculated core saturated velocities with log measurements (sonic log).

I used some basic petrophysical logs such as gamma ray, velocity, density, porosity, saturation, resistivity, clay volume and caliper to analyse and interpret the reservoir as outlined in Figure 5.9.

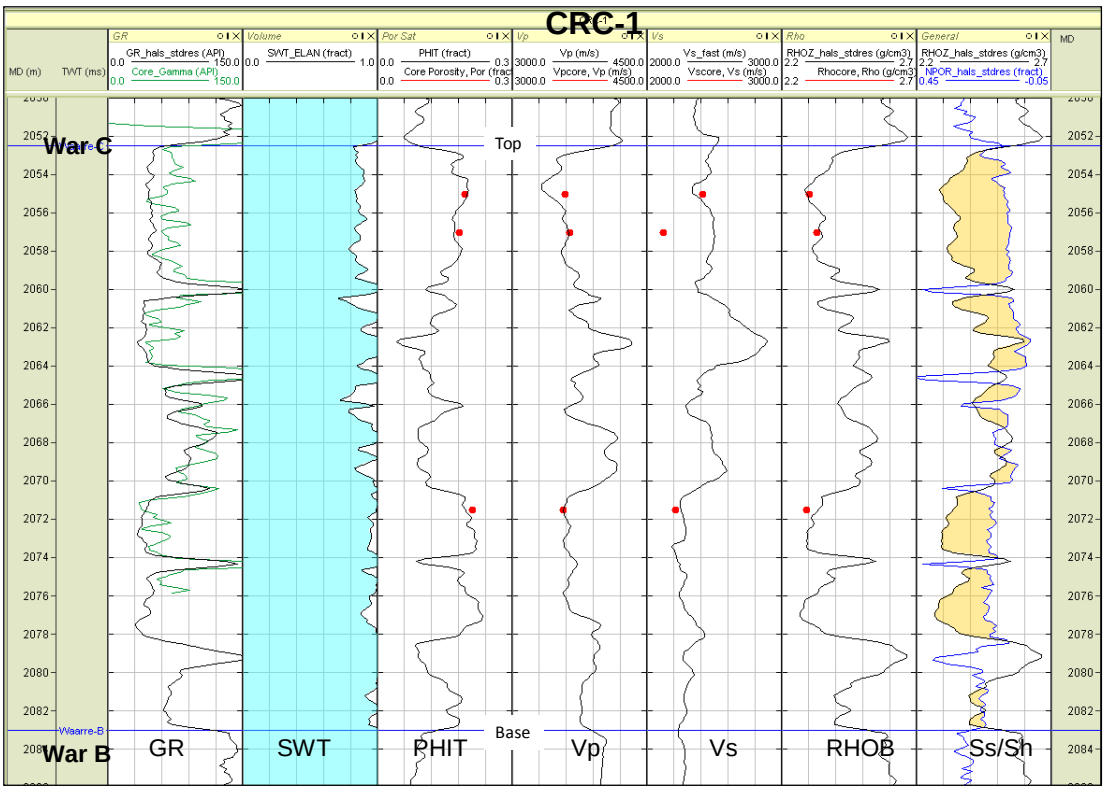

Figure 5.9 CRC-1 well composite logs that show reservoir interval (top and base of Waarre-C) and core samples (red dots). Yellow filled is the sand/shale ratio. The log velocities does agree with core saturated velocities. However S-wave log velocity does not agree with S-wave core saturated velocity at the depth of 2057m due to difficulty in picking S-wave velocity. Gamma log (green curve) suggests the reservoir is heterogeneous. Residual gas does exist within the reservoir.

Core plug was taken from 2071.5, 2055, and 2055 mD. Ultrasonic core measurements were performed under room conditions, with confining pressures up to 55 MPa in steps of 5 MPa. The result in Figures 5.10 to 5-12 show measured and calculated P-and S-wave velocities at the dry and water saturated as a function of

effective pressure. This is consistent with the initial computations for Naylor-1 and CRC-1 wells (Li et al., 2006; Wisman and Urosevic, 2007).

Routine Core Analysis was conducted by Core Laboratories Australia. They measured core porosity, permeability, grain density and gamma at confining stress 2580 psi (17.8 MPa).

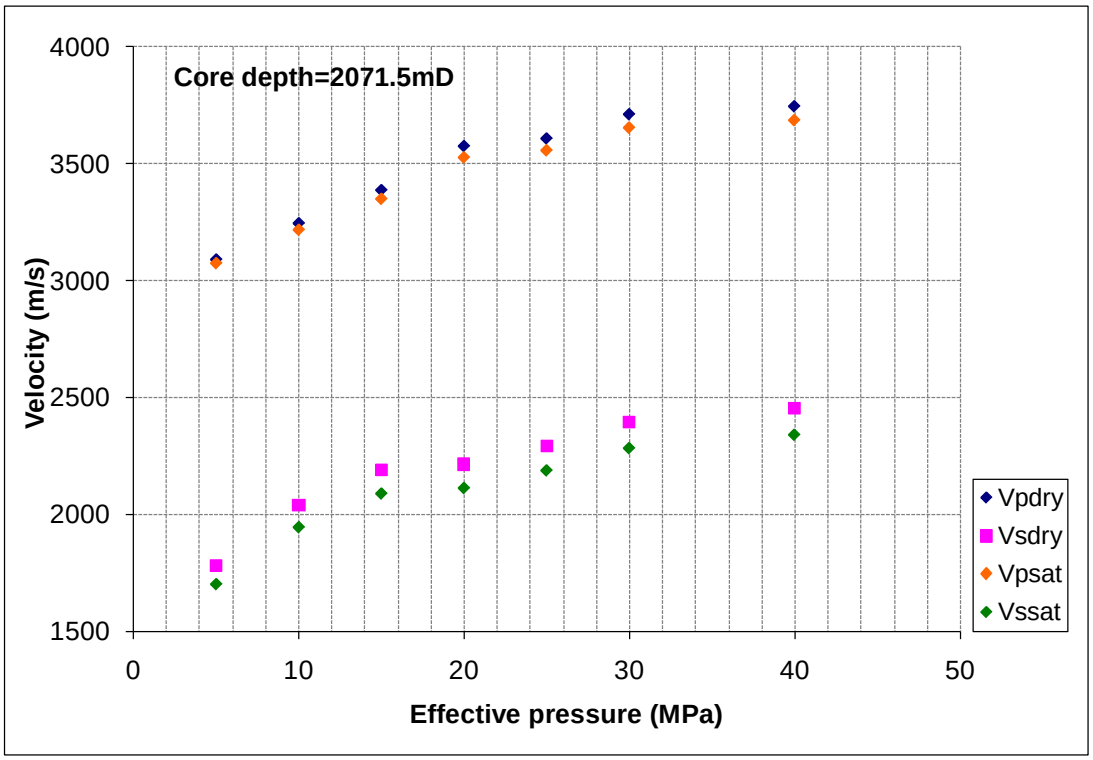

Figure 5.10 Measured and calculated P- and S-wave velocities at dry and water-saturated states with 98.31% saturation, as a function of effective pressure. The difference in S-wave velocity for dry and water saturated cases is higher than P-wave velocity, which shows that the density effect dominates.

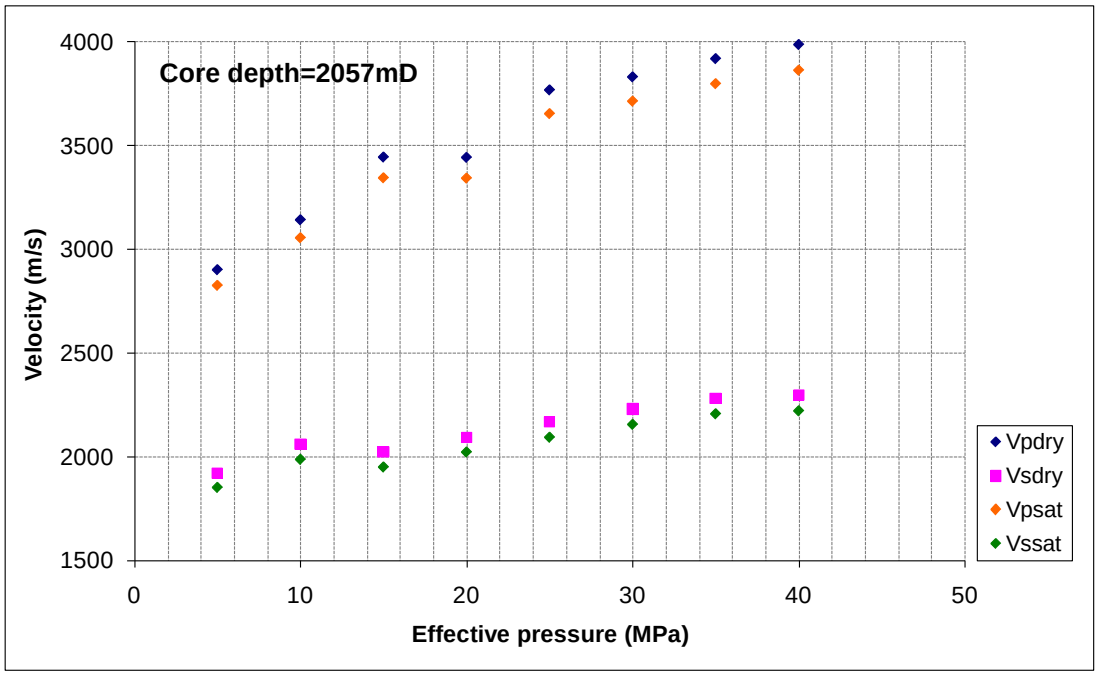

Figure 5.11 Measured and calculated P- and S-wave velocities at dry and water-saturated states with 86.02% saturation as a function of effective pressure. The differences in velocities dry and saturated are similar and constant.

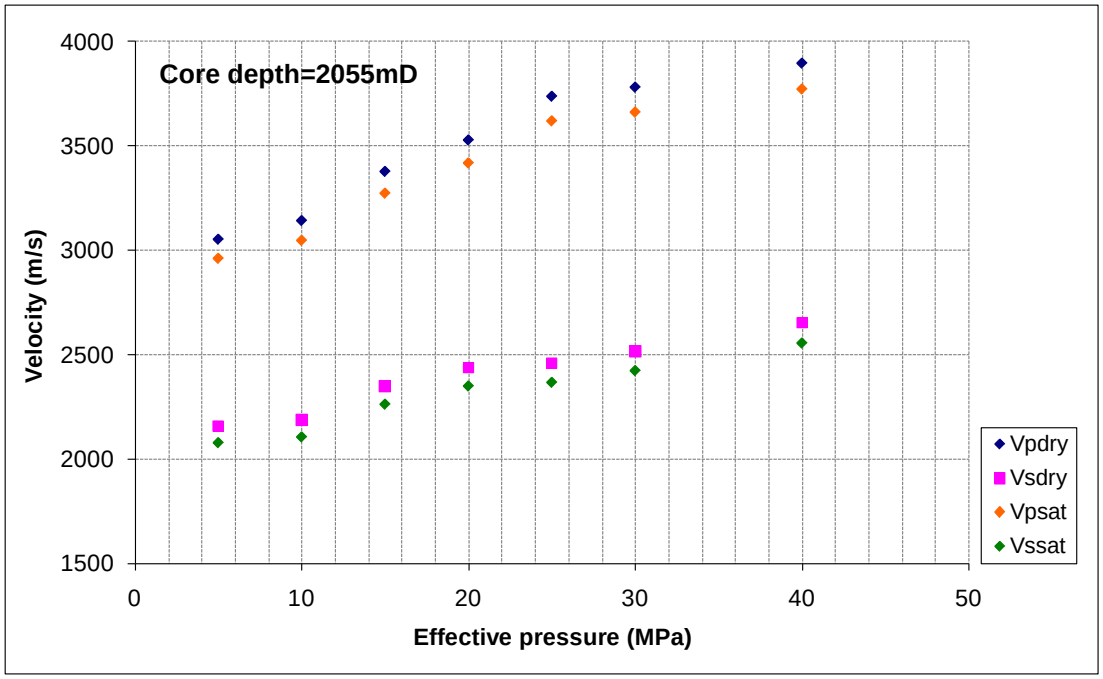

Figure 5.12 Measured and calculated P- and S-wave velocities at dry and water-saturated states with 84.27% saturation, as a function of effective pressure. The differences in velocities dry and saturated are similar and constant with slightly increasing of P-wave velocities at the effective pressure of 25 MPa and above.

5.4.4 Seismic velocities and effective pressure relationship

Core measurements provided relationships between seismic velocities and effective pressure (P_{eff}) of the dry Waarre-C sandstone at the depth of 2071.5m, as follow:

$$V_{pdry} = 2654.1 P_{eff}^{\ 0.0934} (m/s), \tag{5.3}$$

$$V_{sdry} = 1460.3 P_{eff}^{\ 0.1399} (m/s) \quad , \tag{5.4}$$

The same relationships between seismic velocities and effective pressure (P_{eff}) of the dry Waarre-C sandstone at the depth of 2057m reads:

$$V_{pdry} = 2215.3 P_{eff}^{\ 0.1591} (m/s), \tag{5.5}$$

$$V_{sdry} = 1668.3 P_{eff}^{\ 0.0827} (m/s) \quad , \tag{5.6}$$

Finally for the core at 2055m depth we had:

$$V_{pdry} = 2411.2 P_{eff}^{\ 0.1297} (m/s), \tag{5.7}$$

$$V_{sdry} = 1787.6 P_{eff}^{\ 0.1017} (m/s) \quad . \tag{5.8}$$

The estimated effective pressure at reservoir level is 27.25 MPa. Thus I calculated the dry properties using equation (5.3) to (5.8). The results are showed in Table 5.6 and Table 5.7.

Table 5.6 Calculated dry velocities at estimated reservoir effective pressure (27.25 MPa) incorporated with core porosity and core grain density measurements.

Core depth (m)	Vp_{dry} (m/s)	Vs_{dry} (m/s)	Rho_{dry} (g/cm_3)	Rho_{grain} (g/cm_3)	Phi_{core} (%)
2055.0	3701.692	2501.768	2.135	2.645	19.3
2057.0	3747.998	2192.699	2.169	2.651	18.2
2071.5	3613.936	2318.728	2.084	2.641	21.1

Table 5.7 Calculated dry moduli and mineral grain moduli at estimated reservoir effective pressure (27.25 MPa) derived from inverse Krief relation.

Core depth (m)	K_{dry} (GPa)	Mu_{dry} (GPa)	K_{grain} (GPa)	Mu_{grain} (GPa)
2055.0	11.435	13.360	25.377	29.648
2057.0	16.561	10.426	34.598	21.789
2071.5	12.277	11.203	30.230	27.586

The elastic properties of saturated core samples are then compared to field measurement as shown in Table 5.8

Table 5.8 Measured velocities, density and calculated velocities, density of core saturated at estimated reservoir effective pressure (27.25 MPa).

Core depth (m)	Vp_{log} (m/s)	Vs_{log} (m/s)	Rho_{log} (g/cm_3)	Vp_{core} (m/s)	Vs_{core} (m/s)	Rho_{core} (g/cm_3)
2055.0	3414.617	2372.367	2.295	3585.500	2410.100	2.300
2057.0	3627.906	2494.784	2.334	3638.100	2116.600	2.327
2071.5	3567.453	2248.904	2.329	3559.500	2211.800	2.290

The order of magnitude of P-wave velocities are in between 0.2 – 5 % which is 8 – 30 m/s, respectively. However, the orders of magnitude of S-wave velocities are in between 1.6 – 15 % which is 40 - 380 m/s due to the difficulty in S-wave velocity measurements for both core and log data. For the density, it ranges between 0.22 – 1.65 % which is 0.005 – 0.03 g/cm3. The differences between calculated and measurements properties are acceptable, thus the results could be used for fluid substitution.

5.5 Gassmann's fluid substitution

The Gassmann fluid substitution requires several input parameters to calculate fluid effects on seismic velocities for K_{sat}. For that purpose we need dry frame bulk and shear moduli, porosity, grain density and fluid bulk modulus that could be obtained from laboratory measurement or estimated from well logs or empirical relations. However, grain bulk (K_{grain}) and shear moduli are often poorly understood and oversimplified by using mono mineral assumption (Batzle and Wang, 1992; Wang, 2001). In practice, K_{grain} can vary depending on mineral composition, especially if

the clay mineral is present; distribution of the grains and *in-situ* conditions. As a result, the calculated velocity can in some cases significantly differ from the measured velocity when using Gassmann fluid substitution.

Here I proposed the methodology to derive K_{grain} from ultrasonic core measurements if the mineralogy composition is unknown. It is then compared to the results obtained from petrophysical analyses with known mineralogy composition. These results are then verified against the log data.

5.5.1 A methodology for derivation of mineral grain modulus (K_{grain})

The methodologies for computing bulk modulus of mineral grain (K_{grain}) using mono mineral approximation have been extensively used and well-established in the past (Hashin and Shtrikman, 1963; Katahara, 2005; Mavko et al., 1998). Despite approximation, proposed methodologies can produce good results. Recent work by Grochau and Gurevich (2008) showed that core saturated velocities agreed very well with log measurements at reservoir interval when using representative K_{grain}. Siggins (2006) carried out ultrasonic core measurement in Waarre formation from Boggy Creek-1 well, which is located north-east of Naylor-1 and CRC-1 well. His result established that Gassmann's equation can predict velocities for Waarre formation for different CO_2 saturation and effective pressures provided that effective pressures are relatively high. Effective pressures must be sufficiently high so that compliant pore space is compressed and does not contribute to the bulk modulus and influence seismic wave propagation. This justified the use of ultrasonic core measurement for prediction of time-lapse seismic response at this site. Therefore all core samples from CRC-1 well have been measured ultrasonically.

Using stress-velocity relationship derived from these ultrasonic core measurements, I obtained V_{pdry} and V_{sdry} at reservoir's effective pressure, from where K_{dry} can be calculated. Using inverse Krief equation, I obtained "effective" K_{grain}. I then calculated V_p core, using Gassmann's equation with *in-situ* saturation. Once the mineral composition from petrologic analyses is known, an average K_{grain} using Hashin-Shtrikman can be computed. I obtained nearly identical values for K_{grain}

using the two approaches. Hence the computed V_p core saturated and V_p log agreed very well.

5.5.2 Computation of elastic properties

This methodology is depicted in Figure 5.13.

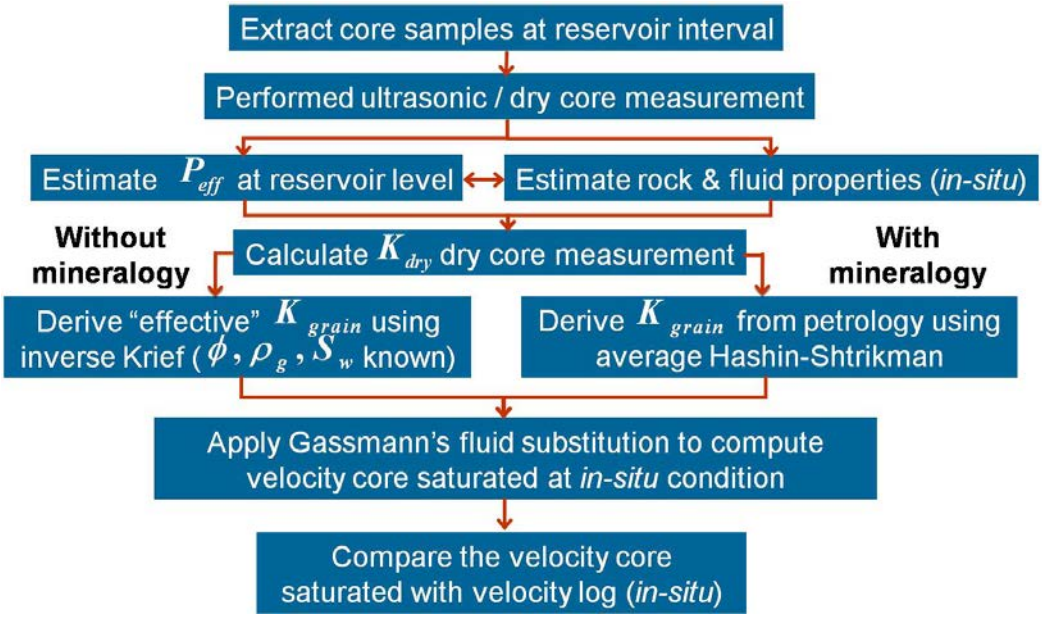

Figure 5.13 The workflow how to derive K_{grain} from core sample.

Gassmann's equation was used to calculate the effective bulk and shear modulus of saturated porous rock taken into account the dry core measurements:

$$K_{sat} = K_{dry} + \frac{\left(1 - \frac{K_{dry}}{K_{grain}}\right)^2}{\frac{\phi}{K_{fluid}} + \frac{1-\phi}{K_{grain}} - \frac{K_{dry}}{K_{grain}^2}}, \tag{5.9}$$

$$K_{dry} = \rho_{dry}(V_{pdry}^2 - 4V_{sdry}^2/3), \tag{5.10}$$

$$\mu_{dry} = V_{sdry}^2 \rho_{dry}, \tag{5.11}$$

where $K_{grain,} K_f, K_{dry}, K_{sat},$ are the bulk moduli of the mineral grain, fluid, dry rock, and saturated rock frame, respectively; and ϕ is the porosity. $V_{pdry,} V_{sdry}$ are

P- and S-wave velocities of the dry rock from core measurements, respectively. ρ_{dry} is the density of the dry rock.

Using the saturation log, I calculated bulk modulus of pore fluids, K_f using Wood's equation:

$$\frac{1}{K_f} = \frac{S_w}{K_w} + \frac{S_g}{K_g}, \tag{5.12}$$

where K_w and K_g are the bulk moduli of water and gas, respectively; S_w and S_g is stand for water and gas saturation ($S_g = (1 - S_w)$). This assumes that the fluid is uniformly distributed within pores.

Knowing the "exact" porosity and K_{dry} calculated from dry core measurement, I derived "effective" K_{grain} with the following equation (Krief et al., 1990):

$$K_{grain} = K_{dry} / (1-\phi)^{\frac{3}{(1-\phi)}} \quad . \tag{5.13}$$

The "effective" K_{grain} is then used to calculate saturated velocities from dry core measurement and bulk modulus of saturated porous rock.

To obtain K_{dry} from log measurement, I used inverse Gassmann's equation as follow:

$$K_{dry} = \frac{K_{sat}\left(\frac{\phi K_{grain}}{K_f} + 1 - \phi\right) - K_{grain}}{\frac{\phi K_{grain}}{K_f} + \frac{K_{sat}}{K_{grain}} - 1 - \phi}, \tag{5.14}$$

Then K_{sat} is:

$$K_{sat} = \rho_{sat}(V_{psat}^2 - 4V_{ssat}^2 / 3), \tag{5.15}$$

and

$$\mu_{sat} = V_{ssat}^2 \rho_{sat}, \tag{5.16}$$

where V_{psat}, V_{ssat} are P and S-wave velocity of saturated rock, respectively (log measurement); $\mu_{sat} = \mu_{dry}$ is shear modulus of saturated/dry rock frame and ρ_{sat} is the bulk density of the saturated rock.

Finally, for saturated core, the velocities are:

$$V_{p\,sat} = \sqrt{\frac{K_{sat} + \frac{4}{3}\mu_{sat}}{\rho_{sat}}} \quad \text{, and} \quad V_{s\,sat} = \sqrt{\frac{\mu_{sat}}{\rho_{sat}}} \quad . \tag{5.17}$$

As shown in Figure 5.14, the core and log based estimates of elastic properties are in agreement.

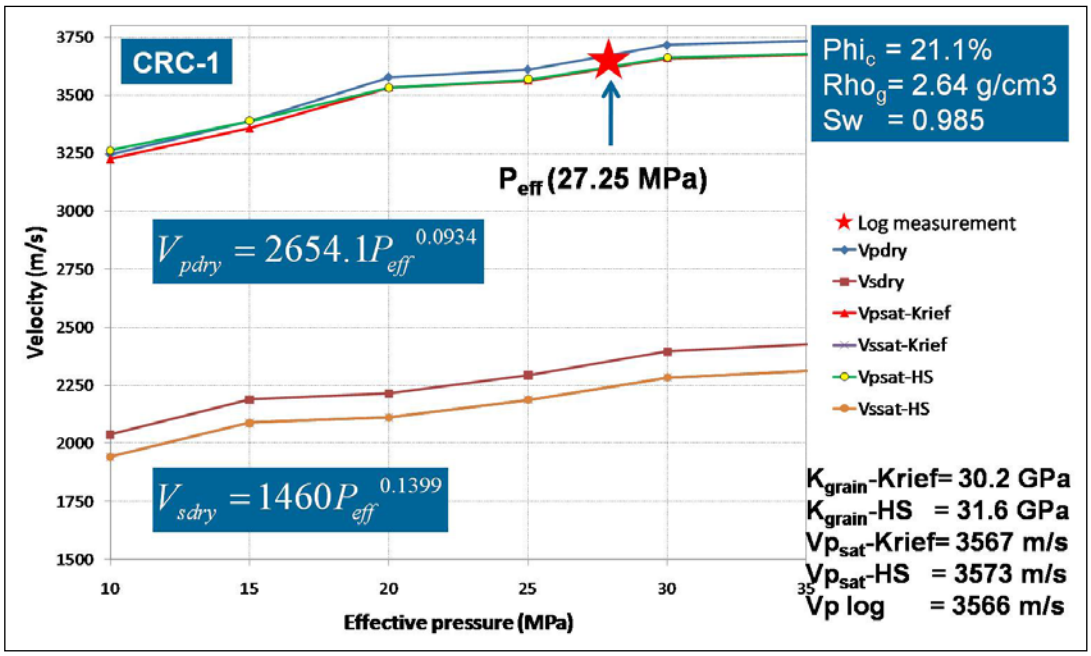

Figure 5.14 Velocity versus effective pressure. V_{pdry} and V_{sdry} versus effective pressure were obtained from dry core sample measurements. *In-situ* reservoir state was calculated from RFT measurements and integrated density log. The effective stress at the reservoir level (P_{eff}) in this case was 27.25 MPa. The core saturated velocities using "effective K_{grain} from Krief and Hashin-Shtrikman (HS) agree closely with V_P log.

5.5.3 Sensitivity analyses

In practice, the measurements are always made with some errors. The problem arises when the input errors to Gassmann's equations are so large that values of the calculated elastic moduli become unreliable. Of particular importance are the errors related to grain elastic moduli and sometimes frame bulk and shear moduli. To gain insight into the effect of measurement errors onto the computation of elastic properties for this area I performed sensitivity analysis. For that purpose I calculated a difference in the elastic properties under *in-situ* reservoir condition with respect to 10% changes in input parameters using the equation:

$$\%change = \frac{\pm 0.1 \cdot (input) - input}{input} \times 100 . \qquad (5.18)$$

Only one input parameter was allowed to change at a time. The input parameters are: water saturation = 98.31%, porosity = 21.1%, grain density = 2.641 g/cm3, grain bulk modulus = 30.2302 GPa, frame bulk modulus = 12.2772 GPa, frame shear modulus = 11.2033 GPa, fluid bulk modulus = 1.1517 GPa, and fluid density = 0.977669 g/cm3. The post injection water saturation is 20%, the rest of input parameters remain the same. Once the input parameters that are more sensitive are established I will use them to constraint the measurement and then apply fluid substitution.

Table 5.9 and Figure 5.15 show the changes in percentage of the calculated *Vp*, *Vs*, *Vp/Vs*, P- and S-wave impedance as the input parameters are varied for ± 10%. For example, as the *in-situ* input porosity to the Gassmann's equation increases by 10% while other parameters are fixed, the error calculated *Vp* increases by 0.52% which is 18.4 m/s, *Vs* increases by 0.78% which is 17.15 m/s, *Vp/Vs* decreases by -0.26%, P- and S-wave impedance decreases by 1.02% and 0.77%. Both tables show that the error calculated *Vp*, *Vs*, P- and S-wave impedance are most sensitive to uncertainties in the input grain density, and will result in *Vp* changes of -151.67 – 173.91 m/s, respectively, the error calculated *Vp*, *Vs*, *Vp/Vs*, P-and S-wave impedance are sensitive to uncertainties in the input frame shear and bulk moduli.

Practically, the input grain density is unlikely to have a 10% uncertainty but such a magnitude of uncertainty in the input frame shear modulus may not be uncommon, due to difficulty in picking shear wave velocity. To reduce the error (by reducing uncertainty), the core grain density is measured then saturated with *in-situ* condition and calibrated with logs. The results show that core measurements agree with logs data. Certain measurement errors do not propagate with any significance into the computation of *Vp* and density. However grain density and frame shear are important to be correctly estimated. As an input grain density error can significantly affect the final result, the core grain density is measured, and saturated with Gassmann's equations at *in-situ* conditions.

Table 5.9 Sensitivity analysis calculated table.

Pre-injection (*in-situ)*

INPUT		OUTPUT									
Parameter	% change	Vp change (%)		Vs change (%)		Vp/Vs change (%)		P-imp change (%)		S-imp change (%)	
		-	+	-	+	-	+	-	+	-	+
Porosity (Ø)	-10, +10	-0.45	0.52	-0.76	0.78	0.31	-0.26	1.07	-1.02	0.76	-0.77
Grain density (ρ_m)	-10, +10	4.89	-4.26	4.89	-4.26	0.00	0.00	-4.66	4.45	-4.66	4.45
Grain bulk modulus (K_m)	-10, +10	-0.45	0.40	0.00	0.00	-0.45	0.40	-0.45	0.40	0.00	0.00
Frame bulk modulus (K_d)	-10, +10	-1.72	1.71	0.00	0.00	-1.72	1.71	-1.72	1.71	0.00	0.00
Frame share modulus (G_d)	-10, +10	-2.61	2.54	-5.13	4.88	2.66	-2.23	-2.61	2.54	-5.13	4.88
Fluid bulk modulus (K_f)	-10, +10	-0.29	0.29	0.00	0.00	-0.29	0.29	-0.29	0.29	0.00	0.00
Fluid density (ρ_f)	-10, +10	0.45	-0.45	0.45	-0.45	0.00	0.00	-0.45	0.45	-0.45	0.45

Post-injection (*prediction*)

INPUT		OUTPUT									
Parameter	% change	Vp change (%)		Vs change (%)		Vp/Vs change (%)		P-imp change (%)		S-imp change (%)	
		-	+	-	+	-	+	-	+	-	+
Porosity (Ø)	-10, +10	-0.95	0.99	-1.01	1.04	0.05	-0.04	1.07	-1.07	1.02	-1.03
Grain density (ρ_m)	-10, +10	5.12	-4.44	5.12	-4.44	0.00	0.00	-4.87	4.64	-4.87	4.64
Grain bulk modulus (K_m)	-10, +10	-0.07	0.06	0.00	0.00	-0.07	0.06	-0.07	0.06	0.00	0.00
Frame bulk modulus (K_d)	-10, +10	-2.19	2.15	0.00	0.00	-2.19	2.15	-2.19	2.15	0.00	0.00
Frame share modulus (G_d)	-10, +10	-2.76	2.68	-5.13	4.88	2.51	-2.10	-2.76	2.68	-5.13	4.88
Fluid bulk modulus (K_f)	-10, +10	-0.05	0.05	0.00	0.00	-0.05	0.05	-0.05	0.05	0.00	0.00
Fluid density (ρ_f)	-10, +10	0.25	-0.25	0.25	-0.25	0.00	0.00	-0.25	0.25	-0.25	0.25

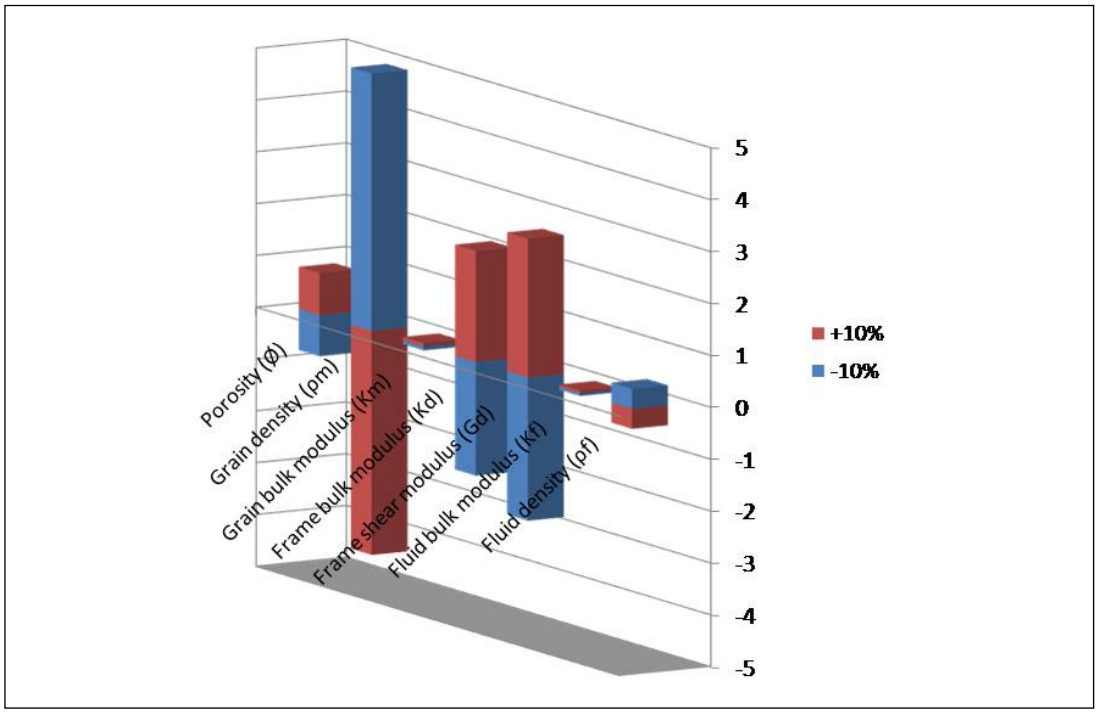

Figure 5.15 The effect of 10% variation in elastic properties on saturated P-wave velocities. The vertical axis is a percent change.

I also calculated the difference in the V*p* under *in-situ* reservoir condition with respect to variations in "effective" K_{grain} from other empirical models as shown in Figure 5.16. Density of mineral composition used is described in Table 5.10.

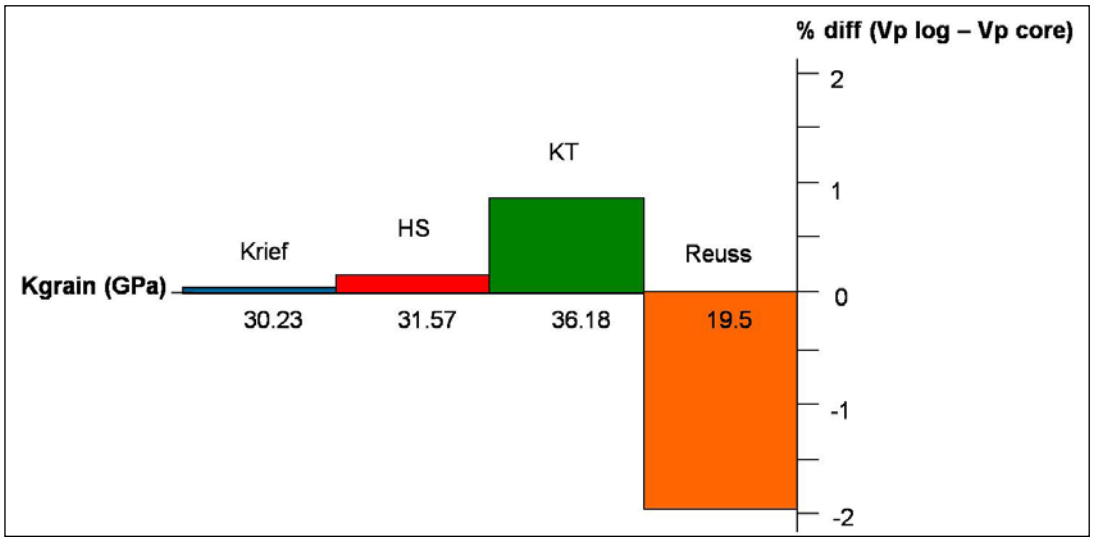

Figure 5.16 The effect of variations in K_{grain} (HS is Hashin-Shtrikman, KT is Kuster-Toksoz). The "effective" K_{grain} calculated from Krief and Hashin-Shtrikman is very close and resulted smallest difference in velocities.

Table 5.10 Modulus and density of minerals (Mavko et al., 1998; Wang and Nur, 2000).

Mineral	Kg	Gg	Rhog
Quartz	37.00	44.00	2.65
Orthoclase	48.00	24.00	2.56
Kaolinite	1.50	1.40	1.58
Illite/Mica	61.50	41.10	2.79
Pyrite	147.00	133.00	4.93
Calcite	76.80	32.00	2.71

I calculated the difference in the elastic properties under *in-situ* reservoir condition with respect to 10% or more variations in "effective" K_{grain} derived from Krief, Hashin-Shtrikman, Kuster-Toksoz and Reuss. This analysis shows 10% variation in "effective" K_{grain} produces small effect on velocity difference between *Vp* core saturated and *Vp* log, with the K_{grain} computed with Krief equation. Estimating the "effective" K_{grain} accurately will minimize fluid substitution modelling errors.

5.5.4 Comparative analyses

In the further analysis I compared the "expected" mineralogy derived from effective K_{grain} with petrographic analyses that was available. The CRC-1 well composite log shows gamma ray, clay volume, porosity and permeability in Figure 5.17. The Waarre-C consists of 4 main facies. Tidal fluvial facies with good porosity and permeability are found at the deepest part. This is followed by gravel dominated facies with poor to moderate porosity and permeability. The upper part of the Waarre-C formation where the injection taken place consists of amalgamated channels and transgressive sand facies with good porosity and permeability. Mineralogy is dominated by quartz with autogenic kaolinite as a pore-filling mineral (cement). The expected mineralogy derived from "effective" K_{grain} and petrographic analyses are very close further confirming a model of "soft" K_{grain} (K_{grain} computed with Krief equation is 30.23 GPa). Figure 5.18 depicts a relationship between K_{grain} and petrology. The softer the rock frame, the bigger the elastic properties changes. This is a first-order requirement for successful time-lapse seismic monitoring (Wang, 1997).

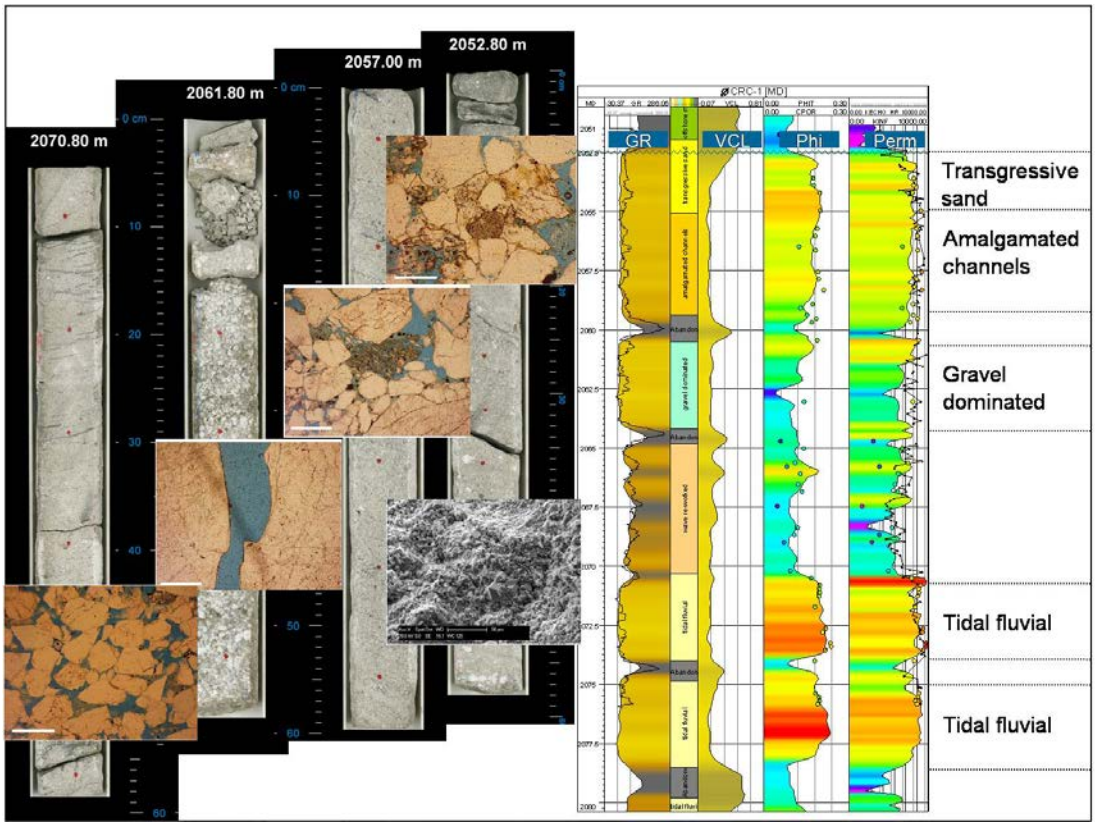

Figure 5.17 Composite logs within the reservoir and representative of the core samples and thin section at different depths based on facies interpretation.

Waarre-C reservoir is a good quality reservoir as it has less than 10% clay content with good porosity (around 20%) and high permeability (>1D). XRD mineralogy suggests the presence of quartz is dominant as a mineral grain, followed by kaolinite, illite/mica, pyrite, and minor calcite. Thin section microscopy and SEM shows abundant autogenic kaolinite cement that coated quartz grains and partially in-filled the pore space. The presence of authigenic kaolinite as mineral cement and pore-filling is fairly common throughout the reservoir. Sedimentary regimes are inferred from thin section microscopy (Dance and Vakarelov, 2007; Schacht, 2008). The interpreted sand facies could be classified as follows:

1. Transgressive sand - Sand A1
2. Amalgamated channels - Sand A2
3. Gravel dominated - Sand B
4. Tidal fluvial - Sand C and D

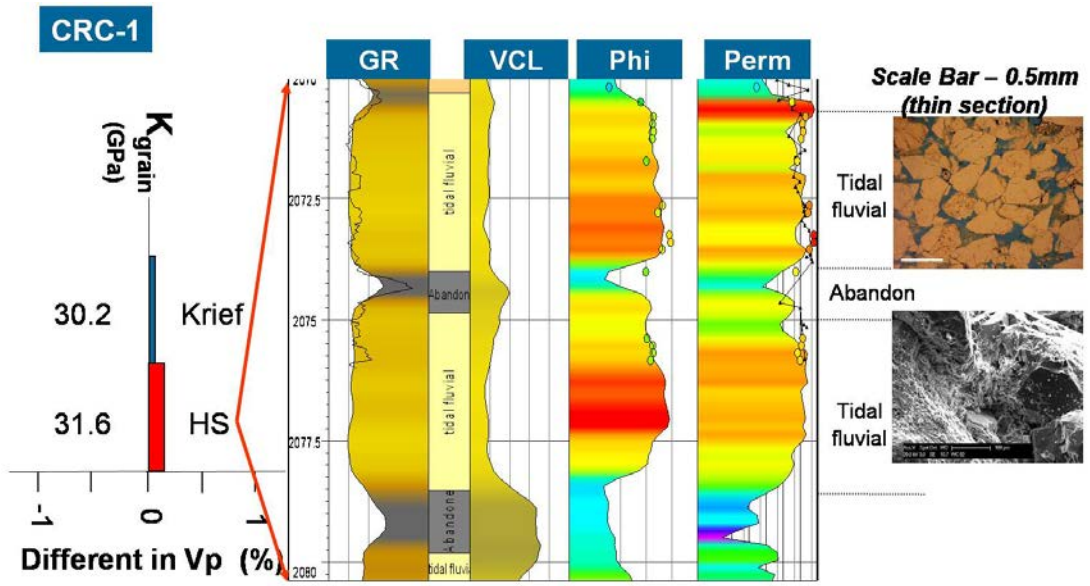

Figure 5.18 Kgrain and Petrology relationship (Dance and Vakarelov, 2007; Schacht, 2008).

Between facies, there are abandoned channels. The X-ray diffraction bulk mineralogy of core samples at different depths is shown below in Table 5.11 (Schacht, 2008).

Table 5.11 The summary of XRD bulk mineralogy of CRC-1 well core samples at several depths.

Depth (m)	Plug No.	Quartz	Ortho-clase	Kaolinite	Illite/Mica	Pyrite	Calcite
2053.65	128	90	2.8	5.8	0	1.6	0
2053.90	127	91	2.9	4.3	0.3	1.1	0
2055.75	123	88	5.0	5.6	0.7	0.3	0.2
2058.55	118	89	5.7	4.4	0.6	0.3	0
2060.45	115	91	4.2	3.5	0.2	1.0	0
2060.95	114	94	2.7	2.0	0.2	0.7	0
2072.60	94	91	4.5	3.9	0.7	0.1	0

Using the mineralogy composition of Table 5.11, I calculated grain moduli using Hashin-Shtrikman average and obtained similar result to "effective" K_{grain} derived from Krief equation (Figure 5.18). This confirmed that a "soft effective" K_{grain} derived from Krief equation can be used when mineral composition is not available. Therefore I proved that for Naylor field, I can use Krief-based "effective" K_{grain} for fluid substitution process.

Finally, bulk and shear mineral grain moduli derived using inverse Krief's equations are shown in Table 5.12. They also match well with log data.

Table 5.12 The bulk and shear moduli of mineral grains.

Depth (m)	Kg	Gg
2055.0	25.3775	29.6475
2057.0	34.5985	21.7819
2071.5	30.2302	27.5859

5.6 Fluid Substitution Model (FSM) Simulator

CO_2 sequestration process will cause change of pore fluid in the short term and change of the minerals composition in the long term (Robertsson and Chapman, 2000). The change will affect seismic response depending on the type of geological storage, reservoir *in-situ* conditions such as depth, pressure, temperature, and saturation (Robertsson and Chapman, 2000; Robertsson et al., 2000). Li et al. (2006) developed a numerical modelling simulator (Fluid Substitution Methodology – FSM simulator) to predict seismic response of CO_2 injection. The main objective of the simulator was to be used to help the design of CO_2 monitoring and storage program. An assessment of seismic response to CO_2 storage process over time needs to be examined at an early stage, certainly before the baseline surveys. The application incorporates many aspects of rock physics, such as estimation of fluid properties under reservoir conditions, estimation of elastic properties of porous rocks and corresponding seismic response changes to different fluid types and their contents, and seismic response changes caused by CO_2 injection into a porous rock. Then later it can be used to assess the changes in seismic response due to pore fluid, pressure, temperature, mineral composition and saturation changes after CO_2 injection.

I used FSM to estimate the fluid properties and calculate the elastic properties of different pore fluids saturation at various stages for CO_2 monitoring and storage program. The fluid substitution was done for sand interval only.

5.7 The link between rock physics properties and sedimentary microstructure

Rock physics models allow us to understand wave propagation in porous media and in that way provides a link between seismic response and lithology. This is used to tackle various ambiguities. For example, to predict seismic velocity of a rock, by knowing only the porosity, the mineralogy composition, and the elastic properties of constituents, we can at best predict the upper and lower bounds of seismic velocities. However if we know rock physics properties of the reservoir rock, how the grains and pores are arranged relative to each other, we can very precisely predict the changes in seismic response and at the same time be able to say something about the heterogeneity of the reservoir rock.

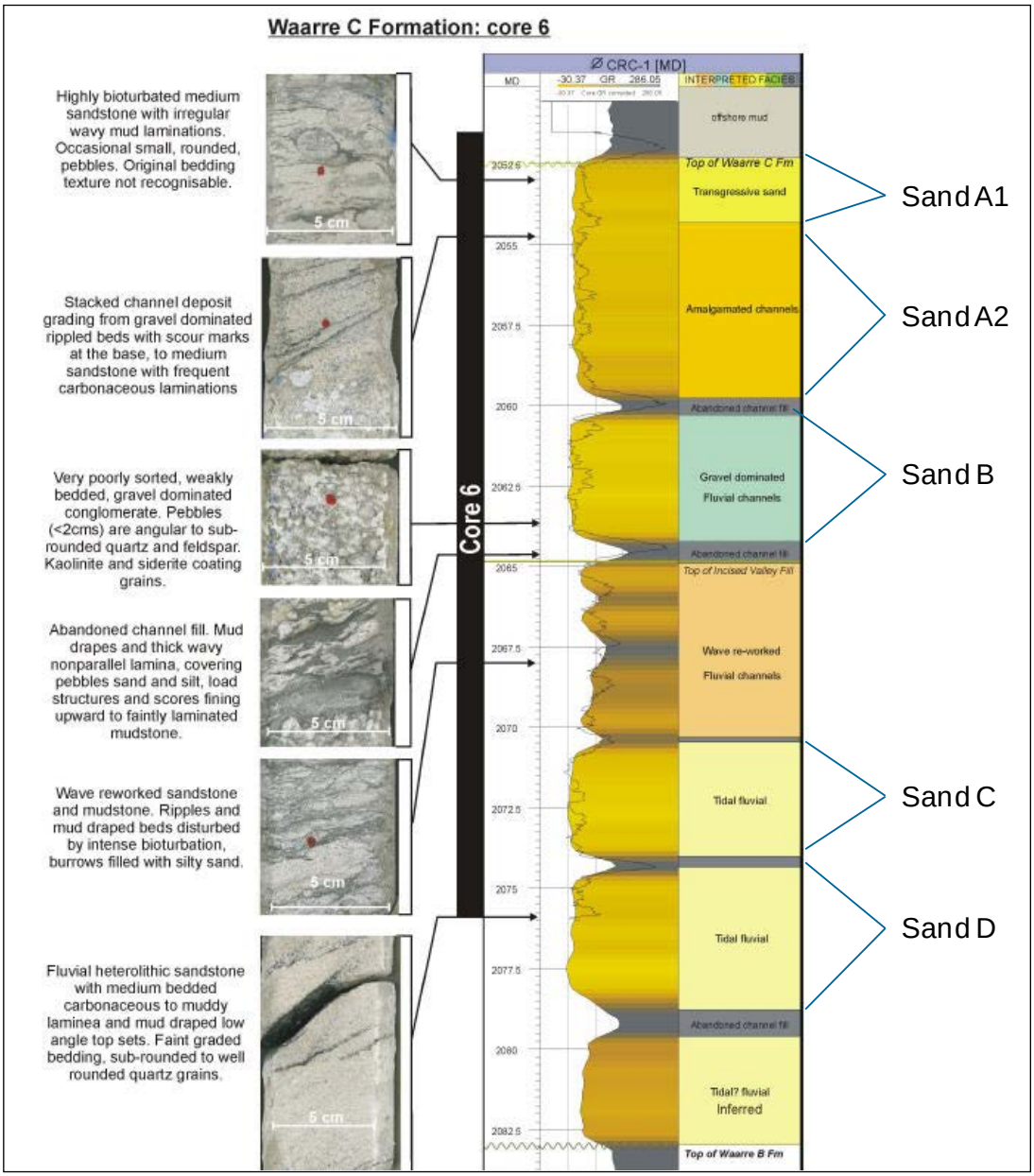

Figure 5.19 Waarre-C facies interpretation. Sand A1 is transgressive sands, Sand A2 is amalgamated sands, Sand B is gravel dominated; Sand C and D are tidal fluvial. The heterogeneity of the reservoir is reflected by different texture of sands from different depositional events. Similarly, amalgamated sands yield internal stratigraphy within sandy intervals modified from Dance and Vakarelov (2007).

The Waarre-C facies interpretation from CRC-1 well (Figure 5.19) shows different depositional environment from the one found in Naylor -1 well. Consequently there

are differences in the elastic properties of the reservoir rock at these two wells as discussed in the next chapter.

5.7.1 Rock physics properties of Waarre-C sandstones

5.7.1.1 Reservoir properties at Naylor-1 well

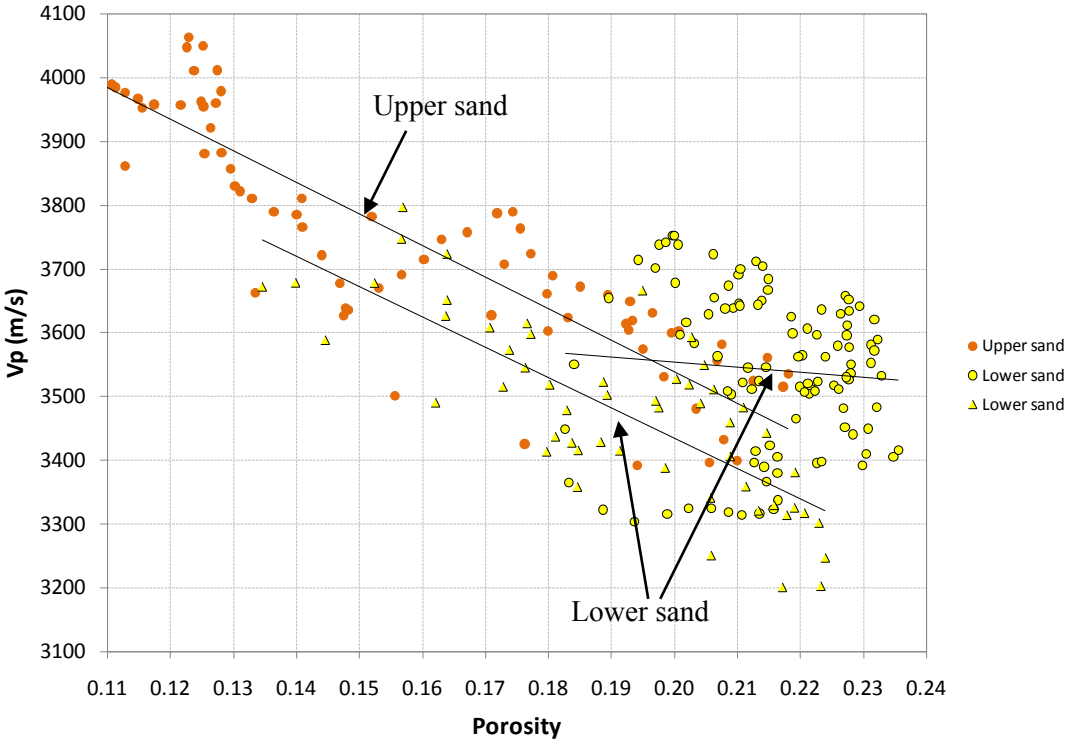

Figure 5.20 P-wave velocity versus porosity. A separation between the upper and lower sands is visible but with poorly defined zoning. The lower sands suggest two different types of sands may occur. A variation in porosity is less organised. It is possible caused by variation in clay content, sorting trends and cementation.

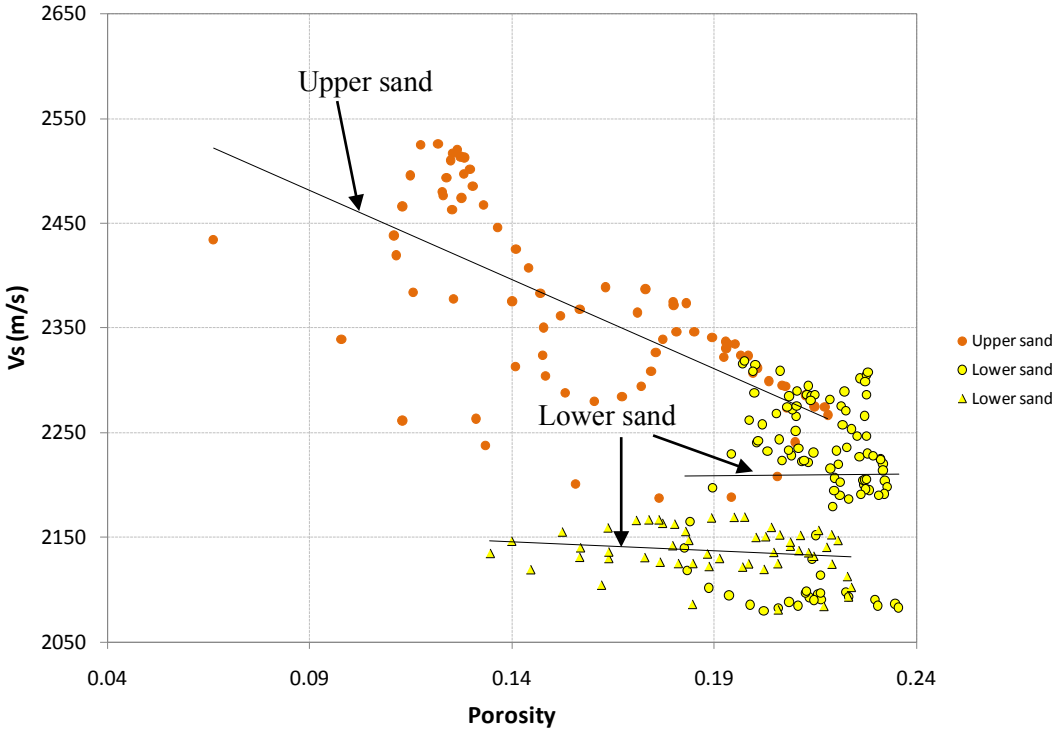

Figure 5.21 S-wave velocity versus porosity. A clear separation exists between the upper and lower sands, forming 2 distinct zones. The lower sands separations confirm there are two different sands types exist in the Waarre-C formation at Naylor-1 well. It may suggest different depositional environments.

The elastic parameters of the reservoir at Naylor-1 well vary with depth. This is cross-plotted in Figures 5.20 and 5.21 where P and S-wave velocity-porosity graphs are shown for the upper and lower sands, respectively. The upper sand is relatively stiff when compared to the lower sand. It is characterized by an increasing velocity trend as porosity decreases. This may be related to increased cementation and/or greater volume of clay. The lower sand is characterised by generally lower velocities that may be related to poor cementation. The velocity-porosity trend is nearly flat suggesting that the reduction in porosity is probably related to increasing clay content. The relationships between P and S-wave velocities versus porosity show enough complexity to grant further investigations. However a certain separation between the two sands do exists. Wide trend exists in V_P and V_S relations suggest variation in fluid saturation throughout the reservoir as shown in Figure 5.22. A cross-plot between acoustic impedance and Vp/Vs ratio shows two distinct regions encompassing upper and lower sands (Figure 5.23). This suggests that seismic acoustic inversion could be used to track lithology changes across the reservoir.

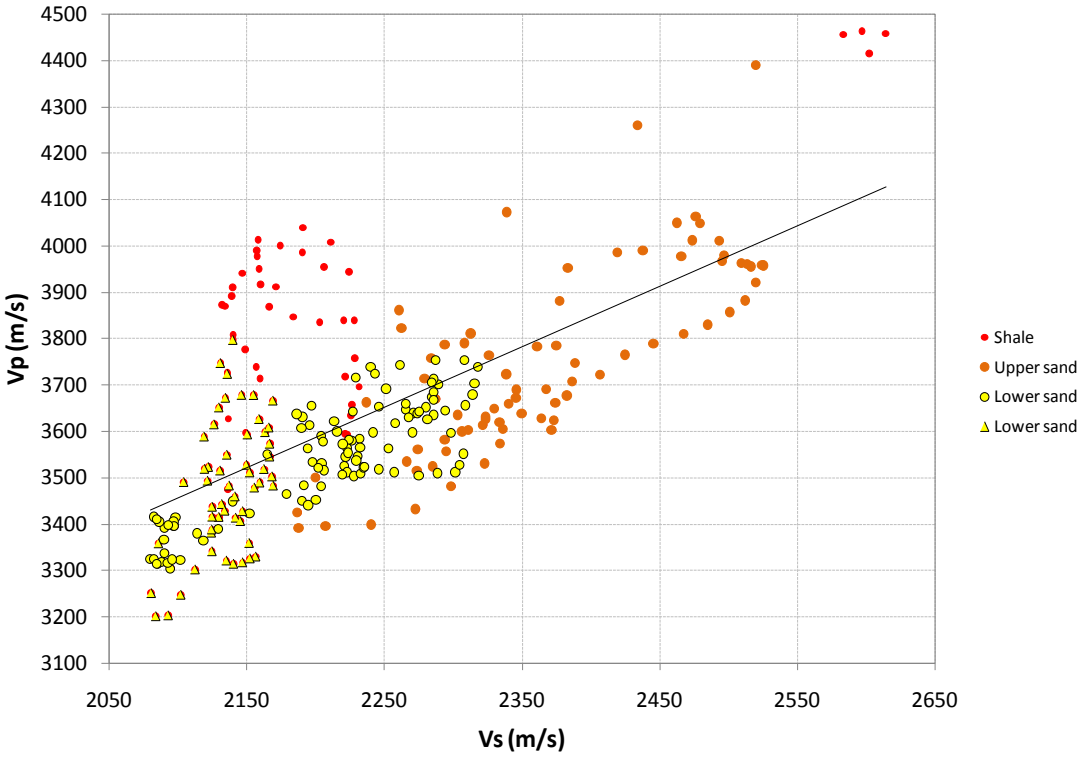

Figure 5.22 Plot of V_P versus V_S from Naylor-1 well pre-production data suggests different level of saturation most likely exist.

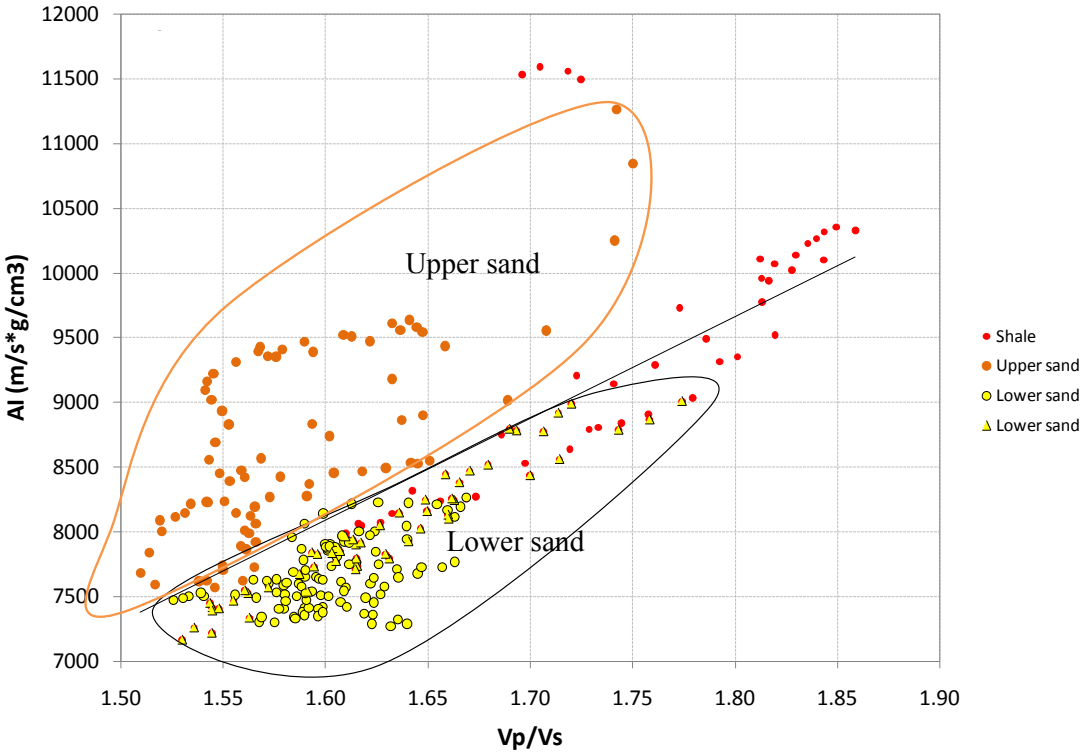

Figure 5.23 A clear separation between upper and lower sands is achieved when cross-plotting AI versus V_P/V_S. Therefore, seismic acoustic inversion can be used to help lithology identification and to map heterogeneities across the reservoir.

A time-lapse cross-plot of acoustic versus shear impedance for the lower sand is shown in Figures 5.24. For simplicity fluid substitution is not applied in upper sand. There seems to be negligible separation in this plot between three cases: pre-CH_4 production, pre-CO_2 injection and post-CO_2 injection. In Figure 5.25, the equivalent time-lapse cross-plot is shown for AI versus V_P/V_S ratio. A clear separation is seen between shale, upper sand and lower sands. Pre-production, pre and post-injection lower sands data fall all in the same region, along the same trend. Thus, CO_2 related changes of elastic properties can be expected to be fairly small. The separation between overlain shales and upper sand with lower sand is still clear suggesting again that seismic may be useful in mapping lateral changes in lithology rather than CO_2 related effects in Waarre-C reservoir.

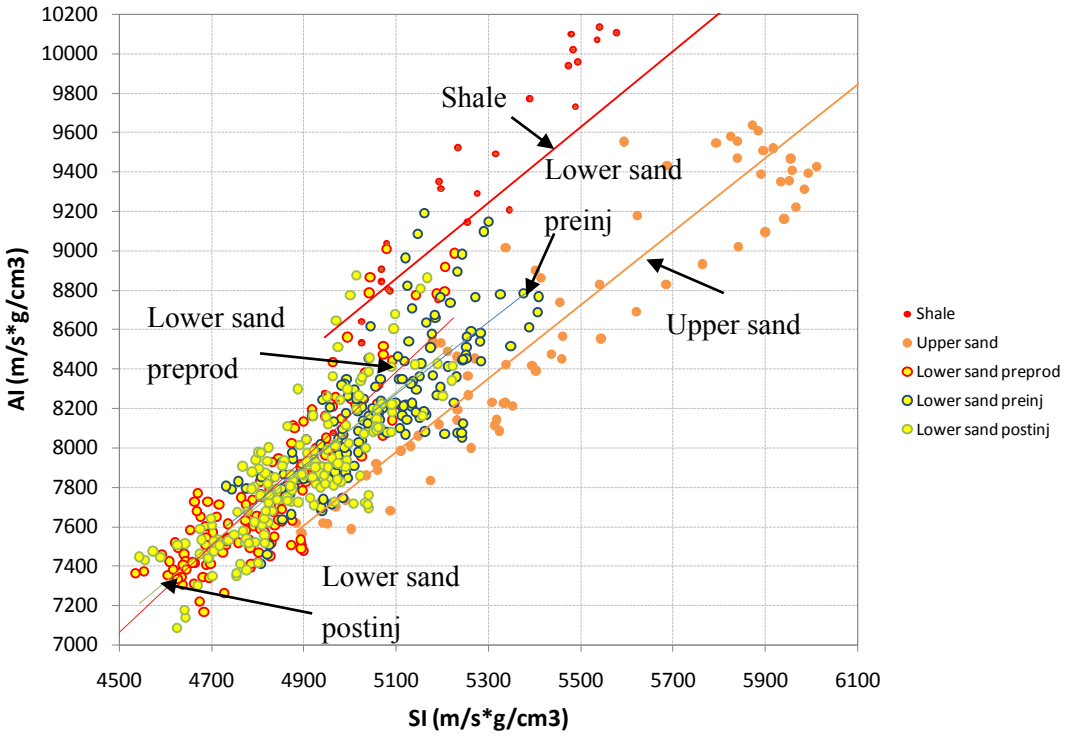

Figure 5.24 Plot of pre-production, pre- and post-injection acoustic impedance and shear impedance.

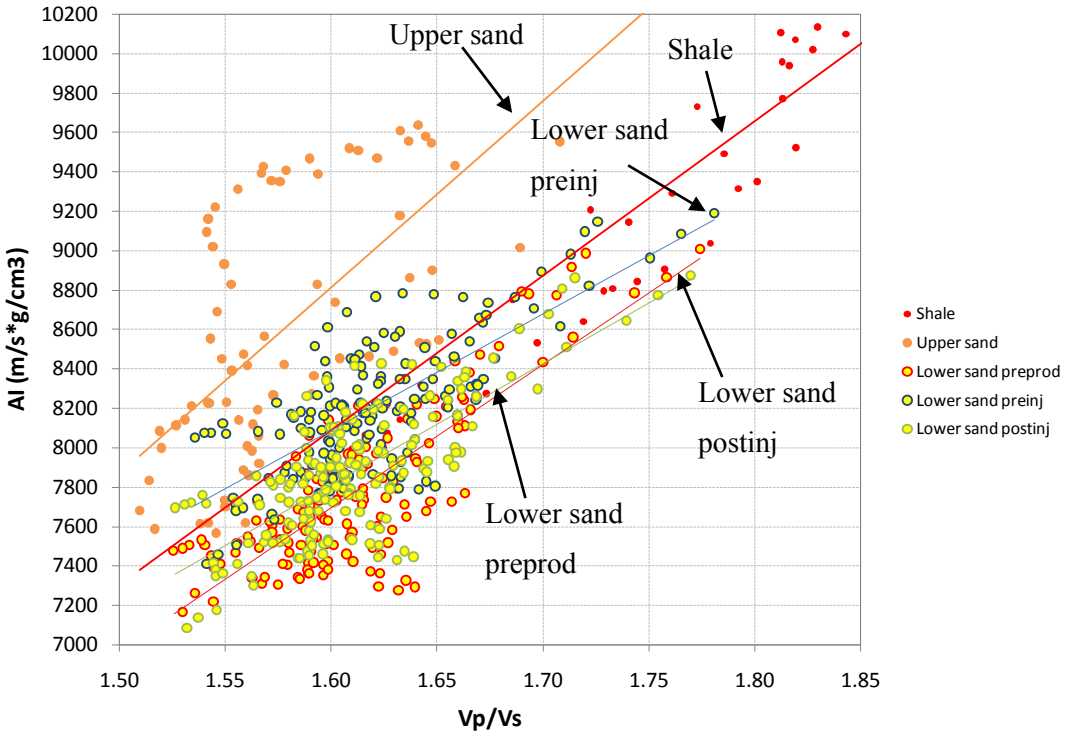

Figure 5.25 Plot of pre-production, pre- and post-injection acoustic impedance and V_P/V_S ratio.

5.7.1.2 Reservoir properties at CRC-1 well

CRC-1 well had more extensive core sampling program in comparison to Naylor-1 and also more complete and more modern logs were acquired in this well. The lithologic column is complex but reasonably well characterised. The saturation profile however is not well defined in the low saturation region where unfortunately changes of the elastic properties are the highest. This is suggested by a highly scattered velocity-porosity plot shown in Figure 5.26. *Vs* versus porosity plot shows in Figure 5.27 displays more ordered behaviour suggesting further that the variable saturation profile contributes to the data scatter in *Vp*-saturation plot. Hence a *Vp* versus *Vs* cross-plot also shows relatively clearly several clusters that can be related to certain lithologies (Figure 5.28).

The saturation plot (Figure 5.29) shows a typical insensitivity of *Vp* to saturation changes. Heterogeneity effects contribute further to data dispersion. The most interesting, from the exploration point of view, behaviour we see in Figures 5.30 and 5.31 where AI versus *Vp/Vs* ratio and AI versus SI are displayed, respectively. Quite distinct separation between various sands comprising the reservoir can be seen in these plots. Since these are the variable we can extract from seismic data it follows that both inversion and AVO reconnaissance attributes can be powerful; tools for lithology identification and rock characterisation.

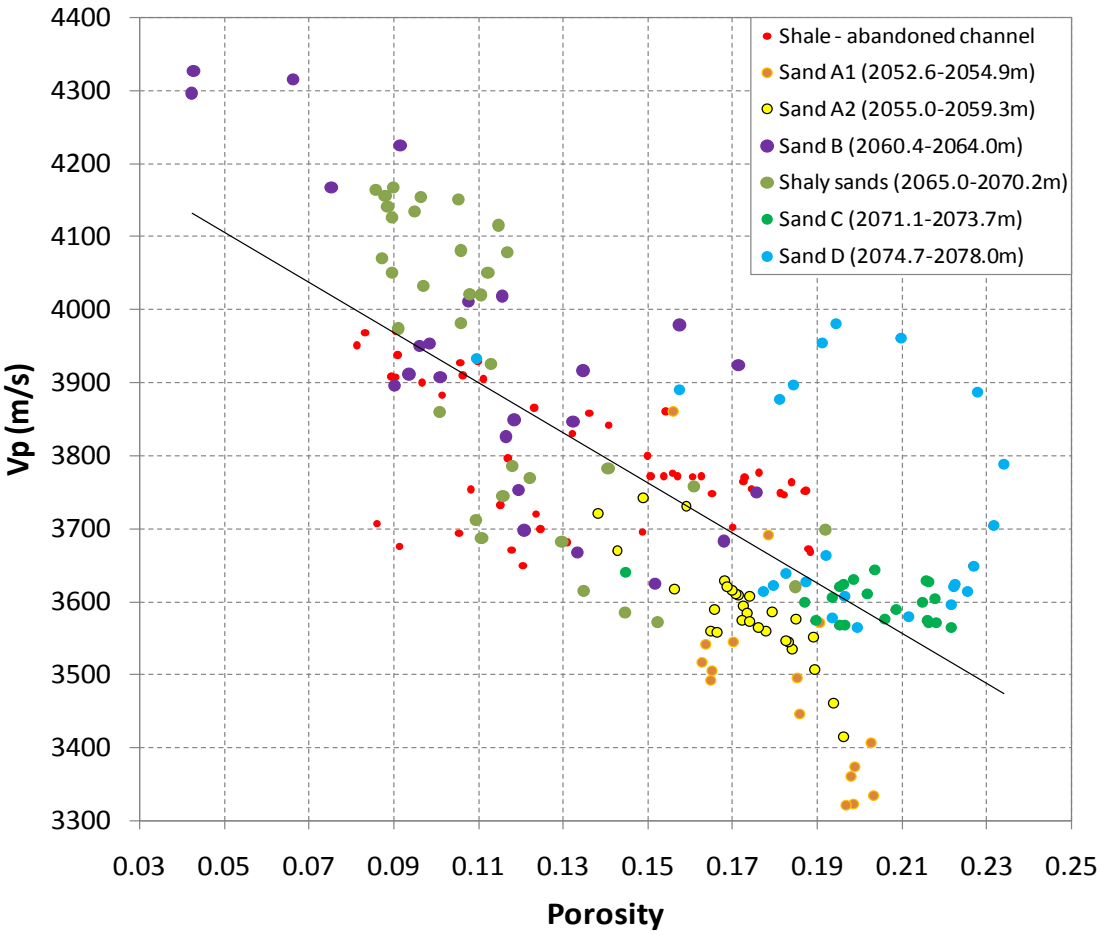

Figure 5.26 P-wave velocity versus porosity. No clear separation exists between the lithofacies

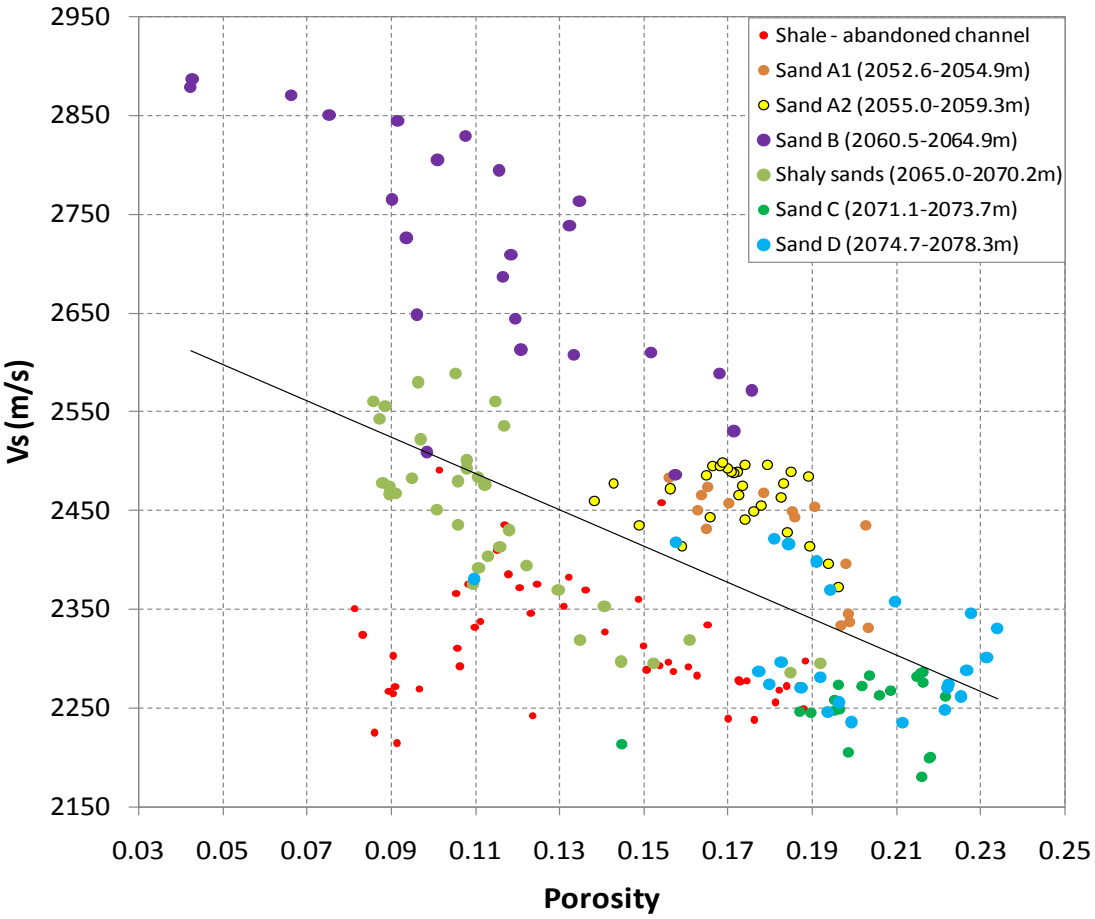

Figure 5.27 S-wave velocity versus porosity. A better lithology separation between various lithologies can be seen.

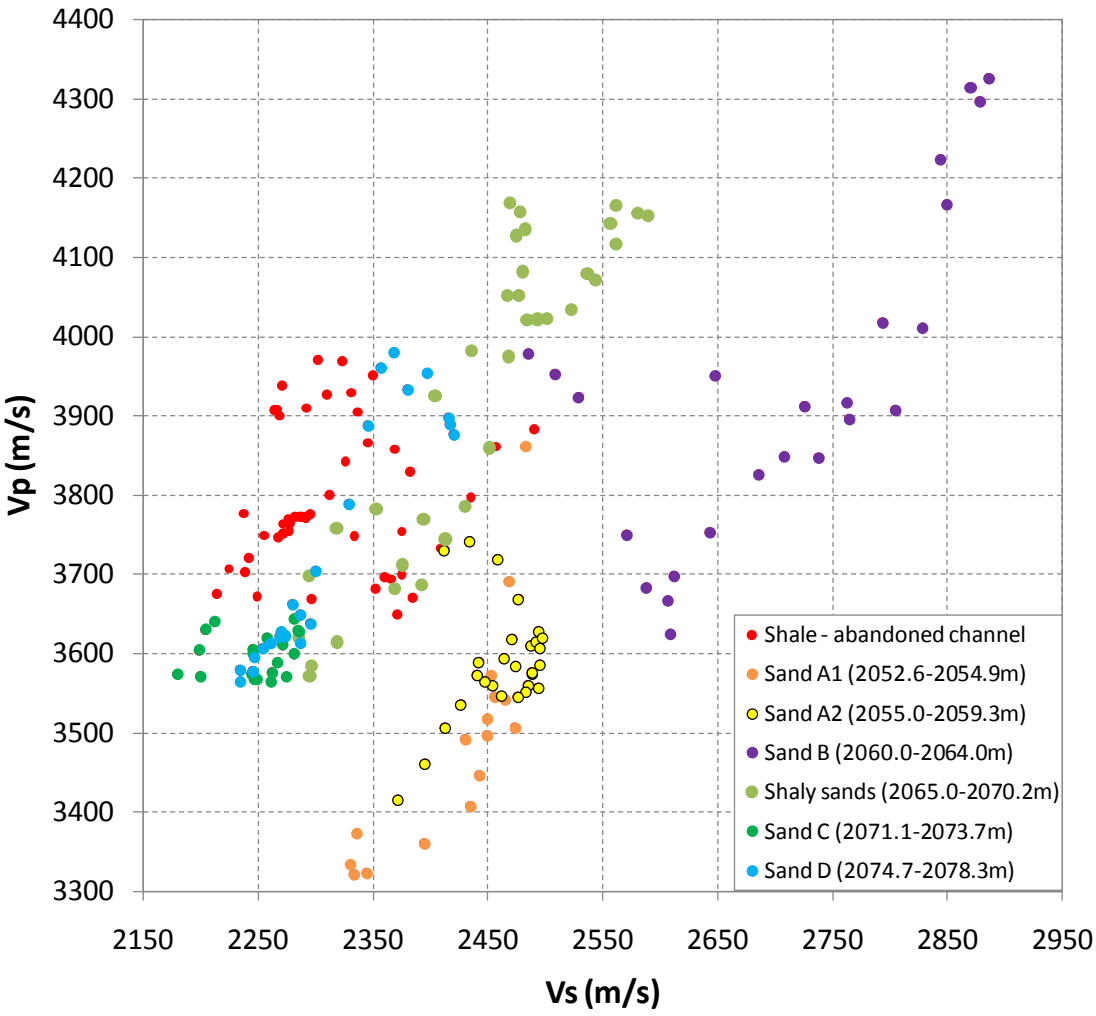

Figure 5.28 Plot of Vp versus Vs shows good lithology separation. It reflects different depositional environments and also separate shale from sand trend.

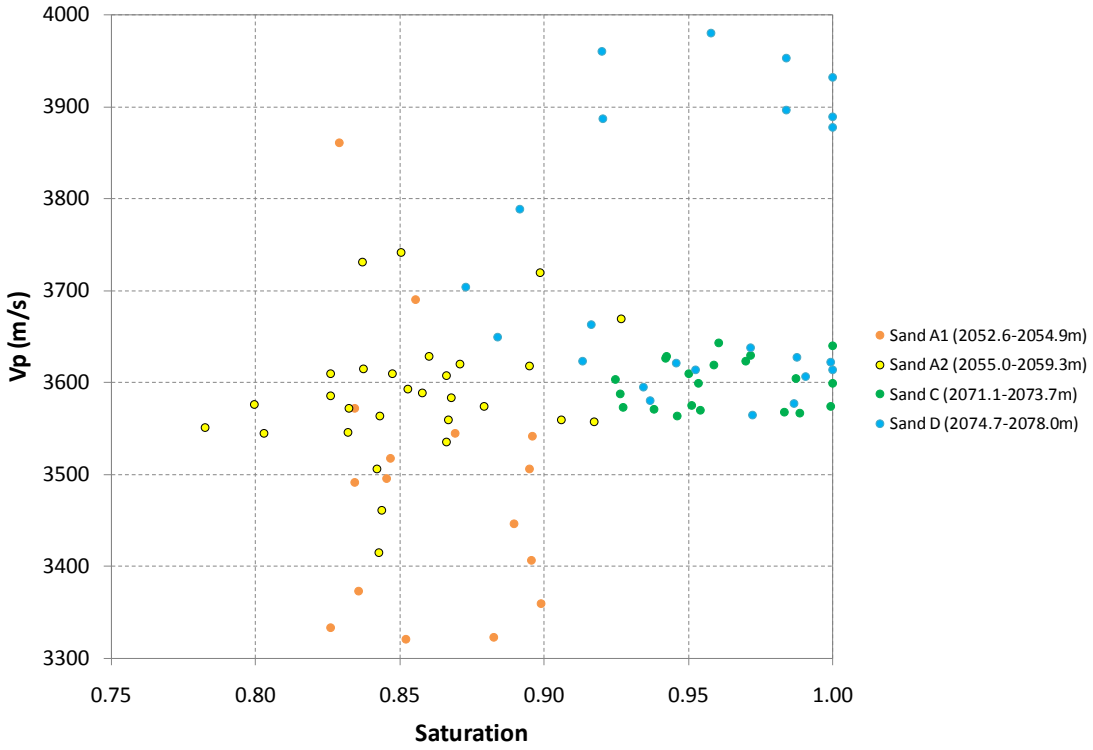

Figure 5.29 Vp versus water saturation. Sands A1 and A2 have higher gas than sand C and D. The scatter for sands A1 and A2 suggests their heterogeneity.

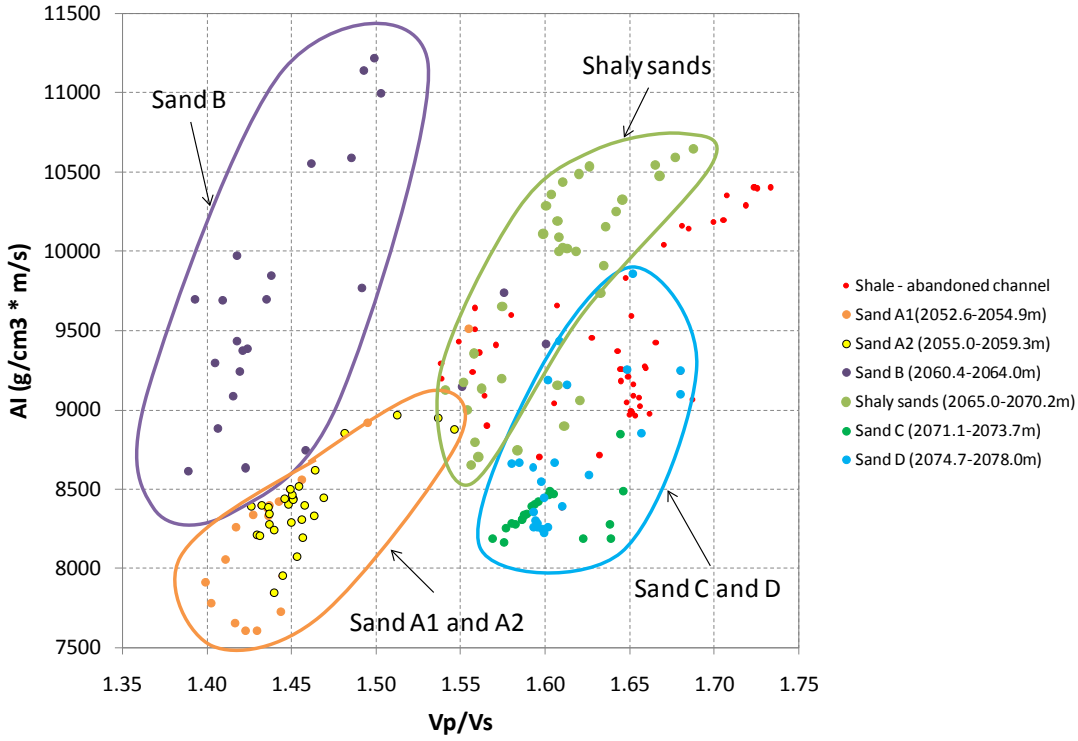

Figure 5.30 Definite zoning related to different lithologies can be mapped.

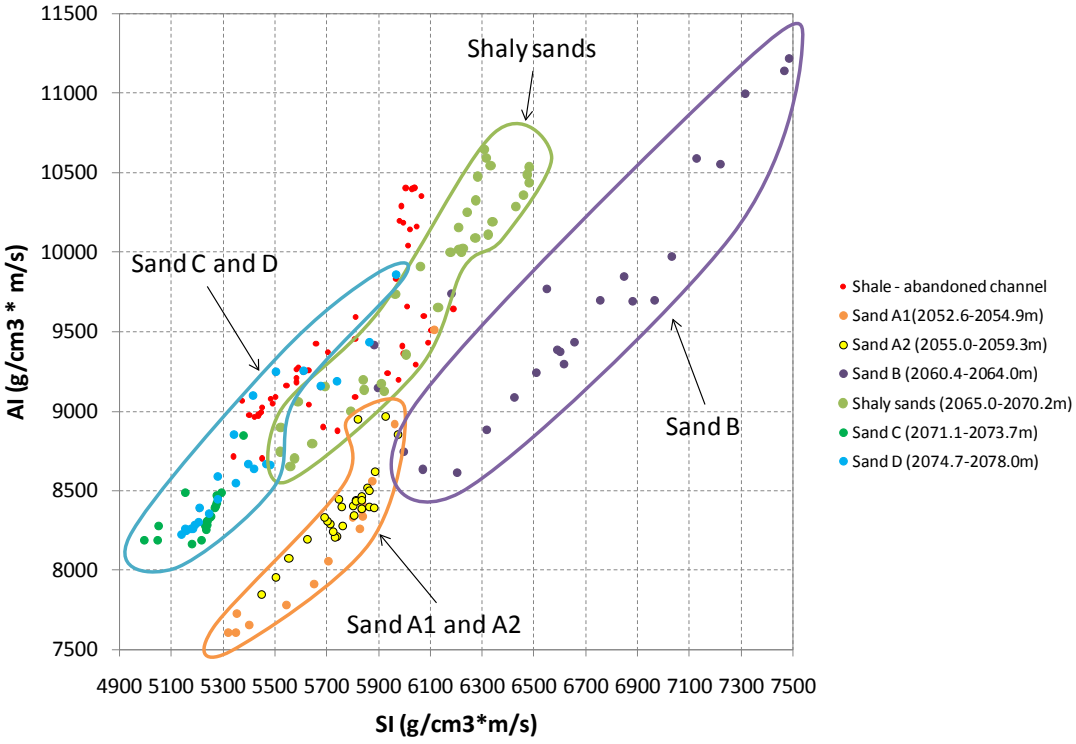

Figure 5.31 Different sands are well separated in this domain.

Well defined lithologic zonings seen in AI - *Vp/Vs* and AI/SI cross-plots does not seem to be disturbed by fluid substitution, that is before and after CO_2 injection (Figures 5.32 and 5.33).

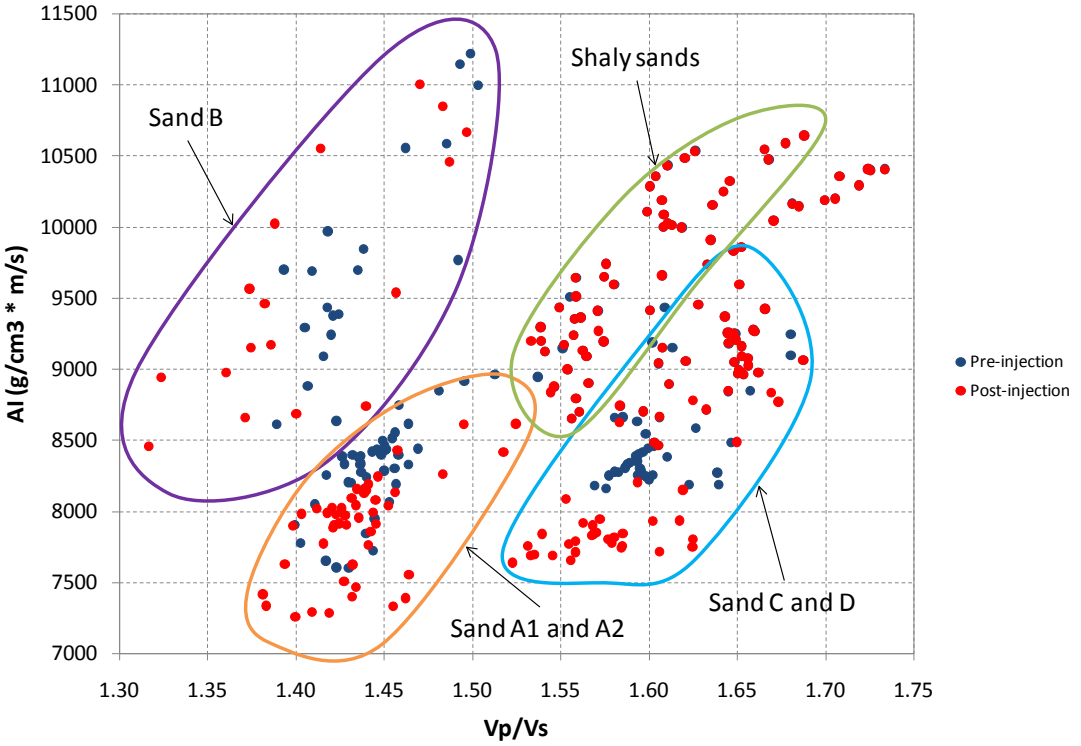

Figure 5.32 The difference in elastic parameters and zoning pattern for post and pre-injection case is negligible.

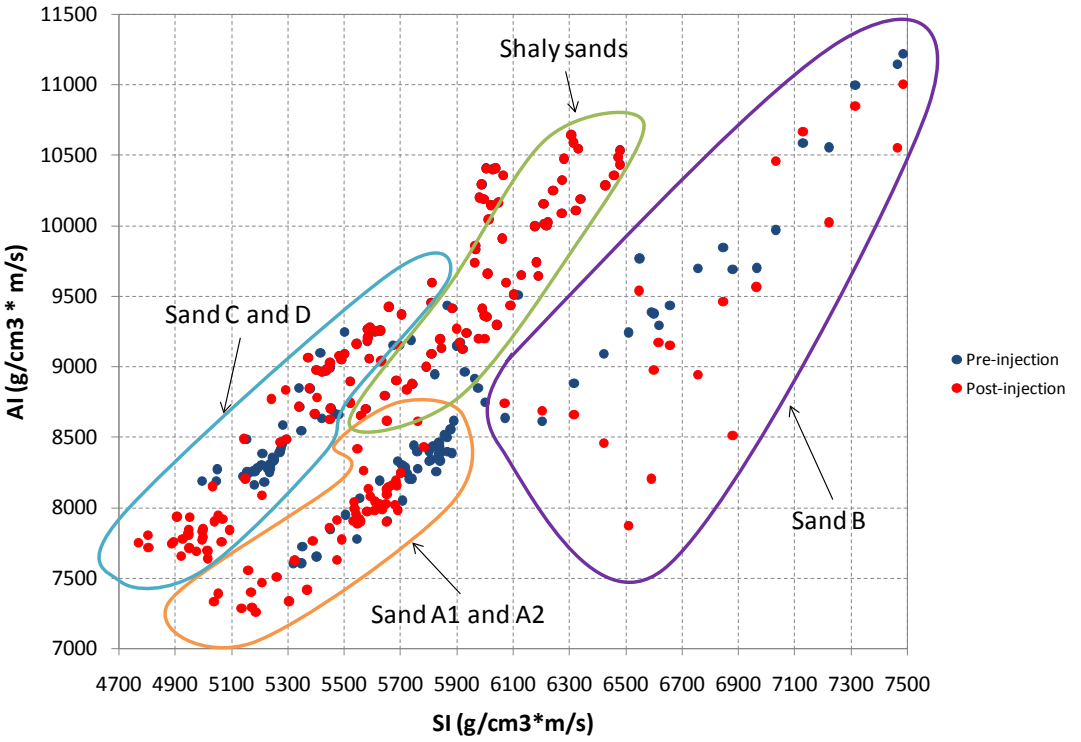

Figure 5.33 The effect of CO_2 injection on this scatter is negligible.

The last two figures suggest that the effect of CO_2 injection is not affecting the scatter which remains to be controlled by the lithologic changes. The main reason is the state of saturation (partial saturation) prior to CO_2 injection. Figure 5.32 shows soft, high porosity rocks (~20%) with good potential for detecting pressure and saturation changes during CO_2 injection. However the initial saturation falls between 75-80% which means that further changes in saturation will be very difficult to detect.

As shown in figures, I substituted the pore fluids of the clean sands zone within Waarre-C formation, which are Sand A1, A2, and C from *in-situ* water saturation (pre-injection) to predicted gas saturation (post-injection). I have estimated the best scenario zone of the CO_2 injection; however the estimated seismic effect is still quite low.

5.7.1.3 Estimation of key elastic parameters: P- and S-wave velocities and density

Modified Hashin-Shtrikman upper bounds described the diagenetic or cementation trend for sedimentary rocks while modified lower bounds relates to the sorting trend. I used log data from CRC-1 well and applied rock physics diagnostic (Dvorkin and Nur, 1996) where I quantify various sedimentologic/diagenetic factors in terms of the rock properties. The rock physics diagnostic is applied by adjusting an effective-medium derived trend to a trend observed for velocity-porosity and then interpreting the rock properties. To do so I organised data into several clusters, characteristic of various facies as shown in Figure 5.34. The sands in CRC-1 well have small initial contact cementation. The porosity decrease from the initial-cement porosity is likely to be due to deteriorating sorting (smaller grain fall in the pore space between larger grains and have a large effect on the porosity especially in the level of S and B; gravel dominated). This analysis is supported by sedimentology and petrology analyses of core samples.

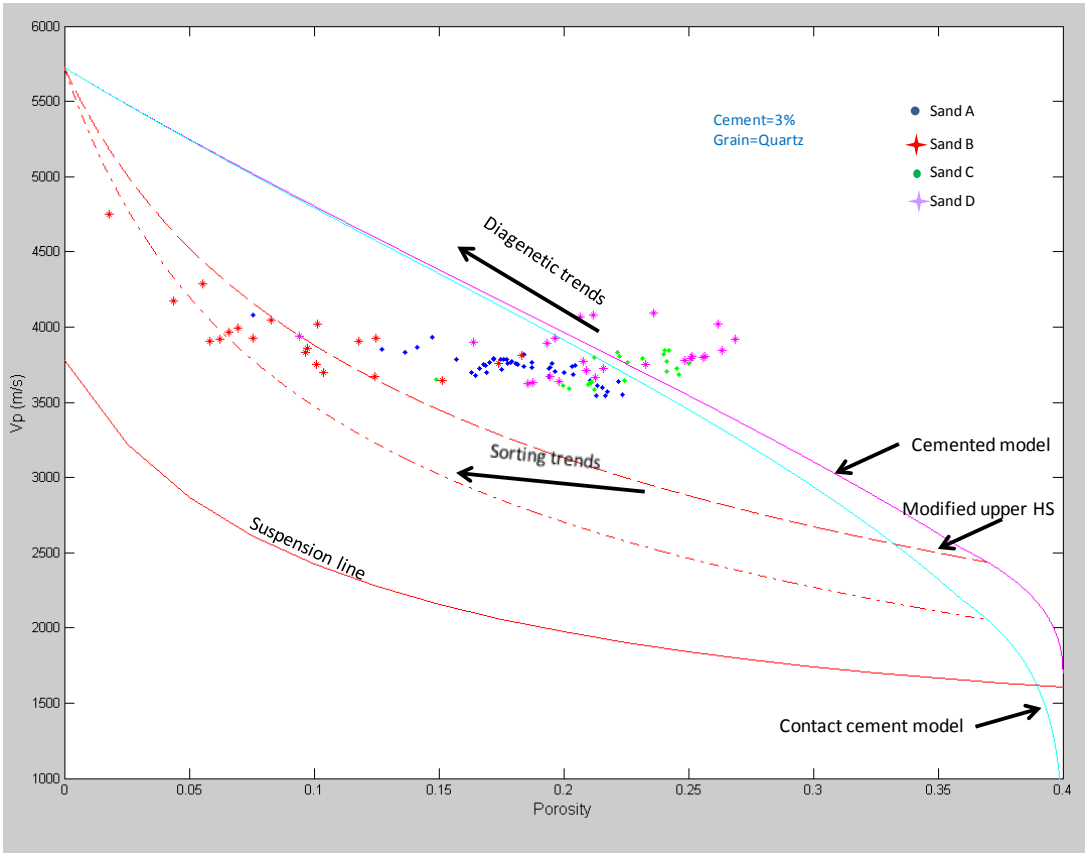

Figure 5.34 Diagenesis and sorting trends. Waarre-C formation (Sand A – A1 and A2 -, Sand B, Sand C and Sand D) shows flatter and wider distribution of porosity but not velocity. It suggests variations in clay content and sorting trends (depositional trends).

The effect of the fluid has to be also considered. One way is to cross-plot elastic (seismic) properties such as AI and Poisson's ratio. In Figures 5.35 to 36, AI versus Poisson's ratio before and after CO_2 injections are shown, respectively. A reduction in both AI and Poisson's ratio can be seen for sands C and D and to a lesser degree for sand A1 and A2 while no change for sand B. This is further supported by plot in Figure 5.37.

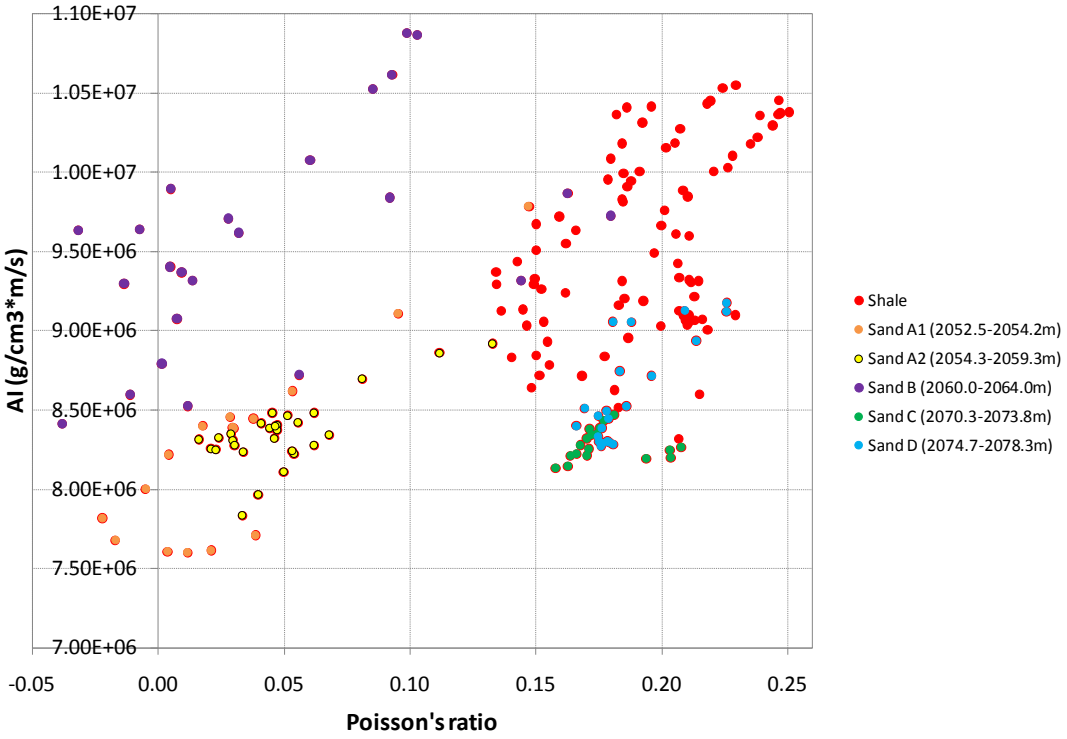

Figure 5.35 Acoustic impedance versus Poisson's ratio crossplot. Shale and water saturated sands can be used as a background trend. A clear separation is seen between the different saturated sands (Sand A1/A2, Sand B, and Sand C/D) and the shale. This suggests the moderate porosity sands exist in this reservoir therefore bigger differences are expected after injection (fluid substitution). Sand B has known having different clustering.

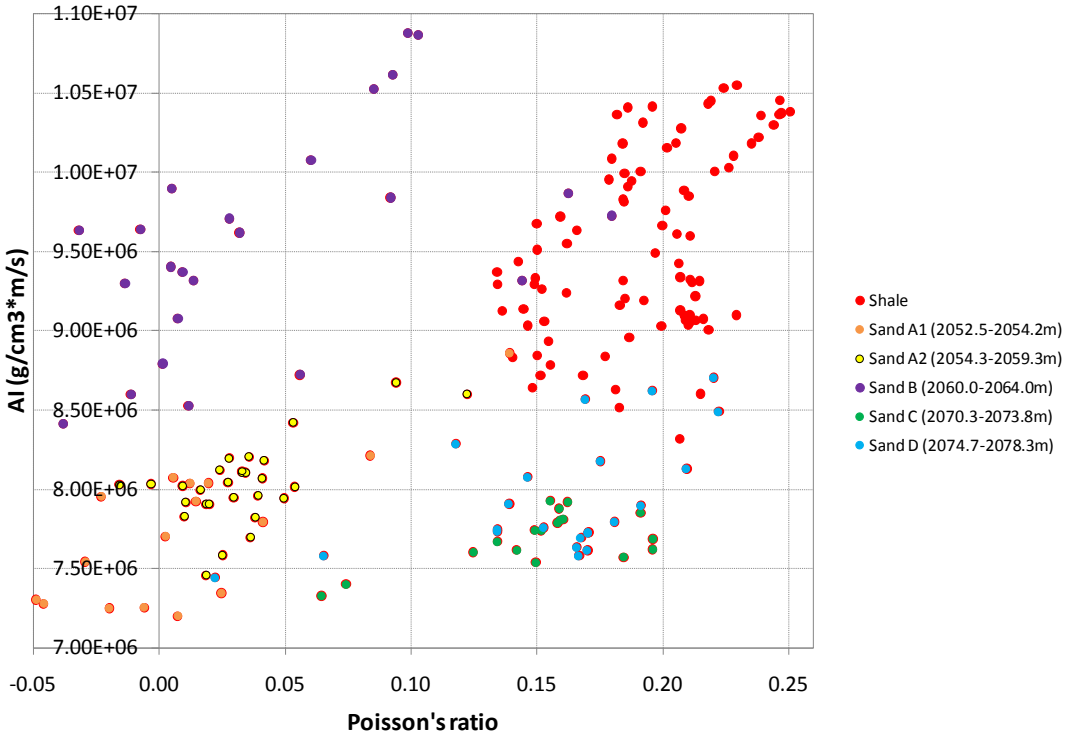

Figure 5.36 Post-injection, shale, and Sand B remain unchanged.

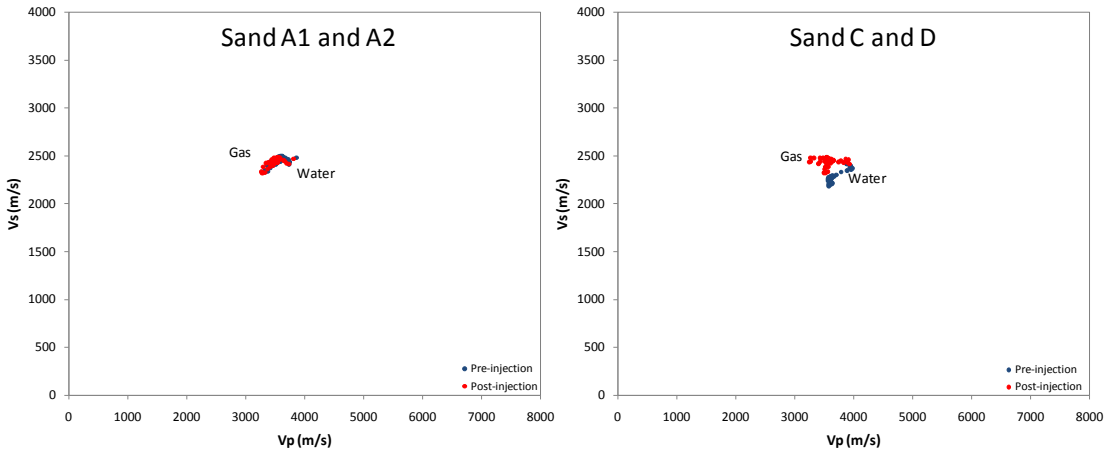

Figure 5.37 Plot of *Vs* versus *Vp* of the clean sands within Waarre-C formation. Fluid effect is better resolved for Sand C and D than for Sand A and B.

5.7.2 Confirming sandstones diagnostic from thin section and SEM analyses

To test the rock physics diagnostic results I referred to the thin section and electron microscopy data. The thin sections and SEM analysis of sample from Waarre-C are shown in Figure 5.38. The sand porosity is about 21% and K-feldspar is widespread. The presence of contact cement seems localized and dominated by authigenic kaolinite and thin quartz overgrowths. Most of authigenic kaolinite is filling inter-granular pore space as seen in Figure 5.39.

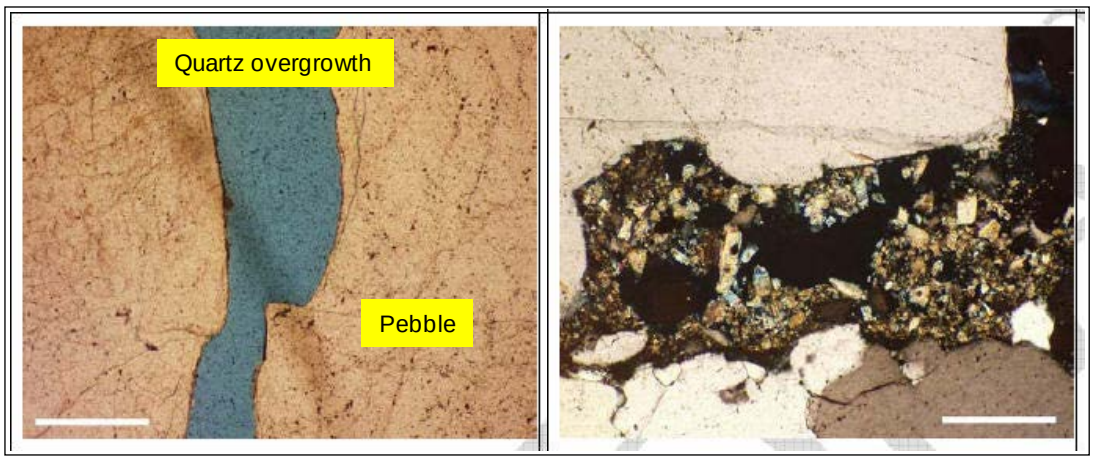

Figure 5.38 Thin sections and SEM images of the CRC-1 core samples from the reservoir level, taken at 2073mD. Clay coating around quartz grains is coloured in blue. Scale bar: left – 0.5 mm and right – 0.25 mm.

Table 5.13 Summary of grain size and sorting characteristics – texture (based on point count data). The thin sections were taken from core samples at different depth. A, B and C represented sand levels. Grain size is classified as C=coarse, VC=very coarse, P=pebble, G=granule and M=medium. Sorting type is classified as MS=moderate sorting, P=poor, MW=moderate well (modified from Schacht, 2008).

	Depth m	Plug No.	Mean Grain Size mm	µm	Phi	Class	Sorting St Dev	Class	Maximum Grain Size mm	µm	Phi	Class
	Waarre C											
	2053.15	128	0.63	626	0.68	C	0.86	MS	2.73	2725	-1.45	G
	2053.40	127	0.78	780	0.36	C	1.17	P	8.25	8250	-3.04	P
	2053.90	125	0.97	969	0.05	C	0.80	MS	3.18	3175	-1.67	G
A	2054.75	123	0.67	675	0.57	C	0.91	MS	2.18	2175	-1.12	G
	2056.80	120	0.71	714	0.49	C	1.01	P	4.23	4225	-2.08	P
	2057.55	118	0.77	769	0.38	C	0.69	MS	2.13	2125	-1.09	G
	2058.15	116	0.99	988	0.02	C	1.21	P	5.68	5675	-2.50	P
	2059.45	115	0.56	557	0.84	C	0.73	MS	1.80	1800	-0.85	VC
B	2062.00	112	1.53	1527	-0.61	VC	1.82	P	7.53	7525	-2.91	P
	2063.67	111	0.56	557	0.84	C	1.31	P	3.95	3950	-1.98	G
	2064.00	110	0.66	659	0.60	C	0.98	MS	3.25	3250	-1.70	G
C	2071.60	94	0.56	559	0.84	C	0.65	MW	2.00	2000	-1.00	VC
	2073.00	92	0.43	433	1.21	M	0.79	MS	1.33	1325	-0.41	VC

a) b)

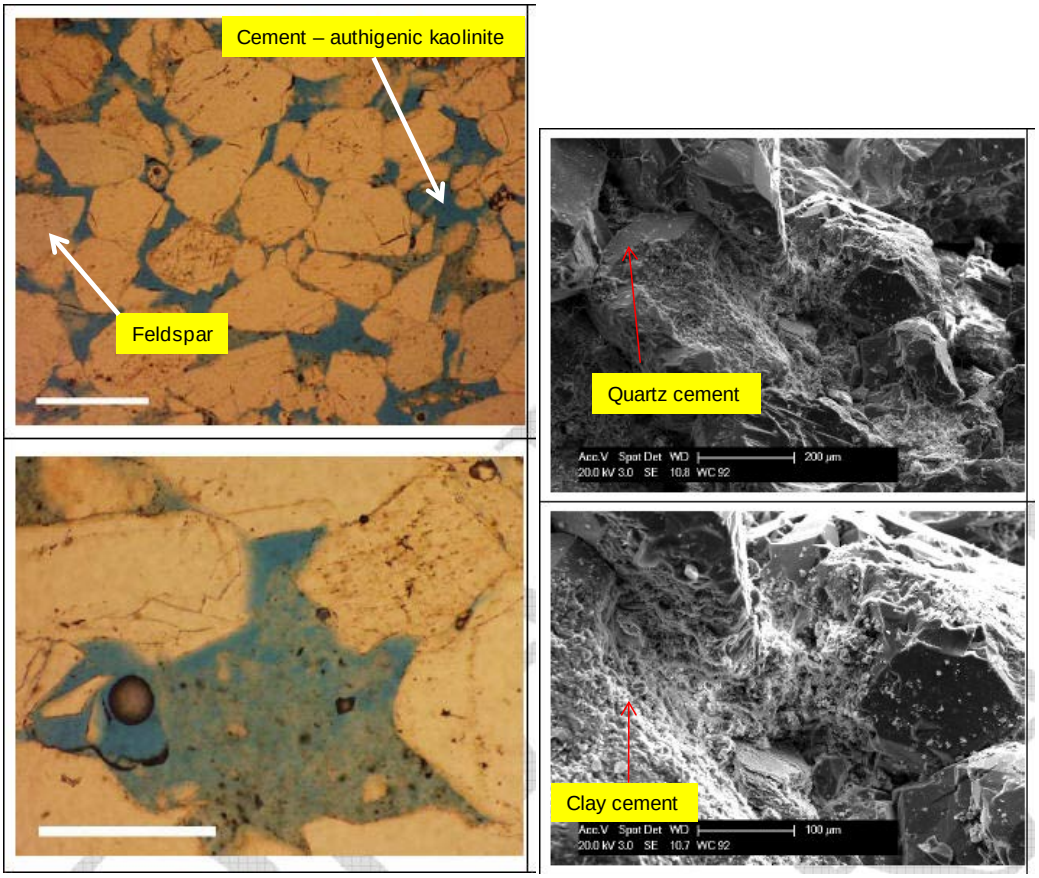

Figure 5.39 a) and b) thin sections of the CRC-1 core samples from the reservoir level, taken at 2062mD. Scale bar above is 0.5 mm and below is 0.25 mm.

Figure 5.39 shows the thin section of Sand B with pebbles as a part of a clean coarse grained subarkose. These quartz overgrowths fill up inter-granular pore. Below thin section is showing macro-pore and secondary pore. It suggests that a wider distribution of porosity is caused by variable grain sorting. No contact cementation is apparent. The clay and quartz overgrowth may explain why the sands in CRC-1 well are less cemented/fragile and loose, as clay coating tends to inhibit quartz cementation. Sorting, frame and grain characteristics are summarised in Table 5.13.

Waarre-C sands exhibit decreasing porosity with deteriorating sorting in depth, increasing in clay content, and localized cementation (see also Figure 5.20). Marion and Nur (1991) studied the effect of clay content and lithology in velocity-porosity relations for unconsolidated sands. She observed V-shaped patterns between porosity and velocity as they go from grain supported to clay-supported sediments. Marion assumed that the pore-filling clay would not affect the frame properties of the rock. Thus we have velocity and density increase, while porosity decreases. This assumption was supported by laboratory measurements. In Figure 5.40 *Vp* and density-porosity logs are anti-symmetric; reduction in porosity corresponds to an increase of velocity. Hence in general, the porosity and velocity changes in the Waarre-C formation should be attributed to the rock texture and grain-size distribution. Schacht (2008) carried out quantitative grain-size analysis of Waarre- C sands thin sections this is shown in Figure 5.41 for five facies, accompanied by corresponding histograms. Highly diverse grain sizes are present in the gravel dominated section, while the other four histograms show fairly uniform grain size. The lowest thin section display even size grains, while the sections above show the largest variation in grain size. Thin section analysis confirms that the degree of sorting varies significantly within the reservoir interval. To study the relationship between derived sorting parameters from the quantitative thin-section analysis and rock physics properties from well logs (velocities and density-porosities) and core measurements, I used standard deviation of sorting parameter as follows;

$$S = \sigma / M \tag{5.19}$$

where S is parameter of sorting σ is standard deviation of grain size and M is mean grain size, respectively. When this value is large the sands are poorly sorted and if it is low the sands are well sorted. The sorting effect on velocity-porosity relation for Waarre-C sands will be discussed more in the next chapter.

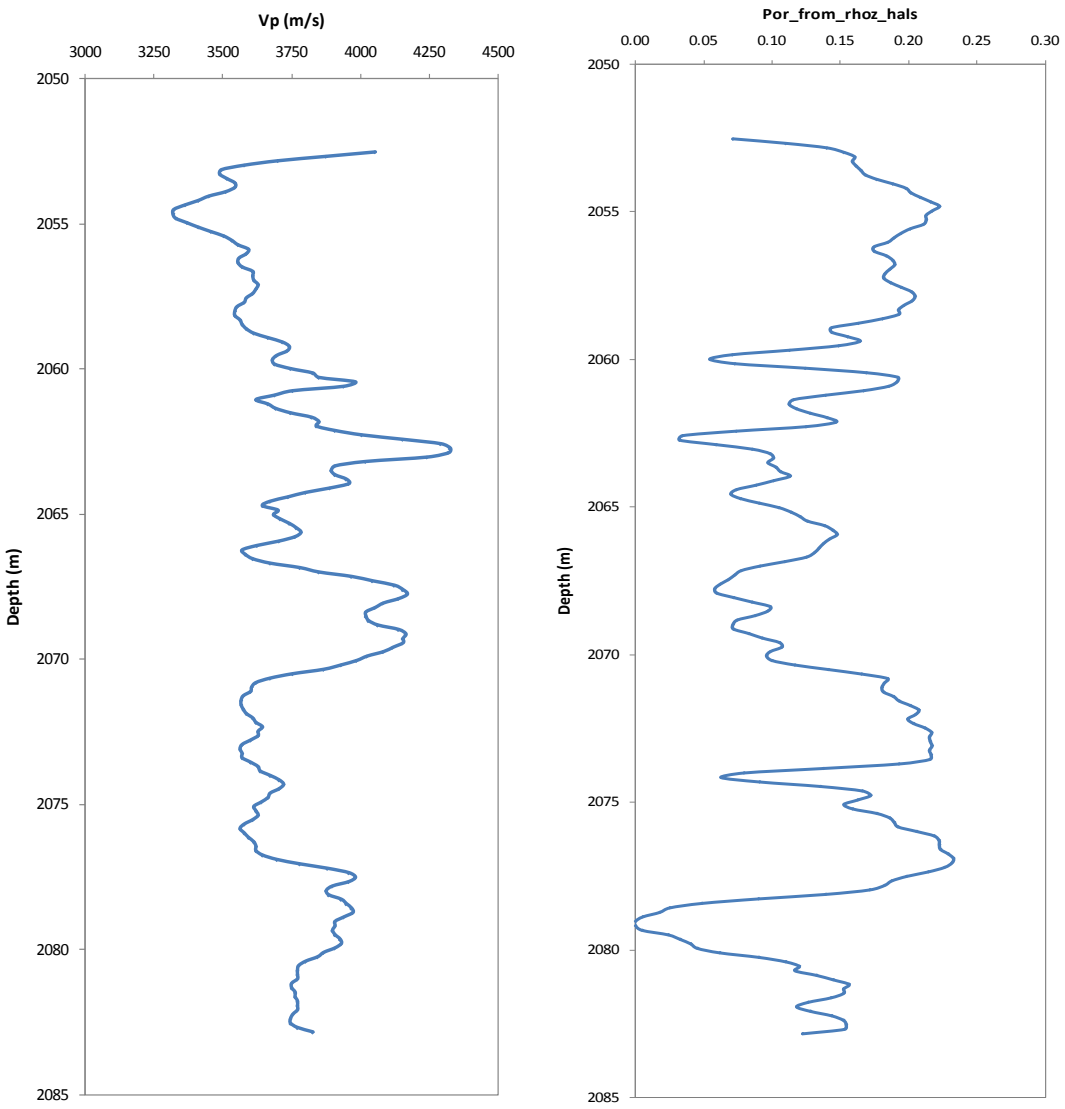

Figure 5.40 *Vp* and density-porosity pattern shows almost mirror – shapes.

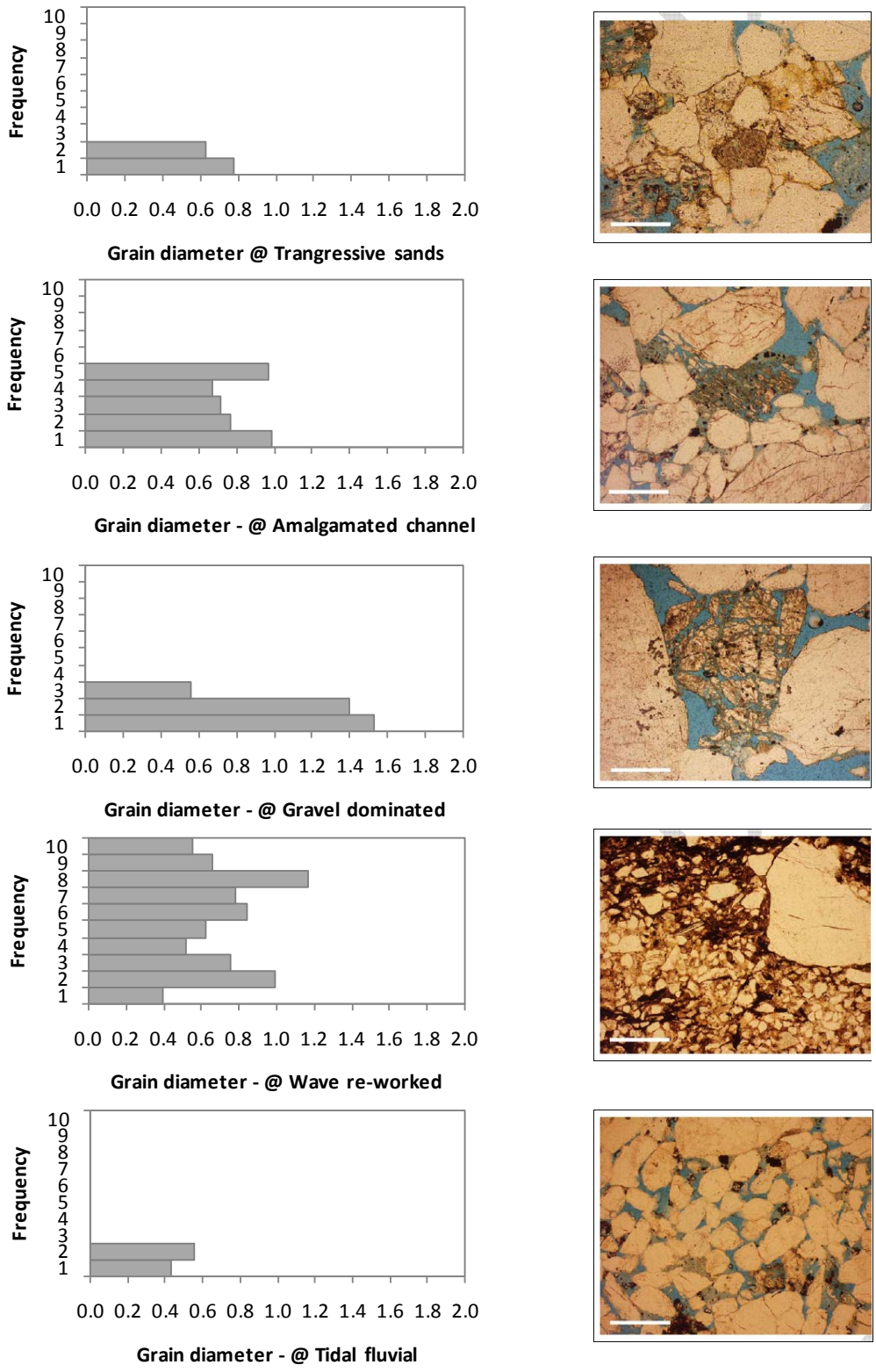

Figure 5.41 Histogram of grain size distribution from different depth interval within reservoir and corresponding thin sections. Most of the intervals are quartz grains dominated except wave-reworked facies where the shale content is abundant (modified from Schacht (2008)).

5.8 Identifying *in-situ* saturation type from well logs

The application of Gassmann's equation assumes that all fluid phases are immiscible and homogeneously distributed throughout the pore space; this is known as homogeneous saturation. This condition is met when the fluid is in equilibrium state over geologic time. However this equilibrium state may be disturbed during drilling, production, and water-flooding. To achieve equilibrium state a longer time may be needed than those encountered during the production or between time-lapse seismic surveys in time-lapse seismic monitoring. Thus, it may occur because fluids are not uniformly distributed throughout the pore space in the reservoir (Brie et al., 1995). This may lead to an inability of pore pressures to equilibrate in the time scale of wave propagation; this is known as patchy saturation. Understanding the state of saturation type will help modelling of the time-lapse seismic response correctly.

To derive a fluid substitution approach that could increase the accuracy of predicted changes in elastic properties of the reservoir rocks it was necessary investigate *in-situ* saturation type and establish whether the reservoir rock should be classified as homogeneous or patchy. For that purpose I used well logs recorded in CRC-1 well (injection well). First, I use ultrasonic core measurements and petrophysical logs to compute dry moduli. The Gassmann's fluid substitution was then applied to compute the properties of the saturated core sample. The dry-frame Poisson's ratio and dry-frame moduli inverted from logs assuming homogeneous saturation show good agreement with ultrasonic core measurement. This suggests that the saturation type is homogeneous (uniform) rather than patchy. Thus, homogeneous saturation is used for fluid substitution and modelling time-lapse seismic response for CO_2 sequestration in the CO2CRC Otway Project.

The Gassmann's fluid substitution requires several input parameters to calculate fluid effects on seismic velocities for K_{sat}. For that purpose we invert the dry frame moduli from the well logs. The porosity, grain density and fluid bulk modulus was obtained from laboratory measurement and estimated from well logs. The grain bulk and shear moduli were derived using effective K_{grain} with known mineral composition. Here I

describe how to identify saturation type from well logs. The results were then verified against the ultrasonic core measurements.

CRC-1 well logs such as velocity (V_P and V_S), density (RHOB), porosity (PHIT), saturation (SWT), dry clay volume (VDCL) were utilised to identify and interpret the reservoir *in-situ* saturation type and then calibrate it with ultrasonic core measurements (Figure 5.42).

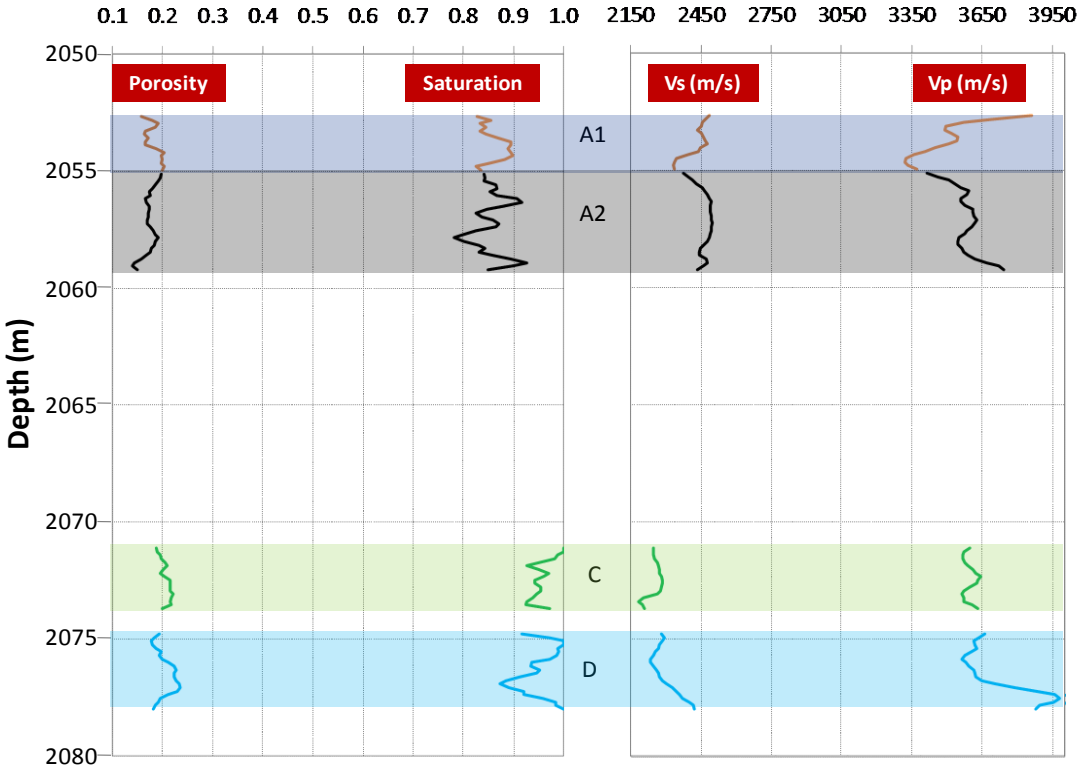

Figure 5.42 CRC-1 well porosity, saturation, P- and S- wave velocities logs from sand interval within the reservoir (highlighted). I use S-wave fast velocity.

The workflow I purposed to identify state of saturation in the reservoir is listed below:

1. Calculate effective bulk and shear moduli of saturated rock.
2. Calculate dry-frame bulk and shear moduli for homogeneous and patchy saturations.
3. Calculate dry-frame Poisson's ratio for homogeneous and patchy saturations.

4. The state of saturation is then evaluated against: a) the values (magnitude) of elastic moduli produced by the inversion and b) the proximity of inverted elastic moduli to the one obtained by ultrasonic core measurement.

In a favourable situation we can obtain dry-frame bulk (K_{dry}) and shear (G_{dry}) moduli from the logs by using inverse Gassmann's equation as follow:

$$K_{dry} = K_s \frac{1-(1-\phi)K_{sat}/K_s - \phi K_{sat}/K_f}{1+\phi-\phi K_s/K_f - K_{sat}/K_s}, \text{ and } \quad G_{dry} = G_{sat} = G, \tag{5.20}$$

where ϕ is porosity, and K_{grain} and K_{fluid} are the bulk moduli of the grain and fluid occupying the pore space, respectively. Bulk modulus of pore fluid is calculated from the saturation log using the iso-stress Reuss's equation:

$$K_f^{-1} = S_w K_w^{-1} + S_g K_g^{-1}, \tag{5.21}$$

where K_W, K_G and S_W, Sg are the bulk moduli and saturation of the water and gas phases, respectively; Sg = 1-Sw.

I then use Hill's equation to find the effective bulk modulus for the case of patchy saturation (KsatP), independent of the shape of the patches:

$$(K_{sat} + \frac{4}{3}G)^{-1} = S(K_0 + \frac{4}{3}G)^{-1} + (1-S)(K_1 + \frac{4}{3}G)^{-1}, \tag{5.22}$$

where K0 and K1 are the bulk modulus of the water- and gas-saturated rock, respectively:

$$K_0 = K_S \frac{\phi K_{Dry} - (1+\phi)K_l K_{Dry}/K_S + K_l}{(1-\phi)K_l + \phi K_S - K_l K_{Dry}/K_S},$$

$$K_1 = K_S \frac{\phi K_{Dry} - (1+\phi)K_g K_{Dry}/K_S + K_g}{(1-\phi)K_g + \phi K_S - K_g K_{Dry}/K_S}, \tag{5.23}$$

K_{Dry}P can be found from equation (5.22) and (5.23) as (Dvorkin and Nur, 1998):

$$K_{Dry} = 0.5(-B + \sqrt{B^2 - 4AC})/A, \tag{5.24}$$

$$A = cq + M(bq + cf), B = pc + dq - M(aq - bp - df + ce), C = dp - M(ap + de);$$
$$a = S\left[(1-\phi)K_l + \phi K_S\right], b = SK_l / K_S, c = \phi K_S - (1+\phi)K_l - K_l G' / K_S,$$
$$d = K_l K_S + (1-\phi)G' K_l + \phi G' K_S, e = (1-S)\left[(1-\phi)K_g + \phi K_S\right], f = (1-S)K_g / K_S,$$
$$p = K_g K_S + (1-\phi)G' K_g + \phi G' K_S, q = \phi K_S - (1+\phi)K_g - K_g G' / K_S;$$
$$M = \rho V_P^2, G' = 4G/3 = 4\rho V_S^2 / 3;$$

where G is shear modulus of the rock, and M is the P-wave modulus.

Dry-frame Poisson's ratio for homogenous and patchy saturations is then:

$$\nu = \frac{1}{2}\frac{V_P^2 / V_S^2 - 2}{V_P^2 / V_S^2 - 1} = \frac{1}{2}\frac{3K - 2G}{3K + G} \quad . \tag{5.25}$$

Knowing VPdry and VSdry from ultrasonic core measurement, and core porosity(ϕ_c) and grain density (ρ_g), we can calculate K_{dry} and G_{dry} of core samples using effective medium theory and dry-frame Poisson's ratio using equation (5.25).

Figure 5.43 shows the dry-frame Poisson's ratio and dry-frame bulk modulus derived from the logs for both saturation types. These are plotted against ultrasonic core measurements. The dashed lines represent the patchy saturation; the solid lines represent the homogeneous saturation; and the red dots represent ultrasonic core measurement.

In the upper part of the reservoir sand (~ 8.5m in thickness) the homogeneous saturation produces K_{dry} close to the one obtained from core tests. Hence patchy saturation in this interval is unlikely. Derived Poisson ratio however does not agree with core tests for either of the two saturation types. This error appears despite I used fast S-wave velocity that is representative of the rock frame. This disagreement is most likely produced by S-wave measurement errors. Both patchy and homogeneous appear possible for the lower part of the reservoir sand (~ 8m in thickness). A somewhat better agreement is obtained for the homogeneous case.

Log estimated fast and slow S-wave velocities are shown in Figure 5.44. If slow S-wave velocity is used the computed elastic properties, good agreements with core results are achieved for both reservoir intervals. In both cases homogeneous case agrees better with core sample results (Figure 5.45).

We conclude that the large error in the upper part of reservoir results from difficulty in measuring the shear wave velocity from logs and core samples. Successful inversion with slow shear wave velocity suggests there is some fundamental difference between the upper and lower reservoir sands both intervals however appear closer to homogeneous saturation than to patchy. Consequently dry-frame bulk modulus (K_{dry}) using homogeneous saturation is applied for fluid substitution and used to predict time-lapse seismic response before and after CO_2 injection as shown in Figures 5.46 and 5.47.

Clearly, it is important to evaluate the potential error caused by assuming wrong saturation types especially for low gas/water saturation (Sw 80% and Sw 20%) as is the case with the CO2CRC Otway Project.

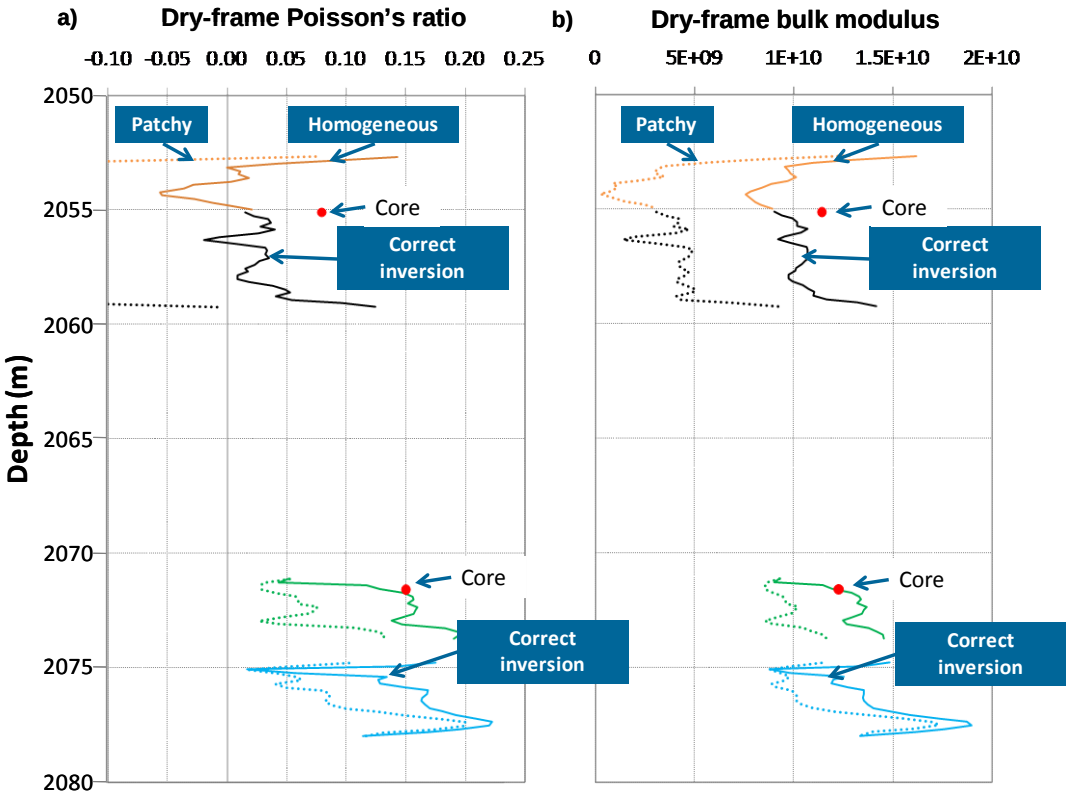

Figure 5.43 Dry-frame (a) Poisson's ratio and (b) bulk modulus. The dashed lines represent the patchy saturation; the solid lines represent the homogeneous saturation; and the red dots represent ultrasonic core measurement. The upper part of reservoir sand interval does not agree with core measurement.

Homogeneous saturation fits well to the lower part of the reservoir sand. Log-derived dry properties use S-wave fast velocity.

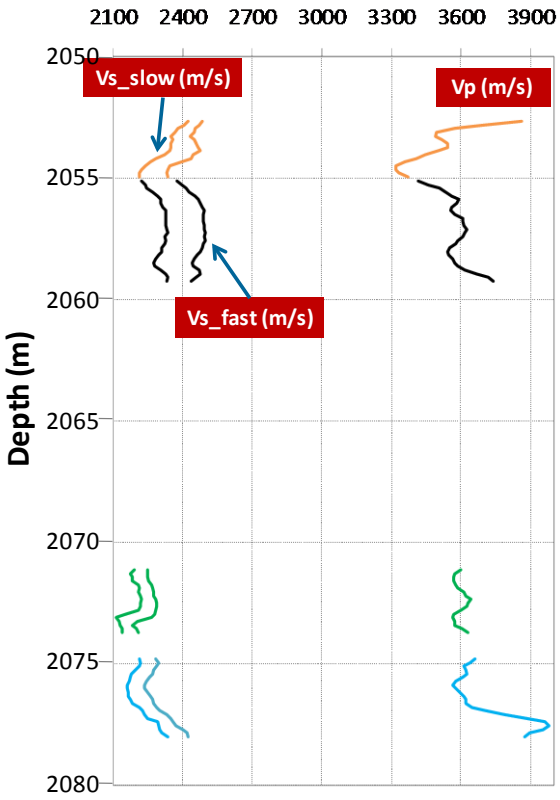

Figure 5.44 CRC-1 well logs show P- and two S- wave velocities, fast and slow.

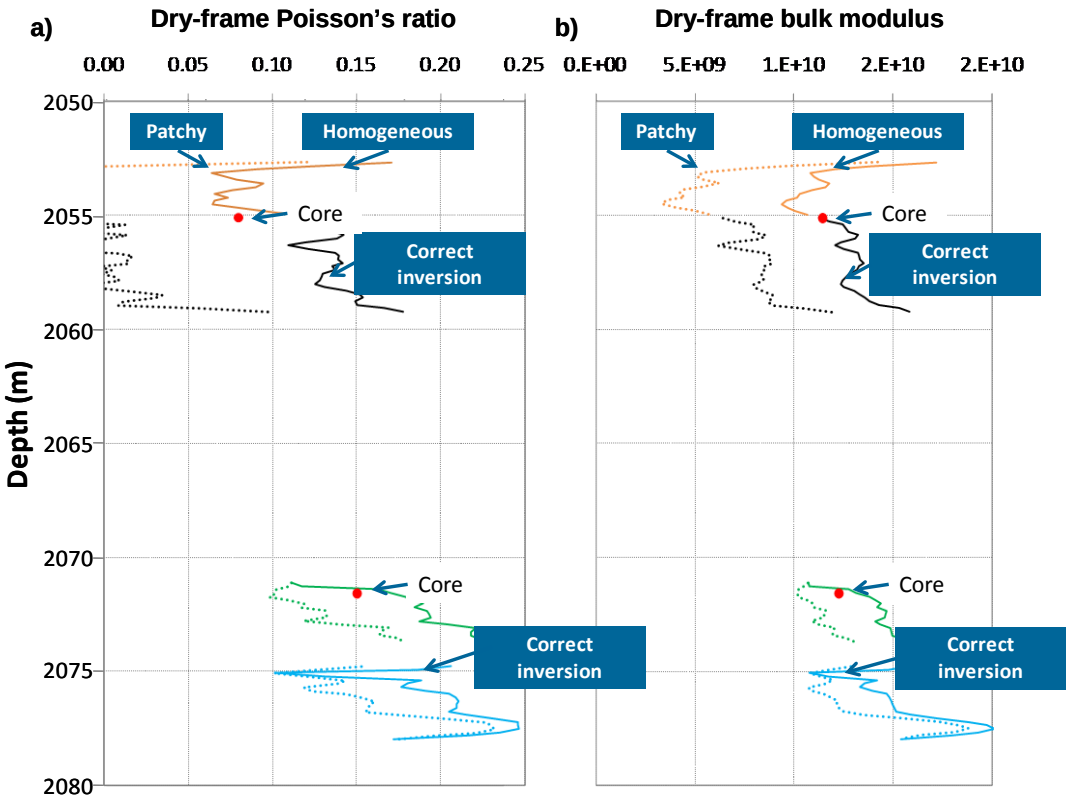

Figure 5.45 Dry-frame (a) Poisson's ratio and (b) Bulk Modulus. The dashed lines represent the patchy saturation; the solid lines represent the homogeneous saturation; and the red dots represent ultrasonic core measurement. The upper and lower parts of reservoir sand agree with ultrasonic core measurement. Log-derived dry properties use S-wave slow velocity.

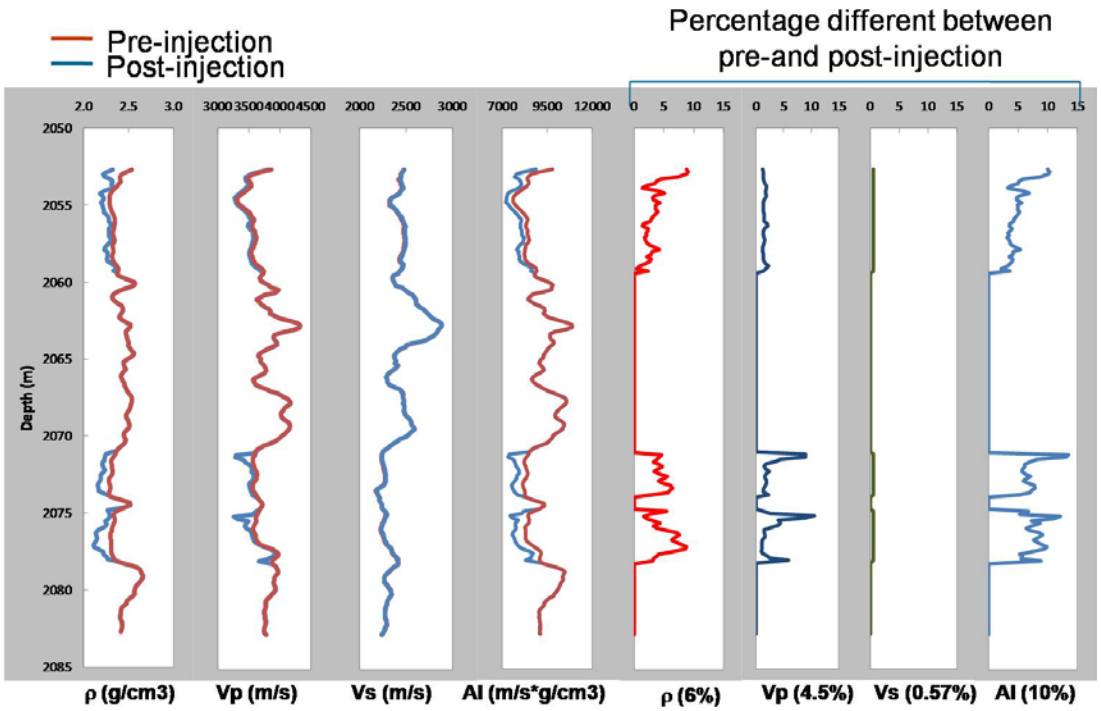

Figure 5.46 Final substitution result of pre and post CO_2 injection at CRC-1 well after applying K_{dry} homogeneous saturation. The elastic properties differences are larger than previously predicted in average.

a)

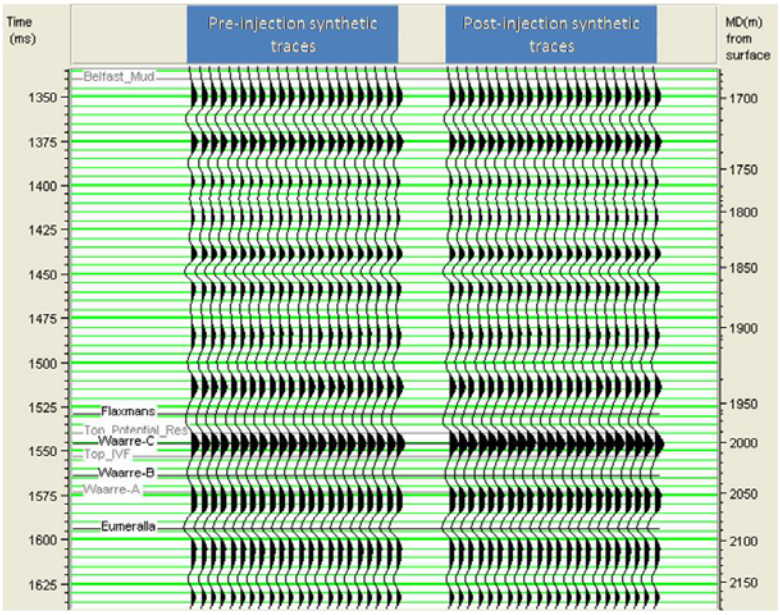

b)

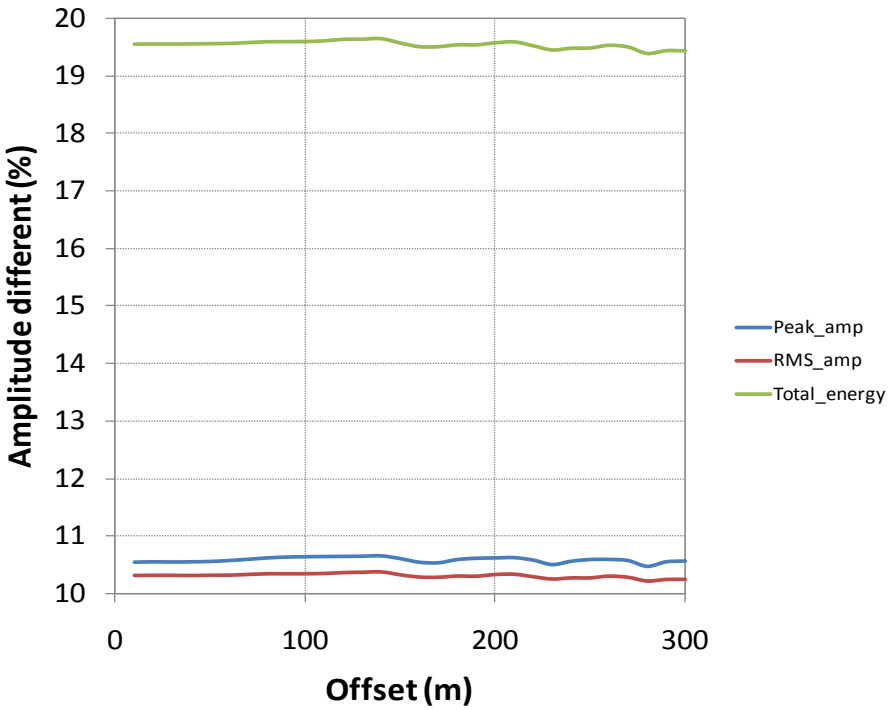

Figure 5.47 a) Synthetic traces of pre and post CO_2 injection at CRC-1 well after applying Kdry homogeneous inversion. The top of reservoir is Waarre-C and the base of reservoir is Waarre-B. b) The amplitude difference of pre- and post-CO_2 injection at the top of the reservoir showed the 10% change is expected. It was confirmed by field measurement.

5.9 Discussion and conclusions

To produce an accurate prediction of CO_2-related time-lapse signal it was necessary to infer the state of saturation in the reservoir. For that purpose I have devised a specific methodology that is capable of identifying the saturation type: homogeneous or patchy by utilising information from both well logs and core measurements, and using them in a comparative manner. This, somewhat lengthy analysis showed that:

- Homogeneous reservoir saturation appears appropriate for Naylor reservoir.
- Uncertainty in estimation of shear wave velocity could significantly affect and subsequently distort fluid substitution results.
- Calibration with ultrasonic core measurement is important and it was proved to be critical for the CO2CRC Otway Project.

Computed time-lapse seismic response resulting from CO_2 injection into the residual gas saturation zone proved to be weak. Hence it is not likely that, at least surface, time-lapse seismic methodology will detect any changes of the elastic properties of the reservoir.

Chapter 6 SEISMIC MODELLING OF SEISMIC RESPONSE OF CO_2 INJECTION INTO WAARRE-C SANDSTONNES

6.1 Introduction

One possibility to do quantitative analysis of seismic response is to match forward seismic modelling results with field data. However, forward seismic modelling has shown that sometimes it can be difficult to use seismic amplitudes directly due to potential errors associated with picking uncertainties, resolution and tunning effects. Alternative approach to lithology and pore fluids prediction is based on seismic inversions, the process of extracting reflectivity and thereafter impedance from seismic reflection attributes. The later could be linked to reservoir properties using appropriate rock physics models.

In this chapter I used concurrently forward modelling and seismic inversion to analyse changes in the reservoir due to CO_2 injection.

6.1.1 Methodology

Using two wells drilled into the Waarre-C reservoir, it was possible to perform model-based inversion over the reservoir interval. For that, a high quality well tie (seismic-log correlation) is required. Since Naylor-1 was drilled before CH_4 production, it was necessary to perform fluid substitution modelling to condition this well at the state that would have been measured before CO_2 injection. Of additional interest was to compute a saturation state in the reservoir, more specific in the CRC-1 well after CO_2 injection. This "updated" model could be than used to evaluate the inversion error and hence the most likely saturation state. To generate fluid substitution logs for Naylor-1 and CRC-, I used the rock physics model described in Chapter-5. Such logs represent a different fluid state for Naylor-1 and CRC-1 based on prediction and simulation models. Subsequently, synthetic seismogram could be generated for pre (2008 - baseline) - and post-injection (2009 – monitoring). The time-lapse signal is then compared to impedance differences found in the field data

One of the main objectives of acoustic impedance inversion of the post-stack seismic was to investigate indirectly, trough evaluation of the inversion error, the fluid saturation state in the reservoir. The model-based inversion method was chosen which iteratively updates a layered initial model and produces full-bandwidth impedance. To update the model, log-based derived impedances are correlated to the field seismic data results for pre- and post-injection cases.

Secondary objective was to indirectly verify the derived rock physics model for Waarre-C sandstonnes. That is to compare the predicted to measured time-lapse seismic signal. Discussion and conclusions are provided at the end of Chapter 6.

6.2 Interpretation of 2008 (baseline/pre-injection) and 2009 (monitoring) seismic data

The reservoir interval (Waarre-C sand) is only about 25m thick and is at the limit of seismic resolution and will exhibit tuning effects. A more precise interpretation of 2008 (pre-injection/baseline) and 2009 (monitoring) 3D seismic data was accomplished after log correlation. Five keys horizons were identified: Eumeralla, Waarre-A, Waarre-B (base reservoir), Waarre-C (top reservoir) and Flaxmans (the order of the key horizons is from the deepest to the shallowest). Additional two horizons above the Flaxmans were also interpreted as Belfast (main seal formation) and Skull creek formations. The Belfast lack continuity and is difficult to map from the data. For that reason a strong seismic event above Belfast was mapped as well as the Skull Creek formation. Eumeralla, Waarre-B, Flaxmans and Belfast were picked on a white trough, where Waarre-A, Waarre-C and Skull-creek were picked on a black peak. SEG negative polarity was used where the black peak represents a decrease in impedance (Figures 6.1 and 6.2). Horizons maps are shown in Figures 6.3 and 6.4 for 2008 (baseline) and 2009 (monitoring) data volumes.

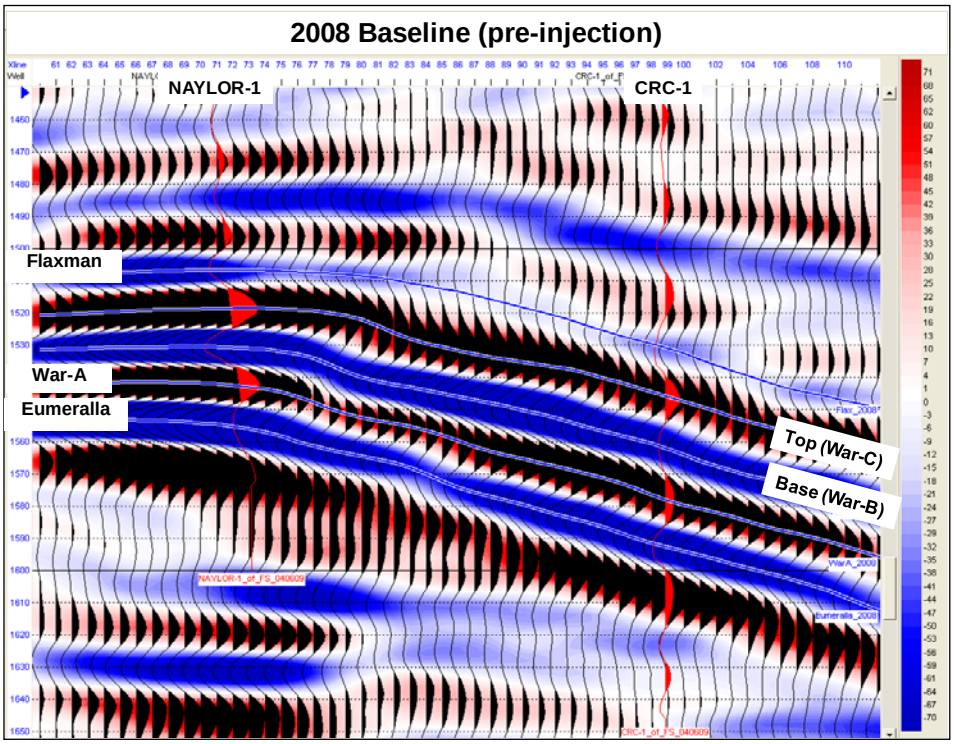

Figure 6.1 Dip line of 2008 (pre-injection/baseline) 3D seismic data across Naylor-1 and CRC-1 wells with horizons interpretation. The red curve is a synthetic seismogram.

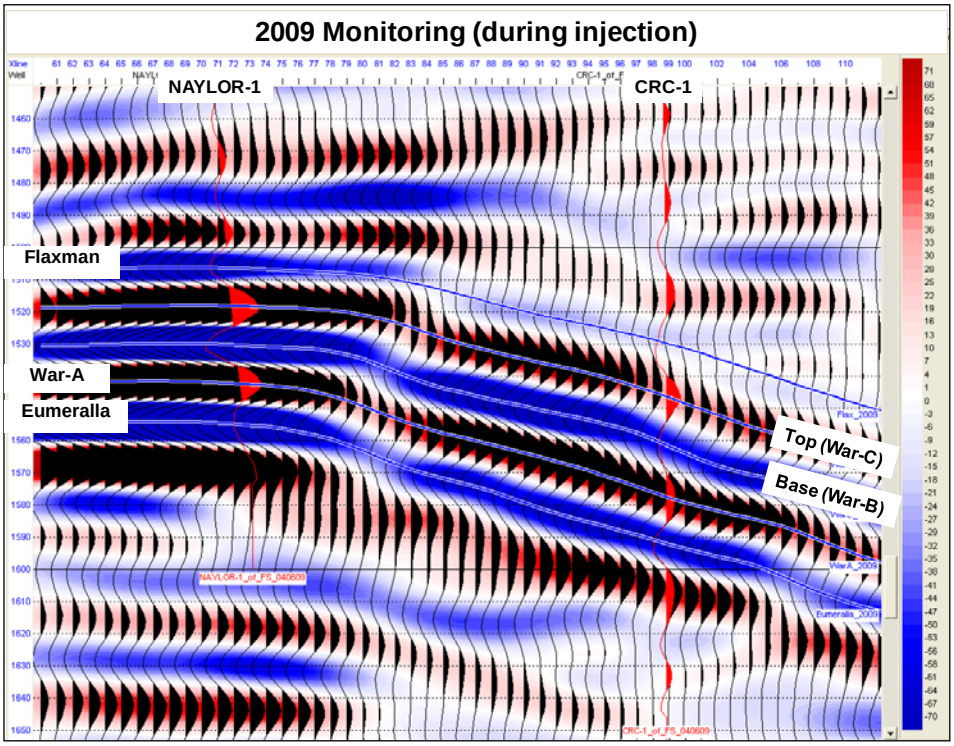

Figure 6.2 Dip line of 2009 (monitoring) 3D seismic data across Naylor-1 and CRC-1 wells with horizons interpretations. The red curve is a synthetic seismogram.

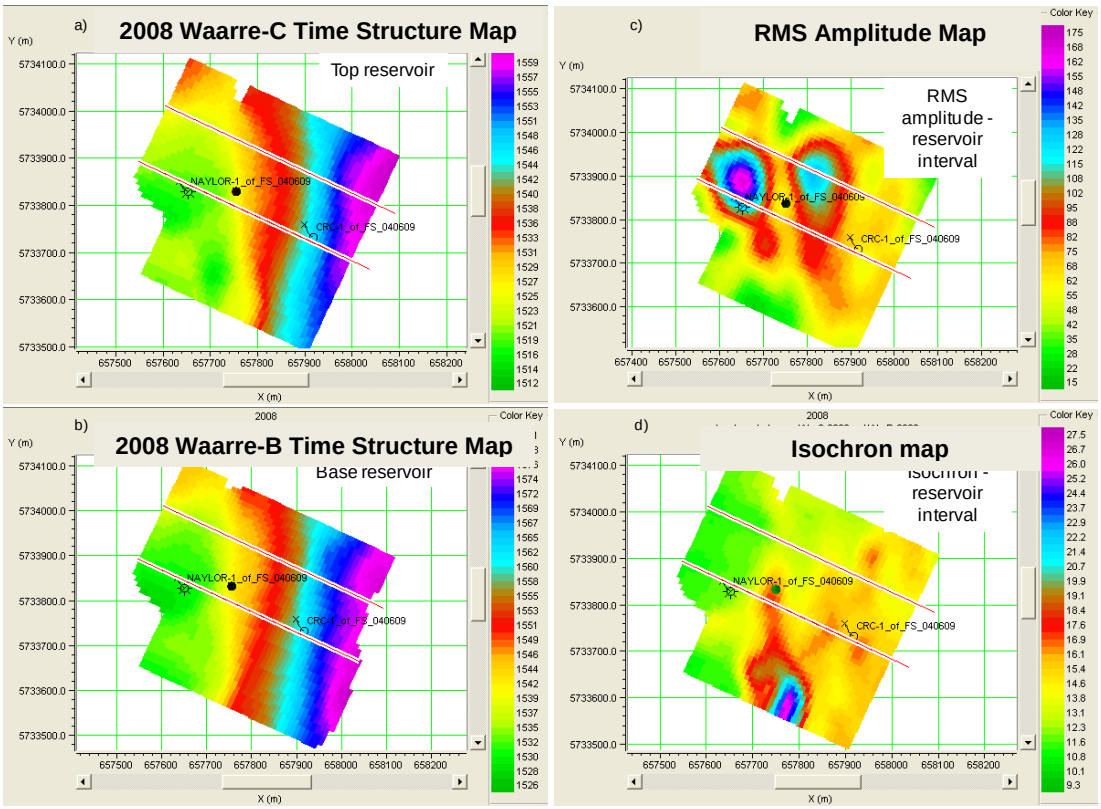

Figure 6.3 2008 (pre-injection/baseline) map of a) Waarre-C (top) reservoir time structure map, b) Waarre-B (base) reservoir time structure map, c) RMS amplitude map and d) Isochron map at reservoir interval, respectively.

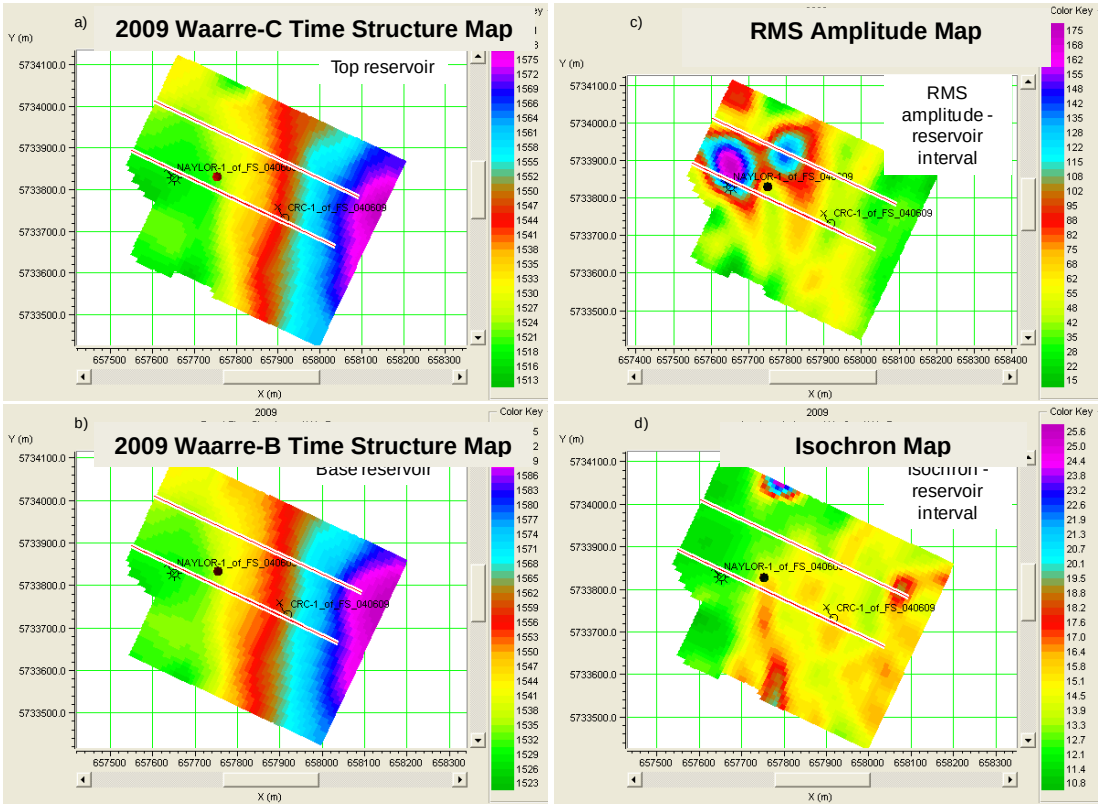

Figure 6.4 2009 (monitoring) map of a) Waarre-C (top) reservoir time structure map, b) Waarre-B (base) reservoir time structure map, c) RMS amplitude map and d) Isochron map at reservoir interval. The green and purple colours represent shallow and deep time structures; low and high amplitudes; thin and thick isochron, respectively.

Both 2008 and 2009 Waarre-C RMS amplitude map show high amplitude anomalies around Naylor-1 well that could be related to re-formation of the methane cap after gas production was stopped (Figures 6.3 and 6.4). It however appears that 2009 amplitude map shows somewhat smaller anomaly as shown in Figure 6.4 c). Heterogeneity of the reservoir may be causing these anomalies but it is more likely related to repeatability issues. The break in the amplitude anomaly could suggest the presence of a less permeable medium (Figure 6.4 c). If this is true it might stimulate the migration of CO_2 plume in up-dip north-west direction along the time structure (buoyancy effect). This anomaly could be related to the shale intercalation as observed in both Naylor-1 and CRC-1 wells.

6.3 Forward modelling of CO_2 injection process

Li et al. (2006) have forward modelled time-lapse seismic response and travel time differences associated with the CO_2 plume spread over Naylor-1 and CRC-1 wells. The results for injection of 100,000 tonnes of CO_2 into Waarre-C suggested small changes in reservoir properties and hence very small time-lapse seismic signal. Consequently the possibility that CO_2 related changes can be directly detected by time-lapse seismic methodology was predicted to be very low. However, the input pore pressure, temperature and gas/fluid compositions did not represent the true pre-CO_2 injection conditions as the CRC-1 well had not been drilled and logged at the time. Therefore this new knowledge was incorporated into the current modelling.

The expectation was that the changes in elastic properties due to CO_2 injection at CRC-1 well will be greater than at the Naylor-1 well. The reason was that CO_2 injection in CRC-1 will result in larger changes of fluid density, while the existing gas cap will overprint the seismic response at Naylor-1.

To test this proposition I developed the following workflow:

- Extract a wavelet from the 2008 (pre-injection/baseline) and 2009 (monitoring) 3D seismic data in the vicinity of Naylor-1 and CRC-1 wells for synthetic modelling.
- Using a statistical wavelet estimated from seismic data perform correlation for each well with the seismic data to optimise the time to depth conversion by matching the events on the synthetic data with the interpreted reflection events (known formation tops).
- Extract a well-based synthetic wavelet from Naylor-1 and CRC-1 using the sonic and density logs.
- Perform well correlation through several iterations to optimise the correlation with the seismic data.
- Perform fluid substitution using various CO_2/CH_4 saturation scenarios, based on reservoir simulation studies. Generate synthetic seismic traces for each case and compare to the baseline state.

Preliminary log analysis showed that log-blocking in not required after 3 point filter was applied to remove spikes.

6.3.1 Wavelet extraction

Initial seismic-log correlation involved statistical wavelet which is derived from the data; basically as a zero-phase wavelet that has identical amplitude spectrum as seismic data surrounding the well. This wavelet was then used to correlate the well logs and seismic data. Once the optimum correlation was achieved, a new time-depth curve is computed. Refined correlation is then achieved by extracting the final wavelet which in this case utilises logs. Very small difference is observed between the two wavelets (statistical and well based as shown in Figures 6.6 and 6.7). Note the spectral difference between baseline and monitor surveys (Figure 6.5) which can be primarily related to the different source used for data acquisition (weight drop and vibroseis, respectively).

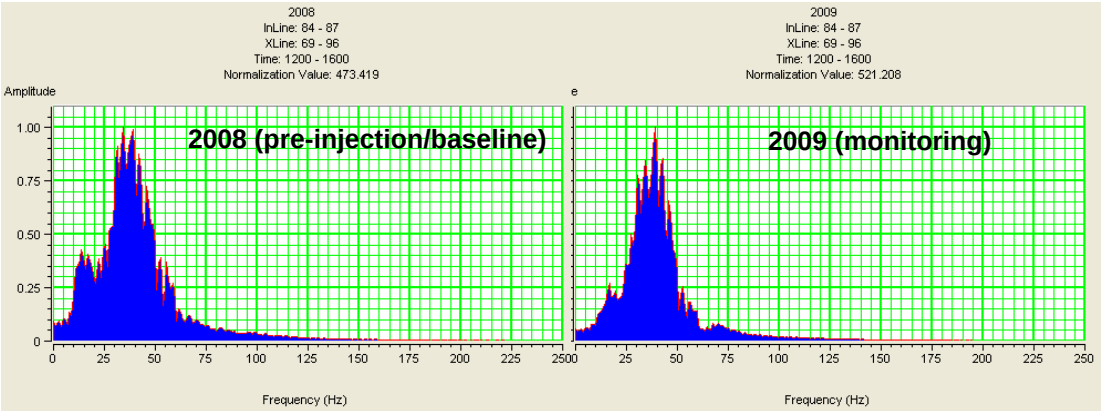

Figure 6.5 Amplitude spectrum of 2008 (pre-injection/baseline) and 2009 (monitoring) 3D seismic data extracted around Naylor-1 and CRC-1 wells. The dip line was from 84-87, the strike line was from 69-96 and time window was from 1200-1600ms. Both spectrums have similar trends. However, 2009 (monitoring) 3D seismic data has higher S/N ratio.

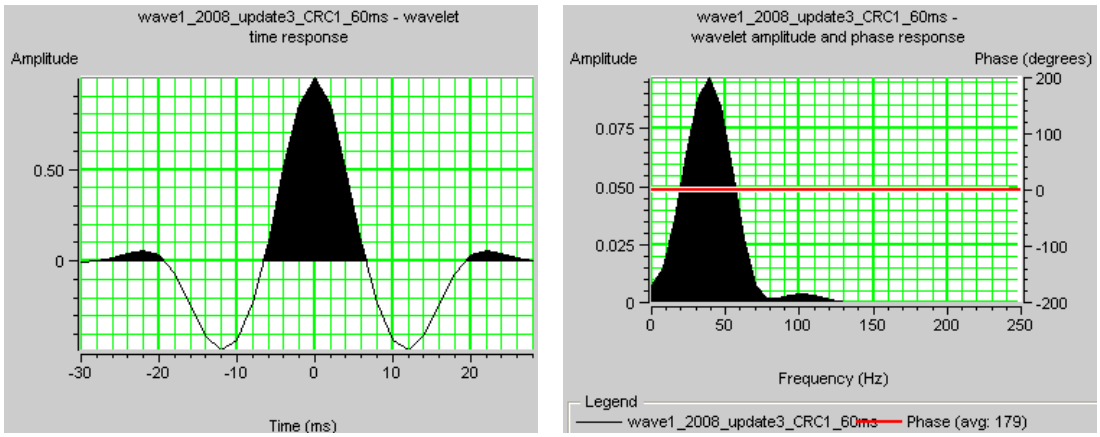

Figure 6.6 Initial wavelet extraction from the 2008 (pre-injection/baseline) 3D seismic data in the immediate vicinity of the CRC-1 well. The polarity is SEG negative where the decrease in acoustic impedance is represented by peak (top reservoir). This wavelet is used to correlate events between the well and seismic data.

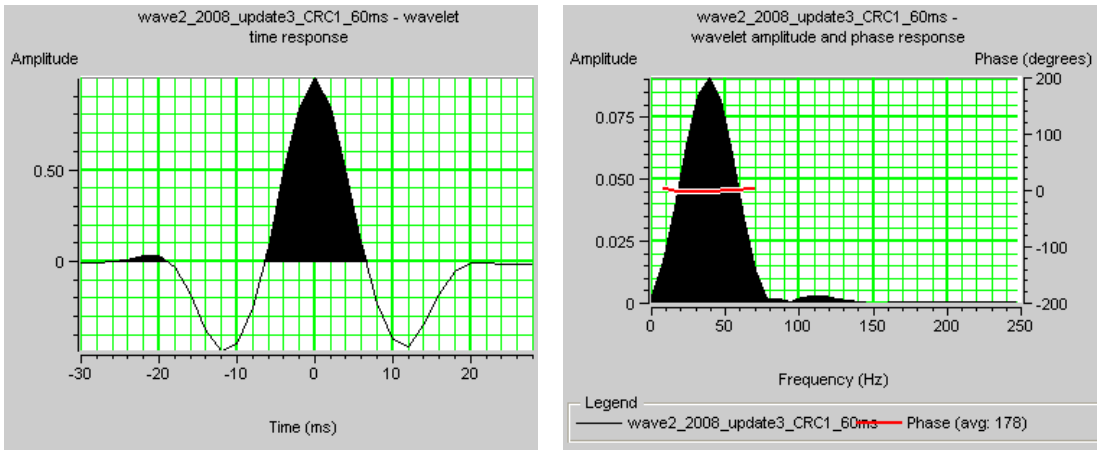

Figure 6.7 Wavelet extraction incorporating the Naylor-1 and CRC-1 well logs. The wavelet gave an improved correlation with the seismic data. Residual phase error has been corrected for both wells.

Wavelet extraction was done in the dip direction within a short time window (400 ms) to incorporate the area of interest and to avoid noisy part of the stacked volume. The wavelet length was 60 ms to minimize unnecessary side lobe (ringing) and the taper was 20 milliseconds. I used both wells to limit the area of wavelet extraction and avoid the phase changing away from the wells within the reservoir. I also applied the same window parameters in both wells during the wavelet extraction incorporating the well data.

Wavelet extractions incorporating well data reveals (approximately) true phase of the data and can then be used to zero-phase seismic data. The best practice (especially for inversion) is to optimize the initial log correlation at the reservoir level iteratively before the wavelet extraction. Log correlation can be done simultaneously using an extracted wavelet from the well data to correct residual phase error. However, rotating the phase is not always required. Correcting to zero-phase is most important for AVO analysis of pre-stack data and elastic inversion, but less significant for acoustic impedance inversion of post-stack data as long as the wavelet phase has the same phase as the seismic.

For modelling and inversion, I selected the wavelet which had the highest correlation coefficient. Statistical and well-based wavelet extraction produced similar results (Figure 6.8). A small improvement in correlation was achieved with well based wavelet which was at the end kept for final inversion work.

I also investigated the potential effects of wavelet variations. A number of 2D inversion tests were carried out using each wavelet from each well and the wavelet extracted from CRC-1 (baseline log) only, which was correlated to 2008 (pre-injection/baseline) and 2009 (monitoring) 3D seismic data. The outputs showed similar trends. At the end, I used CRC-1 well-based wavelet for seismic to well tie at both wells and store it for the subsequent model-based inversion.

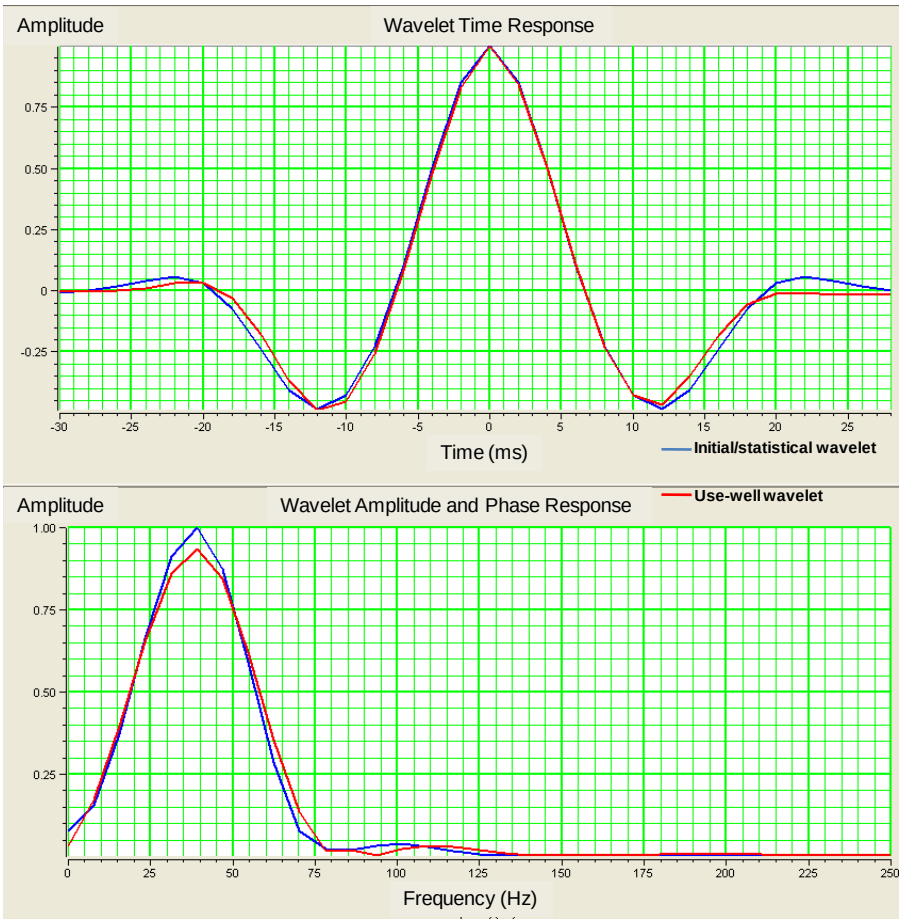

Figure 6.8 Overlay of statistical (blue curve) and use-well wavelet (red curve) extracted from 2008 (pre-injection/baseline) 3D seismic and well log data. The both wavelets are similar.

6.3.2 Fluid flow predictions and elastic wave synthetics

There were several flow simulation study models that attempted to predict pore pressure and fluid saturation for pre-injection, during injection and post-injection states of the reservoir (Leahy, 2009; Xu, 2007) as summarised in Tables 6.1. The outputs from the reservoir simulation were used to generate synthetic seismic models and to examine the changes of the seismic response due to different fluid saturations. I used elastic wave modelling (Simmons and Backus, 1994) which gives a more accurate model of wave propagation, especially for thin layer models with large impedance contrasts. The synthetic modelling results are presented in Tables 6.2 to 6.3 and displayed in Figures 6.9 to 6.10.

Table 6.1 Simulation models of CO_2 injection a) Xu's model for pre- and post-injection (Xu, 2007), b) Leahy's model during injection with specific time/date (Leahy, 2009) and c) Xu's model after 6 months injection.

a) Xu's model for pre- and post-injection

	Time	Pressure	Sg Total	Remarks
CRC-1	Pre	17.6	0.2	(*in-situ* gas composition)
	Post	20	0.8	(Buttress-1 well gas composition)
NAYLOR-1	Pre	17.6	0.2	(*in-situ* gas composition)
	Post	20	0.8	(Buttress-1 well gas composition)

b) Leahy's model during injection

	Time	Pressure	Sg Total	Sg CO2	Remarks
CRC-1	30-Nov	18.9	40	45	(CO2=18%, CH4=22%)
	31-Dec	19	50	55	(CO2=27.5%, CH4=22.5%)
NAYLOR-1	30-Nov	18.6	35	30	(CO2=10.5%, CH4=24.5%)
	31-Dec	18.6	40	35	(CO2=14%, CH4=26%)
CO2 Plume (middle)	30-Nov	18.8	70	65	(CO2=45.5%, CH4=24.5%)
	31-Dec	18.8	75	70	(CO2=52.5%, CH4=22.5%)

c) Xu's model after 6 months injection

	Time	Pressure	Sg Total	Sg CO2	Remarks
NAYLOR-1	Before seismic acquisition (2009 monitoring)	18.9	65	52	(CO2=80%, CH4=20%)

Table 6.2 Summary of synthetic modelling in Naylor-1 based on reservoir simulation model in Table 6.1.

Naylor-1								
Track No.								
Actual seismic		Xu's model	Leahy's model				Xu's model	
1	2	3	4	5	6	7	8	9
2008 (pre-injection/ baseline) 3D	2009 (monitoring) 3D seismic	Pre-injection synthetic traces	30 Nov 08 gas saturated synthetic	31 Dec 08 gas saturated synthetic	30 Nov 08 CO2 saturated synthetic	31 Dec 08 CO2 saturated synthetic	Before seismic acquisition (2009 - monitoring) synthetic traces	Post-injection synthetic traces

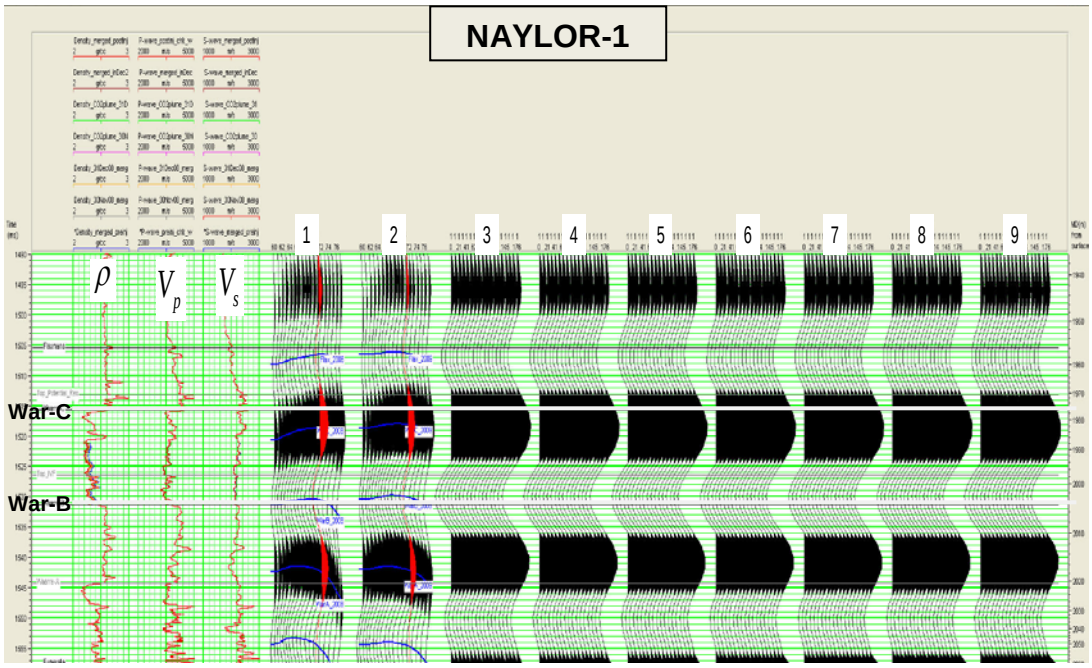

Figure 6.9 Naylor-1 composite logs, seismic and synthetic traces. The logs show *in-situ* log overlay with fluid substitution logs. The density effect is larger compare to velocities.

Table 6.3 Summary of synthetic modelling in CRC-1 based on reservoir simulation model in Table 6.1.

CRC-1					
Track No.					
Actual seismic		Xu's model	Leahy's model		Xu's model
1	2	3	4	5	6
2008 (pre-injection/baseline) 3D seismic	2009 (monitoring) 3D seismic	Pre-injection synthetic traces	30 Nov 08 gas saturated synthetic traces	31 Dec 08 gas saturated synthetic traces	Post-injection synthetic traces

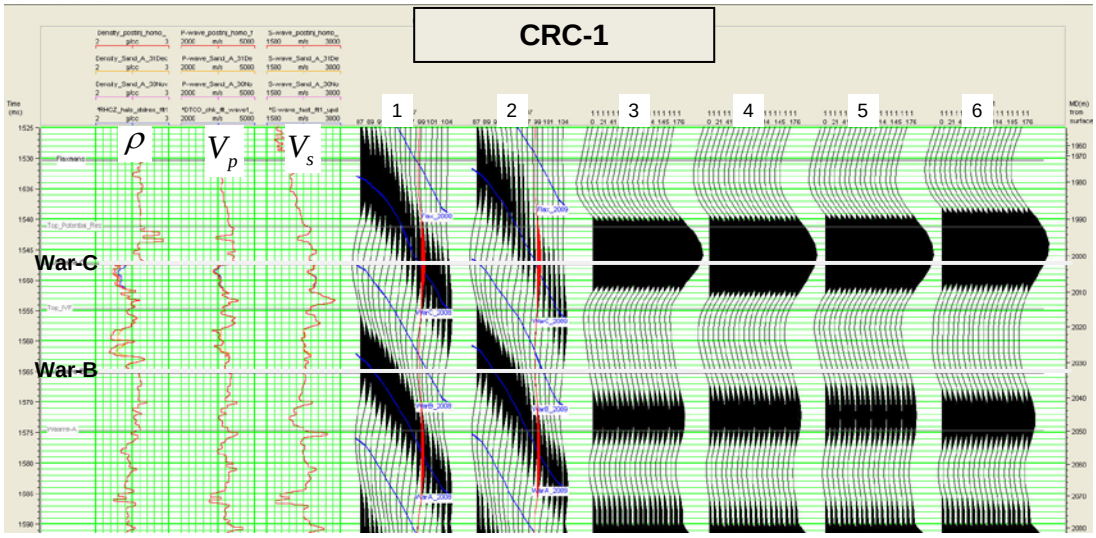

Figure 6.10 CRC-1 composite logs, seismic and synthetic traces. The logs show *in-situ* log overlay with fluid substitution logs. The density effect is larger compare to velocities.

The Naylor-1 synthetics pre-, during and post-injection suggest little changes in the seismic response. The reason is the presence of the gas cap that overprints the seismic response from the reservoir. The CRC-1 synthetics pre-, during and post-injection suggest a small-to-moderate change as well as time/phase shift, which could be related to CO_2 injection because of the changes in fluid density and thickening of CO_2 layer. These observations granted further efforts into a time-lapse signal examination.

6.4 Post-stack seismic inversion

A baseline 3D seismic survey was acquired at the end of year 2007 and the beginning of year 2008. The data was processed in 2008. This data set is referred to as the 2008 (pre-injection/baseline) 3D seismic data. CO_2 injection began in April 2008. Eight months afterwards (during injection), in January 2009, the first repeated 3D seismic survey was acquired and processed. This is referred to as the 2009 (monitoring) 3D seismic data.

Sherlock (2006) generated an acoustic impedance model of the 2000 (pre-production) 3D seismic data incorporating the Naylor-1, Naylor South-1 and Buttress-1 wells. The aim was to give some insight into reservoir heterogeneity (lithological variation). This must be taken into account because heterogeneity could mask the effect of pore fluids on the seismic response.

Following Sherlock's work, I inverted pre- and post-injection volumes. For pre-production data set (2000) only the post stack seismic data was available and ready when the work was performed, thus the inversion was limited to 2008 and 2009 data which were processed with the same parameters and post-stack equalised.

6.4.1 Initial impedance model

Initial inversion volumes were created using pre-injection logs for Naylor-1 and CRC-1 wells. These two wells and 3D picked horizons were used to create initial synthetic impedance cube for constraining the real data inversion. I then built several pseudo-impedance models based on different pore fluid saturation predictions from the simulation models. Each initial model of different saturation states is then used to invert the monitoring data. The aim was to identify the most likely saturation state of the reservoir at the time of injection.

The high frequency initial impedance model utilised Naylor-1 and CRC-1 wells as shown in Figure 6.11. While potentially less stable the high frequency model could potentially map fine details which was of interest for a heterogeneous reservoir such is Waarre-C.

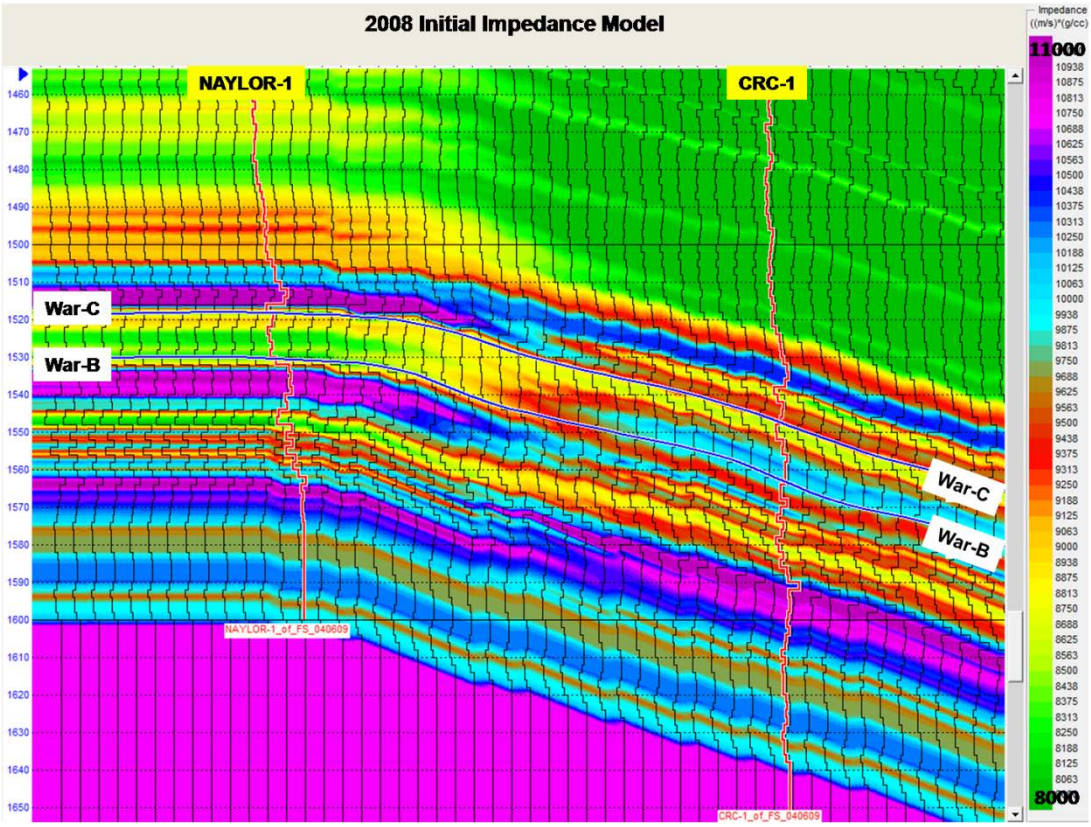

Figure 6.11 2008 (pre-injection/baseline) initial impedance model in dip direction. The top and base reservoirs are Waarre-C and Waarre-B. Naylor-1 well is in average 80% water saturation below GWC/gas cap and CRC-1 well is in average 80% water saturation. The initial impedance model then is to be used as a baseline model for inversion.

6.4.2 Model-based inversion

A model-based inversion was chosen because it allowed the incorporation of the seismic interpretations and well data (low and high frequencies model). This can result in better solution and a hence more meaningful link between the seismic data and the actual lithology, as determined from the well data and geological mapping. However, high frequencies may be coming from the initial "best guess" impedance model and not from the seismic data. To overcome this issue, it is important to honour the horizons interpretation from seismic data and to have good well-tie correlation. Still some inversion errors are to be expected due to non-uniqueness of the process itself.

Figure 6.12 shows the result of the 2008 (pre-injection/baseline) model-based inversion. Naylor-1 has lower impedance than CRC-1 due to residual gas methane. Higher impedance in CRC-1 might be also been contributed by increasing number of shale laminas, apart from the different saturation states.

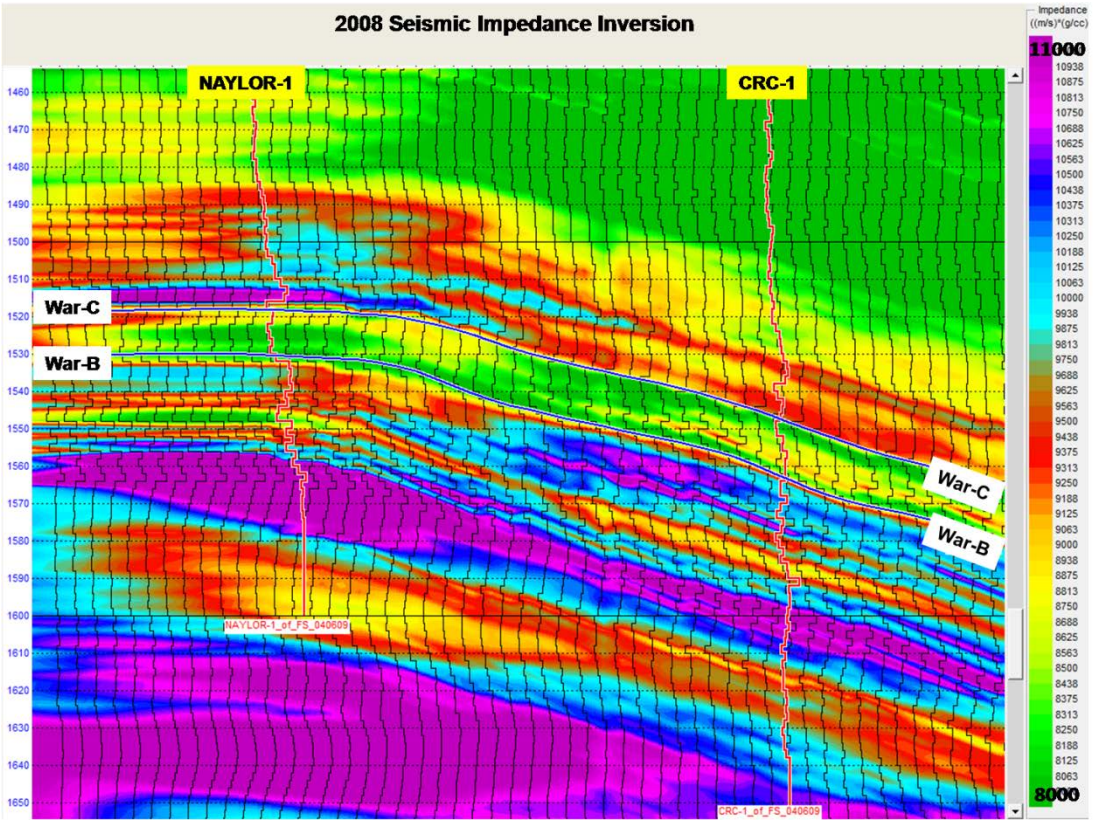

Figure 6.12 2008 (pre-injection/baseline) model-based inversion. The reservoir is in between Waarre-C and Waarre-B horizons. Above and below the reservoir zone remain unchanged. The red curves are impedance logs.

It is necessary to evaluate the relative performance of the different inversion results, which includes comparing the synthetic seismic volumes from the inversion with both seismic surveys (2008 and 2009). The aim is to obtain initial (base case) impedance error from the inversion of the actual seismic data, then from the series of inversions based on simulation models, which one minimises the error (smallest) that will most likely represent *in-situ* saturation. First, I inverted 2008 seismic volume at pre-injection saturation state. Inversion analyses at wells show impedance differences between log derived from inversion result and original log, synthetic error (close to zero indicates that the inversion has performed well) and produced a high correlation

between synthetic and seismic traces as shown in Figures 6.13 to 6.14. 2008 (pre-injection/baseline) derived synthetic volume from the inverted seismic data and 2008 (pre-injection/baseline) seismic amplitude data are shown in Figures 6.15 and 6.16, while their difference is shown in Figure 6.17.

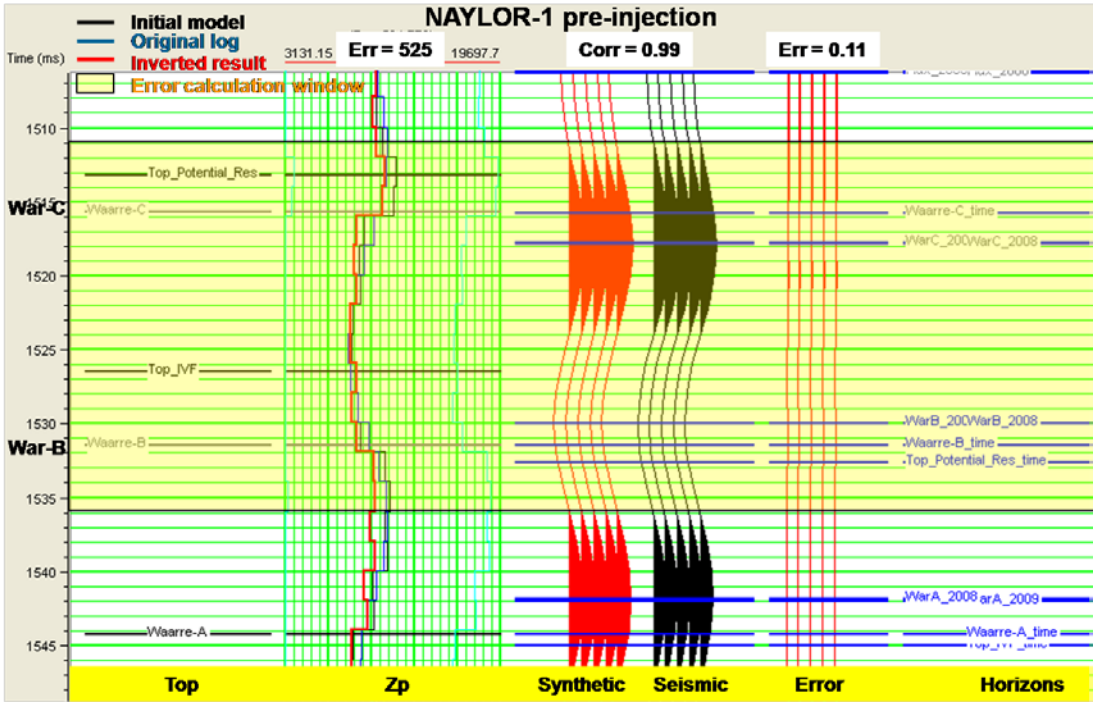

Figure 6.13 Naylor-1 2008 pre-injection inversion analysis. Small differences are calculated between inverted result and original log.

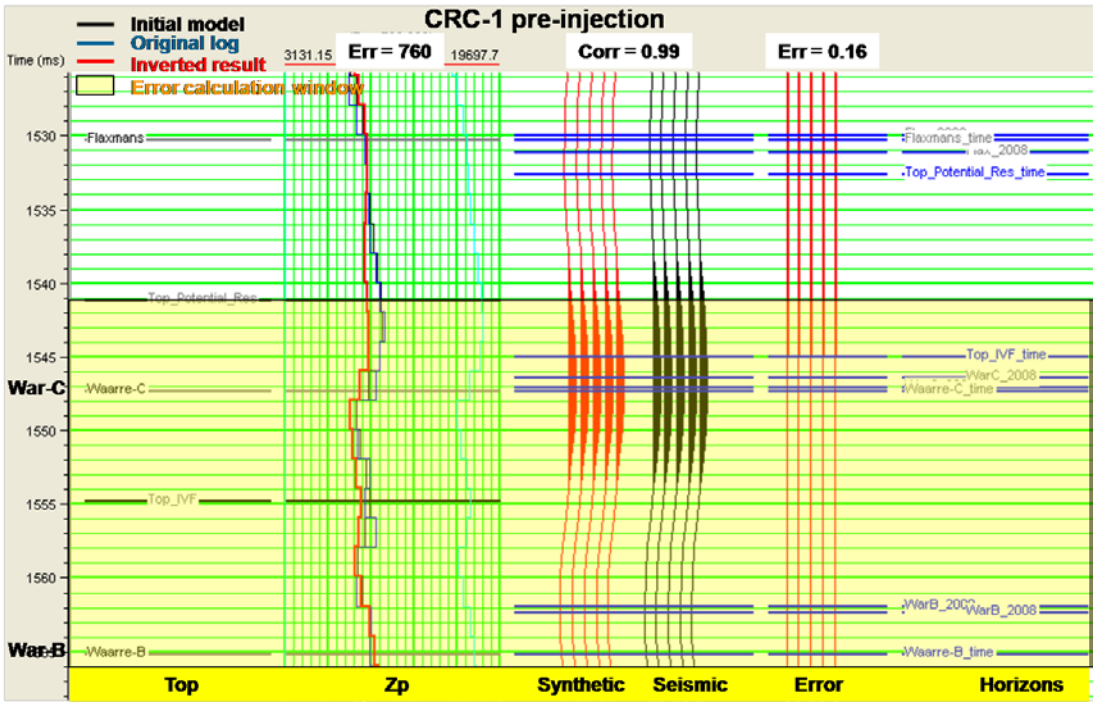

Figure 6.14 CRC-1 2008 pre-injection inversion analysis. Small differences are calculated between inverted result and original log.

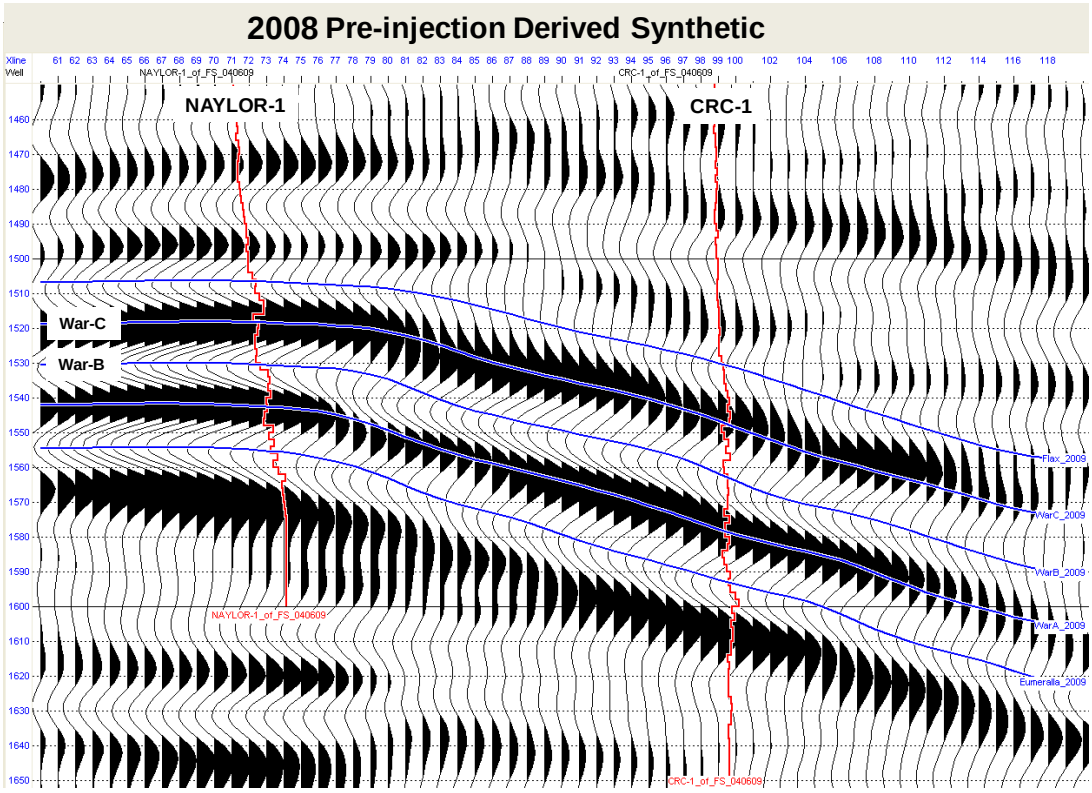

Figure 6.15 2008 (pre-injection/baseline) derived synthetic traces based on inversion result. The red curve is impedance log.

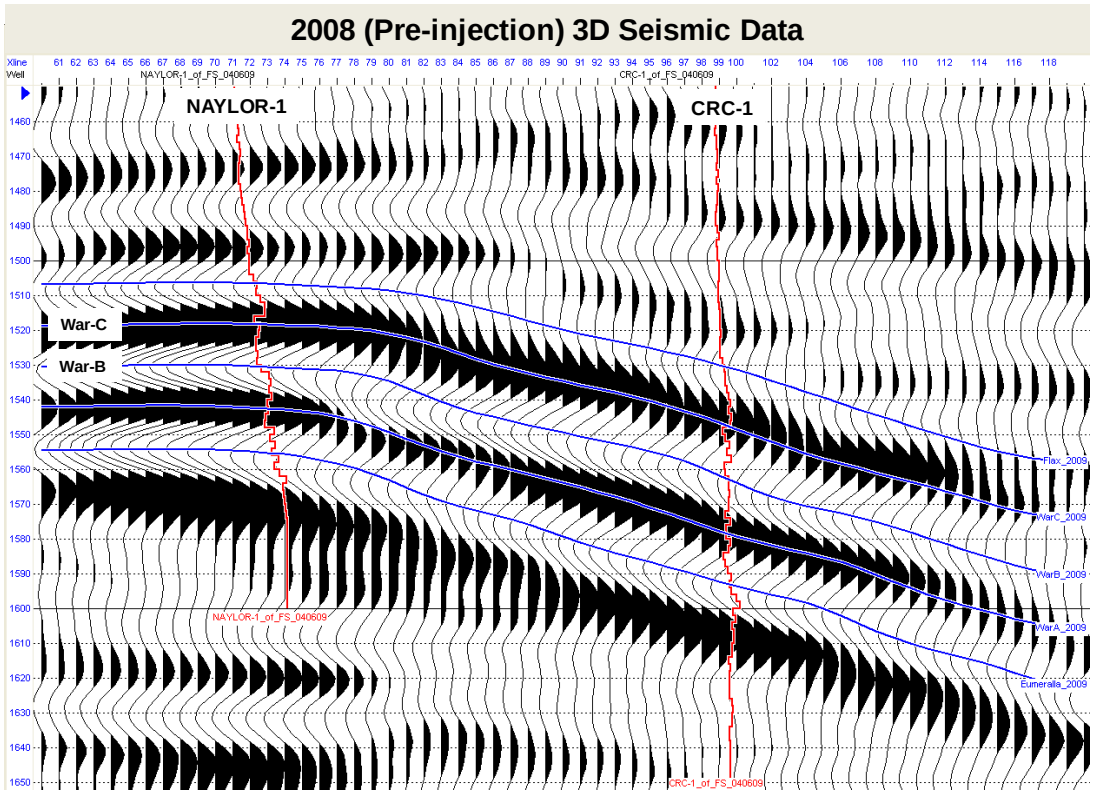

Figure 6.16 2008 (pre-injection/baseline) 3D seismic data is comparable to pre-injection derived synthetic traces in Figure 6.15.

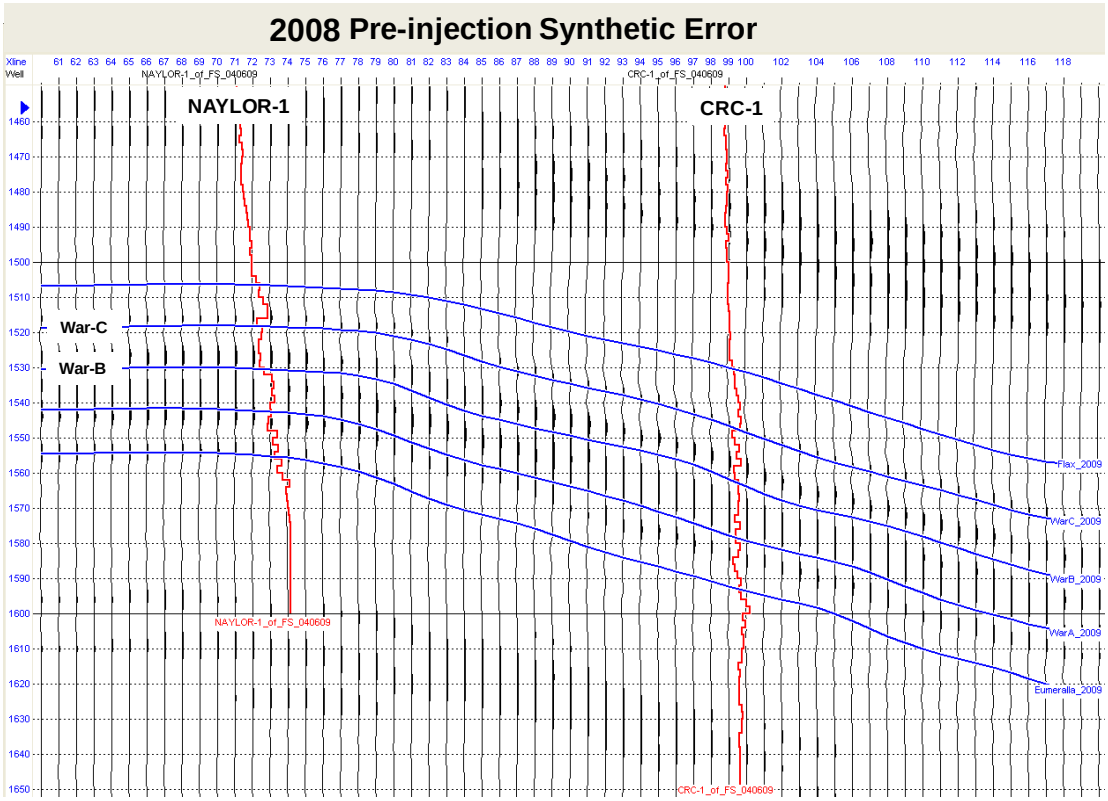

Figure 6.17 2008 (pre-injection/baseline) synthetic error derived by subtracting the derived synthetic traces from the actual seismic data.

The very small coherent error at the reservoir interval indicates that the 2008 derived model is a reasonably good representation of the seismic data. Hence, the 2008 initial impedance model could be used as a baseline for further time-lapse analyses. Furthermore, the impedance volume that used the well-based wavelet honouring the interpretation and wells produce a good match of impedances at the well and the lowest synthetic error.

Second, I inverted 2009 seismic volume using logs conditioned for the pre-injection saturation state. Figure 6.18 displays 2009 impedance inversion volume. Similar workflow was run for inversion analyses. The difference of 2008-2009 initial model-based impedance along Waarre-C horizon (horizon differencing) is shown in Figure 6.19.

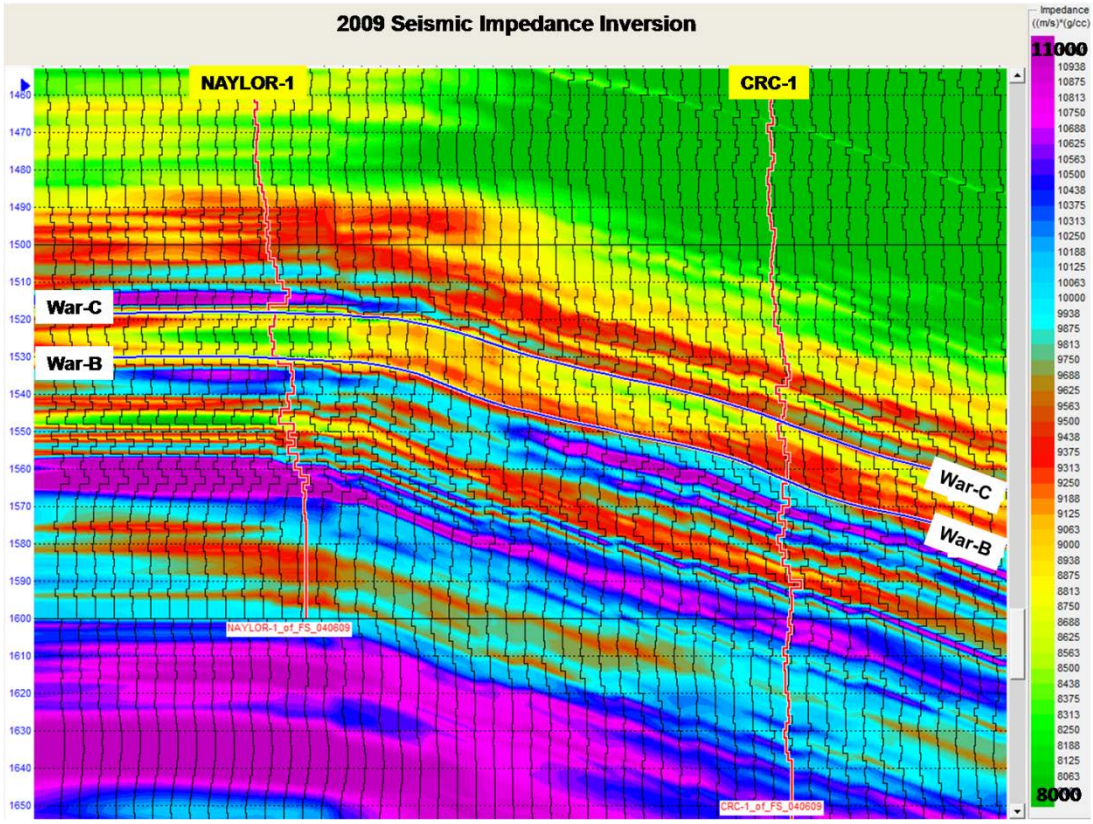

Figure 6.18 2009 model-based inversion of pre-injection. The reservoir is in between the War-C and War-B horizons. Above and below the reservoir zone remain unchanged. The red curves are impedance logs.

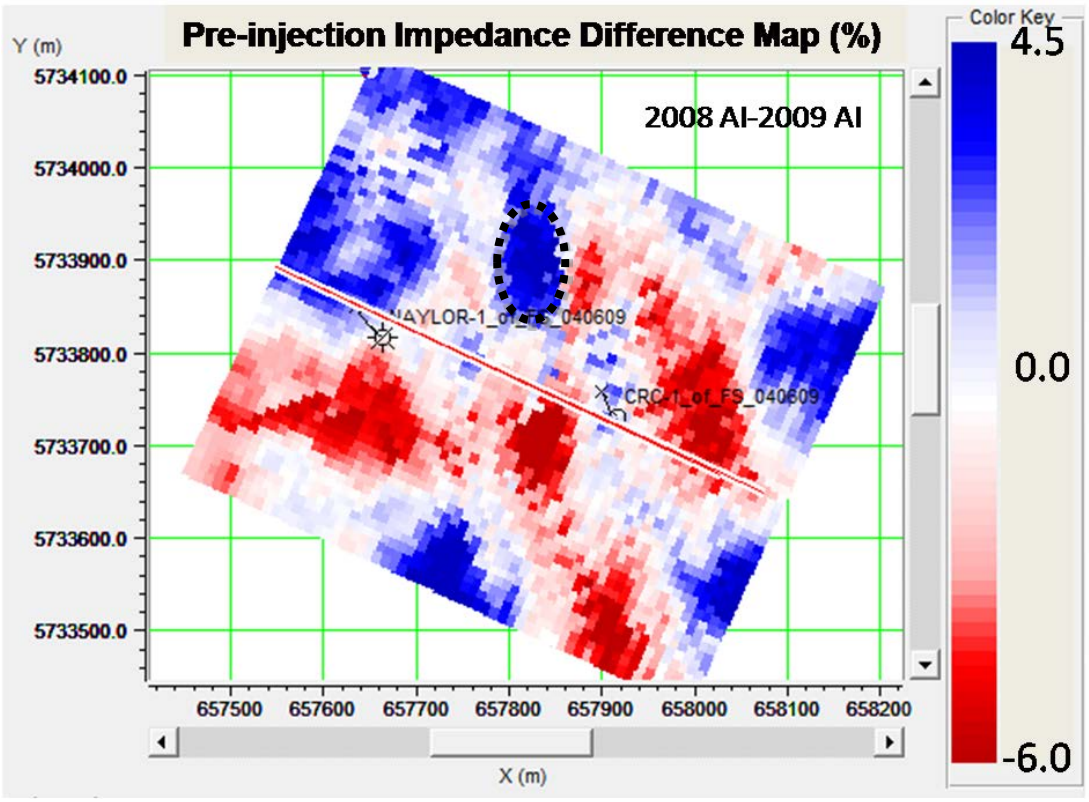

Figure 6.19 Pre-injection impedance difference map as a result of 2008 and 2009 seismic impedance volumes subtraction.

The initial (base case) impedance difference map show the error window within +4.5% to -6.0% with the maximum positive value located between both wells (ellipse dotted line) as shown in Figure 6.19. Positive values suggest 2008 impedance is larger than 2009 impedance and vice versa.

Since the state of the reservoir in terms of fluid saturation was unknown at the moment of the acquisition of the first monitor data I used reservoir simulation studies to perform fluid substitution modelling. The next step was then to utilise these "updated" CRC-1 logs for successive inversion runs. The idea was to analyse the inversion error/difference. The minimum error/difference would then suggest the most likely saturation state of the reservoir.

Therefore I used rock physics models and derived fluid substitution logs based on simulation models for the successive inversions of 2009 data. Figure 6.20 a) and b) show simulation models (Leahy, 2009) of pressure and saturation states that were

used for updating CRC-1 logs. The synthetic and the actual data difference are compared in Figure 6.20 c). This was encouraging result and suggested that further studies of the time-lapse signal are promising.

Since the inversion results is log-depend to some extent (as controlled by the choice of the inversion parameters selected), the fluid substitution methodology could be potentially used to estimate the saturation and pressure state of the reservoir in January 2009, after some 35,000 tonnes of CO_2 were injected. For each reservoir simulation case and predicted state of the reservoir, a new set of fluid substitution logs was computed. These logs, after correlation were then used in inversion. The results are illustrated in Figures 6.21 to 6.24. The best match with the recorded seismic data and the time-lapse match would suggest the state of reservoir after injection of 35,000 t of CO_2.

a)

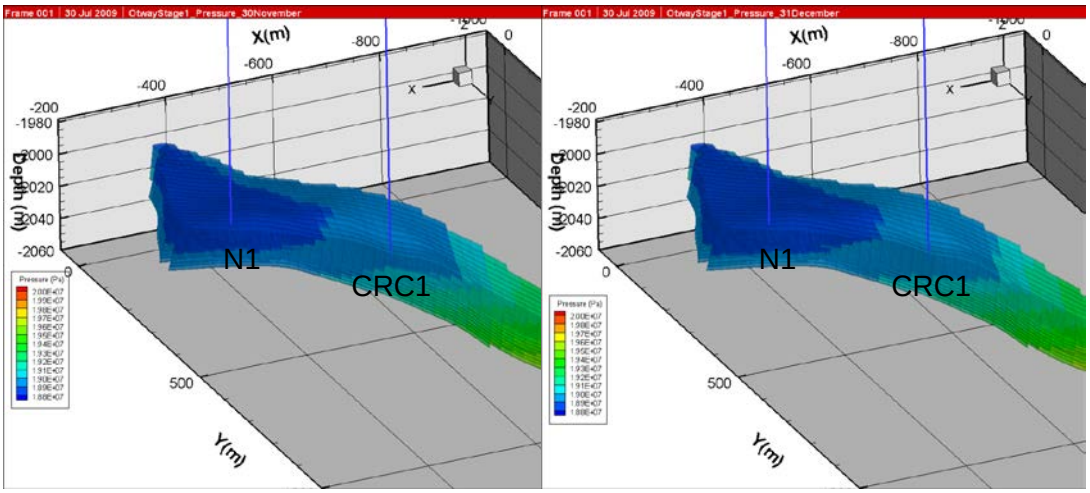

Pore pressure @30 Nov

Pore pressure @31 Dec

b)

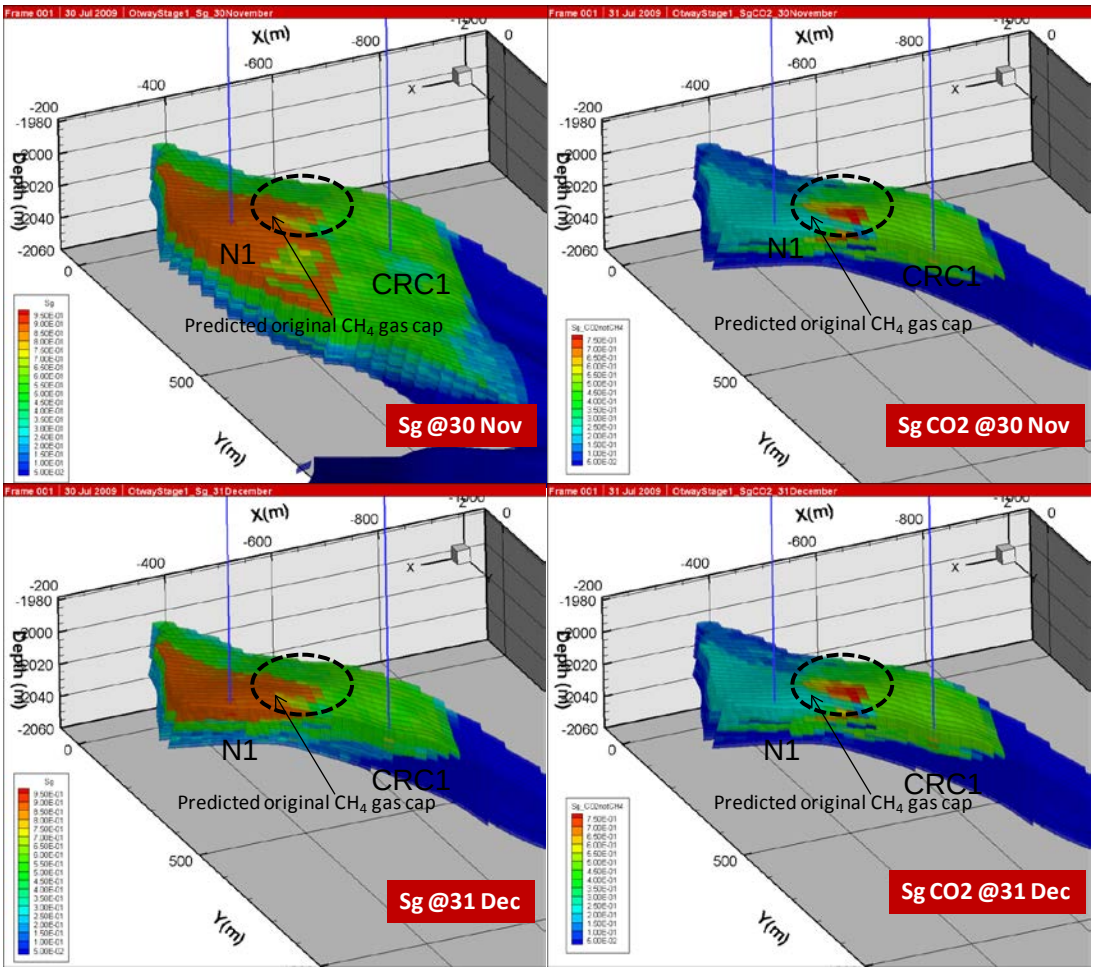

c)

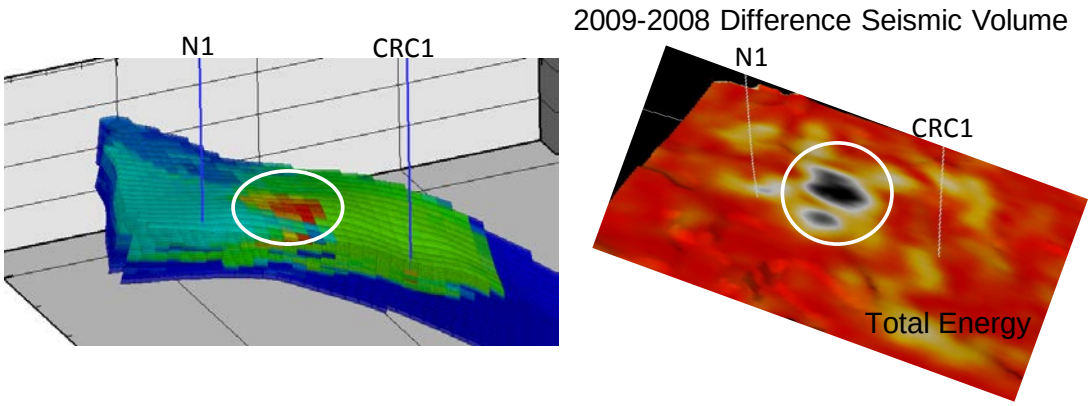

Figure 6.20 Simulation models of a) pore pressure and saturation on 30th Nov and 31st Dec 08, b) total gas saturation and CO_2 saturation on 30th Nov and 31st Dec 08 and c) the comparison between the differences (2008-2009) for the simulation model and the seismic RMS amplitudes. The two appear similar.

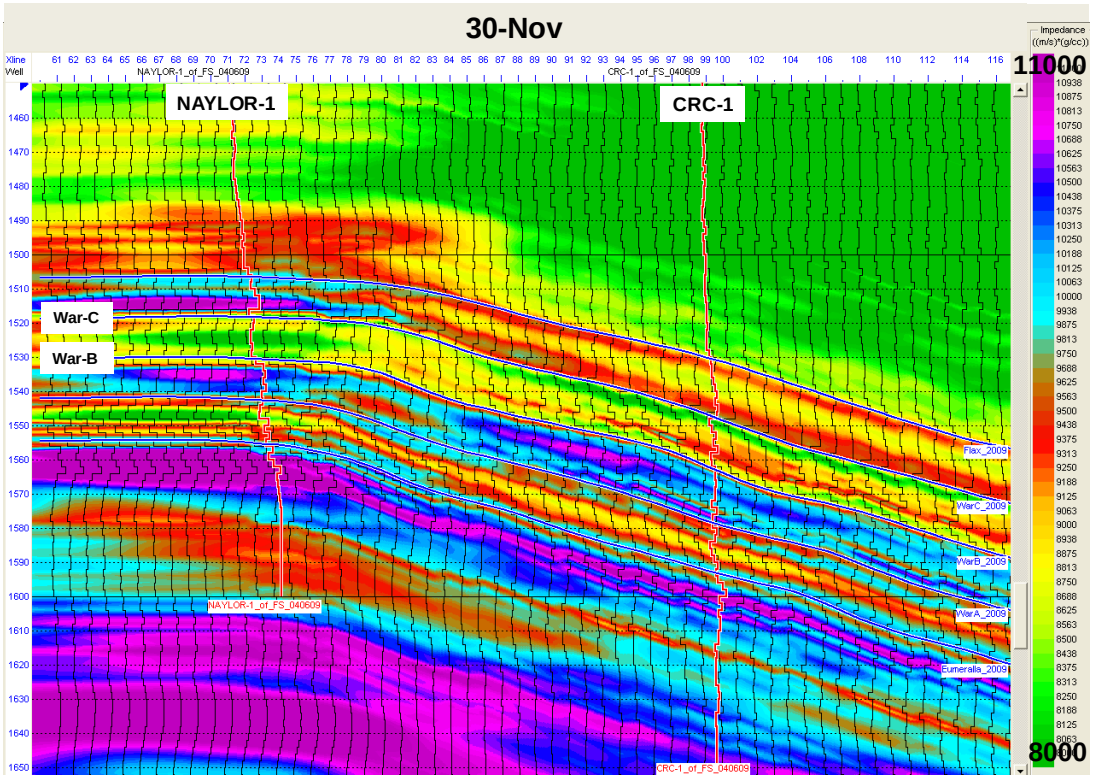

Figure 6.21 30th Nov 08 model-based inversion (Leahy's model). The model simulated 31,000 tonnes CO_2 to be injected at pore pressure 18.9 MPa and 40% of mix gases with CO_2 content around 45% saturation in CRC-1 well; at pore pressure 18.6 MPa and 35% of mix gases with CO_2 content around 30% saturation in Naylor-1 well.

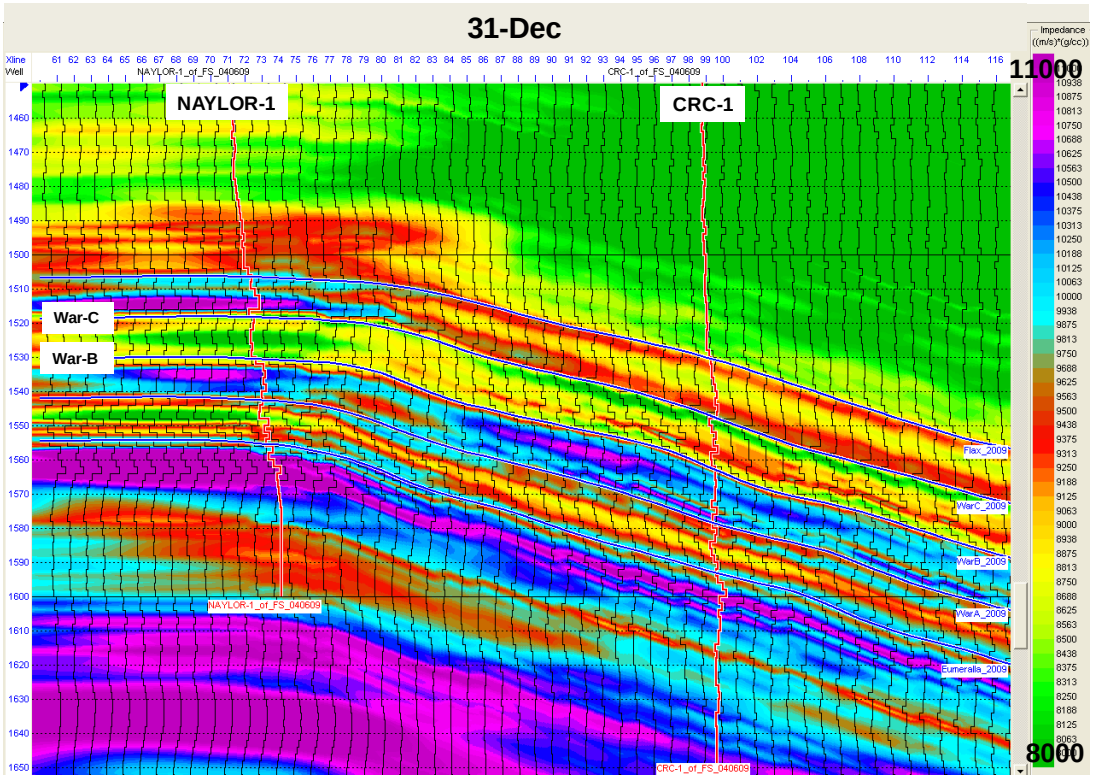

Figure 6.22 31st Dec 08 model-based inversion (Leahy's model). The model simulated 35,000 tonnes CO_2 to be injected at pore pressure 19 MPa and 50% mix gases saturated with CO_2 content around 55% in CRC-1 well; at pore pressure 18.6 MPa and 40% mix gases saturated with CO_2 content around 35% in Naylor-1 well.

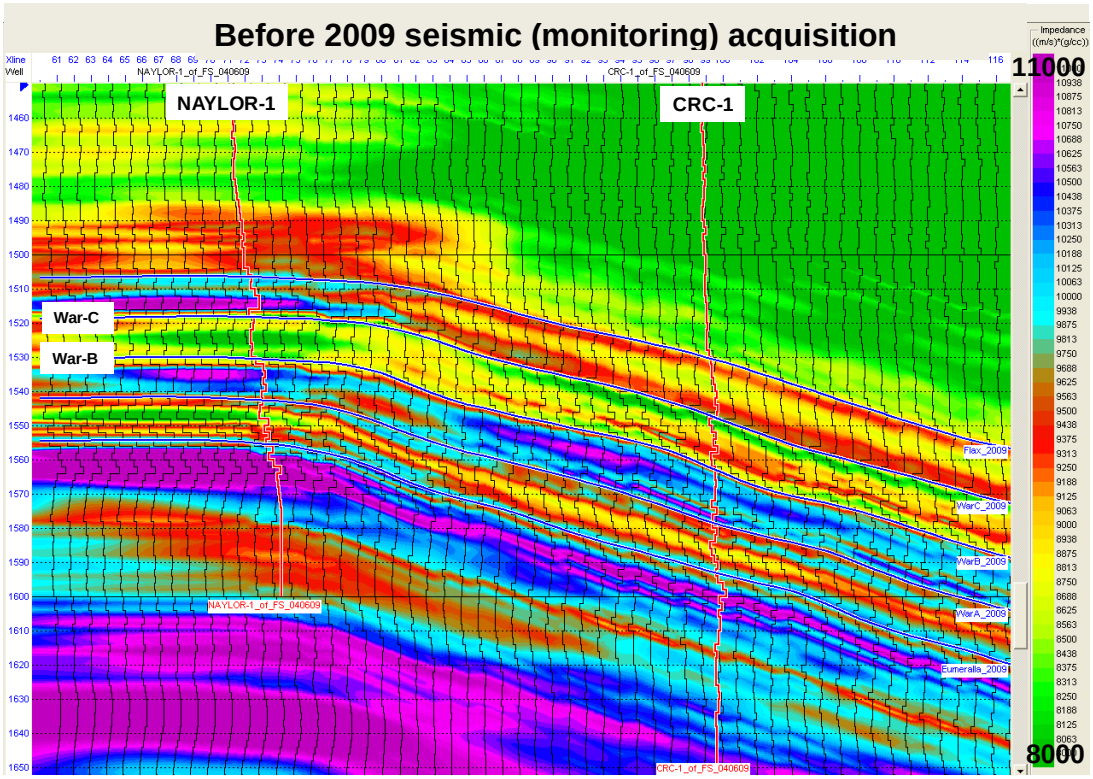

Figure 6.23 Before 2009 seismic (monitoring) acquisition model-based inversion (Xu's model after 6 months of injection – Table 6.1 c). The model simulated after 35,000 tonnes CO_2 to be injected at pore pressure 19 MPa and 50% of mix gases saturated with CO_2 content around 55% in CRC-1 well; at pore pressure 18.7 MPa and 40% mix gases saturated with CO_2 content around 45% in Naylor-1 well.

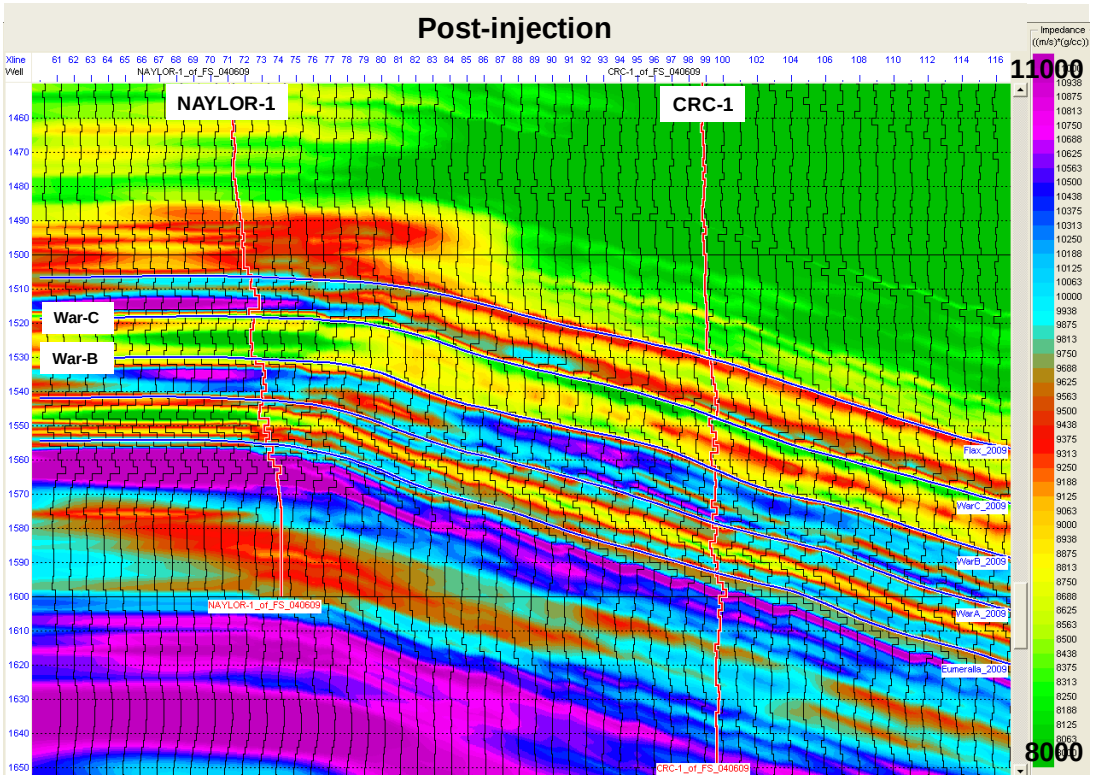

Figure 6.24 2010 post-injection model-based inversion (Xu's model – Table 6.1 a). The model simulated 100,000 tonnes CO_2 to be injected at pore pressure of 20 MPa and 80% mix gases (source is from Buttress-1 well with CO_2 content around 80%) saturated in average, within the reservoir between Naylor-1 and CRC-1 wells.

6.5 Time-lapse study

6.5.1 Difference volumes

I differentiated both synthetic and inversion volumes with actual seismic volume and obtain the best match at the well locations. The percentage difference was calculated using the equation:

$$\%Diff\ (\Delta) = \frac{Baseline - Monitoring}{Monitoring} \times 100, \qquad (6.1)$$

The result will be positive when the baseline value is greater than the monitoring and the result will be negative when the baseline value is less than the monitoring. The difference equation is applied for both seismic and well data. The outputs are amplitude and impedance.

6.5.1.1 Amplitude

Amplitudes were extracted from seismic and synthetic data with varying pressure and saturation states then the differences between the volumes were calculated. 2008 (pre-injection/baseline), 2009 (monitoring) and 2008-2009 difference volumes are shown in Figure 6.25 to 6.27 in a form of a chair display. The effect of the CO_2 plume due to fluid movement is suggested by a modified amplitude shape in Figure 6.26 from initial one displayed in Figure 6.25. The maximum difference between the two is seen in Figure 6.27. Smaller differences were observed at the Naylor-1 well and moderate differences were observed at the CRC-1 well. The simulation model generated similar results. The total energy difference map computed over a 20ms window centred at Waarre-C (Urosevic et al., 2009) showed similar trend as it can be observed in Figure 6.27 c). Magnitudes of changes were small around Naylor-1 and moderate around CRC-1 wells. Subtraction in the area with red circle (CO_2 plume) resulted in negative values where 2009 seismic amplitude are larger than 2008 seismic amplitude and the difference changes are between 10-60%. This is illustrated in Figures 6.28 and 6.29. There could be several possible reasons for such anomaly. One possibility was that some small gas presence in Flaxman formation before CO_2 injection increased after CO_2 injection which would result in the impedance drop and hence positive difference.

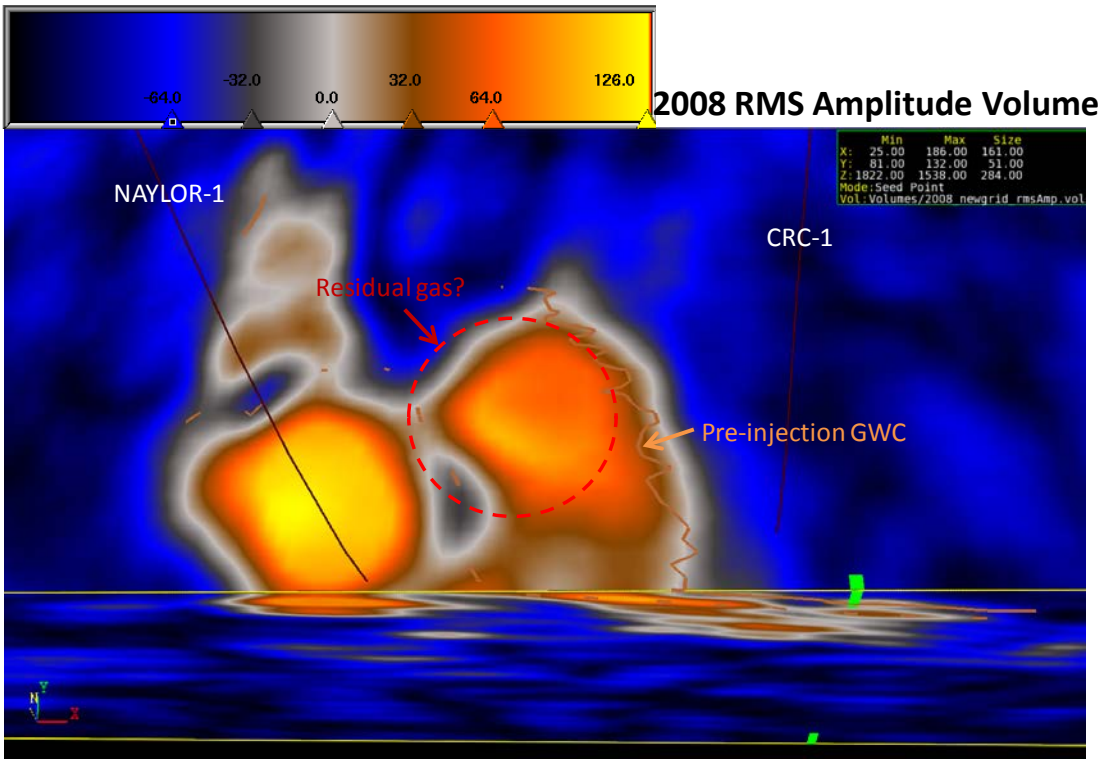

Figure 6.25 RMS amplitude of 2008 (pre-injection/baseline) 3D seismic volume. Pre-injection GWC was coincidence with the edges of the anomaly. The seismic cube is overlain with Waarre-C (top reservoir) interpretation.

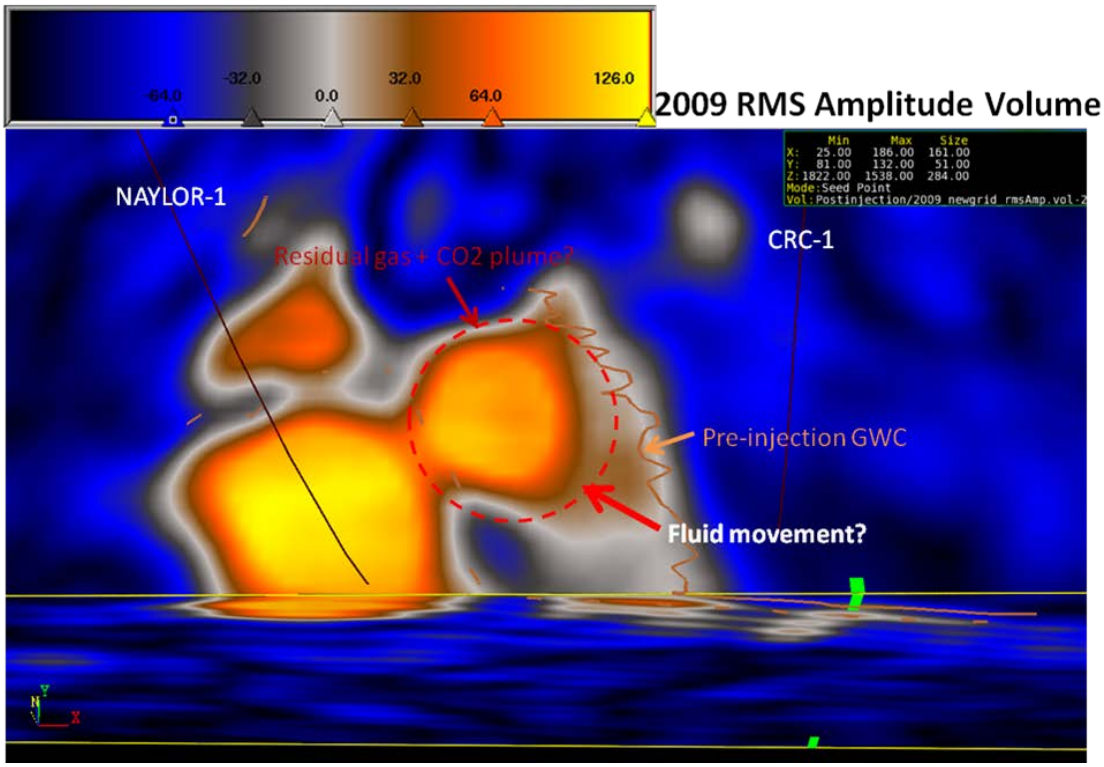

Figure 6.26 RMS amplitude of 2009 (monitoring) 3D seismic volume. Some difference with respect to 2008 data can be seen.

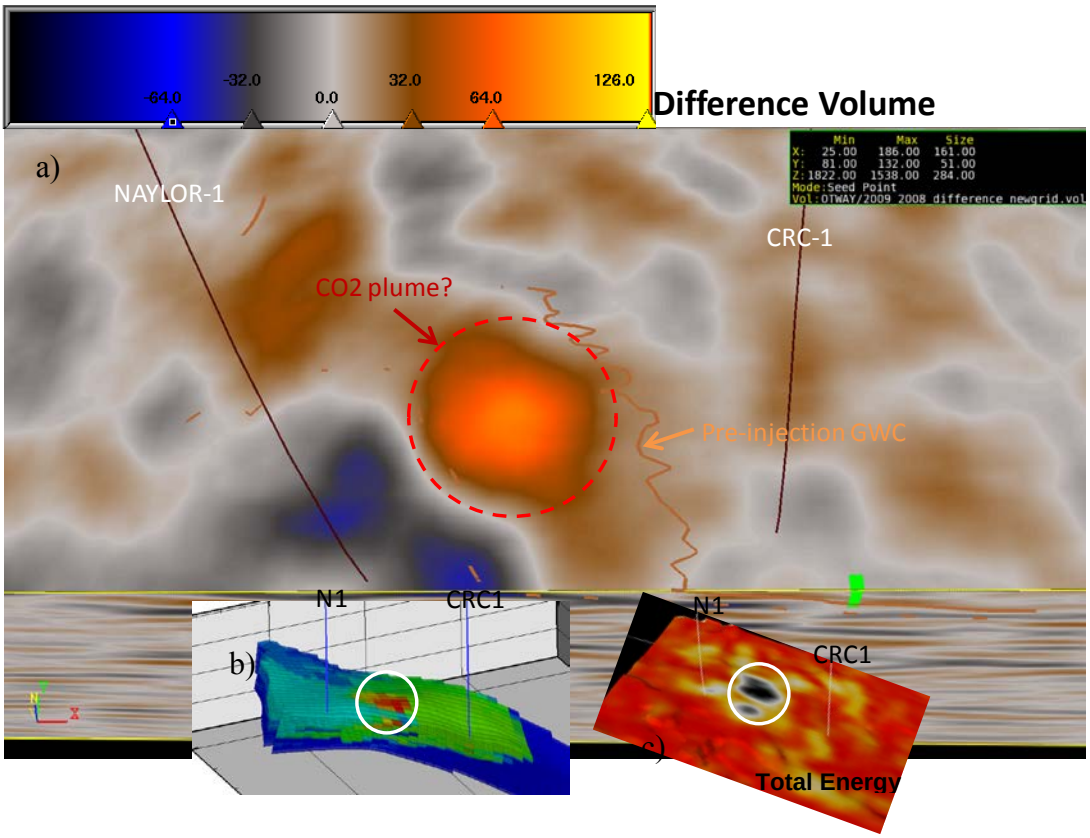

Figure 6.27 a) Difference volumes of 2008-2009 3D seismic data, b) Simulation model and c) Total energy difference map. Similar trends are observed.

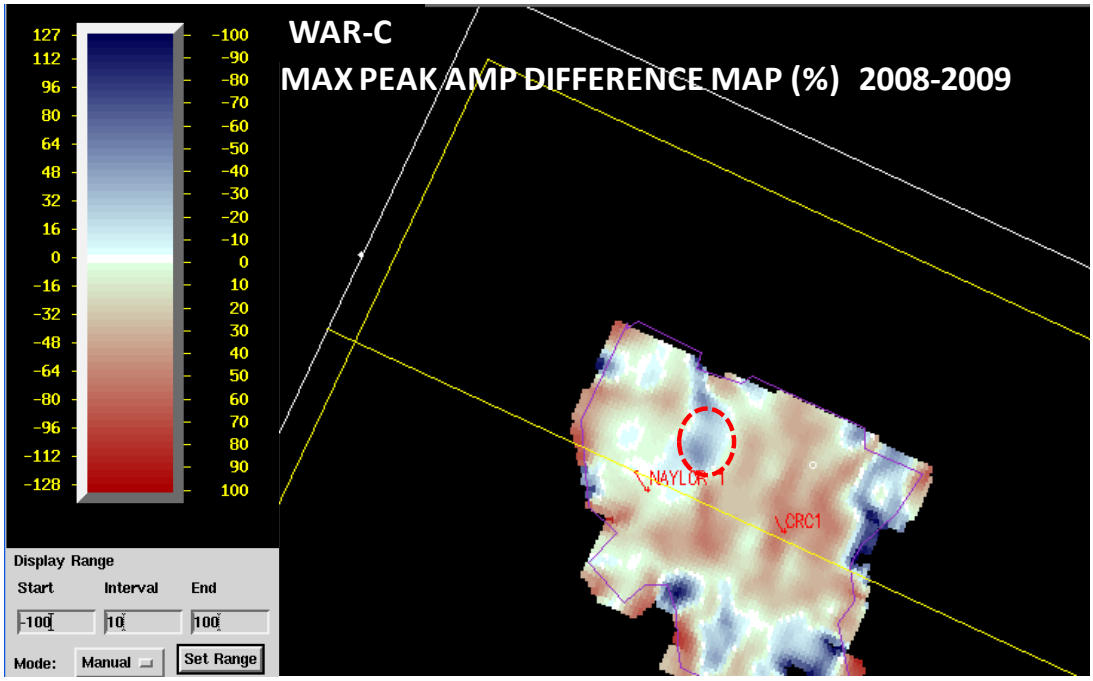

Figure 6.28 Top War-C maximum peak amplitude difference map of 2008-2009 seismic data. The area within the plume (red dotted circle) indicates the magnitude of maximum differences. Anomalous time-lapse signal are observed and similar trends as shown in Figure 6.27.

Figure 6.29 shows the top War-C maximum peak amplitude changes of 2008 (pre-injection/baseline) with 2009 (monitoring) seismic data for all dip lines.

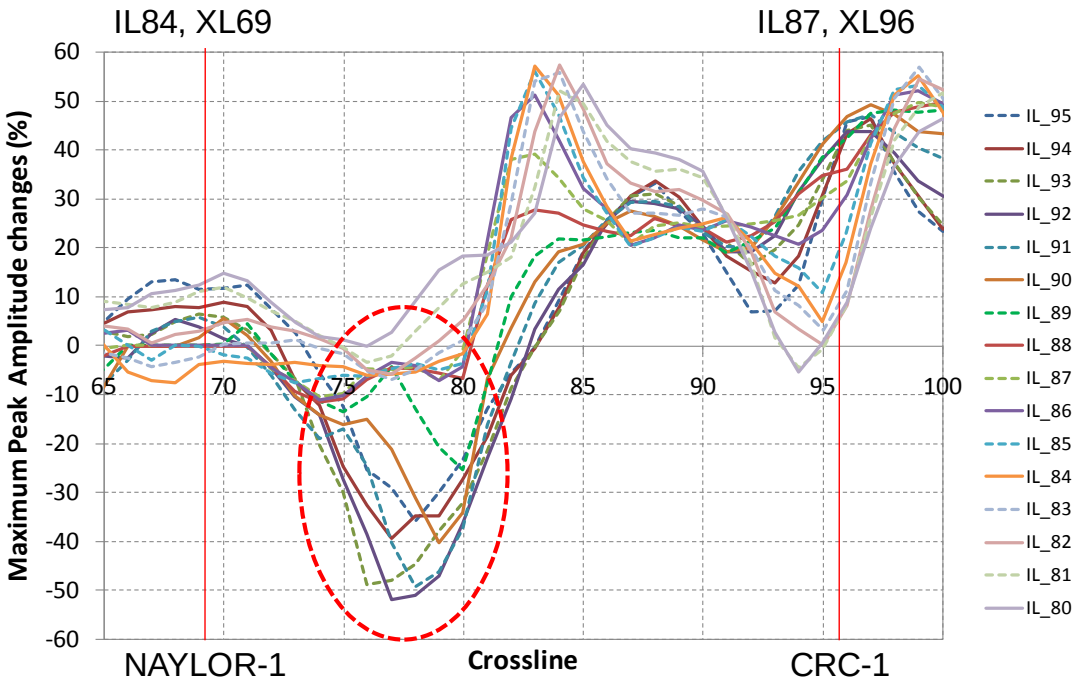

Figure 6.29 Cross plot of top War-C maximum peak amplitude changes at and between wells extracted along dip lines.

Overall, the magnitudes of the changes are ± 60% depending on the dip line number. Amplitude at Naylor-1 suggests very little change while amplitude at CRC-1 suggests more change. The maximum changes happened at dip line 92 associated with the plume (red dotted circle). Amplitudes between wells suggest phase change could likely exist. The differences computed are large, certainly greater than predicted by fluid substitution modelling. Errors related to data processing may play significant part in this estimate, particularly when working with amplitude differences. I extracted the amplitudes from the synthetic traces based on simulation models. I compared the amplitude extraction from the synthetic traces with actual seismic data. The magnitude of the changes of the synthetic amplitude is smaller than the time-lapse amplitude changes of the actual seismic data. However, if we scale up by a factor of 4 then the results agree. Naylor-1 synthetic traces and amplitude differences are shown in Figure 6.30 to 6.32. Pre- and post- CO_2 injection seismograms for Naylor-1 are shown in Figure 6.30. In Figure 6.31 the differences are shown for all cases covered by reservoir simulation. A composite plot documenting seismograms computed for different state of CO_2 saturation is shown in Figure 6.32. Equivalent analysis was done for CRC-1 well. The results are documented in Figures 6.33 to 6.35.

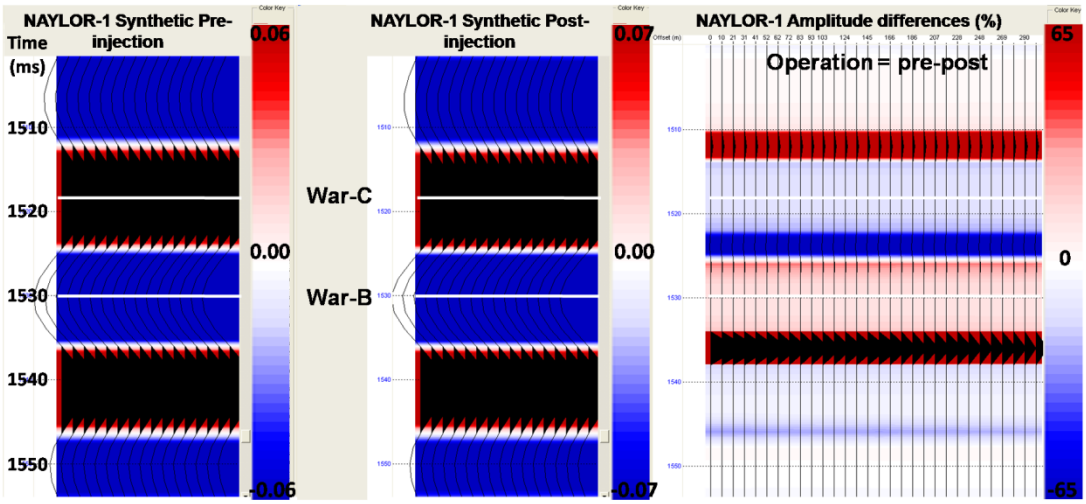

Figure 6.30 Naylor-1 synthetic traces and amplitude differences.

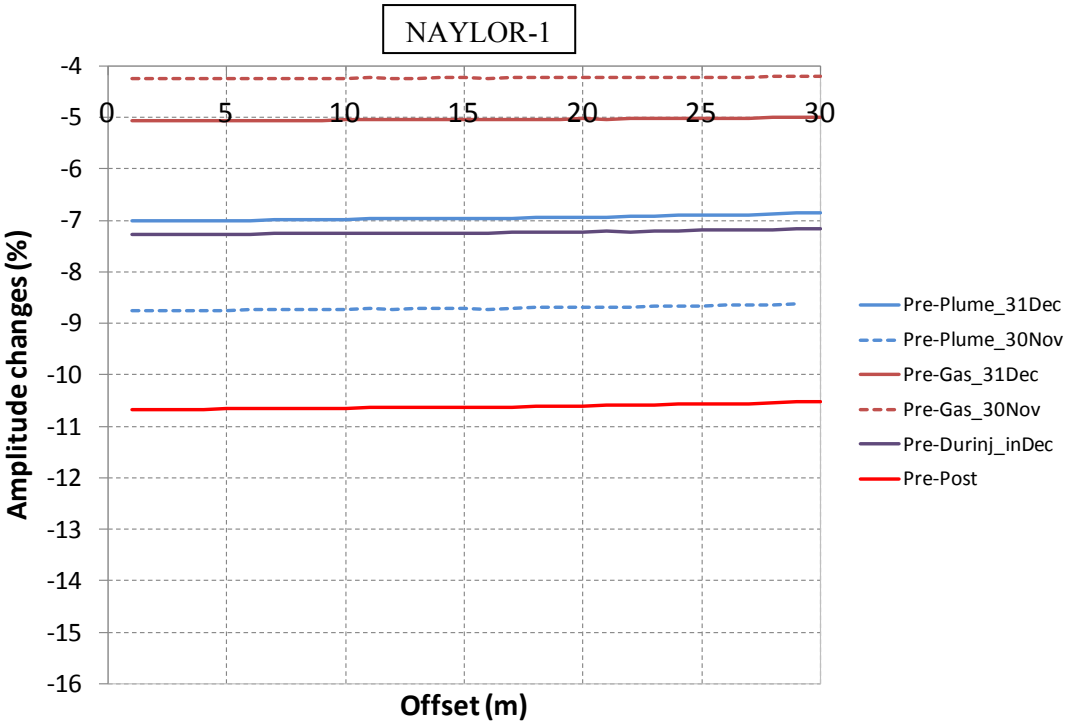

Figure 6.31 Synthetic modelling plots showing the amplitude difference in varying saturation states. Amplitude difference calculated over 20ms window centred at Waarre-C. If it is scaled up by factor of 4, then the result will agree with seismic amplitude. Maximum amplitude changes achieved after post-injection (red line).

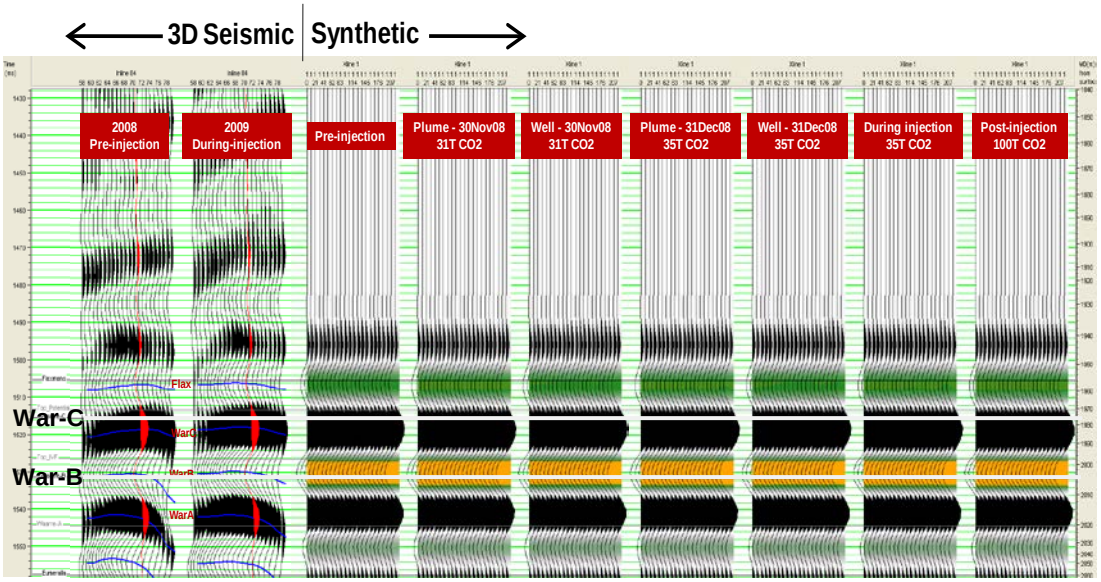

Figure 6.32 Composite display of Naylor-1, seismic data and synthetic traces for different state of CO_2 saturation. 2009 during-injection refers to the time before 2009 seismic (monitoring) acquisition.

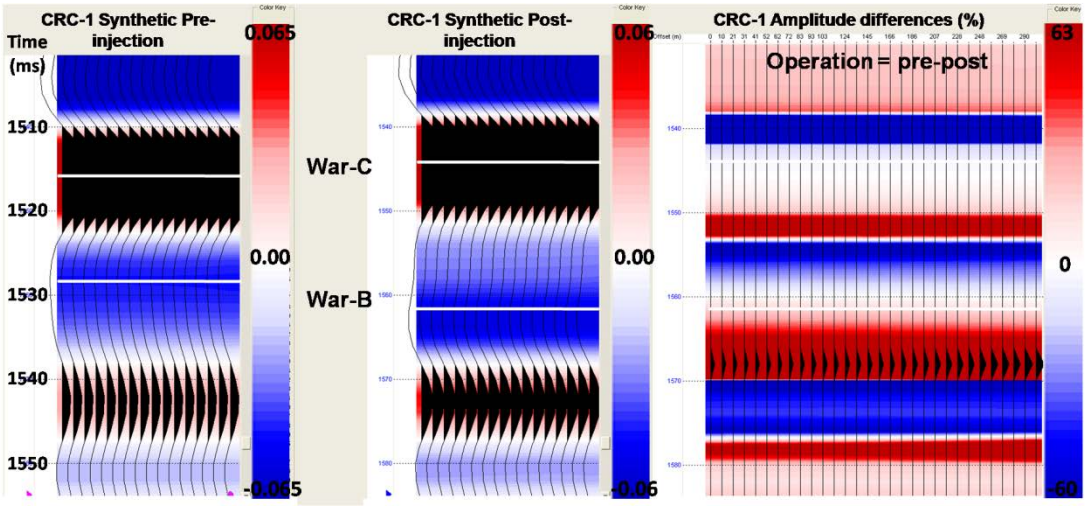

Figure 6.33 CRC-1 synthetic traces and amplitude differences.

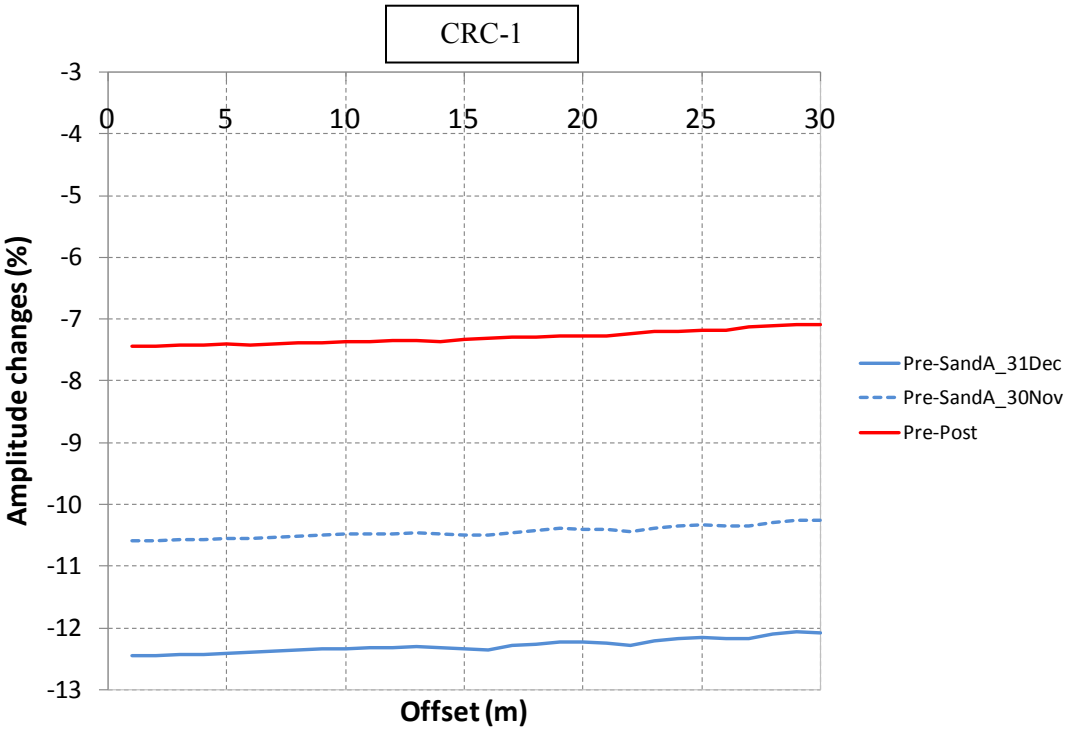

Figure 6.34 Synthetic modelling plots showing the amplitude difference in varying saturation states. Amplitude difference calculated between pre- and post-injection over a 20ms window centred at Waarre-C.

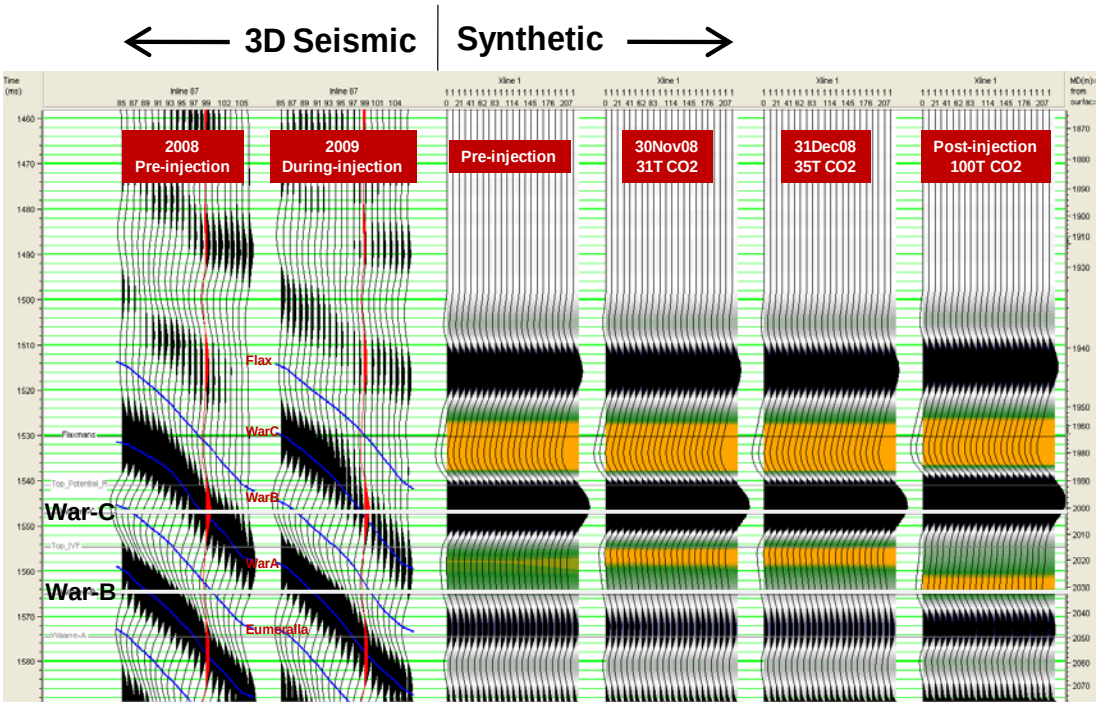

Figure 6.35 Composite display of CRC-1, seismic data and synthetic traces. 2009 during-injection refers to the time before 2009 seismic (monitoring) acquisition.

The results of synthetic data in these Figures 6.31 and 6.34 suggest that the time-lapse differences at CRC-1 are smaller than at Naylor-1 after post-injection (pre-post line) but not at the time of injection. This is perhaps suggested by the seismic data which for 2009 (monitoring) show amplitude dimming at CRC-1 well. Other option, as previously mention is increased gas presence in Flaxman formation, above Waarre-C. In both cases the predicted changes at the boreholes are small and as previously suggested would be very difficult to detect by time-lapse field seismic which suffers from relatively low (and possibly variable) signal to noise ratio.

It was noted that the changes occurred at the upper part of the sand interval where the CO_2 was injected and the thickening of CO_2 layer below Waarre-C was visible. An upward time shift of 2-3ms was clearly observed in the synthetic traces. This may cause problems when computing simple amplitude differences. Consequently further studies were required to shed additional light on the time-lapse amplitude study results.

6.5.1.2 Impedance inversion

The inversion can be thought of as the process of determining the reflectivity of seismic events in the subsurface and relating them to predictive models in an attempt to reveal reservoir properties away from well control. The reflectivity is expressed through the acoustic impedance differences across the interfaces of a series of layers that make up the reflectivity coefficient (RC). Thus the differences of RC can be calculated at well locations as:

$$\Delta RC = \frac{RC_m - RC_b}{RC_b} \times 100, \tag{6.2}$$

where

$$RC_m = \frac{Z_{Waarre-C_m} - Z_{Flaxman_m}}{Z_{Flaxman_m} + Z_{Waarre-C_m}}, \text{ and} \tag{6.3}$$

$$RC_b = \frac{Z_{Waarre-C_b} - Z_{Flaxman_b}}{Z_{Flaxman_b} + Z_{Waarre-C_b}}. \tag{6.4}$$

Subscript *m* and *b* are monitoring and baseline data, respectively. Monitoring (*m*) describes the fluid substitution logs based on simulation models. *Z* is the acoustic impedance. A cartoon diagram of a simple static geological model to be studied is illustrated in Figure 6.36. The dynamic behaviour comes from the variable fluid state in the reservoir.

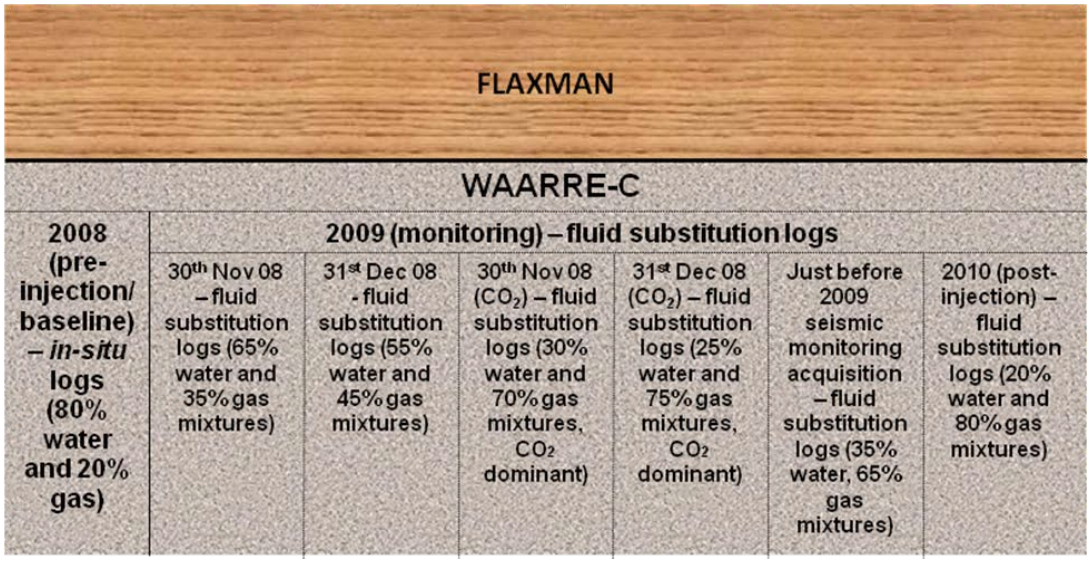

Figure 6.36 Cartoon of a simplified geological model. Elastic properties of Flaxman formation are kept constant (b=m). The *in-situ* (2008) elastic properties of Waarre-C are used as a baseline to derive fluid substitution logs based on reservoir simulation studies.

The impedances derived at the wells are plotted in Figure 6.37 and 6.38. Both plots show the changes at wells and the anomaly or the "bull eyes" plume between Naylor-1 and CRC-1 at different level within reservoir interval. The maximum reflectivity and impedance changes would be achieved when 100,000 tonnes of CO_2 is injected. A 1 - 4.5% change in impedance causes 3.5 – 15% (negative numbers) changes in reflectivity at Naylor-1 as plotted in Figure 6.37. The predicted changes in impedance are within the initial inversion error (Figure 6.19) and reflectivity at Naylor-1 is similar to the trend observed in the field data (Figure 6.29). This difference could be elevated by the chemical reaction between mineral rocks and CO_2 which soften the rock frame and reduces the density and potentially increases the porosity. This will increase the impedance contrast thus boost the amplitude values with respect to predicted changes at wells. However, considering mineral

composition of Waarre-C sand, this is highly unlikely to happen on a considerable scale. It is most likely that the factor of 4 differences between predicted and measured can be attributed to low repeatability and possibly some processing artefacts.

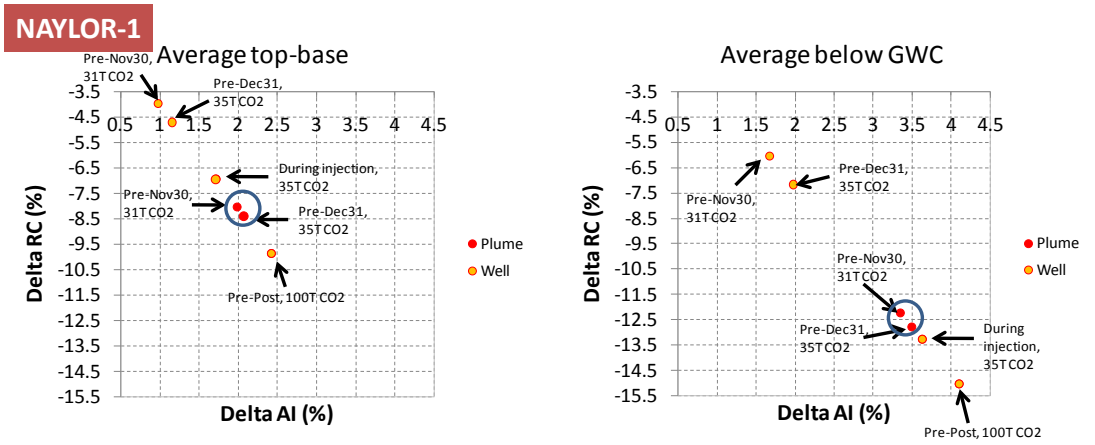

Figure 6.37 Cross plot of Naylor-1 maximum reflectivity and impedance changes at different saturation states.

I simulated changes in CRC-1 when CO_2 was injected in the upper sand interval (Sand-A; 30th Nov and 31st Dec) to align with the time when monitoring survey was acquired. 1.5 - 6% changes in impedances cause 21 – 41% (negative numbers) changes in reflectivity as plotted in Figure 6.38 and 6.29. In general, the predicted impedance change is still within the inversion error window (Figure 6.19).

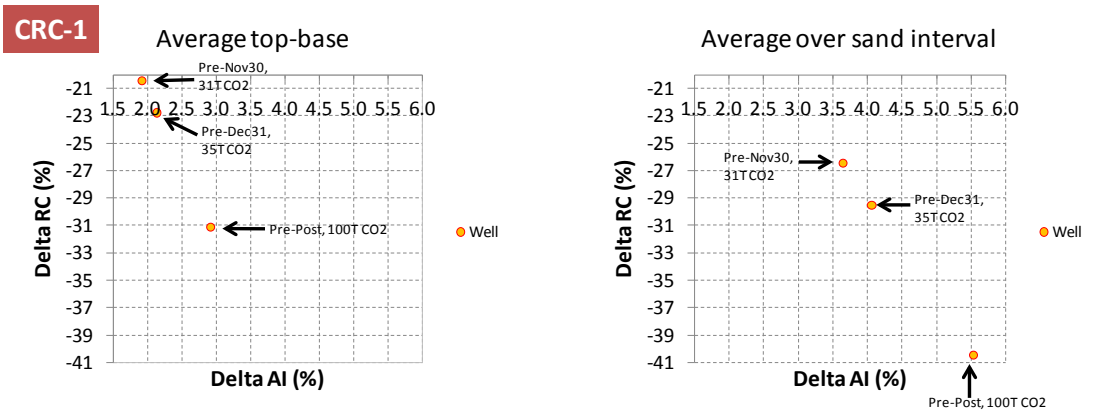

Figure 6.38 Cross plot of CRC-1 maximum reflectivity and impedance changes at different saturation states.

I simplified impedance inversion time-lapse as shown in Figure 6.36 to Figure 6.39. I only selected impedance inversion results that give most time-lapse effect. The difference in impedance changes throughout the reservoir in the vertical sense as well. Hence I made the calculation within 6ms time window in the reservoir interval. Similar impedance differences were calculated from logs.

Impedance inversion and difference map based on simulation models are displayed in Figure 6.40 to 6.42. Table 6.4 summarises these results.

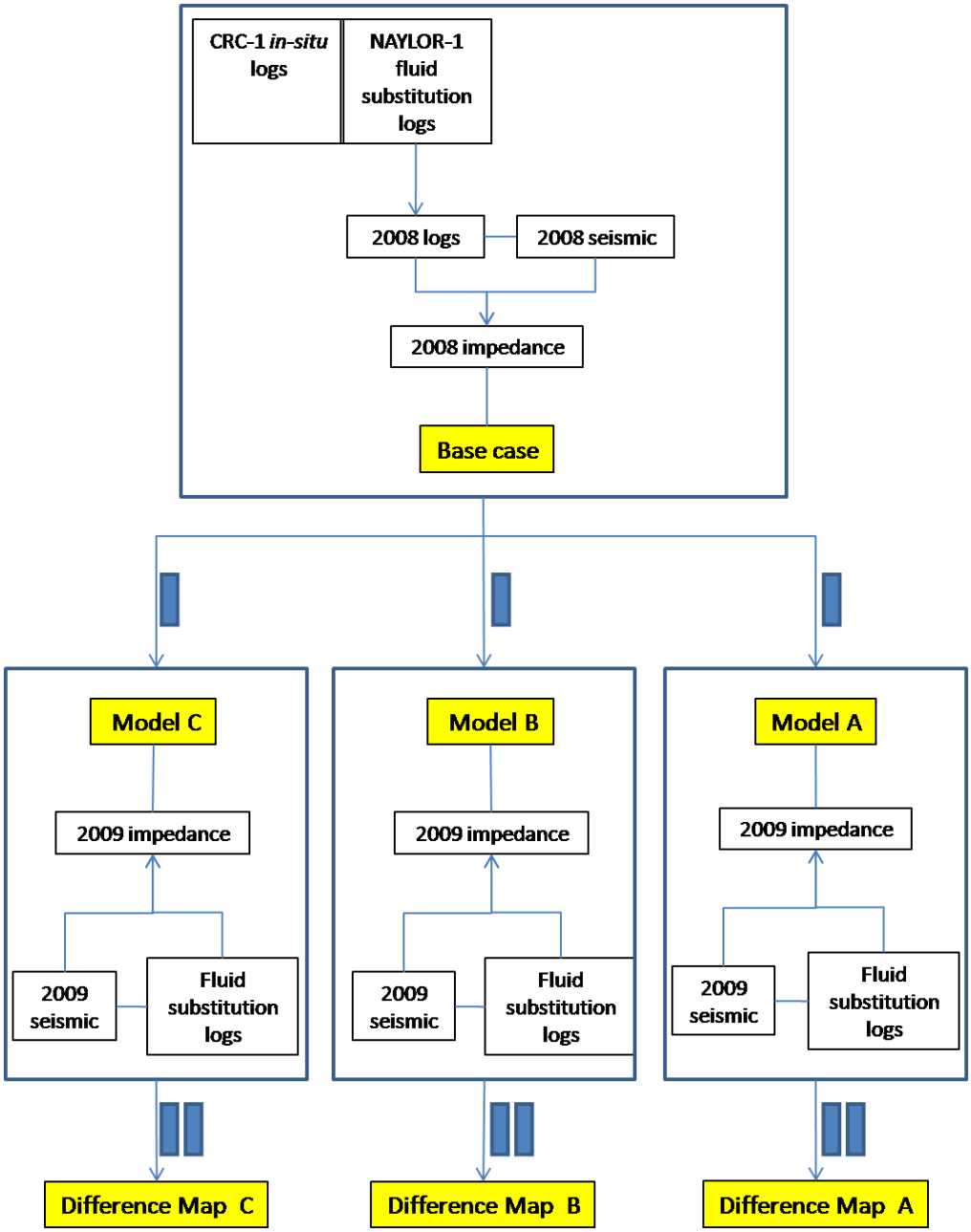

Figure 6.39 A simplified diagram workflow of impedance inversion time-lapse.

Table 6.4 Impedance difference summary

Impedance Difference Summary				Base Case with 2008 seismic
				Pre-injection Logs
				CRC-1 *in-situ* logs/NAYLOR-1 fluid substitution logs - 80% water and 20% CH_4
Models with 2009 seismic	A	Fluid Substitution Logs	30th Nov 08 - 65% water and 35% gas mixtures; 31K t CO_2 injection	(-1)% to (-3)% Impedance difference around wells
	B		Before 2009 seismic (monitoring) acqusition 35% water and 65% gas mixtures; 35K t CO_2 injection	(-1)% to (-2.5)% impedance difference around wells
	C		2010 (post-injection) - 20% water and 80% gas mixtures; 100K t CO_2 injection	0 to (-0.5)% in Naylor-1; 0.5% to 1% Impedance difference around wells

Model A

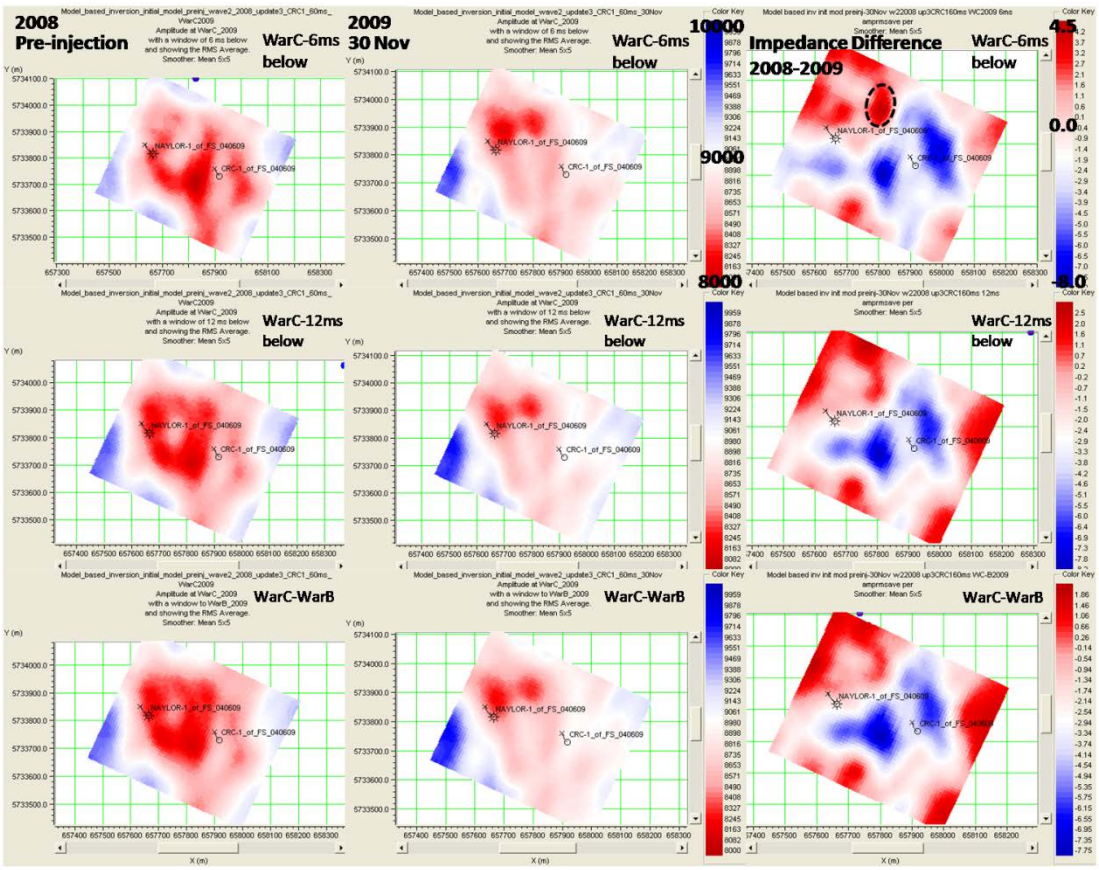

Figure 6.40 RMS amplitude from model-based inversion for the case A of 2008 (pre-injection/baseline), 2009 30 Nov and the differences.

Model B

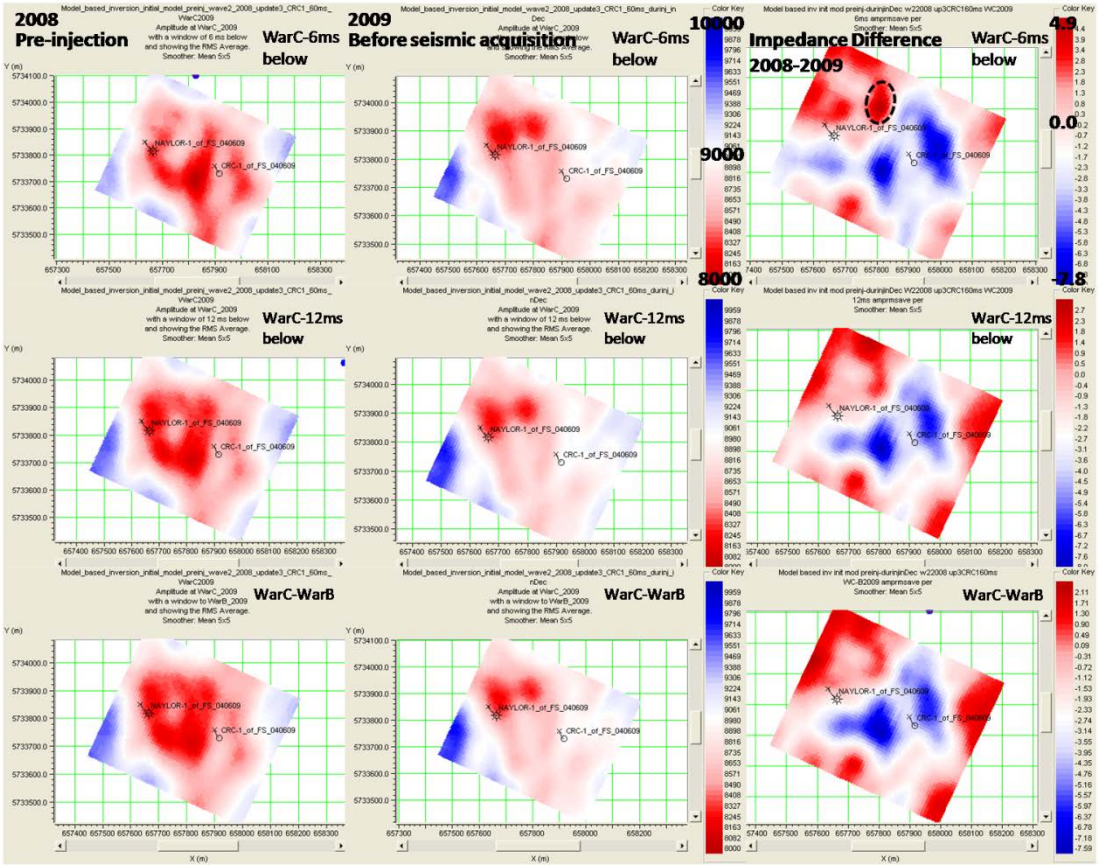

Figure 6.41 RMS amplitude from model-based inversion for the case B of 2008 (pre-injection/baseline), 2009 before seismic acquisition and the differences.

The magnitudes of impedance differences in CRC-1 well suggest higher density effect when CO_2 was injected at that time. The results are similar with Figure 6.40; however the impedance inversion differences at the "bulls-eye" are relatively higher than the impedance derived from logs but still within the range (Figure 6.37).

The 30th Nov impedance inversions differences are similar with 2009 before seismic acquisition as seen in Figures 6.40 and 6.41. It suggests it is not possible to distinguish the changes in seismic response within 31,000 and 35,000 tonnes CO_2 injection with CH_4/CO_2 fluid mixtures (not a CO_2 only) as pore fluids in real data, a part of different saturation state.

Model C

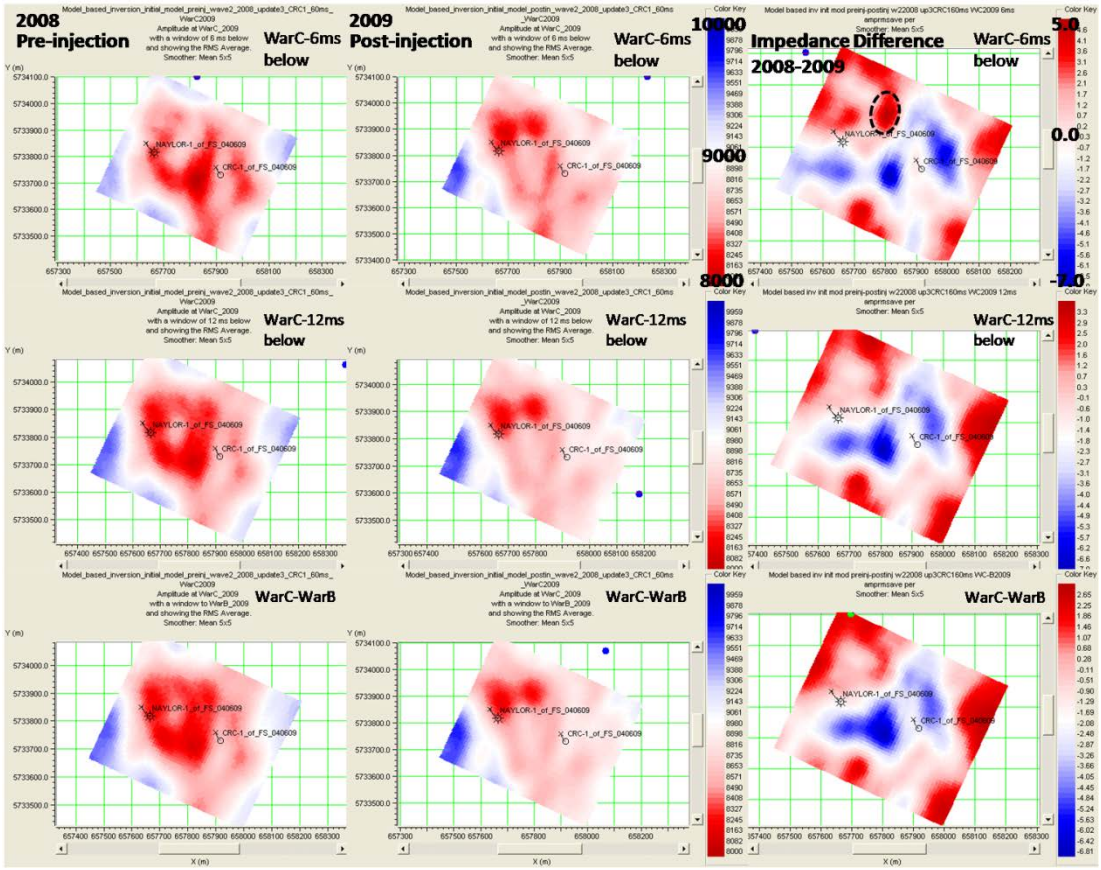

Figure 6.42 RMS amplitude map from model-based inversion for case C of 2008 (pre-injection/baseline), 2009 post-injection and the differences.

Impedance difference at the "bull eyes" (red dotted circle) show consistently maximum positive differences in all saturation states which could be interpreted as a CO_2 plume. Negative difference is given to CRC-1 (Naylor-1 remains unchanged), which likely having increasing of impedance after injection due to density effect as displayed in Figures 6.40 to 6.42. Another possibility is gas content change in the Flaxman formation.

The acoustic impedance inversion differences observed at the Naylor-1 well (Table 6.4) does agree with the impedance derived from the Naylor-1 logs on average from top to base but not on average below the GWC (Figure 6.37) where larger impedance difference is calculated. However, in general it falls within the range of impedance inversion differences expected. An exception is that the impedance inversion

differences observed at CRC-1 well (Table 6.4) are smaller in average over sand interval than the impedance derived from the CRC-1 logs (Figure 6.38). It is possible that some form of "patchiness" took place after injection.

We now assumed that 100,000 tonnes of CO_2 is injected into a homogeneous and isotropic reservoir; the composite computed changes in elastic properties for both wells are modelled in Figure 6.43 a) and b). The objective was now to investigate if 100,000 tonnes of CO_2 will be sufficient to cause measurable time-lapse seismic effects.

The acoustic impedance inversion difference suggested that up to 6% change on average would be expected (Figure 6.40 to Figure 6.43). The similar acoustic impedance results at the wells suggested 3% change on average as plotted in Figures 6.37 and 6.38. A 100,000 tonnes of CO_2 injection produced up to 6% impedance change as shown in Figure 6.43. Changes in impedance greater than or equal to 4% should result in observable seismic responses in the 3D seismic surveys (Lumley et al., 1997). 2008-2009 time-lapse seismic difference volume has confirmed and proved that the largest anomaly observed in the area to the north-east of the Naylor-1 well where the maximum impedance changes exist.

a)

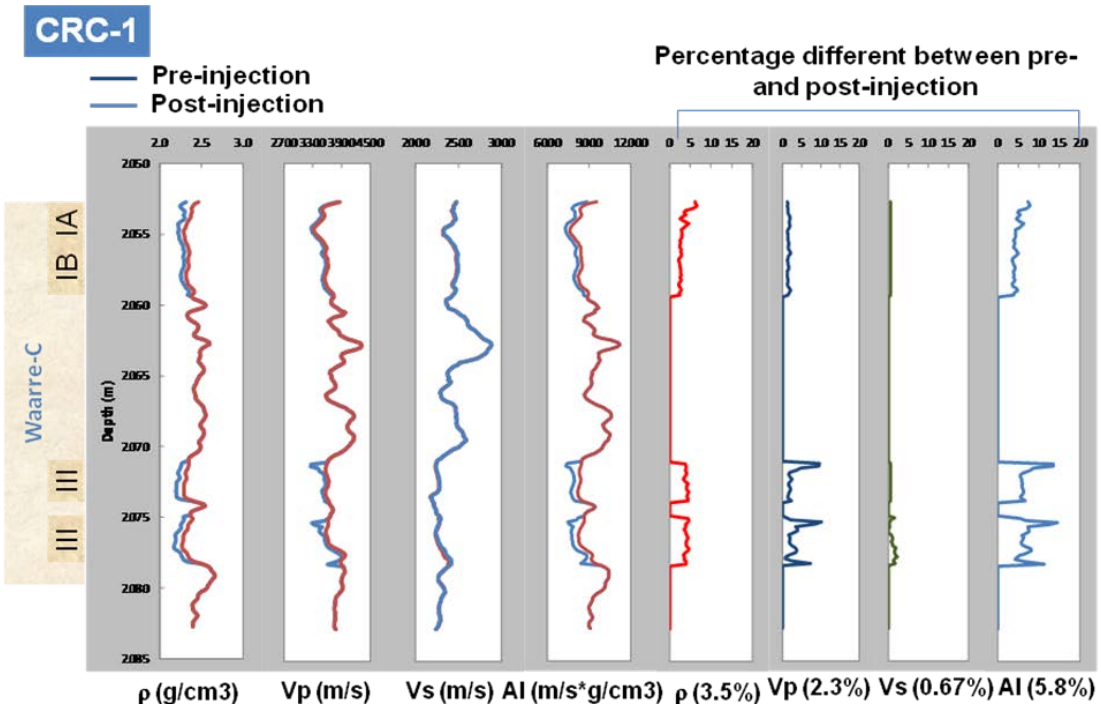

b)

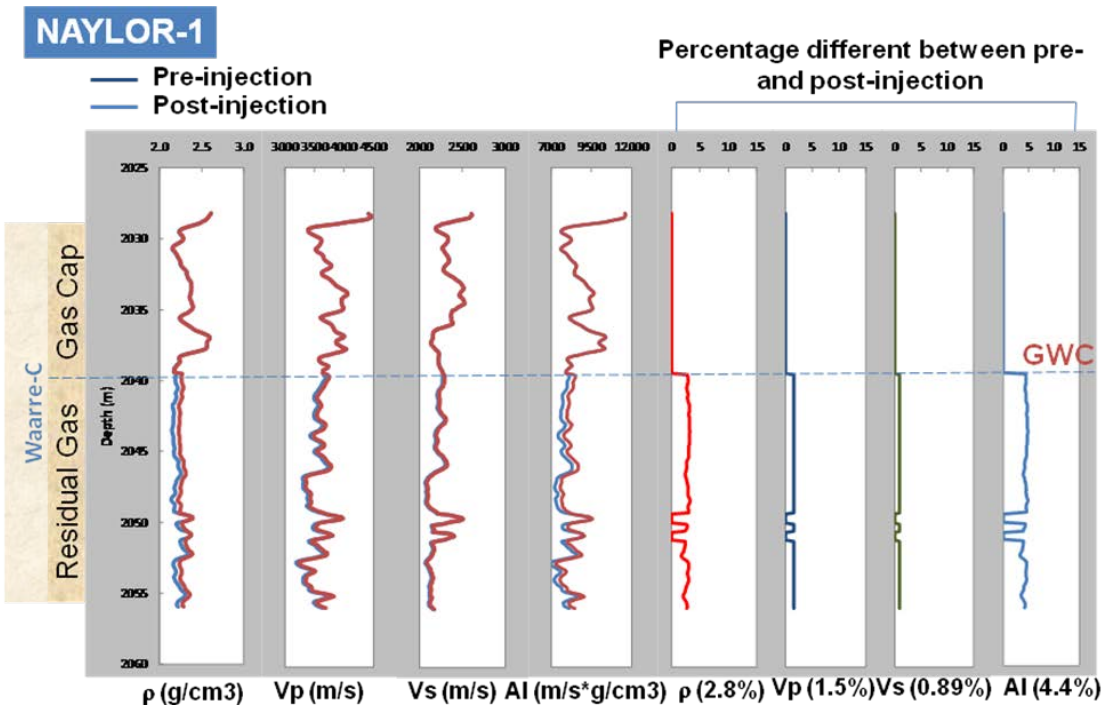

Figure 6.43 The composite computed elastic properties changes of a) CRC-1 and b) Naylor-1 wells when 100,000 tonnes of CO_2 is injected. The impedance changes reached the maximum around 6%.

6.6 Discussion and conclusions

Prediction and measurements of time-lapse seismic effects proved to be exceptionally challenging at Naylor field. Apart from the field small size, reservoir heterogeneity, lack of base line log for Naylor-1 and repeated log for CRC-1 and very small volume of CO_2 injected, additional difficulty are presented in terms or signal to noise ratio of repeated seismic volumes. I have therefore looked for very alternative methodologies to be able to analyse observed seismic anomalies produced within the Otway experimental survey.

Observed time-lapse anomalies are summarised in Figure 6.44.

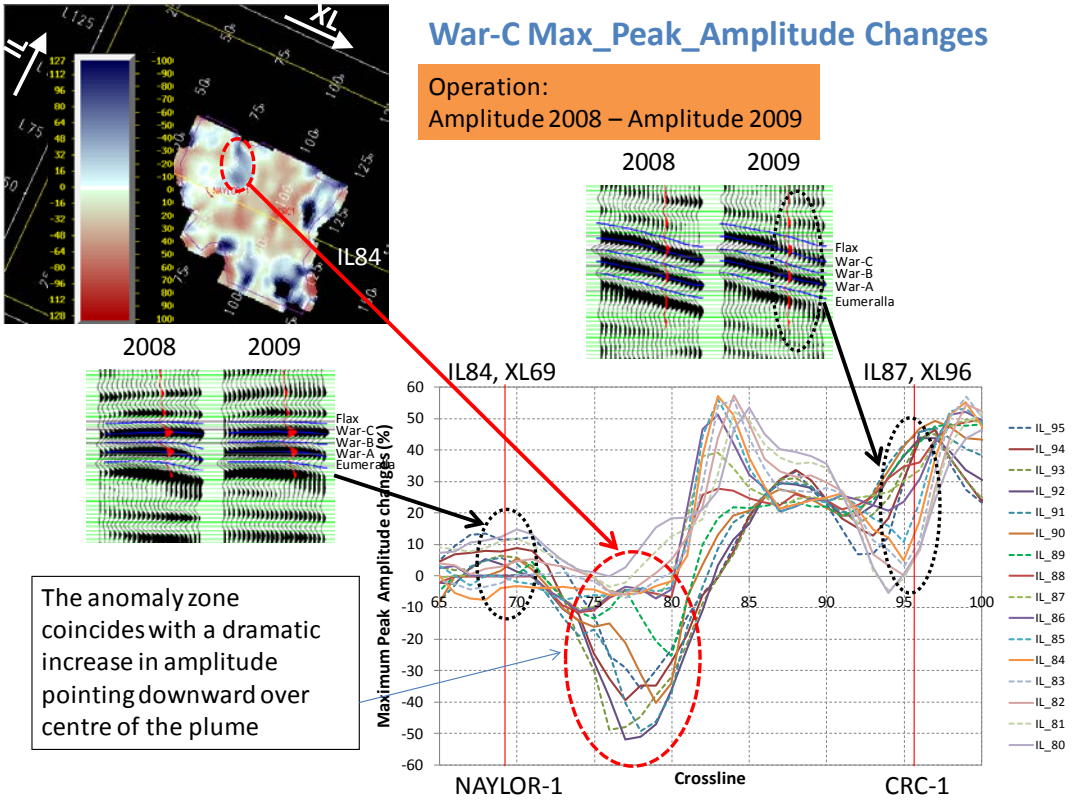

Figure 6.44 Summary of amplitude changes from seismic interpretation.

The maximum peak amplitude changes between 2008 (pre-injection/baseline) and 2009 (monitoring) 3D seismic interpretation reached the maximum of 50% at the "bulls-eye" (red dotted circle), north-west from the two wells. The difference at the "bulls-eye" is represented by negative values; it means the maximum peak amplitude in 2009 (monitoring) 3D seismic interpretation is higher than the maximum peak amplitude of 2008 data (pre-injection/baseline). It is most likely caused by a density

effect as a process of *in-situ* pore fluids replacement. Amplitude changes represented by positive values at Naylor-1 and CRC-1 wells were also observed. It could be interpreted and related to the heterogeneity of the reservoir but it is more likely to be the result of relatively low seismic repeatability.

Extensive numerical analysis combined reservoir models with rock physics models presented in Chapter 5. The fine modelled differences did not agree in magnitude to the field observation. In general, the synthetic model traces agree with the seismic field measurement especially at Naylor-1 well where I do not expect significant changes due to gas cap and existing residual gas. I have observed more changes at the CRC-1 well as expected due to saturation changes (density effect) and possibly pressure changes. It is noted that the 2009 (monitoring) 3D seismic data showed dimming of amplitude at the CRC-1 well which was also observed in the impedance volumes. One assumption is when injection took place, the CO_2 dissolved in water causing lower impedance and hence boosted up the seismic amplitude anomaly at CRC-1. It can be also speculated that CO_2 swept all CH_4 in updip direction.Finally fluid changes in the overlain Flaxman formation could produce similar effects. At present there is no recorded data to prove any of the cases listed. It is howver very likely that relatively low seismic repeatability produced such anomaly.

It is important to remember that residual methane exists throughout the reservoir, making the time-lapse studies challenging. 2008 (pre-injection/baseline) 3D seismic data showed bulls-eye anomaly NE of Naylor-1 well. 2009 (monitoring) 3D seismic data showed similar bull-eye as well but smaller in size and with stronger amplitude. Consequently high negative amplitude anomalies were observed between the two wells on the time-lapse result (2009-2008 difference volume). This could be related to the resistance offered by the methane cap and the reservoir heterogeneity. As a result, the CO_2 is accumulated in a “bulls-eye” like pattern. Such form could have been driven by stratigraphic mechanisms and/or sub-seismic faults. This is the largest time-lapse seismic effect observed in these data sets. Finally this effect could have been amplified by relatively low repeatability of seismic data. Similar amplitude dimming around CRC-1 well (down dip) is also observed in VSP (Pevzner, 2012).

Examination of several 3D impedance volumes showed broadly similar trends within the reservoir with some apparent facies trends orientated approximately NNW-SSE. Figure 6.40 to 6.42 show data slices of the model-based inversion volume at different times between Waarre-C and Waarre-B horizons - which showed the highest impedance difference map, occurred at 6ms below top Waarre-C - that bound the target reservoir. Gradual impedance changes have been observed in different saturation states. The accumulation pathway of CO_2 could be influenced and driven by stratigraphic mechanisms which structurally align above and the below reservoir. This is clearly observed in the time structure map of Waarre-C and Waarre-B.

In general, a reasonable agreement is observed between the seismic, synthetic data and well data. As expected, subtle changes are observed at the Naylor-1 well, while larger changes are observed at the CRC-1 well. A significant anomaly is also observed in the inversion and seismic difference volume data. The magnitude of this anomaly exceeds the predicted one. The cause of these differences is unknown at present. The most likely explanation is that the time-lapse signal is low and would require exceptionally high data repeatability to be properly measured and explained. This was not the case for Otway study. Consequently, the predicted and measured seismic effects can be used as the lower and the upper bound of the expected time-lapse effects at Naylor field, respectively. The method presented here for analysis of a subtle time-lapse signal could be applied to the cases with similar challenges.

Chapter 7 CONCLUSIONS AND RECOMMENDATIONS

7.1 Introduction

The Australia's first sequestration demonstration project, the CO2CRC Otway Project, commenced over the Naylor field in 2005. The Naylor field was produced via a single well, Naylor-1, and rapidly depleted. In 2007, CRC-1 well (injection well) was drilled down-dip from Naylor-1 well (monitoring well) for the purpose of the CO2CRC Otway Project. The logistic for this well was based on the reservoir simulation and seismic time-lapse prediction in this study. The position of CRC-1 well was not optimised with respect to the seismic monitoring objectives and time-lapse study prediction, rather with respect to the project duration and predicted break through time (4-9 months). The CO_2 was injected into Waarre-C sand and by August 2009 about 65,000 tonnes of CO_2 was stored. These effects the main objective than became to investigate if such small amount of CO_2 injected into a depleted gas reservoir could be detected by time-lapse (4D) seismic. Alternative drive for time-lapse seismic application was to monitor potential leaks along the existing large scale fault that surrounds the reservoir.

The availability of time-lapse seismic data was required to analyse. The analysis was hindered by the reservoir small size, heterogeneity, depth, residual gas saturation, high ambient noise (low seismic repeatability), seismic data acquisition issues, etc. To add to this complexity, the base line logs for the pre-production, and now monitoring Naylor-1 well were not available. Hence those needed to be reconstructed in this study.

Considering that the injection took place into a partial saturation zone it became important to accurately predict the time-lapse seismic signal for the monitoring program at this site. Hence the main accomplishments of my research study were:

- Accurately predict the change in elastic properties of Waarre-C through fluid substitution methodology.
- Utilise core sample measurements to increase the accuracy of the time-lapse seismic response prediction.
- Predict the fluid saturation state by using well log analysis and accurate fluid substitution modelling (FSM).
- Perform seismic FSM modelling and inversion. Compare predictions to real time-lapse signal. Assess the change in reservoir saturation state by successive inversions using the predictions of reservoir simulation studies and accompanied updated logs.

7.2 Conclusions

7.2.1 Rock physics model

Pore fluids properties depend on composition, pressure and temperature and strongly influence the seismic properties of the rocks. Hence we need to compute elastic properties of different fluid mixtures to be able to predict seismic response to changes in pore fluid.

In Waarre reservoir, the CO_2 will exist in rocks as a mixed gas and in the supercritical phase due to the *in-situ* depth and temperature of reservoir storage. The compressibility of CO_2 mixed gas in saturated rocks will mimic a gas, while the density will closer to the oil. The higher the CO_2 content the denser the mixed gas. In other words, the density behaviour of CO_2 mixed gas in saturated rocks can vary from a gas to fluid. In Otway case, the CO_2/CH_4 mix will have lower density than pure CO_2. Distribution of CO_2 plume and its CO_2 saturation would be practically impossible to quantify from time-lapse seismic information because of:

1. Deep, small size and thin reservoir, surrounded by faults.
2. Depleted gas field; injection into partially saturated zone.
3. Small quantity of CO_2/CH_4 mix injected.
4. Moderate to poor repeatability of time-lapse seismic.

Therefore, the research presented here was hindered by the above complexities and limitations.

7.2.1.1 Modified fluid substitution

Considering small changes in the reservoir the primary objective of this study became characterisation of the reservoir, its saturation state and subsequent accurate prediction of time-lapse seismic signal. Along this flow I proposed a modified fluid substitution methodology that can accurately predict time-lapse seismic effects due to CO_2 injection into a depleted gas reservoir. For that purpose I combined core tests with logs and various rock physics models to produce a flow suitable for time-lapse signal prediction in a depleted gas reservoir in general.

One of the important point is that my analysis indicates that Vp_{sat} core agree with Vp_{sat} log data when the "effective" K_{grain} is used. Results also suggest that "effective" K_{grain} may be used to represent the average mineralogy of the grains, at least at this site. Petrographic analysis suggested that incorporating "effective" K_{grain} produces reasonable results. In other words, the use of the "effective" K_{grain} is justified by petrographic analysis. Subsequent computing of time-lapse seismic effects is achieved by plugging effective K_{grain} into Gassmann equation. This has increased the modelling precision and changed the predicted effect due to CO_2 injection from 1.5-4.5%, as previously computed to 6%. This is a significant result as 6% changes in AI could be detected by high repeatability seismic surveys. The approach assumed here could be thus useful for future storage sites with similarly challenging geophysical monitoring objectives.

7.2.1.2 Identifying *in-situ* saturation type from well logs

I investigated in-situ saturation type (homogeneous or patchy) from well logs at CRC-1 well (injection well) to derive fluid substitution approach that could increase the accuracy of predicted changes in elastic properties of the reservoir rocks and shed some light to the potential plume distribution in the reservoir. Dry-frame Poisson's ratio and dry-frame moduli inverted from logs assuming homogeneous saturation showed good agreement with ultrasonic core measurement. This suggests that the saturation type is homogeneous (uniform) rather than patchy. Thus, homogeneous saturation is used for fluid substitution and modelling time-lapse seismic response for CO_2 sequestration in the CO2CRC Otway Project. This was important as incorrect saturation type could underestimate or overestimate the changes in the elastic properties of the reservoir arising from injection of CO_2/CH_4 mix. However a small degree of uncertainty remains due to unreliable estimation of shear wave velocity that could affect the result of fluid substitution.

The link between rock physics and microstructure of the sands suggested that the velocity-porosity relations is influenced by the rock texture, grain size variations and increase in clay particles as a pore-filling material. It is hence not improbable that a temporary "patchy" situation could have occurred in the injection period. The calculations with the "static" model certainly do not suggest patchy saturation.

7.2.2 Seismic acoustic impedance inversion and time-lapse studies

To gain additional insight into the reservoir and CO_2 related changes I performed model-based post-stack seismic acoustic inversion. In fact, several inversions were carried out starting with the "baseline case" which incorporated two logs: CRC-1 as measured and Naylor-1 that was reinstated to pre-CO_2 injection state by Gassmann fluid substitution. Using these two wells to tie the post-stack seismic volume is expected to produce the largest inversion "error". Subsequent fluid substitution modellings and inversions were aimed towards the reduction of the inversion error. Hence the modelled fluid saturation case after injection of some 35,000 tonnes of CO_2/CH_4 mix is expected to produce the smallest error with 2009 seismic data. This was a "history" matching exercise applied to seismic data. The results indicated some

changes in the reservoir. However we found it is difficult to quantitatively invert seismic data to accurately estimate CO_2 saturation and its distribution in the reservoir. The primary reason is poor to moderate repeatability of time-lapse seismic data produce. Consequently the expected time-lapse change is of the same magnitude as background noise level. Small size of the seismic volume and some migration artefacts further hinder time-lapse analysis.

Time-lapse analysis of both amplitude and impedance showed a region of anomalously high amplitude and low acoustic impedance between monitoring and injection wells. The location of CO_2 plume is driven by buoyancy in relation to the stratigraphic features. The time-lapse anomaly NE of Naylor-1 is likely to be caused by a channel like feature (possibly increased permeability zone) that can be spotted on the AI cubes. As expected, subtle change in impedance can be seen in Naylor-1 well and bigger changes in CRC-1 well but both are submerged into the background noise level.

Overall the time-lapse seismic anomaly seems to agree with the rock physics predictions and reservoir simulation models. An exception occurs SE of CRC-1 well which is likely caused by CO_2 migrating into the Flaxman formation above Waarre-C. This will cause impedance drop and negative TL anomaly as seen in the analysis (Chapter 6). The observed effects appear to be slightly greater than predicted. This can be explained in many ways. One possibility is that the background noise (poor repeatability) and imperfect processing which did not manage to fully preserve relative amplitude changes (Pevzner, 2012, personal communication) contributed to elevated TL signal. Other possibility is that the reservoir heterogeneity, sub-seismic faults and some effect of CO_2 on the grain bonding could cause elevated response. In any case the observed seismic anomaly exceeds our expectations and predictions derived through the rock physics model, seismic modelling and simulation models. This is likely to be the case in general as the effect of CO_2 onto reservoir property changes is difficult to predict and a "conservative" approach may result in an under-prediction of time-lapse seismic effects. Consequently, the predicted and measured seismic effects can be used as the lower and the upper bound of the expected time-

lapse effects at Naylor field, respectively. The method presented here for analysis of a subtle time-lapse signal could be applied to the cases with similar challenges.

7.3 Recommendations

At the time of this study only the post-stack seismic data from the pre-production (2000) were available for the analysis. The data was recorded with different (sparse) geometry and processed without relative amplitude preservation. It was therefore impossible to include it into my time-lapse study as the pre-production (true baseline) data set. The reservoir setting and properties require also much higher data density (high spatial and temporal resolution) and the application of seismic technologies which are more often used for coal and mineral exploration rather than in oil and gas sector. High data density and bin size of 10x10m used in Otway experiment was unusual at the time of recording. Perhaps nowadays is not so uncommon "thinking" for oil industry to use such parameters.

Despite very weak sources (weight drop, 2008) and (mini-vibrator, 2009), very high data density produced the result worth of analysing. The source change between surveys presented another challenge to time-lapse studies. My analysis suggest that the elastic changes in the reservoir due to only 35,000 tonnes of gas mixture were probably detected despite all the issues related to the source change and intrinsically low signal to noise ratio (weak sources). The later one was largely compensated by high data density and high fold. This suggests that the CO_2 related seismic effects are most likely higher in real rock than actually predicted. To elaborate on this idea further time-lapse studies are required. Those however need to produce much higher data repeatability. This can be achieved by strong sources, permanent geophone (buried) arrays, time-lapse borehole seismic, etc. Then, a methodology for the prediction of time-lapse signal as proposed in this thesis could perhaps be used even for the quantitative prediction of CO_2 related effects.

Reprocessing and re-binning of 2000 3D seismic data and subsequent cross-equalisation with 2008 (pre injection) and 2009, first monitor data sets could go long way in analysing the changes in the reservoir.

7.3.1 Time-lapse studies

The reservoir characterisation at Naylor field was not enough constrained due to the lack of other geophysical and geological information. However the time-lapse prediction of seismic effect was sufficient to develop a monitoring program at Otway site. Of course the end program is a function of funding but the it was clear that that time-lapse seismic methodology is used here primarily to verify CO_2 containment in the reservoir, by not observing any changes between the baseline and the monitor surveys. My study tried to push this limits further by incorporating acoustic impedance analysis using the history matching analogous of a conventional reservoir study.

For further studies at Otway site I would suggest the following:

1. More core sample tests (longer sections to be cored). will enable more effective rock physics studies
2. Time-lapse logging would provide the verification of the rock physics model and firm up prediction of the seismic effects and will enable improved calibration of time-lapse seismic volumes.
3. Permanent surface seismic arrays to achieve better repeatability
4. Strong sources are also desired but it was shown in this case that high data density is equally or even more important.
5. Improved data processing that incorporates surface consistent amplitude processing and pre-stack imaging.
6. Time-lapse studies of seismic anisotropy could enable additional sensitivity needed for the analysis of subtle changes of reservoir properties.
7. Collaboration between disciplines (geology, engineering, geochemistry and geophysics) is essential for analysing complex reservoirs such is found at Otway.

7.3.2 Further research

7.3.2.1 Quantification of CO_2 saturation

The CO2CRC Otway Project stage 2 will be conducted in the near future. Approximately 10,000 tonnes CO_2 will be injected into saline aquifer above Waarre reservoir. This will provide new challenges to the researches but it should not be forgotten to carry on study of Waarre reservoir with perhaps, more modern and sensitive methodologies. This could potentially provide additional information regarding residual trapping, plume distribution, CO_2 interaction with surrounding faults, etc.

7.3.2.2 "Dirty" CO_2 (mixed gases) properties

The "dirty" mix used in Otway experiment makes the rock physics studies more difficult. On the positive side it elevates the seismic effect and gives chance to time-lapse methodology to detect changes in the reservoir. However, this methodology needs to be applied at different, much higher, level at this site to produce reliable results. Novel approaches may need to involve seismic anisotropy, attenuation and dispersion studies to be able to quantify the changes in the reservoir. Seismic attenuation is more sensitive to pore fluid properties than seismic velocity. Attempt to measure absolute attenuation (1/Q) of surface seismic suffer from spectral contamination caused by thin bed tuning, scattering effect, multiple interference and velocity dispersion. Thus a single vintage of attenuation measurement must be interpreted with care as the amount of spectral contamination can change vertically and laterally, making even relative comparisons within a single stratigraphic layer difficult. However if two vintages of data are taken with good repeatability, then the effects of spectral contamination may cancel, allowing accurate measurements of changes in attenuation between vintages of data. An accurate 4D measurement of attenuation could give insights into fluid and pressure migration within the reservoir. Adding time-lapse seismic anisotropy study could further highlight stress-anisotropy effects in relation to pore fluid replacement.

7.3.2.3 Dissolved CO_2 properties

Further laboratory work is required to analyse migration, trapping and dissolution of a dirty gas mix (multi fluid flow). What remains unclear also is if any chemical changes have happened in the reservoir and if so, are they significant for the monitoring studies? The Otway study shows clearly how initially foreseen simple straightforward experiment became readily difficult to master. In other words to fully explain and quantify the CO_2 injection related effects much finer measurements, sophisticated and expensive technologies may need to be deployed.

7.4 Closing remarks

The CO2CRC Otway project has two stages. My research is part of the first stage. The CO_2 injection has now been ceased after 65,000 tonnes of CO_2 has been injected into Waarre-C sand. The geophysical results are encouraging and at least clearly show that we can use time-lapse seismic methodology to verify the CO_2 containment in the reservoir. Also we can use it in the same way to detect if any CO_2 has escaped into the overlain aquifers as such case would produce very strong time-lapse seismic signal. The second stage is underway and some of the methodologies discussed and proposed in this thesis are planned to be implemented in stage 2 of Otway program.

REFERENCES

Aki, K., and P.G. Richards, 1980, Quantitave seismology: W. H. Freeman and Company.

Arts, R., O. Eiken, A. Chadwick, P. Zweigel, L.v.d. Meer, and N. Zinszner, 2004, Monitoring of CO_2 injected at Sleipner using time-lapse seismic data: Energy, **29**, 1383-1392.

Arts, R., O. Eiken, A. Chadwick, P. Zweigel, L. van der Meer, B. Zinszner, J. Gale, and Y. Kaya, 2003, Monitoring of CO2 Injected at Sleipner Using Time Lapse Seismic DataGreenhouse Gas Control Technologies - 6th International Conference, 347-352, Pergamon.

Arts, R.J., P. Zweigel, and A.E. Lothe, 2000, Reservoir geology of the Utsira sand in The Southern Viking graben area - a site for potential CO_2 storage: Presented at 62nd EAGE Conf

Avseth, P., T. Mukerji, and G. Mavko, 2005, Quantitative Seismic Interpretation: Applying Rock Physics Tools to Reduce Interpretation Risk: Cambridge University Press.

Bachu, S., 2000, Sequestration of CO_2 in geological media: criteria and approach for site selection in response to climate change: Energy Conversion & Management, **41**, 953-970.

Bachu, S., W.D. Gunter, and E.H. Perkins, 1994, Aquifer disposal of CO_2: hydrodynamic and mineral trapping: Energy Conversion and Management, **35**, no. 4, 269-279.

Baines, S.J., and R.H. Worden, 2004, Geological storage of carbon dioxide: Geological Society London Special Publications, **233**, no. 1, 1.

Barnes, A.E., 1998, The complex seismic trace made simple: The Leading Edge, **17**, no. 4, 473-476.

Barnes, A.E., 2007, A tutorial on complex seismic trace analysis: Geophysics, **72**, no. 6, W33-W43.

Batzle, M., and Z. Wang, 1992, Seismic properties of pore fluids: Geophysics, **57**, no. 11, 1396-1408.

Batzle, M.L., D.H. Han, and R. Hofmann, 2006, Fluid mobility and frequency-dependent seismic velocity - direct measurement: Geophysics, **71**, no. 1, N1-N9.

Bell, R.E., R. Anderson, and L.F. Pratson, 1997, Gravity gradiometry resurfaces: The Leading Edge, **16**, no. 1, 55-59.

Benson, R.D., and T.L. Davis, 1998, Time-lapse seismic monitoring and dynamic reservoir characterization, Central Vacuum unit, Lea County, New Mexico: SPE (Society of Petroleum Engineers) Reservoir Engineering ; Vol/Issue: 4:4.

Biddle, K.T., and C.C. Wielchowsky, 1994, Hydrocarbon Traps: Memoirs-American Association of Petroleum Geologists, 219-219.

Biot, M.A., 1956, Theory of Propagation of Elastic Waves in a Fluid-Saturated Porous Solid. I. Low-Frequency Range: The Journal of the Acoustical Society of America, **28**, 168.

—, 1957, The elastic coefficients of the theory of consolidation: Journal of applied mechanics, **24**, no. 594-601, 206.

Birch, F., 1961, The velocity of compressional waves in rocks to 10 kilobars, Part 2: J. Geophys. Res, **66**, no. 7, 2199-2224.

Bracewell, R., and P.B. Kahn, 1966, The Fourier Transform and Its Applications: American Journal of Physics, **34**, 712.

Bradshaw, B.E., G. Simon, J. Bradshaw, and V. Mackie, 2005, GEODISC Research: Carbon Dioxide sequestration potential of Australia's Coal Basins:

Bradshaw, J., B.E. Bradshaw, G. Allinson, A.J. Rigg, V. Nguyen, and L. Spencer, 2002, The potential for geological sequestration of CO_2 in Australia: Preliminary findings and implications for new gas field development: APPEA Journal.

Bradshaw, J., and A. Rigg, 2001, The GEODISC program: Research into geological sequestration of CO_2 in Australia: Environmental Geosciences, **8**, no. 3, 166-175.

Brie, A., F. Pampuri, A.F. Marsala, and O. Meazza, 1995, Shear sonic interpretation in gas-bearing sands: SPE Ann. Tech. Conf, 701-710.

Brown, A.R., 2004, Interpretation of three-dimensional seismic data: The Society of Exploration Geophysics.

Brown, L.T., 2002, Integration of rock physics and reservoir simulation for the interpretation of time-lapse seismic data at Weyburn Field, Saskatchewan: M.Sc. thesis, Colorado School of Mines.

Buffin, A.J., 1989, Waarre Sandstone development within the Port Campbell Embayment: The APPEA Journal, **29**, no. 1, 299-311.

Burcik, E.J., 1979, Properties of Petroleum Reservoir Fluids: IHRD.

Carcione, J., S. Picotti, D. Gei, and G. Rossi, 2006, Physics and Seismic Modeling for Monitoring CO_2 Storage: Pure and Applied Geophysics, **163**, no. 1, 175-207.

CGG, 2000, Final report: Seismic data processing OCV00 Curdie Vale 3D: Santos Petroleum, Ltd.

Chadwick, R.A., R. Arts, and O. Eiken, 2005, 4D seismic quantification of a growing CO_2 plume at Sleipner, North Sea, SEG Expanded.

Chadwick, R.A., P. Zweigel, U. Gregersen, G.A. Kirby, S. Holloway, and P.N. Johannessen, 2002, Geological characterization of CO_2 storage sites: Lessons from Sleipner, northern North Sea, SEG Expanded, 1–4.

CO2CRC, 2008, http://www.co2crc.com.au/otway, accessed 16 December.

Cook, P.J., 2006, Carbon dioxide capture and geological storage: research, development and application in Australia: International Journal of Environmental Studies, **63**, no. 6, 731-749.

Cook, P.J., A. Rigg, and J. Bradshaw, 2000, Putting it back where it came from: is geological disposal of carbon dioxide an option for Australia?: APPEA Journal, **1**.

Cooke, D., 1981, Generalized linear inversion of reflection seismic data, Colorado School of Mines.

Cooke, D.A., and W.A. Schneider, 1983, Generalized linear inversion of reflection seismic data: Geophysics, **48**, no. 6, 665-676.

Crampin, S., 1989, Suggestions for a consistent terminology for seismic anisotropy 1: Geophysical Prospecting, **37**, no. 7, 753-770.

Dance, T., L. Spencer, and J. Xu, 2009, Geological Characterisation of the Otway Project Pilot Site: What a Difference a Well Makes: Energy Procedia, **I**, 2871-2878.

Dance, T., and B. Vakarelov, 2007, Sedimentology of the Flaxman Formation and Waarre C Formation from CRC-1 Cores 5&6: CO2CRC Report

Davidson, J., P. Freund, and A. Smith, 2001, Putting carbon back in the ground: IEA Greenhouse Gas R&D Programme.

Davis, T.L., and R.D. Benson, 2001, Monitoring production processess by 4-D multicomponent seismic surveys at Vacuum Field, New Mexico: Presented at SEG Int'l Exposition and Annual Meeting

—, 2004, Weyburn field seismic monitoring project: Presented at SEG Int'l Exposition and 74th Annual Meeting

Davis, T.L., M.J. Terrell, R.D. Benson, R. Cardona, R.R. Kendall, and R. Winarsky, 2003, Multicomponent seismic characterization and monitoring of the CO_2 flood at Weyburn Field, Saskatchewan: The Leading Edge, 696-697.

Dodds, K., D. Sherlock, M. Urosevic, D. Etheridge, D.d. Vries, and S. Sharma, 2006, Developing a monitoring and verification scheme for a pilot project, Otway Basin, Australia: Presented at GHGT-8

DOE, 2008, Carbon sequestration Atlas of United States and Canada: Department of Energy. Office of Fossil Energy, National Energy Technology Laboratory.

Dvorkin, J., D. Moos, J.L. Packwood, and A.M. Nur, 1999, Identifying patchy saturation from well logs: Geophysics, **64**, no. 6, 1756-1759.

Dvorkin, J., and A. Nur, 1996, Elasticity of high-porosity sandstones: Theory for two North Sea data sets: Geophysics, **61**, no. 5, 1363-1370.

—, 1998, Acoustic signatures of patchy saturation.

Efthymiou, E., 2008, Time-lapse seismic analysis of pre-production and post-production data, Naylor gas field, Australia: B.Sc (Honours) thesis, Curtin University.

EIA, 2011, Annual Energy Outlook 2011: U.S. Department of Energy.

—, 2011, International Energy Outlook 2011: U.S. Department of Energy.

Ennis-King, J., and L. Paterson, 2001, Reservoir engineering issues in the geological disposal of carbon dioxide, SEG Expanded.

Esmersoy, C., C. Chang, M. Kane, R. Coates, B. Tichelaar, and E. Quint, 1998, Acoustic imaging of reservoir structure from a horizontal well: The Leading Edge, **17**, no. 7, 940-946.

Fanchi, J.R., 2001, Feasibility of monitoring CO_2 sequestration in a mature oil field using time-lapse seismic analysis: Society of Petroleum Engineers, no. 66569.

Faulkner, A., 2000, A sequence stratigraphy of the late Cretaceous Sherbrook Group, Shipwreck Trough, Otway Basin.: B.Sc. (Hon) thesis, University of Adelaide.

Flett, M.A., R.M. Gurton, and I.J. Taggart, 2004, Heterogeneous saline formations: Long-term benefits for geo-sequestration of greenhouse gases, SEG Expanded, 5–9.

Forster, A., B. Norden, K. Zinck-Jorgensen, P. Frykman, J. Kulenkampff, E. Spangenberg, J. Erzinger, M. Zimmer, J. Kopp, and G. Borm, 2006, Baseline characterization of the CO2SINK geological storage site at Ketzin, Germany: Environmental Geosciences, **13**, no. 3, 145-161.

Freifeld, B.M., T.M. Daley, S.D. Hovorka, J. Henninges, J. Underschultz, and S. Sharma, 2008, Recent advances in well-based monitoring of CO_2 sequestration: Presented at GHGT-9

Gasperikova, E., and G.M. Hoversten, 2006, A feasibility study of nonseismic geophysical methods for monitoring geologic CO_2 sequestration: The Leading Edge, **25**, 1282.

Gasperikova, E., G.M. Hoversten, and F. Cassassuce, 2004, A feasibility study of geophysical methods for monitoring geologic CO_2 sequestration: Presented at SEG Int'l Exposition and 74th Annual Meeting

Gassmann, F., 1951, Über die elastizität poröser medien.

GeoscienceAustralia, 2008, Regional Chronostratigraphic Chart, http://www.ga.gov.au/energy/province-sedimentary-basin-geology/petroleum/offshore-southern-australia/otway.html.

Grochau, M.H., and B. Gurevich, 2008, Investigation of core data reliability to support time-lapse interpretation in Campos Basin, Brazil: Geophysics, **73**, no. 2, E59-E65.

Gunter, W.D., T. Gentzis, B.A. Rottenfusser, and R.J.H. Richardson, 1997, Deep coalbed methane in Alberta, Canada: a fuel resource with the potential of zero greenhouse gas emissions: Energy Conversion and Management, **38**, 217-222.

Gurevich, B., 2004, A simple derivation of the effective stress coefficient for seismic velocities in porous rocks: Geophysics, **69**, no. 2, 393-397.

Hampson-Russell., L., 2010, STRATA: Seismic Inversion Workshop.

Hashin, Z., and S. Shtrikman, 1963, A variational approach to the theory of the elastic behaviour of multiphase materials: Journal of the Mechanics and Physics of Solids, **11**, no. 2, 127-140.

Herawati, I., 2002, The use of time-lapse P-wave impedance inversion to monitor a CO_2 flood at Weyburn field, Saskatchewan: M.Sc. thesis, Colorado School of Mines.

Herawati, I., and T. Davis, 2003, The use of timelapse P-wave impedance inversion to monitor CO_2 flood at Weyburn Field, Saskatchewan, Canada: 73rd Annual International Meeting, SEG: Expanded Abstracts, 1350–1353.

Hill, R., 1952, The Elastic Behaviour of a Crystalline Aggregate: Proceedings of the Physical Society. Section A, **65**, no. 5, 349.

Hitchon, B., 1996, Aquifer Disposal of Carbon Dioxide: Hydrodynamic and Mineral Trapping: Proof of Concept: Geoscience Pub.

Holloway, S., 1997, An overview of the underground disposal of carbon dioxide: Energy Conversion and Management, **38**, no. Supplement 1, S193-S198.

Hovorka, S.D., S.M. Benson, C. Doughty, B.M. Freifeld, S. Sakurai, T.M. Daley, Y.K. Kharaka, M.H. Holtz, R.C. Trautz, and H.S. Nance, 2006, Measuring permanence of CO_2 storage in saline formations: the Frio experiment: Environmental Geosciences, **13**, no. 2, 105-121.

Hovorka, S.D., and K. Cohen, 2006, Update on the Frio Brine Pilot: 15 months after injection, SEG Expanded.

Hovorka, S.D., and P.R. Knox, 2003, Frio Brine Sequestration Pilot in the Texas Gulf Coast: Greenhouse Gas Control Technologies, **1**, 583-586.

IEA, 2003, World Energy Outlook 2003: International Energy Agency.

—, 2011, World Energy Outlook 2011: International Energy Agency.

Ikelle, L.T., and L. Amundsen, 2005, Introduction to petroleum seismology: Society of Exploration Geophysics.

Juhlin, C., R. Giese, K. Zinck-Jørgensen, C. Cosma, H. Kazemeini, N. Juhojuntti, S. Lüth, B. Norden, and A. Förster, 2007, 3D baseline seismics at Ketzin, Germany: The COSINK project: Geophysics, **72**, B121.

Kallweit, R.S., and L.C. Wood, 1982, The limits of resolution of zero-phase wavelets: Geophysics, **47**, no. 7, 1035-1046.

Katahara, K.W., 2005, Effect of mineral Vp/Vs on rock Vp/Vs.

Katz, D.L.V., 1959, Handbook of natural gas engineering.

Klimeck, R., 2000, Entwicklung einer Fundamentalgleichung fur Erdgase fur das Gas- und Flussigkeitsgebiet sowie das Phasengleichgewicht, Ruhr-Universitat Bochum.

Klimeck, R., R. Span, and W. Wagner, 1999, Development of a reference equation for thermal and caloric properties of natural gases. Phase 1: theoritical results: Lehrstuhl fur Thermodynamik, Ruhr-Universitat Bochum

Knight, R., J. Dvorkin, and A. Nur, 1998, Acoustic signatures of partial saturation: Geophysics, **63**, no. 1, 132-138.

Krief, M., J. Garat, J. Stellingwerff, and J. Ventre, 1990, A petrophysical interpretation using the velocities of P and S waves (full-waveform sonic): The Log Analyst, **31**, no. November, 355-369.

Landmark, 2003, PostStack Family Reference Manual.

Landrø, M., 2001, Discrimination between pressure and fluid saturation changes from time-lapse seismic data: Geophysics, **66**, no. 3, 836-844.

Landrø, M., H.H. Veire, K. Duffaut, and N. Najjar, 2003, Discrimination between pressure and fluid saturation changes from marine multicomponent time-lapse seismic data: Geophysics, **68**, 1592.

Lang, S., C.N. Dee, and P.W. Best, 1989, The Otway Basin: The APPEA Journal, **29**, no. 1, 417-429.

Leahy, M., 2009, Personal communication.

Lewis, C.A., and J.H. Shinn, 2001, Global Warming-An Oil and Gas Company Perspective: Prospects for Geologic Sequestration?: Environmental Geosciences, **8**, no. 3, 177-186.

Li, R., M. Urosevic, and K. Dodds, 2006, Prediction of 4D seismic responses for the Otway Basin CO_2 sequestration site: SEG Technical Program Expanded Abstracts, **25**, no. 1, 2181-2185.

Lindseth, R.O., 1979, Synthetic sonic logs; a process for stratigraphic interpretation: Leading edge, **44**, no. 1, 3.

Lumley, D., D. Adams, R. Wright, D. Markus, and S. Cole, 2008, Seismic monitoring of CO_2 geo-sequestration: realistic capabilities and limitations: SEG Technical Program Expanded Abstracts, **27**, no. 1, 2841-2845.

Lumley, D.E., 2001, The next wave in reservoir monitoring: The instrumented oil field: The Leading Edge, **20**, no. 6, 640-648.

Lumley, D.E., R.A. Behrens, and Z. Wang, 1997, Assessing the technical risk of a 4-D seismic project: The Leading Edge, **16**, no. 9, 1287-1291.

Majer, E.L., T.M. Daley, V. Korneev, D. Cox, J.E. Peterson, and J.H. Queen, 2006, Cost-effective imaging of CO_2 injection with borehole seismic methods: The Leading Edge, **25**, no. 10, 1290-1302.

Marion, D., and A. Nur, 1991, Pore-filling material and its effect on velocity in rocks: Geophysics, **56**, no. 2, 225-230.

Mavko, G., and D. Jizba, 1991, Estimating grain-scale fluid effects on velocity dispersion in rocks: Geophysics, **56**, no. 12, 1940-1949.

Mavko, G., T. Mukerji, and J. Dvorkin, 1998, The rock physics handbook - tools for seismic analysis in porous media: Cambridge University Press.

McKenna, J.J., 2004, Seismic response to CO_2 storage in a saline aquifer: PhD. thesis, Curtin University of Technology.

McKenna, J.J., B. Gurevich, M. Urosevic, and B.J. Evans, 2003, Rock physics - Application to geological storage of CO_2: APPEA Journal, **43**, no. I, 567-576.

MNP, 2008, Global CO_2 emissions: increase continued in 2007, http://www.mnp.nl/en/publications/2008/GlobalCO2emissionsthrough2007.html, accessed September.

Myer, L.R., G.M. Hoversten, E. Gasperikova, J. Gale, and Y. Kaya, 2003, Sensitivity and Cost of Monitoring Geologic Sequestration Using GeophysicsGreenhouse Gas Control Technologies - 6th International Conference, 377-382, Pergamon.

Nye, J.F., 1985, Physical Properties of Crystals: Their Representation by Tensors and Matrices: Oxford University Press.

O.Kunz, R. Klimeck, W. Wagner, and M. Jaeschke, 2007, The GERG-2004 wide-range equation of state for natural gases and other mixtures.

Oldenburg, D.W., T. Scheuer, and S. Levy, 1983, Recovery of the acoustic impedance from reflection seismograms: Geophysics, **48**, 1318-1337.

Partridge, A.D., 2001, Revised stratigraphy of the Sherbrook Group, Otway Basin. : Presented at PESA Eastern Australasian Basins Symposium

Peng, D.Y., and D.B. Robinson, 1976, A new two-constant equation of state: Ind. Eng. Chem. Fundam., **15**, 59-64.

Pevzner, R., 2012, Personal communication.

Pevzner, R., and V. Shulakova, 2009, Personnal communication.

Raymer, L.L., E.R. Hunt, and J.S. Gardner, 1980, An improved sonic transit time-to-porosity transform: Presented at Trans. Soc. Prof. Well Log Analyst, 21st Annual Logging Symposium

Reeves, S., 2001, Geologic sequestration of CO_2 in deep, unmineable coalbeds: An integrated research and commercial-scale field demonstration project. : Presented at International Coalbed Methane Symposium

Reeves, S.R., 2003, Enhanced CBM recovery, coalbed CO_2 sequestration assessed: Oil & Gas journal, **101**, no. 27, 49-53.

Ricker, N., 1955, Propagation of Seismic Wavelets: The Journal of the Acoustical Society of America, **27**, 199.

Riddiford, F., C.B. Iain Wright, T. Espie, A. Tourqui, and A. Sonatrach, 2005, Monitoring geological storage the In Salah Gas CO_2 Storage Project: Greenhouse Gas Control Technologies: Proceedings of the 7th International Conference on Greenhouse Gas Control Technologies: 5-9 September 2004, Vancouver, Canada.

Rijks, E.J.H., 1991, Seismic interpretation 29; attribute extraction; an important application in any detailed 3-D interpretation study: The Leading Edge, **10**, no. 9, 11.

Robertsson, J.O.A., and C.H. Chapman, 2000, An efficient method for calculating finite-difference seismograms after model alterations: Geophysics, **65**, no. 3, 907-918.

Robertsson, J.O.A., S. Ryan-Grigor, C.M. Sayers, and C.H. Chapman, 2000, A finite-difference injection approach to modeling seismic fluid flow monitoring: Geophysics, **65**, no. 3, 896-906.

Russell, B., 1988, Introduction to seismic inversion methods: Society of Exploration Geophysicists.

Russell, B., and D. Hampson, 2006, The old and the new in seismic inversion: CSEG Recorder, no. December.

Sakurai, S., T.S. Ramakrishnan, A. Boyd, N. Mueller, and S. Hovorka, 2006, Monitoring saturation changes for CO_2 sequestration: Petrophysical support of the frio brine pilot experiment: Petrophysics(Houston, Tex.), **47**, no. 6, 483-496.

Schacht, U., 2008, Petrological investigations of CRC-1 core plug samples: CO2CRC

Scottish Carbon Capture and Storage, 2013, http://www.geos.ed.ac.uk/sccs/home/expertise/map.html

Sheriff, R.E., 1991, Encyclopedic dictionary of exploration geophysics: Society of Exploration Geophysicists.

Sheriff, R.E., and L.P. Geldart, 1995, Exploration seismology: Cambridge University Press.

Siggins, A.F., 2006, Velocity-effective stress response of CO_2 - saturated sandstones: Exploration Geophysics, **37**, 60-66.

Siggins, A.F., L. Mark, and W. Putri, 2009, Laboratory calibration of the seismo-acoustic response of CO_2 saturated sandstones: Presented at European Geosciences Union

Simmons, J.L., and M.M. Backus, 1994, AVO modeling and the locally converted shear wave: Geophysics, **59**, no. 8, 1237-1248.

Skov, T., H.G. Borgos, K.A. Halvorsen, T. Randen, and L. Sonneland, 2002, Monitoring and characterization of a CO_2 storage site: 56th Conference, SEG Expanded, 1-4.

Spencer, L., and F.L. Pedalina, 2006, Otway Basin Pilot Project, Naylor Field, Waarre Formation Unit C; Reservoir Static Models: Geoscience Australia

Spencer, L., J.-Q. Xu, F. LaPedalina, and G. Weir, 2006, Site characterisation of the Otway Basin carbon dioxide geo-sequestration pilot project in Victoria, Australia: GHGT-8, SEG Expanded.

Spycher, N., K. Pruess, and J. Ennis-King, 2003, CO_2-H_2O mixtures in the geological sequestration of CO_2. I. Assessment and calculation of mutual solubilities from 12 to 100° C and up to 600 bar: Geochimica et Cosmochimica Acta, **67**, no. 16, 3015-3031.

Stevens, S.H., V.A. Kuuskraa, and J. Gale, 2001, Sequestration of CO_2 in depleted oil and gas fields: global capacity, costs, and barriers, SEG Expanded.

Streit, J.E., and A.F. Siggins, 2005, Predicting, monitoring and controlling geomechanical effects of CO_2 injection.

Taner, M.T., F. Koehler, and R.E. Sheriff, 1979, Complex seismic trace analysis: Geophysics, **44**, 1041.

Taner, M.T., and R.E. Sheriff, 1977, Application of Amplitude, Frequency, and Other Attributes to Stratigraphic and Hydrocarbon Determination," Seismic

Stratigraphy-Applications to Hydrocarbon Exploration: Am. Assoc. of Petr. Geol., Memoir, **26**, 301-327.

Telford, W.M., L.P. Geldart, and R.E. Sheriff, 1990, Applied geophysics: Cambridge University Press.

Terrell, M.J., T.L. Davis, L.T. Brown, and R. Fuck, Seismic monitoring of a CO_2 flood at Weyburn field, Saskatchewan, Canada: demonstrating the robustness of time-lapse seismology, Colorado School of Mines, USA.

Thomas, L.K., R.W. Hankinson, and K.A. Phillips, 1970, Determination of acoustic velocities for natural gas: Journal of Petroleum Technology, **22**, 889-892.

Thompson, L., 2002, Understanding seismic anisotropy in exploration and exploitation: Society of Exploration Geophysicists.

Tura, A., and D.E. Lumey, 1999, Estimating pressure and saturation changes time-lapse AVO data.

Urosevic, M., R. Pevzner, A. Kepic, V. Shulakova, P. Wisman, and S. Sharma, 2009, Time-lapse seismic monitoring of CO_2 injection into a depleted gas reservoir - Naylor field, Australia: The Leading Edge.

Vargaftik, N.B., 1975, Handbook of physical properties of liquids and gases: Hemisphere Publishing Corporation.

Wang, Z., 1997, Feasibility of time-lapse seismic reservoir monitoring: The physical basis: The Leading Edge, **16**, no. 9, 1327-1330.

Wang, Z., 2001, Fundamentals of seismic rock physics: Geophysics, **66**, no. 2, 398-412.

Wang, Z., M.E. Cates, and R.T. Langan, 1998, Seismic monitoring of CO_2 flood in a carbonate reservoir: a rock physics study: Geophysics, **63**, no. 5, 1604-1617.

Wang, Z., and A. Nur, 2000, Seismic and acoustic velocities in reservoir rocks, recent developments: Geophysics reprint series, 8-23.

Watson, M.N., C.J. Boreham, and P.R. Tingate, 2004, Carbon dioxide and carbonate cements in the Otway basin: implications for geological storage of carbon dioxide: APPEA Journal, **44**, no. 1, 703-720.

Watson, M.N., and C.M. Gibson-Poole, 2005, Reservoir selection for optimised geological injection and storage of carbon dioxide: a combined geochemical and stratigraphic perspective: 4th Annual Conference on Carbon Capture and Sequestration: The fourth annual conference on carbon capture and storage.

National Energy Technology Laboratory, US Department of Energy, Alexandria, 2–5.

White, J.E., 1983, Underground Sound: Application of Seismic Waves: Elsevier Science Ltd.

Widess, M.B., 1973, How thin is a thin bed?: Geophysics, **38**, no. 6, 1176-1180.

Winterstein, D.F., 1990, Velocity anisotropy terminology for geophysicists: Geophysics, **55**, 1070.

Wisman, P., T. Dance, U. Schacht, and M. Urosevic, 2008, Integrated rock physics models for improved 4D seismic monitoring of CO_2 storage sites: Presented at CO2CRC Research Symposium

Wisman, P., D. Sherlock, and M. Urosevic, 2005, Assessment of existing Otway 3D seismic data: Presented at CO2CRC Symposium

Wisman, P., and M. Urosevic, 2007, Geophysical modelling comparison at varying saturation and pressure: CO_2 sequestration pilot project at Otway Basin: Presented at 19th Geophysical Conference and Exhibition

Wood, A.B., 1955, A Textbook of Sound: The Physics of Vibrations.

Wulff, A., A. Gerhardt, T. Ridsdill-Smith, and M. Smith, 2008, The role of rock physics for the Enfield 4D seismic monitoring project: Exploration Geophysics, **39**, 108-114.

Xu, J., 2006, Personal communication.

—, 2007, The Otway Project flow modeling: peer-review meeting.

Xue, Z., and T. Ohsumi, 2004, Seismic wave monitoring of CO_2 migration in water-saturated porous sandstone: Exploration Geophysics, **35**, 25-32.

Xue, Z., D. Tanase, and J. Watanabe, 2006, Estimation of CO_2 saturation from time-lapse CO_2 well logging in an onshore aquifer, Nagaoka, Japan: Exploration Geophysics, **37**, 111–121.

Yilmaz, O., 2001, Seismic data analysis: processing, inversion, and interpretation of seismic data: Society of Exploration Geophysics.

Yordkayhun, S., 2D and 3D Seismic Surveying at the CO2SINK Project Site, Ketzin, Germany: The Potential for Imaging the Shallow Subsurface: Digital Comprehensive Summaries of Uppsala Dissertations from the Faculty of Science and Technology.

Every reasonable effort has been made to acknowledge the owners of copyright material. I would be pleased to hear from any copyright owner who has been omitted or incorrectly acknowledged.